

Dissertation
submitted to the
Combined Faculties of the Natural Sciences and for Mathematics
of the Ruperto-Carola University of Heidelberg, Germany
for the degree of
Doctor of Natural Sciences

presented by

Ir. Gerrit Lambertus Heuvelman
born in: Rijssen, The Netherlands

Oral examination: 16 July 2008

Development and design of
a spatially and temporally resolved
fluorescence fluctuation microscope
for the analysis of molecular
mobilities and interactions

Referees: Prof. Dr. Dr. Christoph Cremer
PD Dr. Karsten Rippe

Entwicklung und Design eines räumlich und zeitlich aufgelösten Fluktuationsmikroskops für die Analyse von molekularen Bewegungen und Wechselwirkungen

Ein räumlich und zeitlich aufgelöstes Fluktuationsmikroskop (STFM) wurde für die schnelle Bildaufnahme und die Messung und Visualisierung der Beweglichkeiten und Wechselwirkungen von fluoreszenzmarkierten Partikeln entwickelt. Das Instrument erweitert das Konzept eines punktkonfokalen Laser-scannenden Mikroskops zur Beleuchtung und Detektion entlang einer Linie. Für die Konstruktion und die Anwendung des STFM wurden eine theoretische Beschreibung der Strahlgeometrie, der Punkt-Aufweitungsfunktionen und der Auto- und Kreuz-Korrelationsfunktionen abgeleitet. Das entwickelte Gerät ermöglicht eine schnelle konfokale Bildaufnahme und erlaubt die räumlich aufgelöste Detektion der Konzentrationsfluktuationen von Partikeln bis zu einer Zeitauflösung von 15 μ s, parallel gemessen an einigen hundert Punkten. Ein optisches Auflösungsvermögen von 200 x 380 x 700 nm in x-, y- und z-Richtung wurde experimentell bestimmt und die räumlich aufgelösten Fluktuationen von fluoreszenten Nanopartikeln wurden ausgewertet. Schließlich wurden die Möglichkeiten des STFM in Bezug auf die schnelle Bildaufnahme und Beweglichkeitsmessung angewandt, um PML-Kernkörper und grün-fluoreszierendes Protein (GFP) in lebenden Zellen zu untersuchen. Sowohl in vitro als auch in vivo mit dem STFM durchgeführte Fluoreszenz-Korrelationsspektroskopie-Experimente wurden mit Einzelpunkt-Messungen an einem kommerziellen Punkt-Konfokal-Mikroskop und -FCS-System verglichen. Die Ergebnisse zeigen die einzigartigen Möglichkeiten des STFM, die von der Position abhängige diffusive Translokation von Makromolekülen in lebenden Zellen mit sehr hoher Zeitauflösung zu charakterisieren.

Development and design of a spatially and temporally resolved fluorescence fluctuation microscope for the analysis of molecular mobilities and interactions

A spatial and temporal fluctuation microscope (STFM) was developed for fast imaging as well as the measurement and visualisation of mobilities and interactions of fluorescently labeled particles. The instrument extends the concept of a point confocal laser-scanning microscope to illumination and detection along a line. For the construction and application of the STFM, theoretical descriptions of the beam geometry, the point spread functions and the fluorescence auto- and cross-correlation fit functions were derived. The final system provides fast confocal imaging up to 30 images per second and allows for the spatially resolved detection of particle concentration fluctuations down to 15 μ s time resolution at hundreds of points in parallel. An optical resolution of 200 x 380 x 700 nm in x-, y- and z-direction was determined experimentally, and the spatially resolved fluctuations of fluorescent quantum dots were evaluated. Finally, the capabilities of the STFM in terms of fast imaging and mobility measurements were applied to studies of PML nuclear bodies and green fluorescent protein in living cells. Both the in vitro and the in vivo fluorescence correlation spectroscopy experiments conducted with the STFM were compared to single point measurements with a commercial point-confocal microscope and FCS setup. The results demonstrate the unique capabilities of the STFM for the characterisation of position-dependent diffusive translocations of macromolecules in the cell with very high time resolution.

In the beginning God created the heaven and the earth. And the earth was without form, and void; and darkness [was] upon the face of the deep. And the Spirit of God moved upon the face of the waters. And God said, Let there be light: and there was light. And God saw the light, that [it was] good: and God divided the light from the darkness. And God called the light Day, and the darkness he called Night. And the evening and the morning were the first day.

Genesis 1:1-5 (according to the authorized King James version of 1611)

Contents

1 Introduction.....	1
2 Methods and instruments used for the implementation of the STFM.....	5
2.1 Optical microscopy-based techniques.....	5
2.1.1 Confocal laser-scanning microscopy.....	5
2.1.2 Single particle tracking microscopy.....	8
2.1.3 Fluorescence correlation spectroscopy.....	9
2.2 Derivation of a description for the PSF of the confocal microscope.....	13
2.2.1 Illumination, fluorescence and detection.....	13
2.2.2 Confocal illumination and detection geometry.....	15
2.2.3 Approximated point spread function for small numerical aperture.....	17
2.2.4 Illumination point spread function.....	17
2.2.5 Detection point spread function.....	19
2.2.6 The detection probability and its fit function.....	20
2.3 Theory of FCS in a point confocal setup.....	22
2.3.1 The general form of the correlation function.....	22
2.3.2 The correlation function for the case of free diffusive mobility.....	24
2.4 Matrix approach for thick lenses.....	26
2.5 Signal detection and signal scanning instruments.....	28
2.5.1 The CCD sensor.....	28
2.5.2 The EMCCD camera.....	29
2.5.3 F-Theta objective.....	31
3 Theoretical characterization of the STFM.....	33
3.1 Overview of the spatial and temporal fluctuation microscope.....	35
3.2 Beam geometries for line illumination and line detection.....	38
3.2.1 Illumination point spread function for line illumination.....	38
3.2.2 Detection point spread function for line detection.....	40
3.2.3 Detection probability for line illumination and line detection.....	41
3.2.4 Detection probability function for line illumination and line detection.....	42
3.3 FCS autocorrelation function for line illumination and detection.....	45
4 Implementation and construction of the STFM.....	49
4.1 Instrumental requirements.....	49

4.2 Description of the optical pathway of the STFM	51
4.3 Optimization of the optical beam path	56
4.3.1 Determination of the focal lengths	56
4.3.2 The illumination beam path:	58
4.3.3 The detection beam path	60
4.4 Instrument components and their arrangement for the STFM	65
4.4.1 Microscope, objective lens, tubular lens and scan lens	65
4.4.2 EMCCD camera and frame grabber	67
4.4.3 Galvanometer scanner, driver and data acquisition board	68
4.4.4 Laser and corresponding filters	70
4.4.5 Laser beam coupler, fiber and fiber collimator	71
4.4.6 Circuit diagram of the control instruments of the STFM	71
4.4.7 RTSI triggering connecting the two data acquisition boards	73
4.4.8 The mechanical construction of the STFM	74
4.5 Software for the control of the STFM instrument	77
4.5.1 Description of the user-interface of the STFM software	77
4.5.2 Program structure of the STFM software	79
5 Optical alignment of the STFM	83
5.1 Overview of the adjustable modules	83
5.2 Alignment of the illumination and detection pathway	85
5.3 Alignment of the laser coupler	92
6 Performance, evaluation and basic applications of the STFM	95
6.1 Characterization of instrument components used for the STFM	95
6.1.1 EMCCD camera characterization for line-scan detection	95
6.1.2 Galvanometer scanner characterization	99
6.2 Imaging and mobility measurements of particles by STFM	102
6.2.1 STFM focal size measurement by imaging 100 nm beads	102
6.2.2 Fast STFM imaging of mobile PML nuclear bodies	104
6.2.3 Tracking 100 nm beads with the STFM	106
6.2.4 STFM and conventional FCS measurements of quantum dots	108
6.2.5 STFM focal size symmetry measurements	110
6.2.6 Cross-correlation measurements of neighboring pixels of the STFM ..	112
6.3 In vivo measurements of GFP-expressing cells by FCS and STFM	114
7 Conclusions and perspectives	119
8 Literature	123
9 Appendix	133

Chapter 1

Introduction

Light microscopy is a commonly used technique for the study of biological systems as it allows non-invasive measurements of living cells. All processes that take place inside a cell nucleus such as gene transcription, DNA replication, repair and recombination or RNA processing require an efficient transport of molecules and complexes inside the cell nucleus (Cremer and Cremer, 2001; Kett et al., 1992; Nakayasu and Berezney, 1989; Rippe, 2007). These processes involve molecular interactions like the formation of protein complexes or the association of proteins and DNA. The quantification of these processes is important for the understanding of biological mechanisms inside the cell. However, a comprehensive quantitative physico-chemical description of these systems is still far from being complete.

Up to now, many methods have been developed to analyze molecular interactions between proteins and nucleic acids (Berg and von Hippel, 1985; Jameson and Sawyer, 1995; Langowski et al., 2000). These methods are often not compatible with *in vivo* measurements and lack the sensitivity to evaluate low concentrated species. In contrast, methods that are based on optical microscopy allow non-invasive *in vivo* measurements (Kang et al., 1994; Rieger et al., 2004; Wachsmuth et al., 2007). Some of these methods are based on relaxation processes following the disturbance of an equilibrium state as for example the fluorescence recovery after photobleaching (FRAP) approach. The time dependence of the fluorescence recovery curve contains convolved information about binding and diffusion properties. Other methods are based on fluctuation measurements and include single particle tracking (SPT), where a fluorescently marked particle is tracked through time series of microscope images. This method is limited by the time resolution of the microscope, i.e. mainly its imaging rate. Faster methods are based on the measurement of the fluctuations of molecules moving through the focus as for example the fluorescence correlation spectroscopy (FCS) approach, where for example the binding properties are determined by the way the molecules fluctuate (Bacia et al., 2006; Haustein and Schwille, 2007; Pack et al., 2006; Rigler et al., 1993; Wachsmuth et al., 2003).

The methods described above suffer in general from spatial or temporal resolution limits. As the imaging-based tracking method is limited by the image rate of the microscope, information about movements faster than this rate is lost. FCS, on the other hand, enables fluctuation measurement of highly mobile particles, but this

method is spatially limited to single points. However, the characterization of diffusion and transport processes in living cells using FCS becomes increasingly important, because it is a minimally-invasive method with diffraction limited local resolution, without essential disturbances of the local balance of the cells. Using fluorescence correlation microscopy, hydrodynamic properties of fluorescently labeled molecules and their concentrations can be determined by measuring the particle fluctuations in a small focal volume over a period of time. The reason for these mobility fluctuations can be Brownian dynamics or chemical reactions. The average time for a particle needed to move through the focal volume is characteristic for the hydrodynamic properties of this particle in the surrounding medium. Large complexes, for example, will spend more time in the focal volume than smaller and hence faster proteins. In addition, the detected fluorescence intensity variations are a measure for the number of fluorescently labeled particles in the focal volume. With FCS, molecular interactions at extreme low concentration levels down to the nanomolar range can be observed, which is not accessible for most other methods. On the other hand, measurements take 10-60 seconds in order to yield reliable numbers for mobility properties and concentrations. Imaging of the fluctuations by scanning the position of the point-FCS measurement sequentially through the probe is far from feasible due to the very long measurement duration and is therefore often impossible in living cells. Another disadvantage of this scanning FCS approach is the loss of information about correlated fluctuations in neighboring positions.

These constraints gave inspiration for the construction of a novel spatially resolved FCS imaging instrument that allows to overcome them. The instrument should provide an image of the spatial fluctuations of fluorescently labeled particles along a line with an image of their corresponding spatially resolved distribution. This led to the development of the spatial and temporal fluctuation microscope (STFM) described in this thesis. In order to realize this, features of the confocal laser-scanning microscope (CLSM) as for example the axial resolution, are combined with the benefits of the wide-field microscope leading to a new scanning microscope with line illumination and confocal line detection of a series of foci measured simultaneously along a line. This modification allows faster confocal imaging with much higher quantum yield compared to conventional confocal imaging methods.

Additionally, the STFM allows the mapping of the hydrodynamic properties of the particles along the line profile e.g. inside a cell nucleus. This will give a better insight into biological processes inside the cell nucleus. In addition to the autocorrelation measurements, the spatial and temporal fluctuation microscope enables the measurement of the cross-correlation of the intensity fluctuations of two spatially separated positions along the line. This is important for analyzing structural dynamics of and interactions between macromolecules within complex biological structures. Two associated proteins exhibit a certain spatio-temporal correlation while two proteins that do not interact will show no correlation. With regard to the commonly used instruments, the STFM is a genuine alternative, providing high temporal and high spatial resolution in the same instrument. This system offers new applications, which are not possible with existing experimental or commercial setups until now.

This work describes the design, construction and implementation of such a spatial and temporal fluctuation microscope. This thesis focuses on the theoretical characterization of the microscope, its implementation and its experimental evaluation. The theoretical background of the methods and instruments used for the development and implementation of the STFM are described in chapter two. The theoretical description of the point spread function is derived from conventional setups and further developed for the new instrument, as well as the theoretical description of the autocorrelation and cross-correlation fit function needed for the analysis of the FCS measurements, which are described in detail in chapter three. The fourth chapter presents a detailed discussion of the reasons for the selection and the arrangement of the optical and instrumental components and of the mechanical setup chosen for the implementation and construction of the STFM. Additionally, the development of the system control and data recording software are described here. The optical alignment of the microscope is described in chapter five. The theoretical descriptions are proved and evaluated experimentally for the STFM. Additionally, several features of performance of the STFM and new applications for studying the dynamics of cellular processes with the developed instrument are shown and described in chapter six. Chapter seven displays the conclusions and some perspectives for the spatial and temporal fluctuation microscope.

Chapter 2

Methods and instruments used for the implementation of the STFM

2.1 Optical microscopy-based techniques

The spatial and temporal fluctuation microscope (STFM) is based on the confocal laser-scanning microscope (CLSM), which is described in the following section. As the STFM also allows fast imaging, it is a suitable technique for single particle tracking microscopy, an image analysis technique also described in more detail. Moreover, fluorescence correlation spectroscopy (FCS) is introduced since the STFM is a further development of the fluorescence correlation microscopes.

2.1.1 Confocal laser-scanning microscopy

The principle of confocal microscopy was originally described and patented by Marvin Minsky in 1957 (Minsky, 1957) as shown in figure 2.1A. The setup enabled to view clearly deeper layers in a specimen, without first cutting the specimen into layered sections. J. Young and F. Roberts were the first to examine the idea of confocal scanning optical microscopy (Young et al., 1951). However, it took another thirty years and the development of lasers to become a standard technique towards the end of the 1980s (Cremer and Cremer, 1978; Davidovits and Egger, 1969).

In a confocal microscopy setup, a laser beam is focused by a tubular and an objective lens into a small, diffraction limited, focal volume with fluorescently labeled molecules as schematically shown in figure 2.1B. The emitted fluorescence light from the illuminated molecules is then recollecting by the objective lens. A beam splitter separates the fluorescence from the laser light and directs it towards the detector. In the detection pathway, a pinhole allows only fluorescence light from the conjugate detection volume in the probe to pass through. The fluorescence light is detected by a photo detection device, such as a photomultiplier tube (PMT) or an avalanche photodiode. This device transforms the fluorescent intensity signal into an electrical signal, which is recorded by a computer.

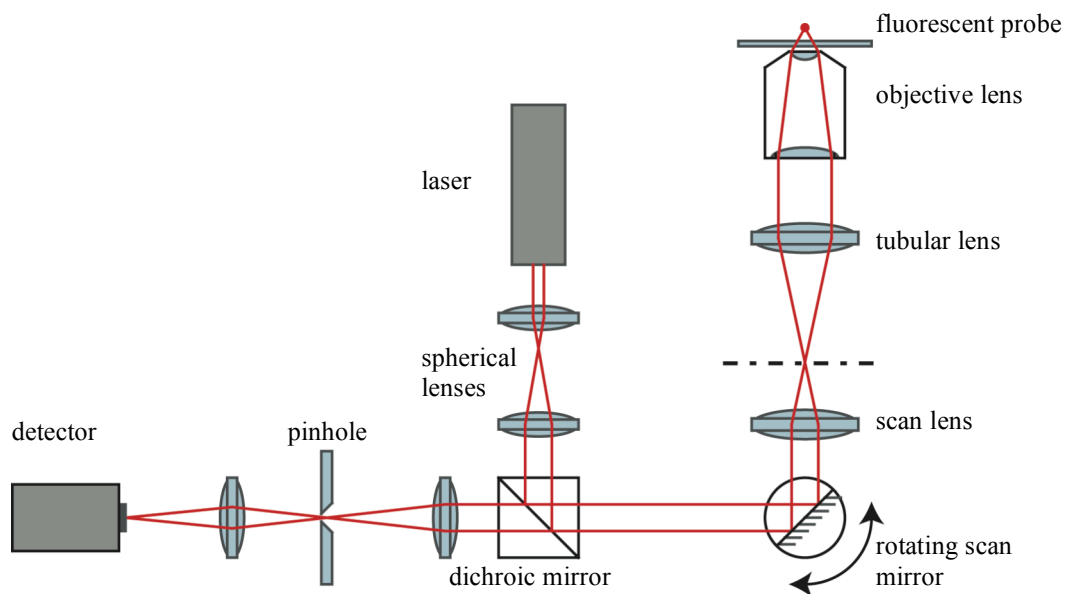
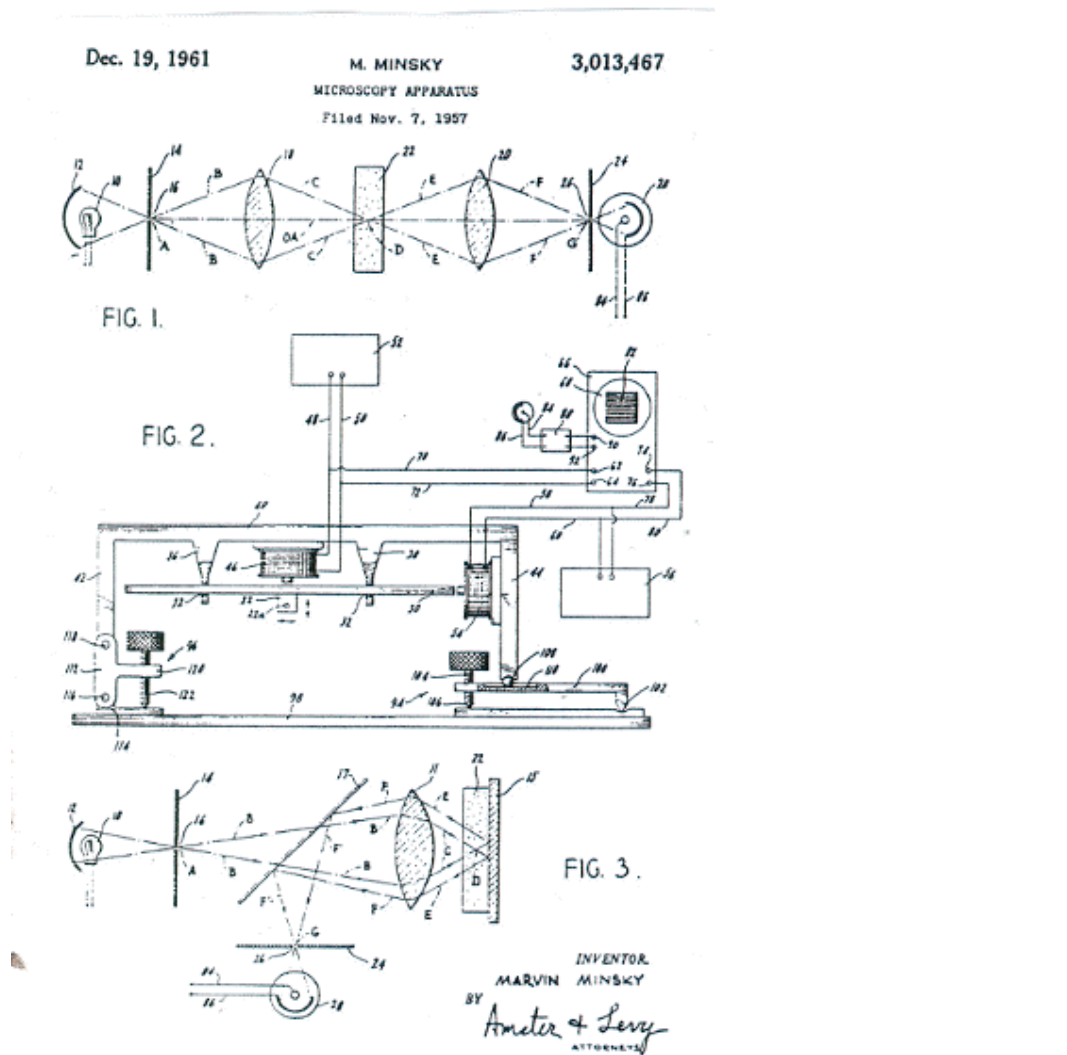
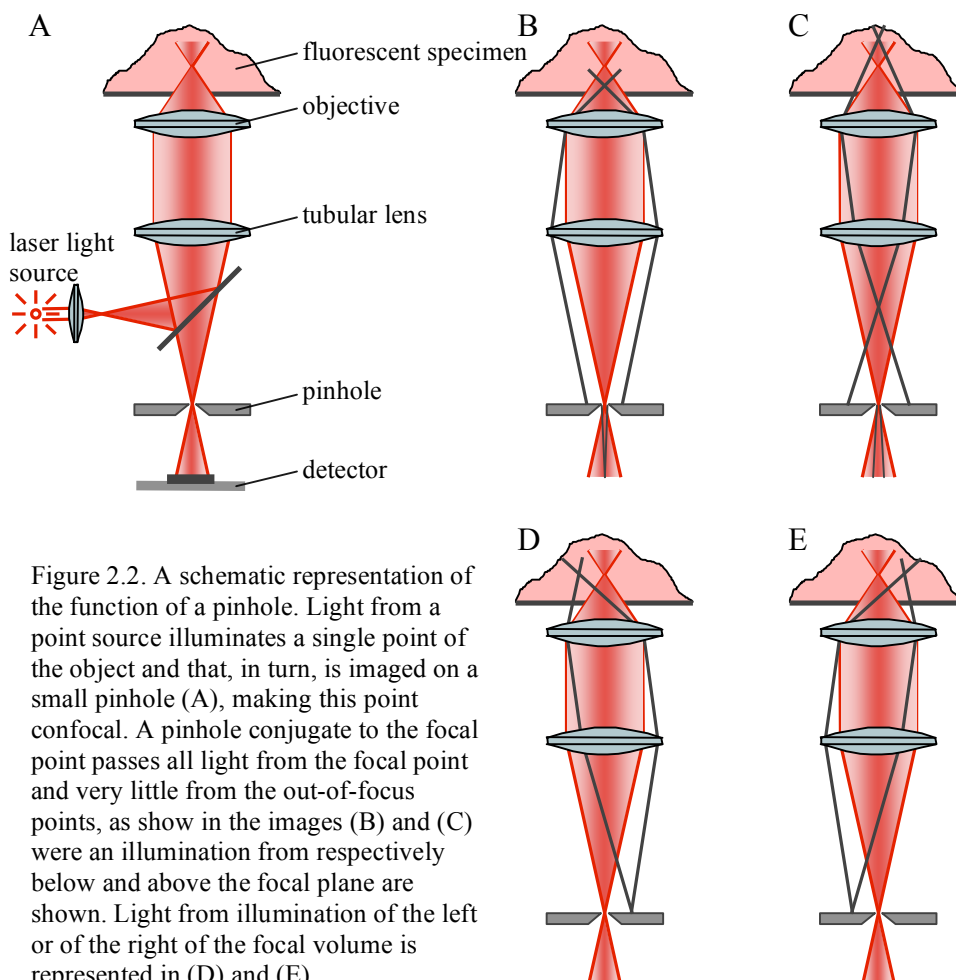


Figure 2.1. (A) The microscopy apparatus according to M. Minsky's patent (Minsky, 1957) and (B) a schematic representation of the confocal laser-scanning microscope (CLSM).

In conventional wide-field microscopy, an image is not only generated from in-focus fluorescence, but also photons from above and below the focal volume are acquired as out-of-focus blur that distort the contrast and sharpness of the final image. Confocal laser-scanning microscopy is a technique for increasing the contrast of microscope images, particular in thick samples by restricting the observation volume. This technique keeps almost only scattered light from the in-focus volume as schematically represented in figure 2.2. Here, a point light source illuminates a point in the object plane. The observation optics forms an image of this illuminated point on a pinhole, so that the source point, the illuminated point in the focal plane and the pinhole in the detection pathway are mutually confocal. The pinhole, conjugate to the focal point, passes all light from the focal point and it obstructs the light that is coming from the out-of-focus points as schematically displayed for the beam path of emitted light from above and below the focal plane (Fig. 2.2B,C), were most of the emitted light is blocked by the pinhole. This allows obtaining images at planes along the z-axis, also known as z stacks, of the sample. Additionally, the confocal microscope setup provides an improvement in lateral resolution as the emitted light from a point on the left or on the right of the focal volume is also blocked by the pinhole (Fig. 2.2D,E). The price for restricting the observation volume is that only one point can be observed at a time. The resolution limit in confocal microscopy depends not only on the probability of illumination but also on the probability of detecting enough photons, which is decreased using a pinhole.



In contrast to the wide-field microscopy, in the confocal microscope a laser spot, is moved through the specimen usually by scanning mirrors. Synchronization of the position of the focus and the data acquisition by the detector allows the reconstruction of the data, which lead to a CLSM image. Information can be collected from different focal planes by raising or lowering the microscope stage of the objective lens, which provides a three-dimensional reconstruction of a series of two-dimensional images from distinct focal planes. Images are acquired point by point, whereas the brightness of a resulting image pixel corresponds to the relative intensity of detected fluorescence light. Unfortunately, the probability decrease in creation of detectable photons negatively affects the signal-to-noise ratio. One can compensate for this effect by using more sensitive photo detectors or by increasing the intensity of the illuminating laser point source or by lowering the image rate, which provide a better signal-to-noise ratio, resulting in better contrast and higher resolution. Increasing the intensity of illumination risks increased bleaching or other damage to the specimen of interest, especially for experiments in which comparison of fluorescence brightness is required.

Different types of confocal microscopes are commercially available. The confocal laser-scanning microscopes as described above were a single point in the probe is illuminated and detected (Zeiss, 2004). Other kind of confocal setups make use of multi-point illumination and detection as for example the spinning-disk or Nipkow disk confocal microscopes (Boyde, 1985; Egger and Petran, 1967; Kino, 1995) and the Programmable Array Microscopes (PAM) (Hanley et al., 2000; Verveer et al., 1998). The spinning disk uses a disc in which a large number of pinholes have been drilled to allow the entire image to be scanned. This method can achieve video rate imaging at a maximum image rate of about hundred of frames per seconds, which is a desirable feature for dynamic observations such as live cell imaging. The Programmable Array Microscope makes use of an array of mirrors to illuminate specific regions. This yields better image quality but the imaging frame rate is very slow; less than 3 frames/second.

For biological purposes, confocal microscopy provides non-invasive imaging of the interior of intact, living cells. As specific labeling of cellular structures is usually based on fluorescence, the sample needs to be treated with fluorescent dyes to make objects visible. This fluorescent cell labeling can be achieved by microinjection, permeabilization of incubation of the cells. However, the actual dye concentration has to be low to minimize the disturbance of biological systems. CLSM is widely used in numerous biological science disciplines, from cell biology and genetics to microbiology and developmental biology.

2.1.2 Single particle tracking microscopy

Single particle tracking microscopy (SPTM) characterizes the motion of individual fluorescently labeled small particles by quantifying their trajectories with high spatial and temporal precision. Within the past few years, single particle tracking techniques have become increasingly important for studying biological systems such as the mobility of genomic sites and nuclear bodies, the infection paths of virus particles

(Cabal et al., 2006; Seisenberger et al., 2001) and membrane receptors (Kusumi et al., 1993; Saxton and Jacobson, 1997). SPTM has proved especially useful in characterizing the motions of small particles attached to proteins inside the cell nucleus (Bacher et al., 2004; Bornfleth et al., 1999; Jegou et al., 2008; Qian and Elson, 1999; Sage et al., 2005) and on cell surfaces with small particles attached to membrane proteins. Single particle methods provide spatially resolved information about the mobility in inhomogeneous systems confined to small domains. These single particle behaviors could not be obtained in measurements of a large population of particles, which show only the averaged quantities. The gathered information from the measurement of single particle trajectories provides information about several aspects of the motion of molecules and their interactions with the environment as the mechanisms and forces that drive and constrain the motion of the particles.

Most of the SPTM studies are based on ultrafast video cameras integrated into wide-field or multi-focal systems. They can detect single particles with an accuracy of 10 - 100 nm in the range of a few milliseconds (Kubitscheck et al., 2000) in contrast to confocal imaging with a time resolution well above 10 ms per frame. Three-dimensional particle tracking is often based on confocal imaging or other camera-based optical sectioning techniques with sequential acquisition of frames in a z-stack and these stacks acquired over time (Bornfleth et al., 1999; Thomann et al., 2002). As these methods are limited to a few images per second, they can only be applied to slow processes.

2.1.3 Fluorescence correlation spectroscopy

Fluorescence correlation spectroscopy (FCS) is a spectroscopic technique that provides insight into the hydrodynamic properties and interactions of molecules in solution. It is based on the measurement of the particle fluctuations of the fluorescence intensity that are caused by the random movement of single molecules diffusing through the focal volume in the solution. The reason for these fluctuations can be Brownian dynamics or a chemical reaction. These fluctuations are related to the size and shape of the particle, as small, rapidly diffusing molecules are highly mobile, whereas larger molecules are less mobile, producing a slower fluctuation. Consequently, any increase in the mass of a molecule, e.g. as a result of an interaction with a second molecule, is detected as an increase in the diffusion time of the particle. In parallel, the FCS measurement shows molecular interactions by a change of the number of measured particles as for example the number of particles when a dimer is formed. This technique is applicable for monitoring a multitude of stochastically driven processes on the molecular level (Hess et al., 2002; Langowski, 2008; Rippe, 2000; Wachsmuth et al., 2003; Weidemann et al., 2002). Over the last thirty years, the FCS technique has become more and more important for biological measurement as it is now among the most successful methods for quantitative measurements inside living cells (Bacia et al., 2006; Bulseco and Wolf, 2007; Kim et al., 2007; Vukojevic et al., 2005; Wachsmuth et al., 2000). Not least due to its simple underlying principle, FCS is an ideal approach for the study of molecular interactions in solution.

Conventional FCS setups employ the same optical setup that is used for CLSM (Fig. 2.1B). Due to this combination, the FCS instrument allows the determination of the spatial distribution of fluorescently labeled molecules in a probe beside the determination of the mobility of these molecules. For the FCS measurements, the detector of the CLSM is replaced by one with a much higher quantum yield, namely an avalanche photodiode, which is a highly sensitive single-photon detector. For FCS measurements, the rotating scan mirror is parked at a certain position to detect information about the corresponding focal volume inside the probe. To record the fluctuation of the intensity signals, the detection volume has to be small; typically, a microscopic focus volume of about 1 femtoliter is illuminated and detected. The particles diffusing through the illuminated volume, give rise to an intensity signal that is recorded over a period of time. Fluorescence intensity fluctuations measured, represent changes in the number or the fluorescence quantum yield of molecules localized in the focal volume as schematically represented in figure 2.3. Accordingly, the fastest fluctuations measured using FCS are limited by the image rate of the detector, which is for the avalanche photodiode usually 24 MHz. In order to achieve a good statistical significance, the photons emitted by the fluorophore in the focal volume are collected over a large time; for at least 1000 times the mean dwell time the molecule spend in the focus as a rule of thumb. This defines the upper range of the measurable particle mobilities. The measurable range for the mean dwell time a molecule spend in the focus using FCS is about 30 μs for small molecules up to 500 ms for large complexes. The lower measurable range of the concentration of the FCS instruments depends on the signal-to-noise ratio of the detector. Concentrations down to a single particle in the focal volume can be measured, which correspond to about 3 molecules/femtoliter, equivalent to a macroscopic concentration of ~ 5 nM. The upper concentration limit is defined by the relative fluctuations of the particles as for a large numbers of molecules; the relative fluctuation is lower as for small numbers, leading to an upper range of about 1 μM .

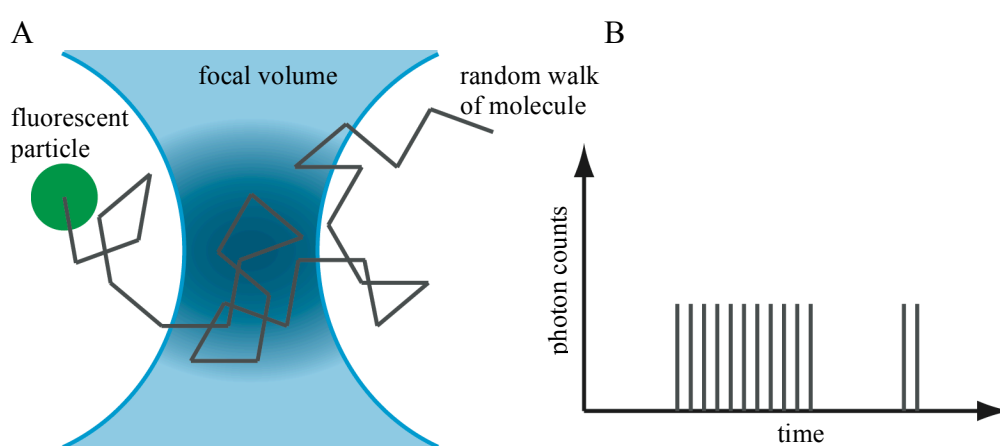


Figure 2.3. Physical origins of fluorescence correlation spectroscopy data. Fluorescent molecules move in and out of the focal volume (A) and are detected as a series of short, randomized fluorescent intensity signals (B).

FCS measurements provide a value for the diffusion time as the mean time a particle spends in the focal volume. This averaged time a particle to moves through the focal volume is related to the size and shape of the particle and characteristic for the hydrodynamic properties of this particle in the surrounding medium. For the FCS measurement, the time-dependent fluorescence intensity signals $F(t)$ are recorded over the measurement time (Fig. 2.4B). Although the pathway of the molecules through the focal volume is random, the mean diffusion time of the molecule can be calculated based on a temporal correlation of the signal of many measured single molecules as shown in figure 2.4C. This autocorrelation function $G(\tau)$ compares the delta fluorescence intensity at time t with the intensity at time $(t + \tau)$, where τ is a variable time displacement. This autocorrelation function is averaged over the measured time series as (Haustein and Schwille, 2004; Webb, 2001)

$$G(\tau) = \frac{\langle \Delta F(t) \cdot \Delta F(t + \tau) \rangle}{\langle F(t) \rangle^2}, \text{ with} \quad (2.1a)$$

$$\Delta F(t) = F(t) - \langle F(t) \rangle \quad (2.1b)$$

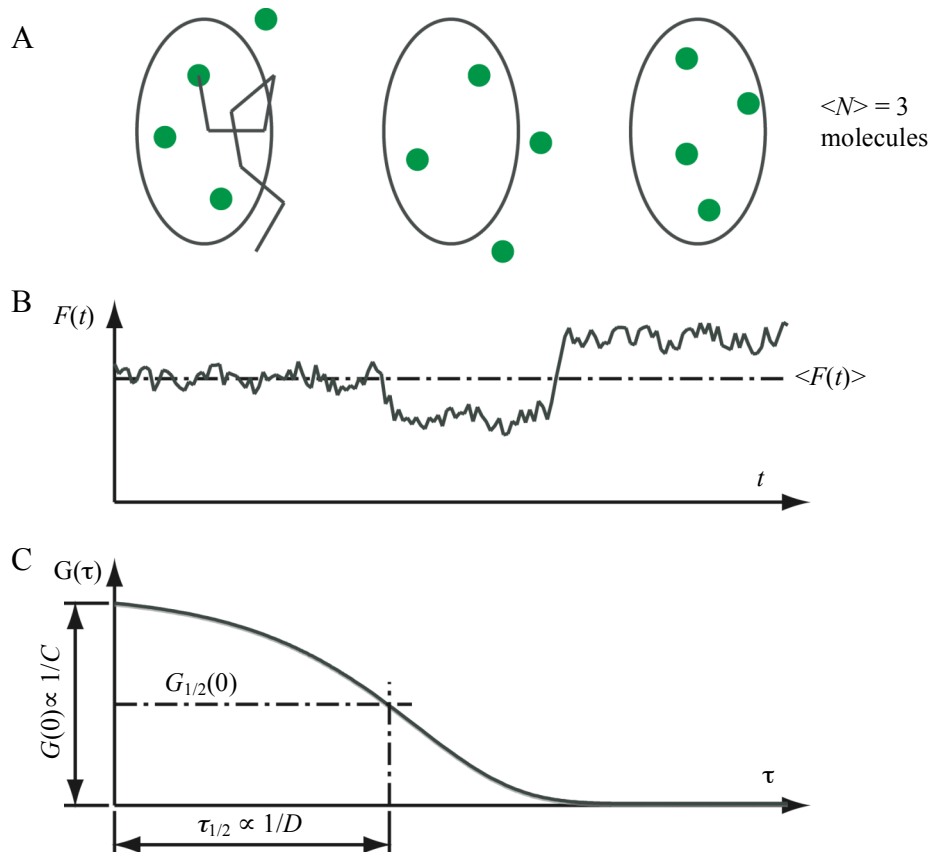


Figure 2.4. Three schematic drawings of the focal volume with N fluorescently labeled molecules inside at different time points (A) with the corresponding fluorescence intensity detection signal $F(t)$ (B) and a typical fit function for the autocorrelation $G(\tau)$ of such an intensity signal (C). The amplitude of the autocorrelation $G(0)$ is proportionally to the concentration C of the measured probe and the half-life period $\tau_{1/2}$ provides a value for the diffusion constant D .

The autocorrelation function decays from its initial value $G(0)$ with a time-dependence that is determined by molecular diffusion rates. The half-life period of the correlation or the diffusion time is correlated to the diffusion constant of the fluorescent molecules in the surrounding solution as shown in figure 2.4C. The initial amplitude of the autocorrelation function is inversely proportional to the number of molecules in the detection volume N and to the concentration C .

Using fluorescently labeled particles with different colors and two-way detection of their corresponding fluorescence intensity signal allows the determination of the cross-correlation function between both signals. The cross-correlation function $CC(\tau)$ compares the delta fluorescence intensity signal of one color at time t with the delta fluorescence intensity signal of the other color at time $(t + \tau)$ and again averaged over the measured time series the same as for the autocorrelation (Bacia et al., 2006; Qian and Elson, 2004; Rigler et al., 1998; Weidemann et al., 2002).

2.2 Derivation of a description for the PSF of the confocal microscope

In a lens system, the diffraction effect tends to spread the image of a point object. The image of the laser is not an infinitely small point but a three-dimensional diffraction pattern, which is close to diffraction limit. This intensity distribution response of the optical system to a point function is called the point spread function (PSF). Accordingly, the effective focus acts as a three-dimensional probe that can be scanned through a transparent specimen. The beam geometry of the spatial and temporal fluctuation microscope (STFM) differs from the conventional confocal laser-scanning microscope (CLSM). The beam geometry of the CLSM is axial symmetric and illuminates a single point whereas for the STFM configuration, a line beam profile is generated. Each point along this illuminated line is imaged on a corresponding pixel of the line detector, a one-dimensional pixel array. Since the STFM is based on confocal laser-scanning microscopy, the theoretical description of the point spread function of the point illuminating confocal microscope is used as foundation to derive a description of the line illuminating confocal microscope. Accurate point spread functions are necessary for noise subtraction using deconvolution (Baddeley et al., 2006; Von Tiedemann et al., 2006) and for the resolution improvement of images (Santos and Young, 2000; Thomann et al., 2002). For FCS, an accurate description of the point spread function is indispensable in order to derive an appropriate fit function for the correlation.

This section gives a theoretical approach to the beam geometry of a point illumination and detection microscope resulting in the three-dimensional non-paraxial PSF for the confocal laser-scanning microscope with a high-aperture objective lens. As the exact PSF is rarely analytically solvable, the analytical ansatz leading to an approximated solution is derived.

2.2.1 Illumination, fluorescence and detection

For a confocal laser-scanning microscope, the detected signal originates from the excitation of fluorophors by a laser. These excited fluorophors radiate fluorescence photons through the optical microscope system that will be converted into electric impulses as they reach the detector. All these steps can be described by instrument-specific and probe-specific parameters and functions. These parameters are, in most cases, wavelength-dependent. The microscope system is divided in the illumination, the fluorescence and the detection part that will be described separately below.

Illumination: A confocal laser-scanning microscope is based on fluorescently labeled molecules excited by laser light, which is focused to a small volume. This laser light can be composed of one or more laser lines with different wavelengths $\lambda_{ill,i}$. The spatial intensity distribution is a result of the wavelength-dependent laser power P_i and an instrument specific-function $\Omega_i(\mathbf{r})$, that describes the beam profile of the laser and the properties of the objective and the whole optical system

$$I_{\text{ill},i}(\mathbf{r}) = P_i \cdot \Omega_i(\mathbf{r}) \quad (2.2)$$

The spectral dependence of the beam profile is mainly caused by diffraction effects and the chromatic errors of the optical system. These dependencies can be described by index i , as for a CLSM, discrete laser lines are used.

Fluorescence: For biological studies, fluorophores are often bound to macromolecules like DNA or proteins. The spectral properties of such biological complexes are given by the type of fluorophores, the number of bindings and the type of the binding of the fluorophore. Upon absorption of a photon of the excitation light, the fluorophore transfers to the first singlet excited state S_1 as schematically shown in figure 2.5. The fluorophore will be excited with wavelength-dependent probability $\epsilon(\lambda)$ according to the absorption spectrum. After excitation, the fluorophore will rapidly relax to the lowest energy level of this excited state, as the fluorescence lifetimes are typically much longer. Successively, the excited fluorophores will transfer back into their ground state upon emission of photons with wavelength-dependent probability $q(\lambda)$ described by the emission spectrum. Another kind of emission is phosphorescence, which is similar to fluorescence, with the exception of a spin conversion of the electron into the triplet state T_1 before returning into the ground state S_0 . As the emission from the triplet state occurs with lower energy, the emitted photons have longer wavelengths relative to fluorescence. The fluorophores will not necessarily return to the ground state as the fluorophore can permanently lose the ability to fluoresce by a process called photobleaching. This occurs due to photon-induced chemical damage or covalent modification of the fluorophores.

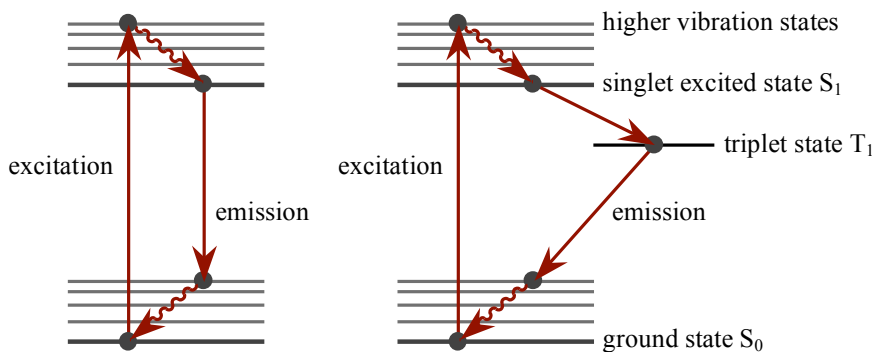


Figure 2.5. Jablonski energy diagrams of fluorescence (A) and of phosphorescence (B).

Detection: The fluorescence photons are isotropically radiated. The probability for these photons to pass through the optical system and to be detected by detector j depends on the position \mathbf{r} in the probe and is called the geometric transfer function $GTF_j(\mathbf{r})$. The optical properties of detection pathway as for example the emission

filter and the spectral efficiency of the detector are considered by the spectral transfer function $\text{STF}_j(\lambda_{\text{det}})$. These two functions together describe the detection.

The functions described above for the illumination, the fluorescence and the detection together leads to a photon flow f_j at detector j originating from a fluorophore radiating at position \mathbf{r} in a probe, which is excited by laser line i of (Tewes, 1998; Wachsmuth, 2001)

$$f_j(\mathbf{r}) = P_i \Omega_i(\mathbf{r}) \varepsilon(\lambda_{\text{ill},i}) \cdot \text{GTF}_j(\mathbf{r}) \int q(\lambda_{\text{det}}) \cdot \text{STF}_j(\lambda_{\text{det}}) d\lambda_{\text{det}} \quad (2.3)$$

The first three terms of equation 2.3 describe the illumination and excitation of a fluorophore molecule multiplied by the second three terms, which describe the emission and detection of the emitted photons due to this excitation. This equation can be transcribed into an excitation wavelength i dependent and a detector channel j dependent constant, σ_{ij} , called the color matrix and a spatial detection probability, $\Psi_{ij}(\mathbf{r})$, known as the molecular detection efficiency MDE (Aragón and Pecora, 1976), which result in

$$\sigma_{ij} = \varepsilon(\lambda_{\text{ill},i}) \cdot \int q(\lambda_{\text{det}}) \cdot \text{STF}_j(\lambda_{\text{det}}) d\lambda_{\text{det}} \quad (2.4)$$

$$\Psi_{ij}(\mathbf{r}) = \Omega_i(\mathbf{r}) \cdot \text{GTF}_j(\mathbf{r}) \quad (2.5)$$

Using more than one excitation wavelength will result in a detector signal

$$f_j(\mathbf{r}) = \sum_i P_i \cdot \sigma_{ij} \cdot \Psi_{ij}(\mathbf{r}) \quad (2.6)$$

The color matrix is defined by the fluorophore properties and by the optical elements of the system as laser line and emission filter. Under ideal conditions, also when using more than one laser lines, the non-diagonal elements of the color matrix are zero, i.e. no crosstalk between different channels occurs.

2.2.2 Confocal illumination and detection geometry

For both CLSM and FCS, it is desirable that the focus is as small as possible. An emitting laser point in the intermediate image plane (Fig. 2.6) will be smeared out over a finite area in the microscope focus plane rather than focused to a point because of diffraction and the possible presence of aberrations. This spread of intensity is described mathematically by the point spread function of the illumination, $\text{PSF}_{\text{ill}}(\mathbf{r})$ (Hecht, 1989). Only photons from inside this point spread function will contribute to the fluorescence emission. This emission profile again will also be widened up on its way to the detector through the optical system by the detection point spread function, $\text{PSF}_{\text{det}}(\mathbf{r})$. Not all emitted fluorescence photons will be detected. Only fluorescence photons from the detection volume, which is defined by the pinhole and the emission point spread function, will be detected. Accordingly, for the confocal setup the

detection probability Ψ also referred to as molecular detection efficiency (MDE) can be described by the multiplication of the illumination point spread function with the detection point spread function.

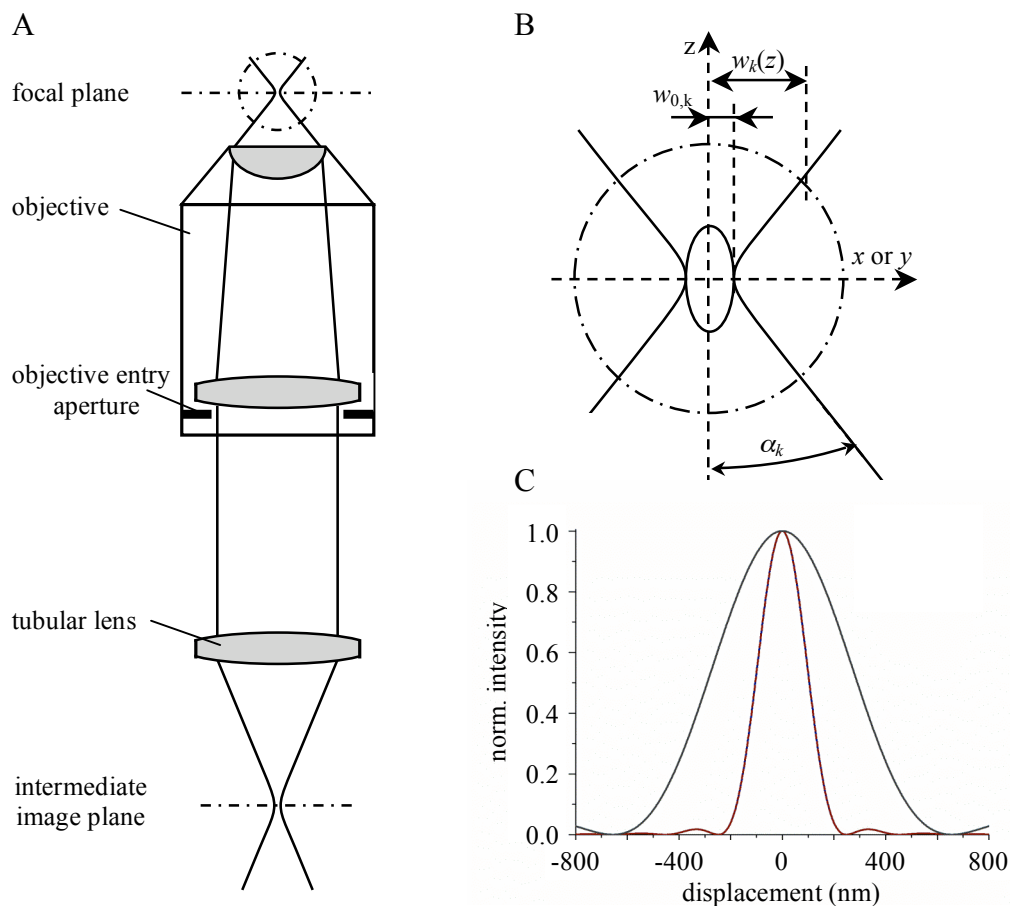


Figure 2.6. A schematic setup of the illumination of a confocal laser scanning microscope (A) and the enlargement of the focal volume with the geometric parameters used (B) and the normalized illumination intensity versus x- (red) and versus y- (blue) and versus z-displacement (grey) (C).

For the confocal condition, the detection probability of equation 2.5 can be transcribed using the spatial functions for illumination $\Omega_i(\mathbf{r})$ according to equation 2.2 and for detection $GTF_j(\mathbf{r})$ in equation 2.3, which is respectively the illumination and the detection point spread function. Accordingly, for the detection probability for a laser line i and detection channel j follows

$$\psi_{i,j}(\mathbf{r}) = \text{PSF}_{\text{ill},i}(\mathbf{r}) \cdot \text{PSF}_{\text{det},j}(\mathbf{r}) \quad (2.7)$$

This equation describes the probability distribution of finding a photon at the detection device, which originates from fluorescence molecules inside the illuminated volume.

2.2.3 Approximated point spread function for small numerical aperture

When illuminating the entrance aperture of the objective lens with a Gaussian laser beam whose $1/e^2$ radius is the same as the radius of the aperture, the intensity distribution in the sample will be approximately a lateral two-dimensional Gaussian function with an axial Lorentzian profile as

$$PSF_{\text{ill}}(\mathbf{r}) = \left(\frac{w_0}{w(z)} \right)^2 \cdot \exp\left(-2 \frac{x^2 + y^2}{w^2(z)} \right) \quad (2.8a)$$

with

$$w(z) = w_0 \cdot \sqrt{1 + \frac{z^2 \alpha^2}{w_0^2}}, \quad w_{0,k} = \frac{\lambda_{\text{ill},k}}{n\pi\alpha}, \quad NA = n \cdot \sin(\alpha) \quad (2.8b,c,d)$$

In these expressions, w_0 is the beam radius in the focal plane, $w(z)$ the beam radius along the optical axis, NA is the numeric aperture of the objective, α the aperture angle of the incident light and n the index of refraction. These equations are an approximation for numerical apertures of $NA < 0.7$. For larger numerical apertures, as is the case for the objectives usually used for confocal microscopy and FCS, a more precise calculation must be applied.

2.2.4 Illumination point spread function

A regularly used approach to describe the point spread function is the Debye theory. This analytical approach consists in expressing the PSF using diffraction theory and knowledge of the optical microscope components. The illumination amplitude distribution h_{ill} can be expressed by a scalar Debye diffraction integral. The scalar Debye theory states that the amplitude of the electro-magnetic field at a point near the focus can be expressed as a superposition of plane waves integrated over the lens aperture field. This leads to an expression for the illumination amplitude distribution function of (Born, 1999; Hecht, 1989)

$$h_{\text{ill}}(x, y, z) \propto \iint_{\text{area}} e^{-i\mathbf{k}_{\text{ill}} \cdot \mathbf{r}} dS \quad (2.9)$$

A point illuminating confocal system consists of circular lenses and a circular pinhole as depicted schematically in figure 2.7. Accordingly, a wavefront propagates through the lens system, here represented by a plane. This propagating wavefront is diffracted by the lens system and illuminates the probe at the focal plane of the objective. The excitation amplitude distribution of a circular system shows axial symmetry. Thus, the propagation vector can be split up into a lateral and an axial contribution that can be parameterized by the convergence angle θ . The objective lens is assumed to be illuminated by a plane wavefront with propagation vector \mathbf{k} . According to these considerations, the lateral and axial contribution to the illumination amplitude distribution are given by

$$h_{\text{ill}}(x, y, z) \propto \iint_{\text{area}} e^{-ik_{\text{ill}} \sqrt{x^2 + y^2} \sin \theta} e^{-ik_{\text{ill}} z \cos \theta} dS \quad (2.10)$$

As this expression can rarely be solved, the following simplification is made: The whole excitation amplitude distribution is split up into a lateral and an axial part in such a way that the axial excitation amplitude distribution is described for $x = y = 0$ and the radial excitation amplitude distribution for $z = 0$. This assumption is only true for the far-field case compared to the xy -deviations. The radial part of the excitation amplitude distribution is given by

$$h_{\text{ill}}(x, y, 0) \propto \iint_{\text{area}} e^{-ik_{\text{ill}} \sqrt{x^2 + y^2} \sin \theta} dS \quad (2.11)$$

Solving equation 2.11 finally leads to the illumination point spread function (Hecht, 1989)

$$\text{PSF}_{\text{ill}}(x, y, 0) = |h_{\text{ill}}(x, y, 0)|^2 = \left(\frac{2J_1(v_{\text{ill}})}{v_{\text{ill}}} \right)^2, \text{ with} \quad (2.12a)$$

$$v_{\text{ill}} = n \frac{2\pi}{\lambda_{\text{ill}}} \sqrt{x^2 + y^2} \sin \alpha \quad (2.12b)$$

where J_1 is the Bessel-function of order one. This equation describes the radial part of the excitation amplitude distribution for $z = 0$. It makes use of the definition of the propagation wavenumber $k = n2\pi/\lambda$, with the illumination wavelength λ_{ill} and the refractive index n . Figuratively speaking, equation 2.12 is the intensity distribution due to the diffraction at a circular aperture (Guenther, 1990; Sheppard and Matthews, 1987).

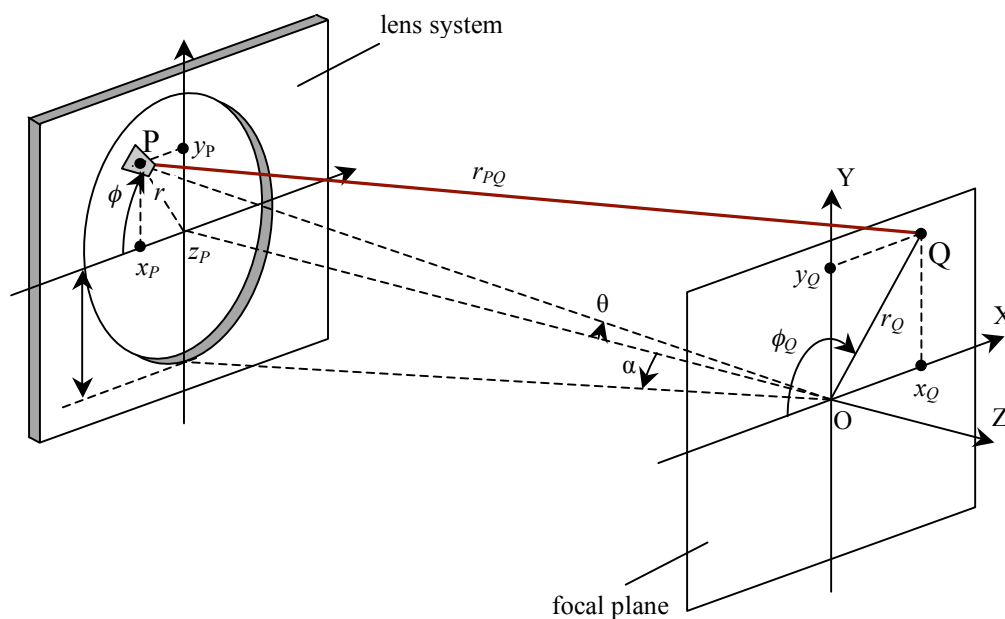


Figure 2.7. A schematic setup of the illumination wave front through a circular lens system of a confocal laser-scanning microscope.

According to equation 2.10, the axial illumination amplitude distribution is given by

$$h_{\text{ill}}(0,0,z) \propto \int_{\theta=0}^{\alpha} \int_{\phi=0}^{2\pi} e^{-ik_{\text{ill}}z \cos \theta} r_p^2 \sin \theta d\phi d\theta \quad (2.13)$$

For this equation, the propagation vector \mathbf{k} is multiplied by $\cos(\theta)$ to get its axial component. Solving this equation finally leads to

$$PSF_{\text{ill}}(0,0,z) = |h_{\text{ill}}(0,0,z)|^2 = \left(\frac{\sin(u_{\text{ill}})}{u_{\text{ill}}} \right)^2, \text{ with} \quad (2.14a)$$

$$u_{\text{ill}} = n \frac{2\pi}{\lambda_{\text{ill}}} z_Q \sin^2(\alpha/2) \quad (2.14b)$$

This equation describes the axial part of the illumination amplitude distribution for $x = y = 0$. It makes use of the definition of the propagation wavenumber $k = n2\pi/\lambda$, with illumination wavelength λ_{ill} and the refractive index n . Figuratively speaking, equation 2.14 is the intensity distribution due to the diffraction at a slit (Guenther, 1990; Sheppard and Matthews, 1987).

Combing the axial and the lateral contribution leads to the excitation point spread function for a perfect diffraction-limited optical system without any aberrations

$$PSF_{\text{ill}}(\mathbf{r}) = \left(\frac{\sin(u_{\text{ill}})}{u_{\text{ill}}} \right)^2 \cdot \left(\frac{2J_1(v_{\text{ill}})}{v_{\text{ill}}} \right)^2, \text{ with} \quad (2.15a)$$

$$u_{\text{ill}} = n \frac{2\pi}{\lambda_{\text{ill}}} z \sin^2(\alpha/2) \text{ and } v_{\text{ill}} = n \frac{2\pi}{\lambda_{\text{ill}}} \sqrt{x^2 + y^2} \sin \alpha \quad (2.15b,c)$$

As an illustration, consider a single point object situated at the focal point of the microscope and much brighter than the background. For the confocal system with a point illumination and detection, the intensity in the detector plane is a so-called Airy distribution. The illumination profiles are plotted in figure 2.6C; the red/blue curves show the profile of the point spread function in the lateral x- and y-direction. According to equation 2.15, these components are equal. The gray curve shows the profile of the point spread function in the axial z-direction.

2.2.5 Detection point spread function

Not all emitted fluorescence photons originating from the illumination focus volume will be detected as the fluorescence photons will radiate in all direction. Only the fluorescence photons out of the detection volume will be detected. This detection volume is defined by the pinhole and the emission point spread function. Accordingly, the detection point spread function of a confocal microscopy is defined by the

emission intensity distribution, generated by the diffraction of the fluorescence photons, convolved with the area of the detector projected into the object space

$$\text{PSF}_{\text{det}}(x, y, z) = \left(|h_{em}^2(x, y, z)|^2 * D(x, y) \right) \quad (2.16)$$

The * in equation 2.16 denotes the convolution, D describes the shape of the pinhole in the detection pathway or that of the detector, and h_{em} is the emission amplitude distribution. As in confocal microscopy, the size of the pinhole is usually chosen to be smaller than or equal to the size of the central lobe of the detection PSF, the pinhole can be approximated as delta function. Thus, the approximated detection point spread function for a confocal microscope is described solely by the emission point spread function. With regard to the illumination PSF, the emission amplitude distribution can be expressed using the scalar Debye diffraction for a circular lens. This leads to the same shape for the detection PSF as for the illumination PSF. The only difference is a small wavelength shift between the emission and the excitation wavelength. This leads for the detection PSF for a perfect diffraction-limited optical system without any aberrations to

$$\text{PSF}_{\text{det}}(\mathbf{r}) = \left(\frac{\sin u_{\text{det}}}{u_{\text{det}}} \right)^2 \cdot \left(\frac{2J_1(v_{\text{det}})}{v_{\text{det}}} \right)^2, \text{ with} \quad (2.17a)$$

$$u_{\text{det}} = n \frac{2\pi}{\lambda_{\text{det}}} z \sin^2(\alpha/2) \text{ and } v = n \frac{2\pi}{\lambda_{\text{det}}} \sqrt{x^2 + y^2} \sin \alpha \quad (2.17b,c)$$

As an illustration, consider a single point object situated at the focal point of the microscope and much brighter than the background. For the confocal system with a point illumination and detection, the intensity in the detector plane is a so-called Airy distribution.

2.2.6 The detection probability and its fit function

The combined point spread function, also called molecular detection efficiency (MDE) of a confocal microscope is defined by the product of the illumination point spread function and the detection point spread function according to equation 2.7.

$$\text{PSF}(\mathbf{r}) = \left(\frac{\sin u_{\text{ill}}}{u_{\text{ill}}} \right)^2 \cdot \left(\frac{2J_1(v_{\text{ill}})}{v_{\text{ill}}} \right)^2 \left(\frac{\sin u_{\text{det}}}{u_{\text{det}}} \right)^2 \cdot \left(\frac{2J_1(v_{\text{det}})}{v_{\text{det}}} \right)^2, \text{ with} \quad (2.18a)$$

$$u_{\text{ill}} = n \frac{2\pi}{\lambda_{\text{ill}}} z \sin^2(\alpha/2), \quad v_{\text{ill}} = n \frac{2\pi}{\lambda_{\text{ill}}} \sqrt{x^2 + y^2} \sin \alpha, \quad (2.18b,c)$$

$$u_{\text{det}} = n \frac{2\pi}{\lambda_{\text{det}}} z \sin^2(\alpha/2) \text{ and } v_{\text{det}} = n \frac{2\pi}{\lambda_{\text{det}}} \sqrt{x^2 + y^2} \sin \alpha \quad (2.18d,e)$$

For the analytical calculation of the correlation function, this overall point spread function is too complicated. However, as the size of the illumination PSF and the detection PSF are different as they scale with different wavelengths, the side lobes of the sinc-function and those of the Bessel-function are negligible upon multiplication of these point spread functions (Wachsmuth, 2001). Accordingly, in a confocal setup with a high numerical aperture, the detection probability can be approximated by a rotation-symmetrical three-dimensional Gauss-function around a point \mathbf{p}_k (Aragón and Pecora, 1976; Qian and Elson, 1991; Rigler et al., 1993)

$$\Psi_k(\mathbf{r}) = \exp\left(-2\frac{(x - x_{p,x})^2 + (y - y_{p,y})^2}{w_k^2} - 2\frac{(z - z_{p,z})^2}{z_k^2}\right) \equiv \text{PSF}(\mathbf{r}) \quad (2.19)$$

with the $1/e^2$ radii w_k lateral and z_k axial to the optical axis. The z-axis is chosen as optical axis.

2.3 Theory of FCS in a point confocal setup

A fluorescence correlation spectroscopy (FCS) measurement results in a correlation function of the fluctuations of fluorescence signals emitted by the molecules in a microscopic focus volume when excited with laser light. These fluctuations can be assigned to different sources such as diffusion processes or the transfer to a different conformational state. To characterize these processes, a suitable theoretical correlation function must be adapted in each case to the measured one. The usually used correlation fit function for FCS measurements is calculated in earlier work (Elson and Magde, 1974; Magde et al., 1974; Wachsmuth, 2001; Widengren et al., 1995). In addition, the influence of the beam geometry on the correlation functions has been studied for different kinds of experimental microscopes, in particular as a result of the further development of high-resolving confocal microscopy (Aragón and Pecora, 1976; Chen et al., 1999; Elson and Magde, 1974; Hess and Webb, 2002; Kastrop et al., 2005; Qian and Elson, 1991; Rigler et al., 1993). For the description of the correlation fit function, the statistical particle number variations are assumed to be caused by diffusions. Chemical interactions between the particles are neglected for the analytical approach. The resulting correlation fit function can be adapted afterwards for these chemical reactions. The theoretical fundamentals of the FCS in this section are based on previous work (Eigen and Rigler, 1994; Elson and Magde, 1974; Elson and Webb, 1975; Hess and Webb, 2002; Rigler, 1995; Schwille and Hausteiner, 2002; Tewes, 1998; Thompson, 1991; Wachsmuth, 2001; Widengren and Rigler, 1998).

2.3.1 The general form of the correlation function

Consider a system of N non-interacting particles in a certain volume V . These particles are fluorescently labeled with fluorophors with one color, $k \in \{1,2\}$ for autocorrelation or with fluorophors of two colors, which is the case for cross-correlation FCS. These fluorophors can be assigned to two different detection channels, $k \in \{1,2\}$. The function $\Psi_k(\mathbf{r})$ describes the detection probability of these fluorescently labeled particles at position \mathbf{r} in the probe detected at channel k . The corresponding detector signal $f_{k,n}$ describes the detector signal at channel k of particle n at position $\mathbf{r}(t)$ (equation 2.5 and 2.6). All single particles contribute to the total detection signal, which can be described by

$$F_k(t) = \sum_{n=1}^N f_{k,n}(t) \quad (2.20)$$

Is the particle at time t located at position \mathbf{r}_1 and at time $t+\tau$ at position \mathbf{r}_2 , the corresponding detector signal at channel $k, l \in \{1,2\}$ is given by

$$f_{k,n}(t)f_{l,n}(t+\tau) \propto \Psi_k(\mathbf{r}_1)\Psi_l(\mathbf{r}_2) \quad (2.21)$$

When the particles are Markov processes, i.e. the future movements of the particle are independent of the movements in the past, the probability P_D for a particle to be at time $t+\tau$ located at position \mathbf{r}_2 that at time t was located at position \mathbf{r}_1 is given by (Schwille, 2001; van Kampen, 1992; Wachsmuth, 2001)

$$P_D(\mathbf{r}_2, t + \tau | \mathbf{r}_1, t) d^3 \mathbf{r}_2 = P_D(\mathbf{r}_2, \tau | \mathbf{r}_1, 0) d^3 \mathbf{r}_2 \quad (2.22)$$

Implying that the particle movements are independent of time shift. The probability for a particle to be located at position \mathbf{r}_1 is described by the particle density W_D as

$$W_D(\mathbf{r}_1) d^3 \mathbf{r}_1 \quad (2.23)$$

For a finite probe volume, the probability of finding the particle somewhere in this volume is one. As the concentration is assumed to be constant over the whole volume, the probability distribution of a particle $W_D(\mathbf{r}, t) = 1/V$. The fluorescence intensity averaged over the acquisition time is composed of the multiplication of the detection probability and the particle density integrated over the whole volume

$$\langle f_{k,n}(t) \rangle \propto \iiint_V W_D(\mathbf{r}_1) \Psi_k(\mathbf{r}_1) d^3 \mathbf{r}_1 \quad (2.24)$$

Leading for the correlation function of equation 2.21 to

$$\langle f_{k,n}(t) f_{l,n}(t + \tau) \rangle \propto \iiint_V \iiint_V W_D(\mathbf{r}_1) \Psi_k(\mathbf{r}_1) P_D(\mathbf{r}_2, \tau | \mathbf{r}_1, 0) \Psi_l(\mathbf{r}_2) d^3 \mathbf{r}_1 d^3 \mathbf{r}_2 \quad (2.25)$$

In an FCS experiment, the normalized correlation function $G_{kl}(\tau)$ of the fluctuations of the measured intensity signals $F_k(t)$ is determined. The subscripts $k, l \in \{1, 2\}$ indicate the detection channel. For the normalized autocorrelation, $k = l$ while for the normalized cross-correlation, $k \neq l$. The normalized correlation function can be written as

$$G_{kl}(\tau) = \frac{\langle \Delta F_k(t) \cdot \Delta F_l(t + \tau) \rangle}{\langle F_k(t) \rangle \langle F_l(t) \rangle} = \frac{\langle F_k(t) \cdot F_l(t + \tau) \rangle}{\langle F_k(t) \rangle \langle F_l(t) \rangle} - 1 \quad (2.26a,b)$$

$$= \frac{\sum_{n,m=1}^N \sum_{m=1, m \neq n}^N \langle f_{k,n}(t) f_{l,m}(t + \tau) \rangle}{\langle \sum_{n=1}^N f_{k,n}(t) \rangle \langle \sum_{n=1}^N f_{l,n}(t) \rangle} - 1 \quad (2.26c)$$

This equation describes the correlation function for N particles. As the particles are assumed non-interacting, $f_n(t)$ and $f_m(t)$ are independent for all $n \neq m$. Thus, the expectation value of these products is equal to the product of their expectation values. In addition, considering one representative particle n will describe the correlation function, which leads to (Wachsmuth, 2001)

$$G_{kl}(\tau) = \frac{N \langle f_{k,n}(t) f_{l,n}(t+\tau) \rangle + N(N-1) \langle f_{k,n}(t) \rangle \langle f_{l,n}(t) \rangle}{N^2 \langle f_{k,n}(t) \rangle \langle f_{l,n}(t) \rangle} - 1 \quad (2.27a)$$

$$= \frac{1}{N} \frac{\langle f_{k,n}(t) f_{l,n}(t+\tau) \rangle}{\langle f_{k,n}(t) \rangle \langle f_{l,n}(t) \rangle} - \frac{1}{N} \quad (2.27b)$$

$$= \frac{1}{N} \frac{\iiint_V \iiint_V W_D(\mathbf{r}_1) \Psi_k(\mathbf{r}_1) P_D(\mathbf{r}_2, \tau | \mathbf{r}_1, 0) \Psi_l(\mathbf{r}_2) d^3 \mathbf{r}_1 d^3 \mathbf{r}_2}{\iiint_V W_D(\mathbf{r}_1) \Psi_k(\mathbf{r}_1) d^3 \mathbf{r}_1 \iiint_V W_D(\mathbf{r}_1) \Psi_l(\mathbf{r}_1) d^3 \mathbf{r}_2} - \frac{1}{N} \quad (2.27c)$$

This equation gives a theoretical approach to the correlation fit function. The geometric and spectral properties of the optical system determine the detection probability, whereas diffusion properties of the probe and photobleaching are described by the particle transfer probability.

2.3.2 The correlation function for the case of free diffusive mobility

Free diffusion describes the random Brownian motion of particles in the absence of external forces. For this case, Fick's first law of diffusion can be applied, which describes the correlation between the particle flow and the concentration. This equation and the continuity equation, which describes that the concentration within the diffusion volume does not change with respect to time, leads to Fick's second law of diffusion, which is (van Kampen, 1992)

$$\frac{\partial c(\mathbf{r}, t)}{\partial t} = D_0 \nabla^2 c(\mathbf{r}, t) \quad (2.28)$$

For this equation, the diffusion coefficient D_0 is assumed constant, which is the case for an isotropic system. This diffusion coefficient is reversely proportional to the friction coefficient f by

$$D_0 = kT/f = kT/6\pi\eta R_h \quad (2.29)$$

where η is the viscosity and R_h the hydrodynamic radius of the particles. The solution of Fick's second law of diffusion using the boundary condition, $c(\mathbf{r}_2, 0) = \delta(\mathbf{r}_2 - \mathbf{r}_1)$, leads for the transition probability of equation 2.22 to

$$P_D(\mathbf{r}_2, \tau | \mathbf{r}_1, 0) = c(\mathbf{r}_2 - \mathbf{r}_1, \tau) = \frac{1}{(4\pi D_0 \tau)^{d/2}} \exp\left[-\frac{|\mathbf{r}_2 - \mathbf{r}_1|^2}{4D_0 \tau}\right] \quad (2.30)$$

In this equation, d is the degree of freedom for the translation of the particles. Inserting this transition probability for free diffusion, the three-dimensional Gaussian fit function of equation 2.19 and equation 2.23 into the correlation function of equation 2.27c leads to (Schwille, 2001; Wachsmuth, 2001)

$$G_{kl}(\tau) = \frac{1}{cV_{eff}} \left(1 + \frac{\tau}{\tau_{diff}}\right)^{-1} \left(1 + \frac{\tau}{\kappa^2 \tau_{diff}}\right)^{-1/2} \exp\left(-\frac{d_x^2 + d_y^2}{4D_0\tau + w_0^2} - \frac{d_z^2}{4D_0\tau + \kappa^2 w_0^2}\right) \quad (2.31)$$

This equation describes the correlation fit function G for free diffusion. The distance \mathbf{d} describes the mismatch between both illumination/detection volumes, which is zero for the autocorrelation fit function, but cannot be neglected for the cross-correlation fit function. The structure factor κ describes the geometry of the focal volume, which is elongated in the axial z -direction. The characteristic diffusion time τ_{diff} expresses the mean time a particle spends in the focus. Those parameters and the effective volume V_{eff} and the concentration c are described by

$$\kappa = \frac{z_0}{w_0}, \quad \tau_{diff} = \frac{w_0^2}{4D_0}, \quad V_{eff} = \frac{\pi^{3/2}}{\kappa w_0^3} \ll V \quad \text{and} \quad c = \frac{N}{V} \quad (2.32b,c,d,e)$$

These equations are only valid when the detection probability can be approximated by the product of three independent Gaussian functions. This description is an approximation as otherwise the correlation function cannot be expressed analytical.

2.4 Matrix approach for thick lenses

Snellius's lens equation cannot be used directly to find images formed by a system of thick lenses. The thickness of the lens alters the focus position. In addition, the center of the thick lens generally cannot be used as the lens position. For systems of multiple thick lenses, it is useful to represent the optical system using the matrix approach for thick lenses. This matrix M describes the deflection and the translation of the beam according to (Meyer-Arendt, 1995)

$$\begin{bmatrix} y_2 \\ \alpha_2 \end{bmatrix} = M \begin{bmatrix} y_1 \\ \alpha_1 \end{bmatrix} \quad (2.33)$$

Using Snellius's law and the approximation that distance, $d \ll s_1$ and s_2 , for the deflection at a spherical plane, as shown in figure 2.8, can be derived

$$M_B = \begin{bmatrix} 1 & 0 \\ -\frac{n_2 - n_1}{R} & 1 \end{bmatrix} \quad (2.34)$$

In this equation, n_1 and n_2 are the refractive indices of the medium at respectively the entrance and at the exit side of the surface as shown in the figure below.

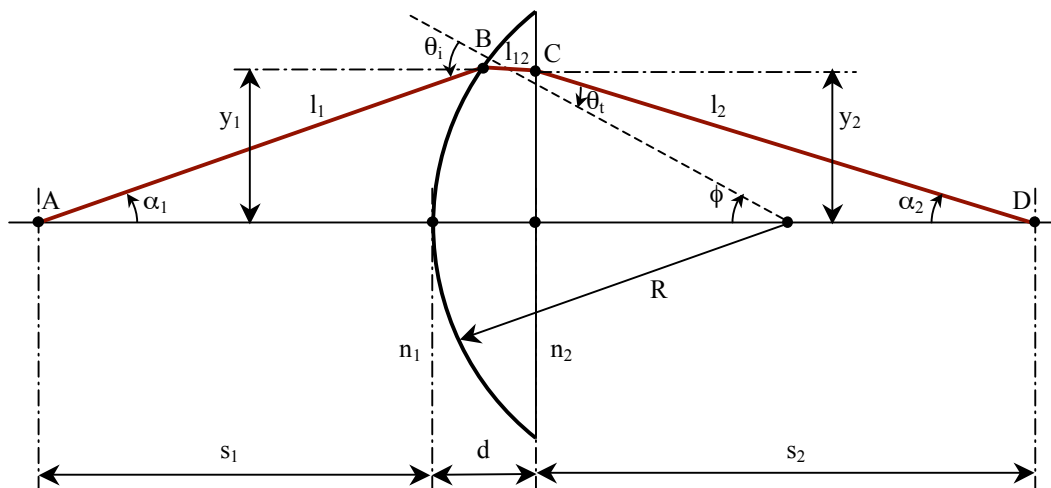


Figure 2.8. A schematic representation for deflection at a spherical surface with the parameter used.

In a homogeneous medium, there is no diffraction of the beam and this matrix is described by

$$M_T = \begin{bmatrix} 1 & \frac{d}{n} \\ 0 & 1 \end{bmatrix} \quad (2.35)$$

In this equation, the distance d is the path length through the medium and n the refractive index of the medium. The overall matrix describing the whole lens system is built up by multiplying all single matrices describing the successive surfaces and mediums.

2.5 Signal detection and signal scanning instruments

The digital camera is a fundamental component of the STFM. Hence, the light detection and the process how the images are recorded are described. Additionally, the f-theta lens is described in more detail.

2.5.1 The CCD sensor

A charge coupled device (CCD) sensor is an array of analog shift registers. The shift registers are light sensitive electrodes that convert the incoming photons into electrons by the photoelectric effect. This process occurs in certain materials when a photon with high enough energy hits the material and a free electron is created. The more light illuminates the electrode, the more electrons are captured. The ratio of released electrons per photon describes the quantum efficiency of the camera. Non-conductive boundaries between the shift registers keep the electrons within. During the integration time of the camera, free electrons will be created for the corresponding pixel. A control circuit transfers the electric charge to the neighboring electrode as schematically shown in figure 2.9. Accordingly, each shift register consists of three electrodes that control the charges represented by ϕ_1 , ϕ_2 and ϕ_3 respectively. Applying a positive potential V_H to the electrodes ϕ_1 and ϕ_3 and a lower potential V_L to electrode ϕ_2 will capture the charge in potential well of ϕ_2 . Sequentially changing the voltage at the three electrodes of each pixel leads to the transfer of the charges. At the end of the shift register, the charges are converted into a voltage and amplified. Accordingly, the control circuit converts the entire contents of the shift register into a voltage signal.

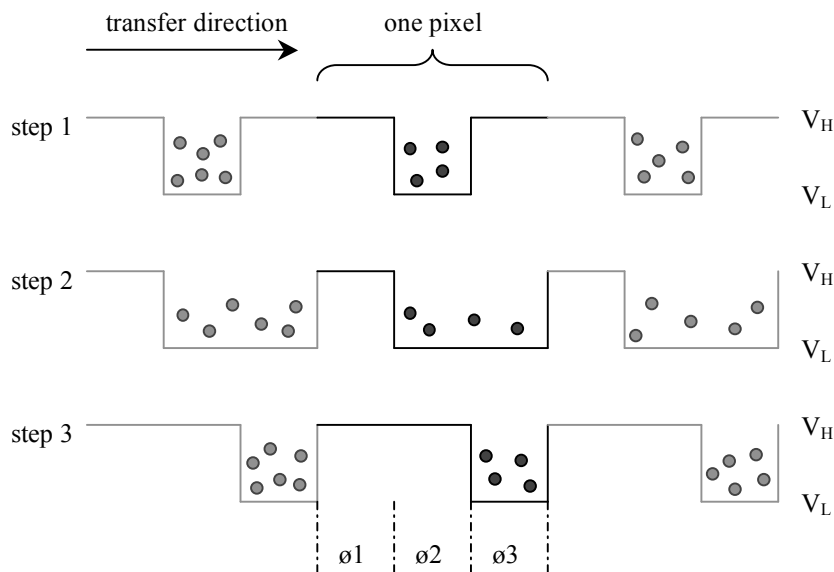


Figure 2.9. A schematic representation of the charge transfer in the readout register of a CCD sensor. The image is adapted from Andor (UK, Belfast).

There exist different kinds of CCD sensor architectures including the full-frame and frame-transfer CCD sensor. For the full-frame CCD, the whole image area of the sensor is active over the total period of imaging. During the readout phase, cells are shifted vertically row by row into the serial readout register, where the charges are then shifted horizontally to readout each individual pixel. Because the collection of the photons and the charge transfer into the readout register occurs simultaneously, the image will smear out when the shifting is not fast enough. For the frame-transfer CCD, the CCD sensor is divided into two distinct parts. One is the image area, which collects incoming photons and stores electrons in its cells, the other so-called storage area has the same size and functionality as the image area but is protected from illumination light by an opaque mask, typically aluminum. Because the transfer of the collected charges from the image area to the storage area is rather quick, the smear out of the image is acceptable. The storage area then can be readout through the serial output register at a speed necessary to measure correctly the charge of the cells. Simultaneously, the image area can collect new photons.

2.5.2 The EMCCD camera

The electron-multiplying charge coupled device (EMCCD) uses a modified shift register to provide an additional gain to the photoelectrons. Those cameras allow high sensitivity measurements, up to single photon detection combined with high image rates. Regularly, the EMCCD sensor architecture is the frame-transfer sensor. The shift register is extended to include an additional gain register placed between the shift register and the output amplifier as shown in figure 2.10A. During readout of the sensor, the photoelectrons are shifted through this multiplication register where amplification occurs prior to be readout by the charge amplifier. This on-chip electron multiplying gain structure multiplies the charges before the signal is readout, i.e. before the readout noise is added. For traditional CCD cameras, the signal is amplified after readout of the signal. Hence, the readout noise is also multiplied. This on-chip electron multiplying gain leads, especially for low intensity measurements, as is regularly the case for fast imaging, to a substantial increase of the signal-to-noise ratio. The amplification process of the EMCCD sensor is schematically represented in figure 2.10B for only a small part of the multiplication register as it regularly consists of hundreds of cells multiplying the charges successively in each cell. The electrons are multiplied by the so-called impact ionization process, which occurs when the electron has sufficient energy to create another electron-hole pair and hence a free electron. To enhance the charge amplification, the EMCCD technique makes use of the following. Firstly, the probability of creating an electron is increased by applying a high voltage during the charge transfer, which increases the impact ionization probability. Secondly, the amplification register of the EMCCD consists of hundreds of cells in which impact ionization can occur. Although the multiplying probability of the amplification in one cell is quite low, over the whole register, the probability increases and gains up to thousands can be achieved.

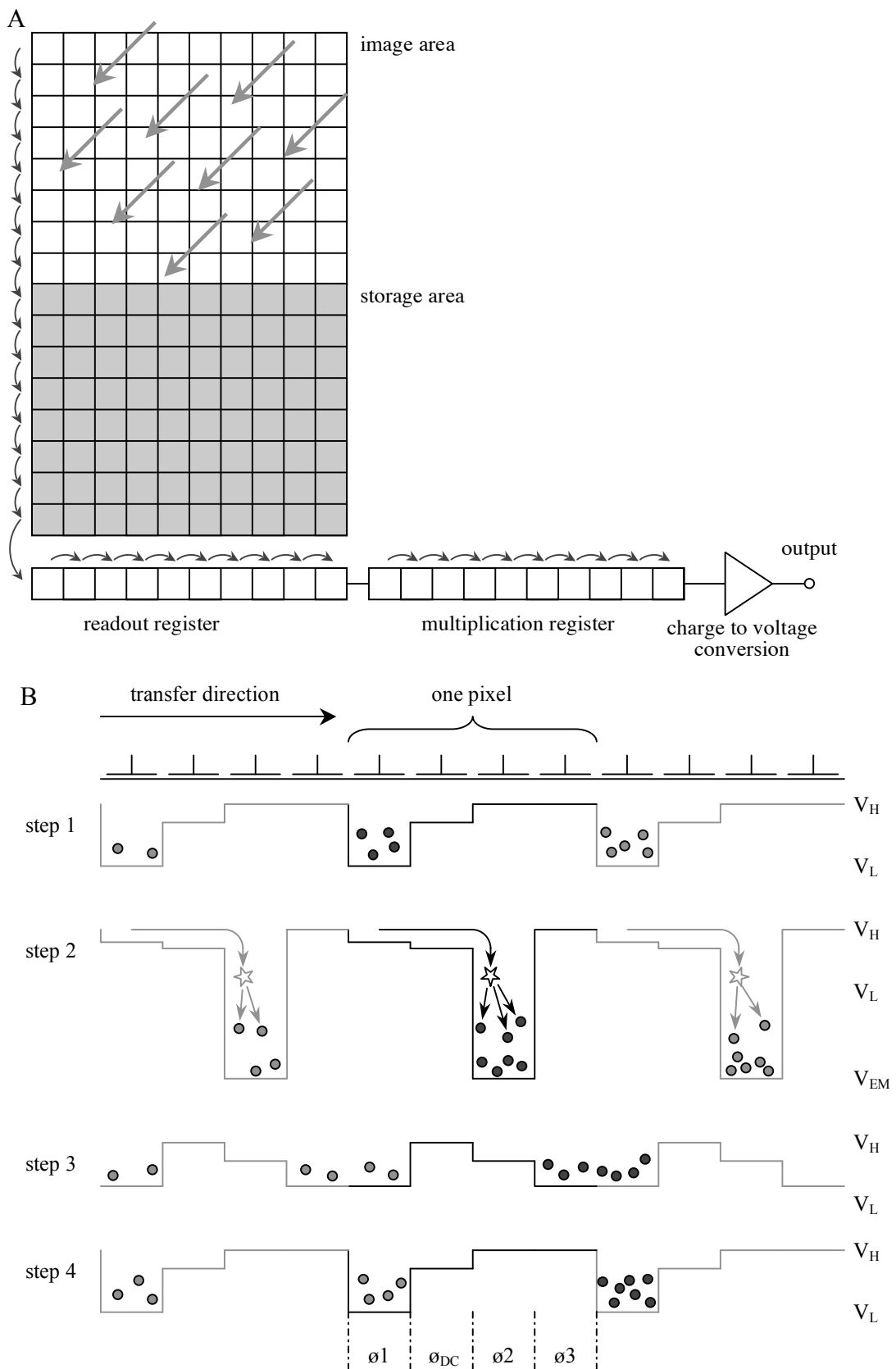


Figure 2.10. A diagram of the EMCCD readout structure (A) and a schematic representation of the charge transfer in the readout register of an EMCCD structure (B). The images are adapted from Andor (UK, Belfast).

2.5.3 F-Theta objective

A lens with focal length f transforms a collimated beam passing through the back focal point with an angle θ to the optical axis into an image height y according to

$$y = f \tan \theta \quad (2.36)$$

For larger angles, spherical aberration becomes significant, as the image formed by the lens is distorted as a result from the deviation of spherical surfaces from an ideal shape for image formation. A scanning or F-theta lens supplies an image in accordance with the so-called F-theta condition

$$y = f\theta \quad (2.37)$$

The object is translocated linear to the scanning angle θ as schematically shown in figure 2.11. F-theta lenses are often used for image scanning with a laser beam. For instance, in a confocal laser-scanning microscope, a laser beam is deflected by movable mirrors and focused by an F-theta lens. Proportionality between the scanning angle and the image height ensures proportionality between the angular velocity of the deflecting system and the scanning speed in the image plane.

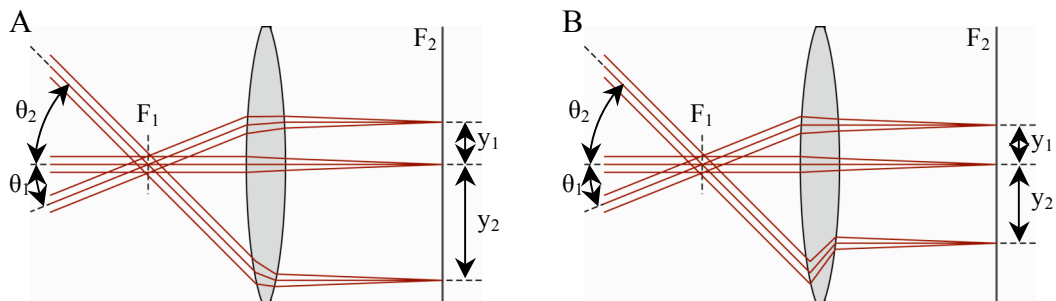


Figure 2.11. A schematic representation of the image formation at an ideal normal lens (A) and the same image formation at an F-theta lens (B). The relation between the angles, $\theta_2 = 2\theta_1$. A real F-theta lens is composed of a couple of lenses here schematically represented as only one lens.

Chapter 3

Theoretical characterization of the STFM

Biological relevant mobilities are based on diffusion processes, transport processes and interaction processes, which can be visualized by acquiring time series of two-dimensional images or three-dimensional image stacks as fast as possible. Many processes for example inside the cell nucleus are even faster and therefore cannot be recorded using the conventional imaging methods. For these faster processes, the fluorescence correlation spectroscopy (FCS) is a commonly used approach (Chu, 1979; Elson et al., 1976; Grunwald et al., 2005; Magde et al., 1972; Rigler et al., 1979; Sorscher et al., 1980). Conventional fluorescence correlation spectroscopy (FCS) is often based on confocal laser-scanning microscopy (CLSM). The setup of such a confocal microscope is shown in figure 2.1B. Due to the combined imaging and FCS functionality, these instruments provide an image of the spatial distribution of fluorescently labeled particles in a probe. In addition, the corresponding mobility of these particles can be measured at different positions using FCS.

Figure 3.1B displays a CLSM image of fluorescently labeled histones H1, which is a protein mainly localized inside the cell nucleus. The FCS measurements are evaluated at four different positions inside the cell nucleus (Fig. 3.1A,D,E,F) and at one position in the cytoplasm (Fig. 3.1C) as indicated (Wachsmuth et al., in preparation). One way to present the FCS results is by displaying the average time the molecules spend in the focal volume τ_{diff} . These values and the number of molecules in the focal volume N are represented on top of each FCS autocorrelation plot. With regard to the displayed measurements, it would be interesting to compare a spatial distribution image of the fluorescently labeled molecules using CLSM with an image of the mobility of the molecules measured by FCS. As the fluctuation point-measurement is a statistical method, the photons emitted by particles in the point focus are detected over a large period of time. The measurable range of the mean time a molecule spends in the focus is between 30 μs for small molecules up to 500 ms for large complexes. In order to get a confident statistical average value of these mean dwell times of the particles in the focal volume, the duration of the measurement will take between 30-90 seconds per detection point. Due to these long measurement times, it is almost impracticable to use FCS as an imaging technique by scanning the position of the point-FCS measurement and therefore often impossible in living cells.

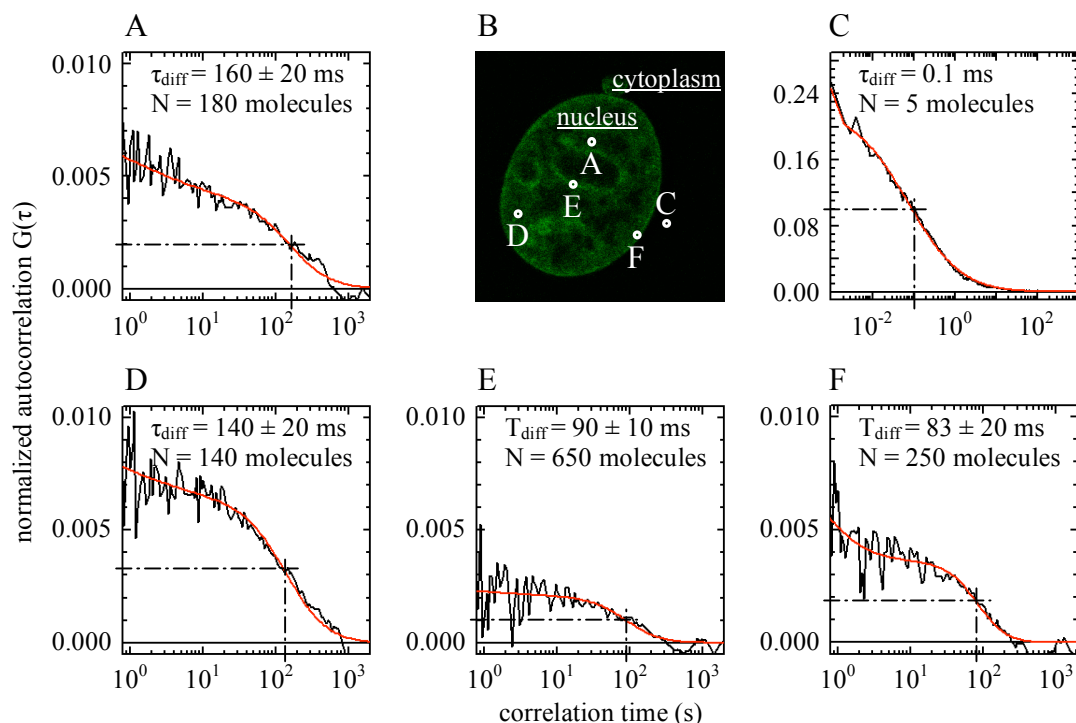


Figure 3.1. Mobility measurements of histone H1 by fluorescence correlation microscopy imaged by the laser scanning confocal microscope (B) and the corresponding normalized autocorrelation functions at the indicated points in image (A), (C), (D), (E) and (F). The diffusion time τ_{diff} , is the mean time the molecules spend in the focal volume indicated by the half-height of the amplitude of the autocorrelation. N gives the mean number of molecules in this focal volume during the measurement. These figures are adapted from (Wachsmuth et al., in preparation).

An additional disadvantage of this scanning FCS approach is the loss of information about the correlation between fluctuations at neighboring positions. Since the measurement of mobilities and interactions in a spatially differentiated way towards imaging is of great interest for many applications, the conventional FCS was extended to use FCS as an imaging technique.

3.1 Overview of the spatial and temporal fluctuation microscope

In the scope of this thesis, the point measurement of the conventional FCS was parallelized to a line imaging system. The STFM is a line-scanning confocal setup and shares properties of both the CLSM and of the wide-field microscope. The illumination beam in the sample is focused in only one direction resulting in a line illumination profile (Fig. 3.2A). The line illumination and detection setup was chosen as parallelization because this can easily be implemented for both the scanning of a line in the sample and the detection of a line using a line detector. In addition, the determination of spatial correlations at different time and length scales require adjacent detection positions. Fluorescently labeled particles inside this line illumination volume will emit fluorescence photons that contribute to intensity signals at the line detector. A dedicated spatially resolved FCS imaging instrument was developed that provides not only an image of the spatial distribution of the fluorescently labeled particles but also an image of the corresponding local fluorescence fluctuations. This extended FCS approach, which combines high temporal and spatial resolution in one instrument, is called spatial and temporal fluctuation microscope (STFM).

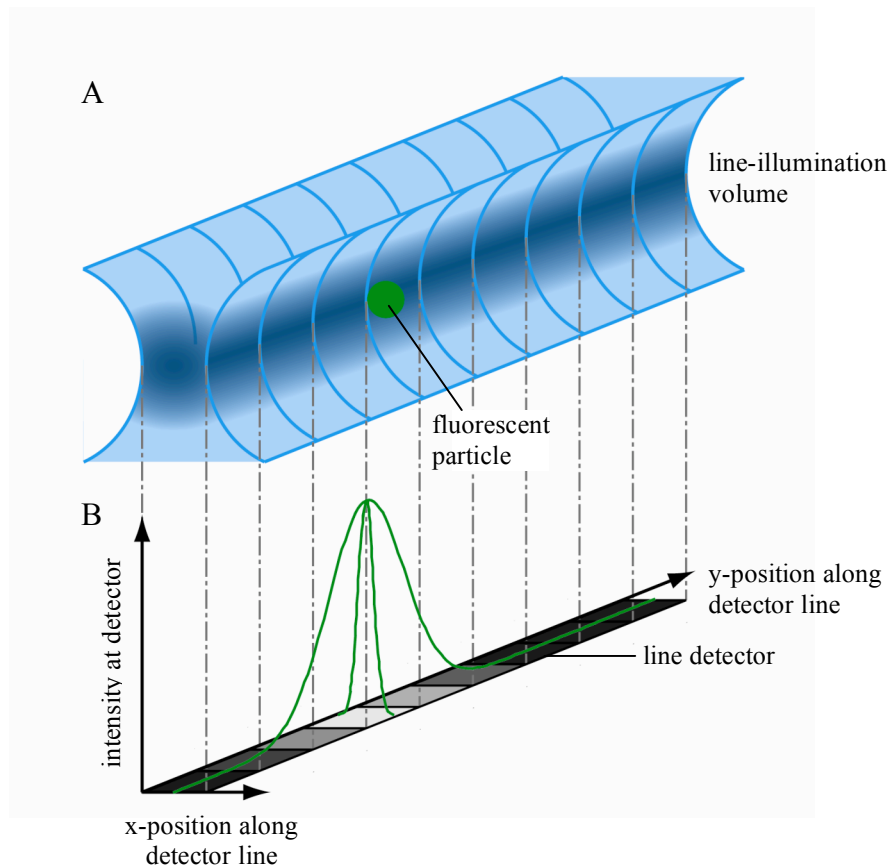


Figure 3.2. Physical origin of spatial and temporal fluctuation microscopy data. A fluorescently labeled particle in the illuminated volume (A) gives rise to a spreaded intensity profile on the line detector (B), which defines the detection focal volume.

A single fluorescently labeled particle in the line illumination volume will be imaged as a blurred intensity profile at the line detector, spread out over a certain area as schematically shown in figure 3.2B. The intensity profile will be smeared out because of the diffraction and the possible presence of aberrations. Accordingly, the detection volume can be considered as a small focal volume and not, as is the case for the illumination, a line. In other words, each pixel of the line detector corresponds to an individual focal volume in the probe that can overlap each other. As a result, the STFM enables the simultaneous acquisition of the fluorescence signal from each of these individual foci. For the illumination focus, the intensity along the z-axis drops down as the intensity is spread out over a larger area. For the STFM, this intensity area increases linear with the position along the z-axis and accordingly, the illumination intensity drops down. As a comparison, for the conventional CLSM, the intensity area increases quadratic.

Figure 3.3A shows schematically a fluorescently labeled particle that moves through the illuminated line volume. The dashed grey lines schematically represent the focal detection volumes corresponding to a certain pixel through the illuminated line. The fluorescently labeled particle moves in and out of the detection focal volumes, which will be detected at the corresponding pixel of the line detector (Fig 3.3B) as a series of short, randomized fluorescence signals. The spatial and temporal fluctuation microscope measures the fluctuations of the fluorescent molecules along the illuminated line.

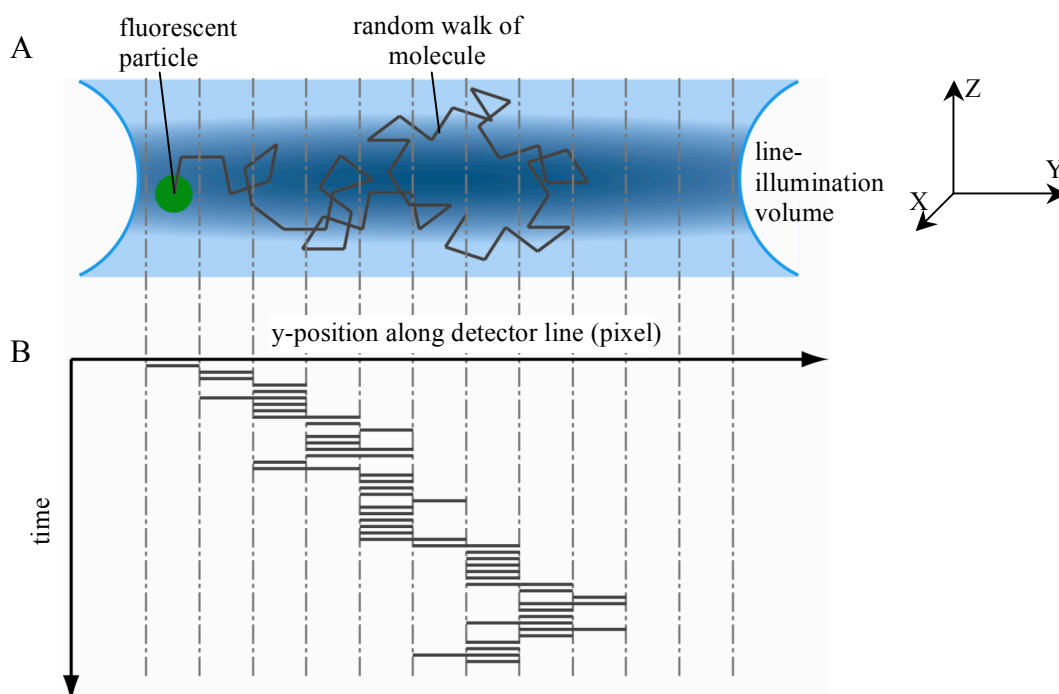


Figure 3.3. A fluorescently labeled particle inside the illuminated line volume (A) gives rise to a signal at the corresponding pixel at the line detector (B). The fluorescently labeled particle moves in and out of the focal detection volumes, which will be detected as a series of short, randomized fluorescence signals at the corresponding pixel of the line detector.

In summary, the substantial and additional advantages of the spatial and temporal fluorescence microscope are:

Advantages for imaging:

- Confocal resolution, however slightly worse than a point confocal system.
- High frame rate for imaging.
- Due to a longer dwell time for a whole line in comparison to the illumination of a single focus, the laser intensity per pixel can be decreased resulting in a higher photon yield and less photobleaching.

Advantages for FCS measurements:

- FCS becomes an imaging technique.
- Parallelized FCS measurements reduce the data acquisition time significantly *in vitro* and *in vivo*.
- Correlation measurements of temporal and spatial intensity fluctuation are possible. For spatial correlation measurements, different positions on the detected line can be cross-correlated with each other and for temporal correlation measurements, the signal of one detected pixel position can be autocorrelated with itself.

3.2 Beam geometries for line illumination and line detection

The intensity profile at the line detector of a STFM originating from a single fluorescently labeled particle in the illumination volume will be spread out. This spread of intensity is described mathematically by the detection PSF for line illumination and detection. The line detector of the STFM will detect only photons that are depicted at it. This imaging feature of the detection pathway is defined by the slit and detection parameters and the emission PSF of the optical system. These detected photons originate from the illuminated volume, which is, for the STFM system, a line illumination profile is described by the illumination PSF for line illumination and detection. The same as for the point illumination setup, the detection probability Ψ for line illumination can be described by the multiplication of the illumination PSF with the detection PSF for line illumination and detection. The point spread function can be described by

$$\Psi = \text{PSF}_{\text{ill}}(x, y, z) \text{PSF}_{\text{det}}(x, y, z) = |h_{\text{ill}}^2(x, y, z)|^2 \left(|h_{\text{em}}^2(x, y, z)|^2 * S(x, y) \right) \quad (3.1)$$

where $*$ denotes the convolution, S describes the shape of the slit or the pixel size of the line detection, and h_{ill} and h_{em} are the illumination and emission amplitude distributions for the line illumination and detection setup, respectively. Along the slit in the y -direction, the slit and the length of the line detector are assumed infinite. Accordingly, the y -dependence of the detection area $S(y)$ is defined by the pixel size. Across the slit in the x -direction, the width of the slit is usually chosen to be smaller than or equal to the pixel size of the line detection. Hence, $S(x)$ is defined by the width of the slit. The pixel size is usually chosen to be smaller than or equal to the size of the central lobe of the detection PSF. Hence, the pinhole can be approximated as delta function. Thus, the approximated detection point spread function for a confocal microscope is described solely by the emission point spread function.

3.2.1 Illumination point spread function for line illumination

For the line illumination setup as described here, the beam profile at the back aperture of the objective lens is altered in one direction compared to point illumination whereas in the other direction it is left unaltered. To get a line illumination in the specimen, the back focal plane of the objective has to be illuminated as shown in figure 3.4. In order to describe the illumination profile, the x - and y -direction are separated. The entrance aperture of the objective lens in x -direction is illuminated in the same way as for the point illumination (red curve). Upon illumination of the tubular lens with a parallel laser beam, as shown in figure 3.4A (blue line), the laser light will be focused at the back focal plane of the objective. This in return leads a constant illumination in the focal plane in y -direction. Combining those leads to a line illumination profile in the focal plane.

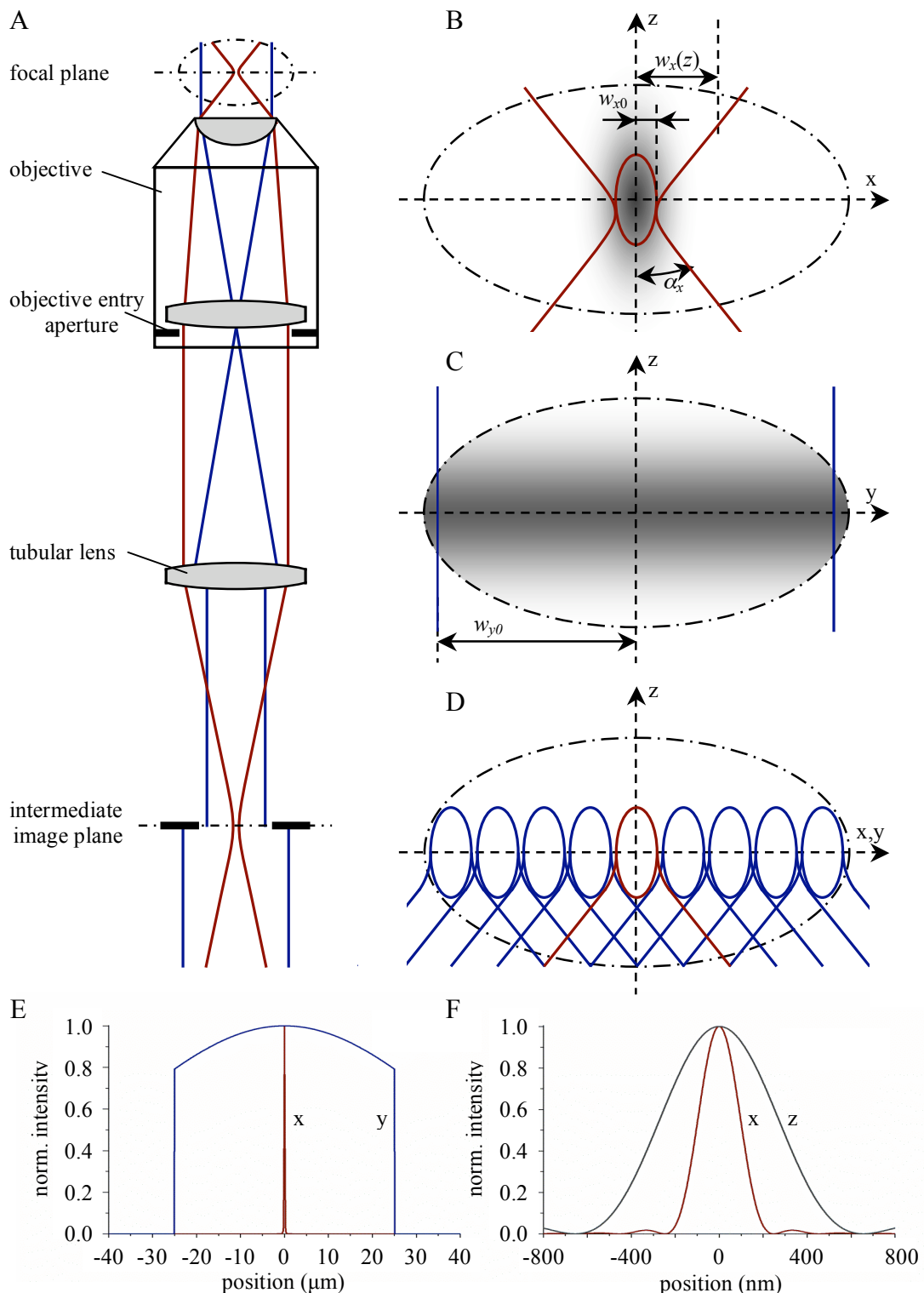


Figure 3.4. A schematic setup of the illumination part of a line-illuminating laser-scanning microscope (A). The laser beam in the probe is focused in only one direction called x (red). For the other direction, the laser leaves the objective with a parallel illumination beam called y (blue). This line-illumination profile is enlarged for the focal plane showing the x -dependence across the line (B) and the y -dependence along the line (C), with the geometric parameters as indicated. The detection volume for each pixel can be regarded as a focal volume (D) with one focus in the x -direction (red) and a series of foci in the y -direction (blue). The illumination intensity beam profiles (E) and (F) are plotted for the x - (red), y - (blue) and z - (grey) direction as indicated.

As for point illumination, the point spread functions are described using the scalar Debye theory. The illumination amplitude distribution near the focal volume can be written as the integration of the plane waves according to the angle of convergence. For line illumination, the light is convergent in x-direction and parallel in y-direction. According to equation 2.9, the illumination amplitude distribution for line illumination is thus described by

$$h_{\text{ill}}(x, z) = \int_{\theta=-\alpha}^{\alpha} e^{-ik_{\text{ill}}x\sin\theta} e^{-ik_{\text{ill}}z\cos\theta} \sin\theta d\theta \quad (3.2)$$

where α is the angle of the incident light in x-direction corresponding to the optical axis, k_{ill} is the illumination wave number. As optical axis, the z-axis is chosen. The integration in y-direction is left out in contrast to the PSF for point illumination, as the PSF for line illumination is not rotation symmetrical anymore. Because the original beam has approximately a Gaussian shape, the tubular lens is illuminated with a Gaussian beam also along the line, although the width of the Gaussian in this y-direction is much wider than it is across the line in the x-direction. Accordingly, the illumination beam profile along the line in the probe will also show a Gaussian illumination profile. The width of this Gaussian is defined by the beam size at the intermediate plane multiplied by the magnification factor of the objective-tubular lens pair. This Gaussian beam profile along the line is displayed in figure 3.4E (blue line). Only a small part of the Gaussian illumination beam is used as the sides are blocked. Hence, for simplification, the illumination intensity profile is considered constant along the line i.e. independent of y. The intensity distribution in the specimen will approximately be a line profile. In the x-direction, the point spread function is the same as for a point illumination and in the y-direction it has a constant value. According to the solution for the point illumination PSF (equation 2.15), this leads to an approximated illumination point spread function for the line illumination for a high numerical-aperture objective lens as given by

$$\text{PSF}_{\text{ill}}(\mathbf{r}) = \left(\frac{\sin(u_{\text{ill}})}{u_{\text{ill}}} \right)^2 \cdot \left(\frac{2J_1(v_{\text{ill}})}{v_{\text{ill}}} \right)^2, \text{ with} \quad (3.3a)$$

$$u_{\text{ill}} = n \frac{2\pi}{\lambda_{\text{ill}}} z \sin^2(\alpha/2) \text{ and } v_{\text{ill}} = n \frac{2\pi}{\lambda_{\text{ill}}} x \sin \alpha \quad (3.3b,c)$$

The illumination profiles in x- and y-direction are plotted in figure 3.4E and in x- and z-direction plotted in figure 3.4F. They are fully determined by the numerical aperture of the objective lens and the wavelength used.

3.2.2 Detection point spread function for line detection

Similarly to a point illuminating confocal microscope, the emission amplitude distribution in front of the slit can be expressed by the scalar Debye diffraction integral for a circular lens. As each single point along the line in the probe will be

imaged as one point on the detector, as is the case for point illumination, this leads to a detection point spread function for line detection that is the same as the detection point spread function described above for point illumination (see equation 2.17).

$$\text{LSF}_{\text{det}}(\mathbf{r}) = \left(\frac{\sin(u_{\text{det}})}{u_{\text{det}}} \right)^2 \cdot \left(\frac{2J_1(v_{\text{det}})}{v_{\text{det}}} \right)^2, \text{ with} \quad (3.4a)$$

$$u_{\text{det}} = n \frac{2\pi}{\lambda_{\text{det}}} z \sin^2(\alpha/2) \text{ and } v_{\text{det}} = n \frac{2\pi}{\lambda_{\text{det}}} \sqrt{x^2 + y^2} \sin \alpha \quad (3.4b,c)$$

3.2.3 Detection probability for line illumination and line detection

The observation volume of the line illumination and detection setup is defined by the illumination PSF in equation 3.3 and the imaged volume by the detection PSF of equation 3.4. The combined point spread function, also called molecular detection efficiency (MDE) of a line illuminating and detecting microscope is defined by the product of the illumination point spread function and the detection point spread function according to equation 3.1. According to equation 3.3 and 3.4, the combined PSF is described by

$$\text{PSF}(\mathbf{r}) = \left(\frac{\sin(u_{\text{ill}})}{u_{\text{ill}}} \right)^2 \cdot \left(\frac{\sin(u_{\text{det}})}{u_{\text{det}}} \right)^2 \cdot \left(\frac{2J_1(v_{x,\text{ill}})}{v_{x,\text{ill}}} \right)^2 \cdot \left(\frac{2J_1(v_{\text{det}})}{v_{\text{det}}} \right)^2 \quad (3.5a)$$

$$u_{\text{ill}} = n \frac{2\pi}{\lambda_{\text{ill}}} z \sin^2(\alpha/2), \quad u_{\text{det}} = n \frac{2\pi}{\lambda_{\text{det}}} z \sin^2(\alpha/2) \quad (3.5b,c)$$

$$v_{x,\text{ill}} = n \frac{2\pi}{\lambda_{\text{ill}}} x \sin \alpha \text{ and } v_{\text{det}} = n \frac{2\pi}{\lambda_{\text{det}}} \sqrt{x^2 + y^2} \sin \alpha \quad (3.5d,e)$$

General properties of the sinc- and Bessel-functions are their side lobes that will give a contribution to the intensity profile. As these functions are squared, the first side lobes of the Bessel-function reduce to 1.75% and those of the sinc-function to 4.7%. The size of the illumination PSF and the detection PSF are different as they scale with different wavelengths. In addition, the illumination point spread function is multiplied with the detection point spread function. Accordingly, the side lobes of the sinc-function and those of the Bessel-function for the x- and z-direction decreases to zero upon multiplication of the point spread functions. According to figure 3.5, this decrease to zero is only partly true as for the y-direction (along the line) the y-dependence of the illumination point spread function fails. Experimental data shows the appearance of these side lobes for a line illuminating confocal microscope, as shown in figure 3.6 Thus along the line, these side lobes cannot be neglected (Dusch et al., 2007).

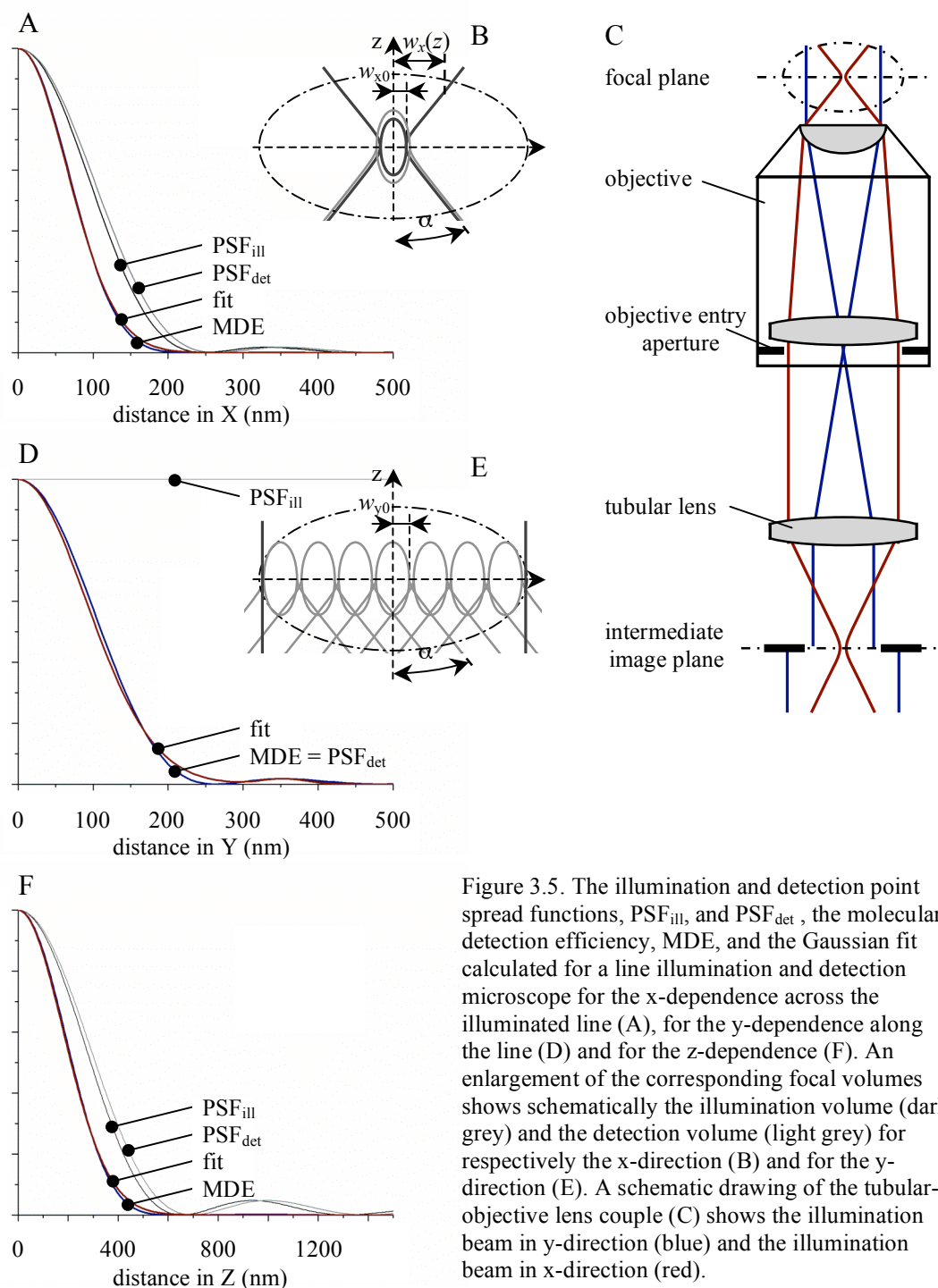


Figure 3.5. The illumination and detection point spread functions, PSF_{ill} , and PSF_{det} , the molecular detection efficiency, MDE, and the Gaussian fit calculated for a line illumination and detection microscope for the x-dependence across the illuminated line (A), for the y-dependence along the line (D) and for the z-dependence (F). An enlargement of the corresponding focal volumes shows schematically the illumination volume (dark grey) and the detection volume (light grey) for respectively the x-direction (B) and for the y-direction (E). A schematic drawing of the tubular objective lens couple (C) shows the illumination beam in y-direction (blue) and the illumination beam in x-direction (red).

3.2.4 Detection probability function for line illumination and line detection

In a confocal setup with a high numerical aperture (NA), the detection probability can be approximated by a rotation symmetrical three-dimensional Gauss-function, with $1/e^2$ radius of w_k lateral and z_k axial to the optical axis (see section 2.2.6). This approximation with a three-dimensional Gaussian is necessary for the analytical

calculation of the correlation function described in detail below, because for the analytical calculation of the correlation function, the derived overall point spread function is too complicated. However, for the line illumination system, the side lobes cannot be neglected, and will affect the analytical description of the correlation fit function. Including the first two side lobes into the detection probability fit function leads to three three-dimensional Gaussians. This Gaussian fit for the detection probability centered at position \mathbf{p}_k becomes

$$\begin{aligned} \Psi(\mathbf{r}) = & \exp\left(-2\frac{(x-p_{k,x})^2}{w_{k,x}^2} - 2\frac{(y-p_{k,y})^2}{\kappa_{y,ml}^2 w_{k,x}^2} - 2\frac{(z-p_{k,z})^2}{\kappa_z^2 w_{k,x}^2}\right) + \\ & A_{1sl} \exp\left(-2\frac{(x-p_{k,x})^2}{w_{k,x}^2} - 2\frac{((y-y_{1sl})-p_{k,y})^2}{\kappa_{y,1sl}^2 w_{k,x}^2} - 2\frac{(z-p_{k,z})^2}{\kappa_z^2 w_{k,x}^2}\right) + \\ & A_{1sl} \exp\left(-2\frac{(x-p_{k,x})^2}{w_{k,x}^2} - 2\frac{((y+y_{1sl})-p_{k,y})^2}{\kappa_{y,1sl}^2 w_{k,x}^2} - 2\frac{(z-p_{k,z})^2}{\kappa_z^2 w_{k,x}^2}\right) \end{aligned} \quad (3.6a)$$

with

$$A_{1sl} = 0.0175, \quad y_{1sl} = \frac{5.14 \cdot \lambda_{det}}{2\pi \cdot n \cdot \sin \alpha} \quad \text{and} \quad \kappa_{y,1sl} = 0.342 \cdot \kappa_{y,ml}, \quad (3.6b,c,d)$$

where $w_{k,x}$ is the $1/e^2$ radii of the Gaussian fit for the x-direction schematically displayed in figure 3.7. The structure parameters $\kappa_{y,ml}$, $\kappa_{y,1sl}$ and κ_z are introduced as structure factor describing the geometry of the Gaussian fit for the y-direction of the main lobe, for both side lobes of the Bessel-function and for the z-direction, respectively (Fig. 3.7). The width of the side lobes is described by their own structure parameter, as they are narrower than the width of the main lobe. The width of these first side lobes are related to the width of the main lobe (equation 3.6d) since the position of the first zero-crossing of a Bessel-function is at a distance of $v_{det} = 3.83$ of the main lobe and the maximum of the first side lobe $v_{det} = 5.14$ of the main lobe. The height of these first side lobes is $A_{1sl} = 0.0175$ when the maximum of the main lobe is normalized to one.

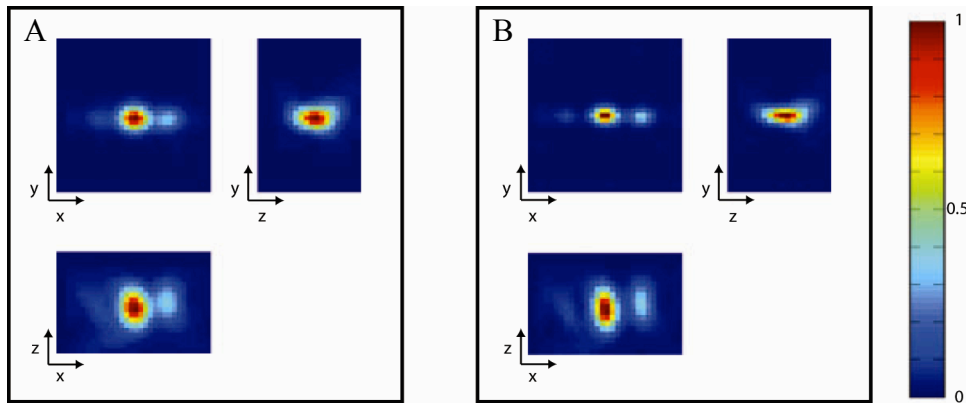


Figure 3.6. xy-, xz- and yz-views of the measured point spread functions before (A) and after deconvolution (B). The measured point spread functions represents an average of more than 150 beads. Figure adapted from (Dusch et al., 2007)

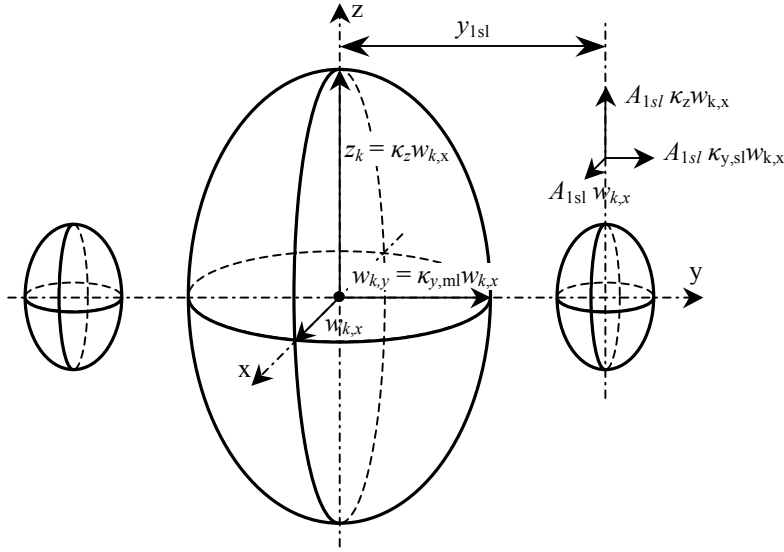


Figure 3.7. A schematic drawing of the main focal volume and the both side lobes, with the used parameters as indicated.

Figure 3.5 shows the illumination (light grey) and detection (dark grey) point spread function for a line illuminating confocal microscope across the line in x -direction (Fig. 3.5A), along the line in y -direction (Fig. 3.5D) and in the axial direction (Fig. 3.5F). The small difference between the illumination and detection PSF is due to the small wavelength shift between excitation and emission. The point spread functions shown are computed and displayed for a typical experimental configuration. The illumination wavelength is, $\lambda_{\text{ill}} = 488 \text{ nm}$ and the detection wavelength is, $\lambda_{\text{det}} = 519 \text{ nm}$. The used water-immersion objective has a numerical aperture, $NA = 1.2$ and the refractive index of water is, $n = 1.34$, which defines the maximal angle of convergence, $\alpha = 63.6^\circ$.

The molecular detection efficiency (MDE) is plotted as the blue curve in the three plots of figure 3.5. Along the illuminated line, the illumination point spread function is constant. Accordingly, the detection point spread function and the molecular detection efficiency are equal. The Gaussian fit for the molecular detection efficiency according to equation 3.6 is plotted in red. This fit leads to the following $1/e^2$ -radii for the experimental parameter used: $w_{k,x} = 130 \text{ nm}$, $w_{k,y} = \kappa_{y,ml} w_{k,x} = 180 \text{ nm}$ and $z_k = \kappa_z w_{k,x} = 360 \text{ nm}$. In addition, other used parameters are $A_{y,1sl} = 0.0175$, $y_{1sl} = 354 \text{ nm}$ and $\kappa_{y,1sl} = 0.342$.

3.3 FCS autocorrelation function for line illumination and detection

The beam geometry of the spatial and temporal fluctuation microscope (STFM) differs from the conventional confocal laser-scanning microscopy (CLSM). The beam geometry of the CLSM is symmetrical perpendicular to the optical axis whereas in the STFM configuration, a line beam profile is illuminated and the beam geometry is no longer symmetrical. Fluorescence correlation spectroscopy (FCS) uses a certain correlation fit function, which is described in section 2.3. In addition, the influence of the beam geometry on the correlation functions has been researched for different kind of experimental microscopes, in particular because of the further development of high-resolving confocal microscopy (Aragón and Pecora, 1976; Elson and Magde, 1974; Qian and Elson, 1991). As for the STFM, the beam profile is altered, the correlation fit function must be adapted for this new beam geometry. The theoretical fundamentals for the line illuminating fluorescence correlation spectroscopy described in this section are derived from the theoretical fundamentals described in chapter 2.3 for the point illumination setup. These equations for point illumination FCS are extended to apply to the line illumination FCS. To yield an expression for the normalized autocorrelation function of equation 2.37, the solution of Fick's second law according to equation 2.40, the derived detection probability for the line illumination microscope (equation 3.6) and the probability distribution of a particle in a finite volume with constant concentration $W_D(\mathbf{r},t) = 1/V$ are used.

The diffusion is assumed to be isotropic, i.e. without directed movements. Therefore, the correlation function can be factorized in an x-, a y- and a z-component as

$$G(\tau) = \frac{V}{N} g_x(\tau) g_y(\tau) g_z(\tau) - \frac{1}{N} \quad (3.7)$$

The x-component of the correlation fit function $g_x(\tau)$ is described by

$$g_x(\tau) = \frac{2}{\pi w_k w_l} \frac{1}{\sqrt{4\pi D_0 \tau}} \int_{x_1=-\infty}^{\infty} \int_{x_2=-\infty}^{\infty} e^{-2\frac{(x_1-p_{k,x})^2}{w_{k,x}^2} - 2\frac{(x_2-p_{l,x})^2}{w_{l,x}^2} - \frac{(x_1-x_2)^2}{4D_0\tau}} dx_2 dx_1 \quad (3.8)$$

As the volume of the probe is much larger than the focal volume, the integral boundaries are chosen to be infinity. The substitution of $\mathbf{u} = \mathbf{r}_1 - \mathbf{p}_k$, $\mathbf{v} = \mathbf{r}_2 - \mathbf{p}_l$ and $\mathbf{d} = \mathbf{p}_k - \mathbf{p}_l$ leads to

$$g_x(\tau) = \frac{2}{\pi w_k w_l} \frac{1}{\sqrt{4\pi D_0 \tau}} \int_{u_x=-\infty}^{\infty} \int_{v_x=-\infty}^{\infty} e^{-2\frac{u_x^2}{w_{k,x}^2} - 2\frac{v_x^2}{w_{l,x}^2} - \frac{(u_x - v_x + d_x)^2}{4D_0\tau}} dv_x du_x \quad (3.9)$$

which is the integral of a function with dimensionless units $u_x/w_{k,x}$ and $v_x/w_{l,x}$, over the complete metric space, \mathbb{R}^2 . Accordingly, it is allowed to apply a suitable rotation

of the coordinate system. Using $w_0^2 = (w_k^2 + w_l^2)/2$, the following rotation is chosen (Wachsmuth, 2001)

$$\sqrt{2}\alpha = \frac{u_x}{w_0} \frac{w_l}{w_k} + \frac{v_x}{w_0} \frac{w_k}{w_l}, \sqrt{2}\beta = \frac{u_x}{w_0} - \frac{v_x}{w_0} \quad \text{with } \alpha^2 + \beta^2 = \frac{u_x^2}{w_k^2} + \frac{v_x^2}{w_l^2} \quad (3.10a,b,c)$$

This leads for the x-component of the correlation fit function $g_x(\tau)$ based on equation 3.9 to

$$g_x(\tau) = \frac{2}{\pi} \frac{1}{\sqrt{4\pi D_0 \tau}} \int_{\alpha=-\infty}^{\infty} e^{-2\alpha^2} d\alpha \int_{\beta=-\infty}^{\infty} e^{-2\beta^2 - \frac{(\sqrt{2}w_0\beta + d_x)^2}{4D_0\tau}} d\beta \quad (3.11a)$$

$$= \frac{1}{\sqrt{\pi} w_0} \left(1 + \frac{4D_0\tau}{w_0^2}\right)^{-1/2} \exp\left(-\frac{d_x^2}{4D_0\tau + w_0^2}\right) \quad (3.11b)$$

Defining the characteristic diffusion time, $\tau_{diff} = w_0^2/4D_0$, which is the mean dwell time of the particle in the focal volume, this yields

$$g_x(\tau) = \frac{1}{\sqrt{\pi} w_0} \left(1 + \frac{\tau}{\tau_{diff}}\right)^{-1/2} \exp\left(-\frac{d_x^2}{4D_0\tau + w_0^2}\right) \quad (3.12)$$

The shape of the z-component of the detection probability Ψ is equal to that of the x-component. The only difference is the width of the Gaussian of the detection probability, which for the z-component is equal to z_k . A structure factor $\kappa_z = z_0/w_0$ is introduced, which describes the geometry of the focal volume. The z-component of the correlation fit function (Eq. 3.7) becomes

$$g_z(\tau) = \frac{1}{\sqrt{\pi} \kappa_z w_0} \left(1 + \frac{\tau}{\kappa_z^2 \tau_{diff}}\right)^{-1/2} \exp\left(-\frac{d_z^2}{4D_0\tau + \kappa_z^2 w_0^2}\right) \quad (3.13)$$

The y-component of the correlation fit function $g_y(\tau)$, as defined by equation 3.7, is more complicated to derive. This is because the detection probability Ψ for this direction shows side lobes according to equation 3.6. The y-component of the correlation fit function can be described by

$$g_y(\tau) = \frac{\sum_{n=1}^3 A_n \sum_{m=1}^3 A_m g_{y,nm}(\tau)}{\sum_{n=1}^3 A_n \sum_{m=1}^3 A_m} = \frac{\sum_{n=1}^3 A_n \sum_{m=1}^3 A_m g_{y,nm}(\tau)}{\left(\sum_{n=1}^3 A_n\right)^2} \quad (3.14)$$

with $A_{n,m}$ being the amplitude of the corresponding fitted Gaussians. The height of the side lobes is 1.75% of the maximum of the main lobe. Using the x-component of

the correlation fit function $g_x(\tau)$ (Eq. 3.12), this leads for the y-component of the correlation fit function to

$$g_y(\tau) = \left(\sum_{n=1}^3 A_n \right)^{-2} \cdot \sum_{n=1}^3 \sum_{m=1}^3 A_n A_m \frac{2}{\sqrt{\pi} \kappa_{y,nm} w_0} \left(1 + \frac{4D_0\tau}{\kappa_{y,nm}^2 w_0^2} \right)^{-1/2} \cdot \exp\left(-\frac{(d_y - (B_n - B_m))^2}{4D_0\tau + \kappa_{y,nm}^2 w_0^2} \right) \quad (3.15)$$

The distance $(B_n - B_m)$ describes the displacement between the corresponding lobes, which is for example for $n=1$ and $m=2$ the distance between main and side lobe y_{1sl} . $w_{y,nm}$ is the $1/e^2$ radii of the fitted Gaussian lobes and $\kappa_{y,nm}$, the structure factor for the width of the corresponding Gaussians, which differs for the main and side lobes. According to equation 3.15, this leads to a 3x3 matrix for the y-component of the correlation fit function. However, the contributions are recursive, which means that the contribution of the left side lobe with the main lobe is equal to the contribution of the main lobe with the left side lobe. In addition, side lobe-side lobe contributions are negligible. This leads to three remaining terms

$$g_y(\tau) = \left(\frac{1}{1 + 2A_{1sl}} \right) \cdot \left[\begin{aligned} & \left(\frac{1}{\sqrt{\pi} \kappa_{y,ml} w_0} \right) \cdot \left(1 + \frac{4D_0\tau}{\kappa_{y,ml}^2 w_0^2} \right)^{-1/2} \cdot \exp\left(-\frac{d_y^2}{4D_0\tau + \kappa_{y,ml}^2 w_0^2} \right) + \\ & \left(\frac{A_{1sl}}{\sqrt{\pi} \kappa_{y,1sl} w_0} \right) \cdot \left(1 + \frac{4D_0\tau}{\kappa_{y,1sl}^2 w_0^2} \right)^{-1/2} \cdot \exp\left(-\frac{(d_y - y_{1sl})^2}{4D_0\tau + \kappa_{y,1sl}^2 w_0^2} \right) + \\ & \left(\frac{A_{1sl}}{\sqrt{\pi} \kappa_{y,1sl} w_0} \right) \cdot \left(1 + \frac{4D_0\tau}{\kappa_{y,1sl}^2 w_0^2} \right)^{-1/2} \cdot \exp\left(-\frac{(d_y + y_{1sl})^2}{4D_0\tau + \kappa_{y,1sl}^2 w_0^2} \right) \end{aligned} \right] \quad (3.16a)$$

Substituting those x-, y- and z-component of the correlation fit function into equation 3.7 yields

$$G_{kl}(\tau) = \frac{1}{c\pi^{3/2}V_{\text{eff}}} \left(1 + \frac{\tau}{\tau_{\text{diff}}} \right)^{-1/2} \cdot \left(1 + \frac{\tau}{\kappa_z^2 \tau_{\text{diff}}} \right)^{-1/2} \cdot \exp\left(-\frac{d_x^2}{4D_0\tau + w_0^2} - \frac{d_z^2}{4D_0\tau + \kappa_z^2 w_0^2} \right) \cdot \left[\begin{aligned} & \left(\frac{1}{(1 + 2A_{1sl})} \right) \cdot \left(1 + \frac{\tau}{\kappa_{y,ml}^2 \tau_{\text{diff}}} \right)^{-1/2} \cdot \exp\left(-\frac{d_y^2}{4D_0\tau + \kappa_{y,ml}^2 w_0^2} \right) + \\ & \left(\frac{\kappa_{y,ml} A_{1sl}}{\kappa_{y,1sl} (1 + 2A_{1sl})} \right) \cdot \left(1 + \frac{\tau}{\kappa_{y,1sl}^2 \tau_{\text{diff}}} \right)^{-1/2} \cdot \exp\left(-\frac{(d_y - y_{1sl})^2}{4D_0\tau + \kappa_{y,1sl}^2 w_0^2} \right) + \\ & \left(\frac{\kappa_{y,ml} A_{1sl}}{\kappa_{y,1sl} (1 + 2A_{1sl})} \right) \cdot \left(1 + \frac{\tau}{\kappa_{y,1sl}^2 \tau_{\text{diff}}} \right)^{-1/2} \cdot \exp\left(-\frac{(d_y + y_{1sl})^2}{4D_0\tau + \kappa_{y,1sl}^2 w_0^2} \right) \end{aligned} \right] \quad (3.17)$$

with,

$$A_{1sl} = 0.0175, \quad y_{1sl} = \frac{5.14 \cdot \lambda_{\text{det}}}{2\pi \cdot n \cdot \sin \alpha} \quad \text{and} \quad \kappa_{y,1sl} = 0.342 \cdot \kappa_{y,ml}, \quad (3.17\text{b,c,d})$$

This equation uses the characteristic diffusion time $\tau_{\text{diff}} = w_0^2/4D_0$, which is the mean dwell time of the particle in the focal volume, $c = N/V$ is the concentration of the specimen, with N the total number of particles and V the total volume of the whole specimen. The vector \mathbf{d} is the mismatch of the illumination/detection volumes for both wavelengths, which is zero for the autocorrelation. In addition, a several structure factors describe the geometry of the focal volume (Fig. 3.7). The width of the x-component of the Gaussian beam is defined as w_0 and chosen as the basic width to describe the other dimensions. The structure factor for the z-direction is $\kappa_z = z_0/w_0$. The structure factor in the y-direction is described using two structure factors as the width of the main lobe and that of the side lobes are different. The structure factor for the main lobe in y-direction is $\kappa_{y,ml} = w_{y,ml}/w_0$ and that for the first side lobe in y-direction is $\kappa_{y,1sl} = w_{y,1sl}/w_0$, which is equal to $\kappa_{y,1sl} = 0.342 \cdot \kappa_{y,ml}$. The effective focal volume V_{eff} can be defined for $V_{\text{eff}} \ll V$ by

$$V_{\text{eff}} = \pi^{3/2} \kappa_{y,ml} \kappa_z w_0^2 \quad (3.18)$$

As $cV_{\text{eff}} \ll N = cV$, is equal to the average number of particles in the focus volume, the term $1/N$ of equation 3.7, which is the inverse of the total number of particles of the whole volume, is neglected.

Chapter 4

Implementation and construction of the STFM

In order to turn FCS into an imaging method, the conventional FCS instrument with point detection based on the CLSM was extended. The developed microscope setup is described in detail in chapter 3. This section describes the optical and mechanical implementation of the spatial and temporal fluctuation microscope (STFM) including the requirements a description of the optical pathway, the used instrumental components and the control of them.

4.1 Instrumental requirements

The STFM system developed in this thesis work was designed to fulfill the following requirements:

- Simultaneous measurement of the spatially resolved correlation functions of fluorophors at a series of positions along a line.
- Measurement of solutions as well as measurement in living cells.
- Capability to make confocal fluorescence microscopic images in addition to the FCS measurements to compare the spatial distribution of the fluorophors with their corresponding temporal fluctuations.
- High spatial resolution.
- High temporal resolution to measure fast particles that spend down to 50 μs in the focal volume.
- Image size of at least 25 μm x 25 μm , to image a complete cell nucleus.
- Mechanical long-term stability.
- Uncomplicated alignment of the whole instrument.

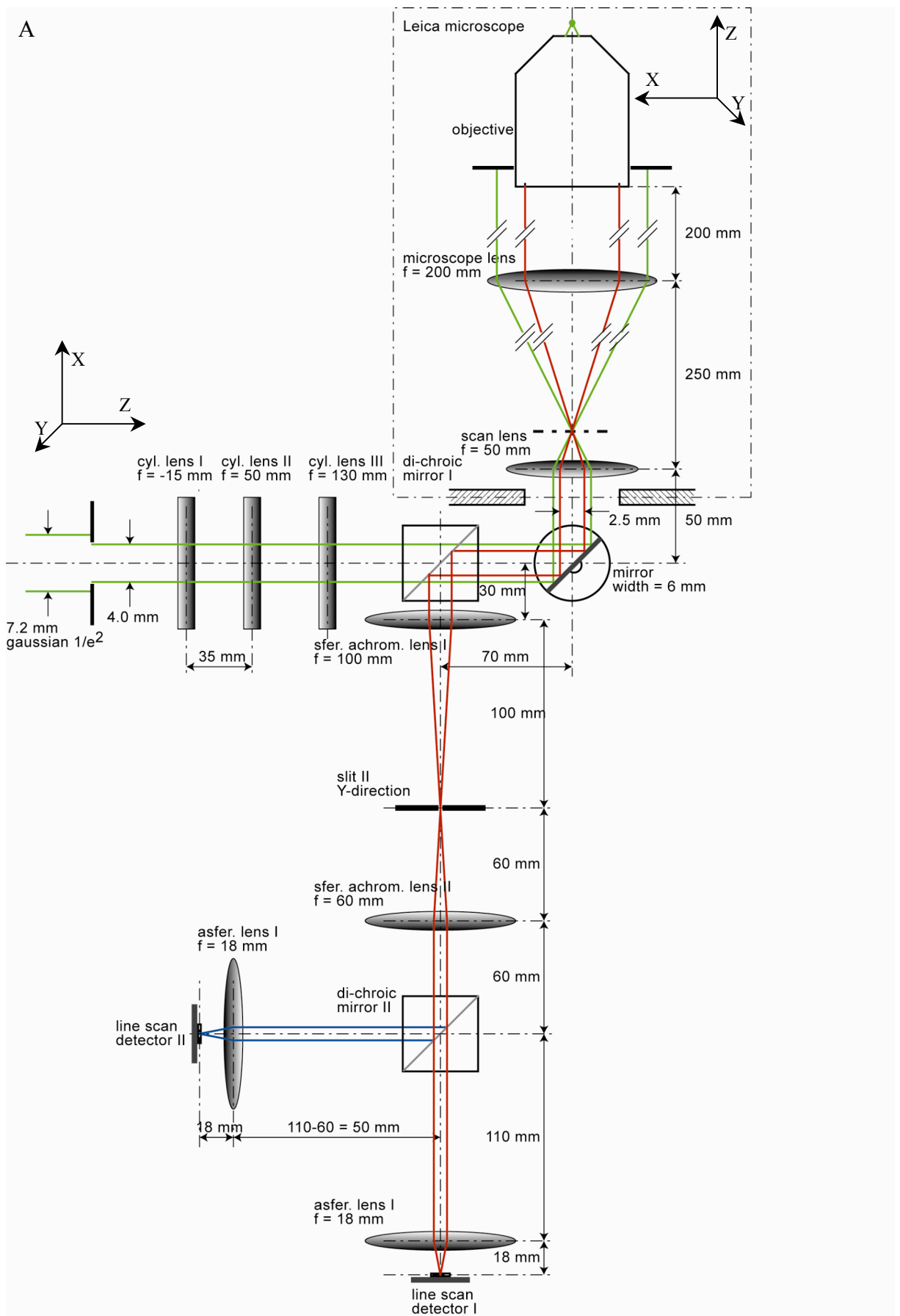
- Modular design allowing easy exchange of lasers and the corresponding filters and detectors.
- Upgradable to two-color detection for fluorescence cross-correlation spectroscopy measurements.
- Applicable to routine measurements by different users.

4.2 Description of the optical pathway of the STFM

The STFM is a confocal line-illuminating microscope. The setup is an extension of a Leica inverted fluorescence microscope. For this line microscope, the optical pathway is no longer axially symmetric. The upper view and the side view of the optical pathway show different beam geometries and are therefore plotted separately (Fig. 4.1A,B). The axial and radial dimensions of the beams are plotted proportional to each other with a ratio of 5:1. In the two-dimensional plot, the optical pathway after the scanning mirror is perpendicular to the paper. Hence, it is turned to the right for both plots. In addition, at both dichroic mirrors of figure 4.1B, the further pathway is plotted below. According to these figures, the laser beam enters the STFM instrument at the left of the figure. This laser beam enters the Leica microscope through its side port. The optical pathway in the Leica microscope, direct after the scan lens, is abbreviated displayed by two inclined lines.

In the probe a line is illuminated, which is focused in x- and parallel in y-direction. To obtain a focused illumination beam in x-direction, the back focal plane of the objective has to be illuminated with a parallel laser beam in this direction with an almost constant intensity distribution over the whole aperture. The diameter of the aperture of the back focal plane is 10 mm, which is illuminated by a laser beam with a $1/e^2$ diameter of more than 20 mm. This constructive feature and the beam enlargement by the scan and tubular lenses, defines the diameter of the entering laser beam. This 488 nm laser beam passes through a laser beam coupler, a single-mode fiber and enters the instrument via a fiber collimator. This fiber collimator lens determines the width of the laser beam, which was chosen to provide a diameter of 7.2 mm at the $1/e^2$ width of the Gaussian beam. To get a parallel illumination beam in y-direction, the back focal plane of the objective has to be illuminated with a focused laser beam in this direction. Cylindrical lenses are used in the illumination pathway to obtain a focused illumination in the x- and a parallel illumination in the y-direction. The illumination profile along the illumination line in the probe will show a Gaussian profile as the laser beam has a Gaussian shape. Accordingly, only 2.5 mm of the laser beam with $1/e^2$ diameter of 7.2 mm was used, which results in an intensity decrease of 20% on both sides with the intensity profile along the line shown in figure 4.2. By varying the size of the 2.5 mm opening, the length of the illumination line can be varied, which enables the possibility to change the imaging size. However, this would result in an enlarged intensity decrease at both sides, because the width of the Gaussian beam remains the same. The size of the illumination line is chosen to be 50 μm , which defines the optical enlargement of the three cylindrical lenses in the illumination pathway. The 130 mm cylindrical lens was used for geometrical reasons, as this distance was needed for the size of the dichroic mirror and that of the scanning mirror. To obtain a more or less constant illumination profile within 20% intensity decrease at the sides (Fig. 4.2), the cylindrical lenses -15 mm, 50 mm and 130 mm were used successively in the illumination pathway.

Implementation and construction of the STM



B

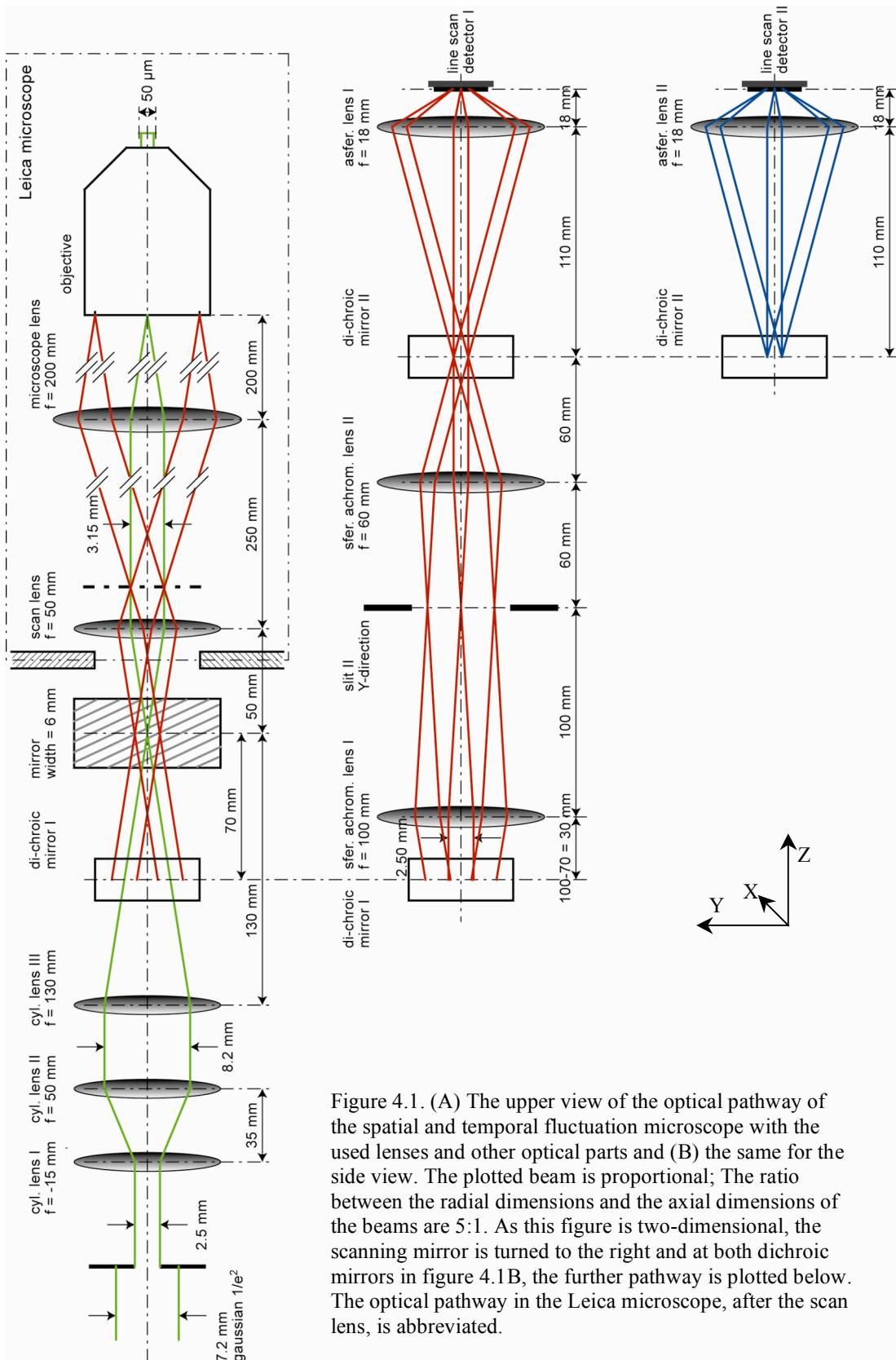


Figure 4.1. (A) The upper view of the optical pathway of the spatial and temporal fluctuation microscope with the used lenses and other optical parts and (B) the same for the side view. The plotted beam is proportional; The ratio between the radial dimensions and the axial dimensions of the beams are 5:1. As this figure is two-dimensional, the scanning mirror is turned to the right and at both dichroic mirrors in figure 4.1B, the further pathway is plotted below. The optical pathway in the Leica microscope, after the scan lens, is abbreviated.

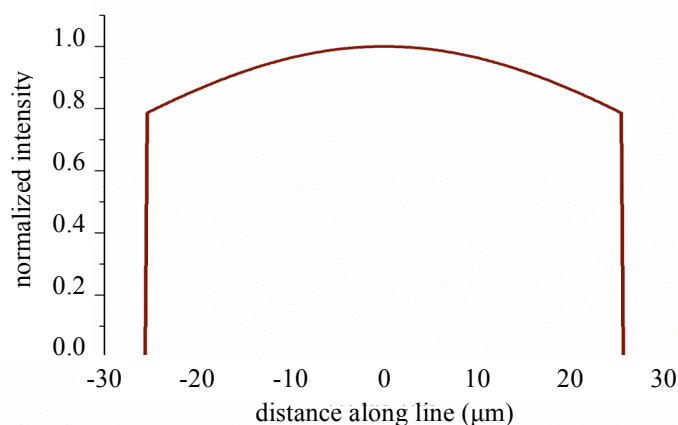


Figure 4.2. The normalized intensity profile along the line in the probe. The illumination profile displays a Gaussian profile blocked at the sides.

The emitted fluorescence light leaves the Leica microscope at the side port. This fluorescence beam differs from the illumination beam as shown in figure 4.1A and 4.1B. In the x -direction, the decreased beam size is defined by the size of the aperture of the back focal plane, which is 10 mm. The resulting beam size at the side port right after the scanning lens is 2.5 mm. The beam path in the y -direction is more altered, since for this direction each point along the illuminated line will emit fluorescence photons, which results in a parallel beam at the back focal plane of the objective, with an angle corresponding to the position along the line in the probe (Fig. 4.2B). The resulting fluorescence beam width at the side port right after the scanning lens is for each parallel beam 2.5 mm, the same as for the x -direction. However, these parallel beams contain angles between $\pm 1.8^\circ$ (Fig. 4.2B). The angle value 1.8° corresponds to the beam angle originating from the edges of the illuminated line.

The fluorescence light beam with different shapes in the x - and y -direction was detected by an EMCCD camera. The camera was modified to a line-scan detector with a line width of up to 656 pixels. The pixel size of the EMCCD camera is $7.4 \mu\text{m}$. Reducing the amount of illuminated pixels will increase the readout rate of the camera. For the detection pathway, the x - and y -direction of the beam are considered separately. For the x -direction, across the illuminated line, the beam must be focused to only one line on the camera, as otherwise the image will be smeared out. The pixel size of $7.4 \mu\text{m}$ defines the angle of the incident beam on the detector by equation 2.8. In these expressions, w_0 is the beam radius in the focal plane, which was assigned below half the pixel size. Accordingly, the maximum angle of the convergent beam was below 2.6° . The width of the slit imposed several constraints for the lenses in the detection pathway. The width of the slit was calculated according to the $1/e^2$ -diameter in the probe, which was about 200 nm (Eq. 3.5). Slits are commercially available for slit widths in the range of $5 \mu\text{m}$ up to $200 \mu\text{m}$. Smaller widths imply a larger NA of the corresponding lenses (Eq. 2.8) and vice versa and thus to larger convergent angles. Large convergent angles require a more exact positioning of the slit with regard to smaller convergent angles. However, smaller convergent angles will increase the length of the optical pathway and accordingly the size of the instrument. These

considerations lead to the lens choices for the detection pathway of successively 100 mm, 60 mm and 18 mm and a slit width of 50 μm . The pixel size of the line detector was 7.4 μm . Accordingly, the width of 1 line of the line detector corresponds to 200 nm in the probe.

For the y-direction, along the illuminated line, each parallel fluorescence beam leaving the Leica microscope must be focused on the camera sensor with an angle of the parallel beam that corresponds to the position on the sensor (Fig 4.2B). For the focal lengths of the lenses used for the x-direction, 200 nm in the x-direction of the probe will be imaged on 1 pixel. For an image size in the probe of 50 μm , this leads to an illumination of 250 pixels on the detector. Changing the focal length of these lenses will alter the angle of the convergent beam of the lens system on the detector, which implies a change of each beam radius w_0 in the focal plane. In other words, this will have an impact on the size of the foci in the probe imaged on the detector. In addition, this will also affect the length of the imaged line on detector, i.e. the probe size that is imaged on 1 pixel. Unfortunately, increasing the length of the imaged line in the probe on the detector will increase the size of the imaged foci. Accordingly, the chosen focal lengths for the x-direction were left unaltered for the y-direction, which lead to spherical lenses in the detection pathway of the STFM. Additionally, the commercial available spherical lenses provide a much larger variety of for example the correction for chromatic and spherical aberrations. To reduce spherical aberrations along the line at the detector, the sixth lens, right before the detector, is an aspherical lens.

Accordingly, the object dimension of the STFM of 200 nm x 24 μm in the probe were imaged on a line with a width of 1 pixel (= 7.4 μm) and a length of 120 pixels of detector. The decrease of the image size from 50 μm to 24 μm is caused by the limited height of the commercial available slits, which was 3 mm. A height of 6 mm would be optimal.

4.3 Optimization of the optical beam path

The requirement of long-term mechanical stability leads to a mechanical rigid construction in which the position of all elements are predetermined with only limited degrees of freedom. Accordingly, the position of each lens must precisely be determined with the needed degrees of freedom to adjust lenses and slit.

4.3.1 Determination of the focal lengths

The focal lengths of the each lens must be determined with high precision. Due to the wavelength dependency of the focal length of the lenses, the specifications of the manufacturer are incomplete. Therefore, the focal lengths are calculated using the matrix approach for thick lenses described in section 2.4. Figure 4.3 summarizes the determined focal lengths relative to the surfaces of the lenses for the three lenses in the illumination pathway (Fig. 4.3A) and for the three lenses in the detection pathway (Fig. 4.3B).

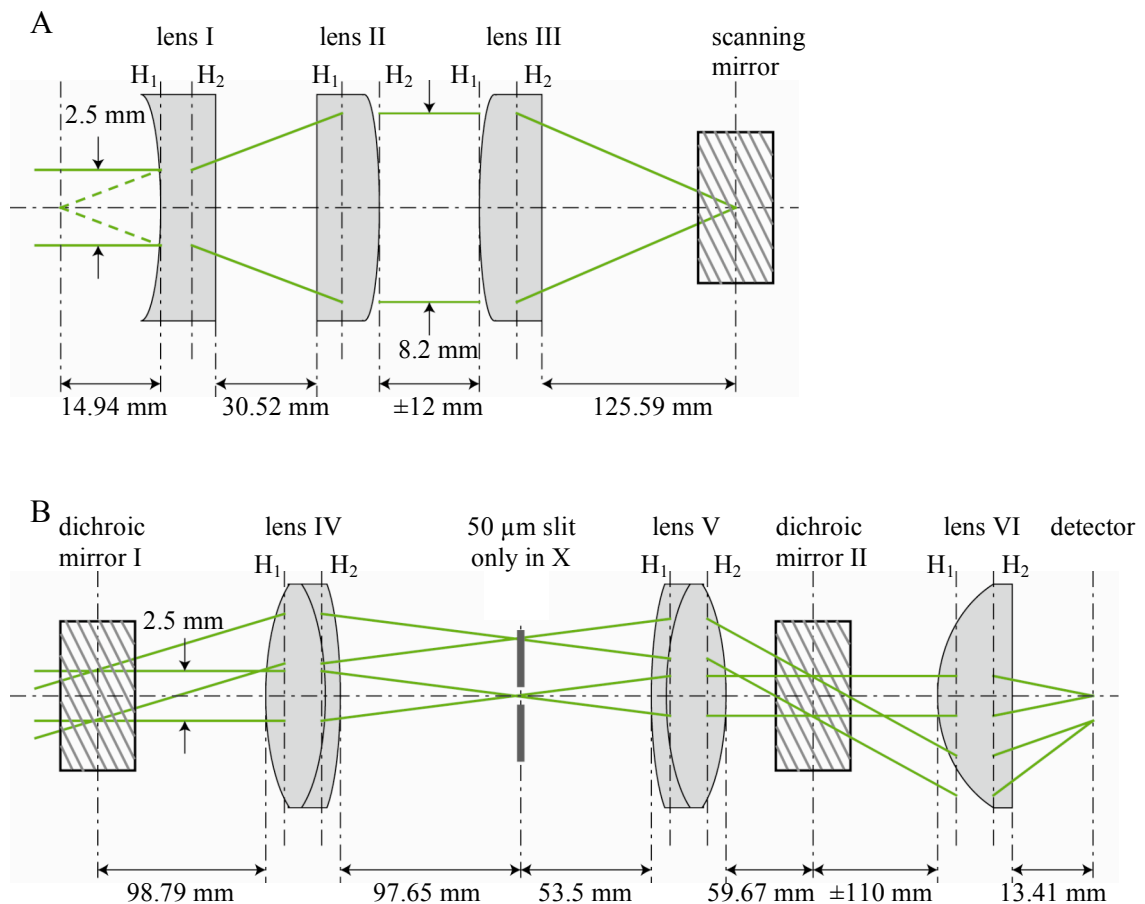


Figure 4.3. All lenses used for the spatial and temporal fluctuation microscope with the determined focal lengths relative to the surfaces of the lenses for the illumination beam path (A) and for the detection beam path (B).

The determined positions of the principle planes $H_{1,2}$ related to the surfaces of the lenses, the corresponding focal length f and the focal lengths relative to the surfaces of the lenses $s_{1,2}$ are listed in table 4.1. The refractive index used for the calculation depends on the material and the illumination and detection wavelength. The material and the corresponding refractive index are listed too in the table.

	lens I	lens II	lens III	lens IV	lens V	lens VI
lens nr.	LK1753 L2-A	LJ1821 L2-A	LJ1640 L1-A	AC254- 100-A1- ML	AC254- 060-A1- ML	AL2018-A
lens type	plano- concave cylindrical	plano- convex cylindrical	plano- convex cylindrical	achromatic doublet	achromatic doublet	aspheric lens
material	BK7	BK7	BK7	BK7 SF5	FD10 BAF11	S-LAH64
refractive index	1.5218 @488nm	1.5218 @488nm	1.5218 @488nm	1.5202 1.6830 @514nm	1.7408 1.6734 @514nm	1.7961 @514nm
specified focal length (mm)	-15	50	130	100	60	18
centre thickness (mm)	2.0	4.01	4.69	4.0 2.5	8.0 2.5	7.4
edge thickness (mm)	3.4	2.0	3.0	4.7	8.2	2.0
surface radii (mm)	-7.75	25.84	67.18	62.75 -45.71 -128.23	230.7 25.88 -41.69	(21.2)
principle plane: H1 (mm)	0.00	2.63	0.00	1.27	5.24	
principle plane: H2 (mm)	-1.31	0.00	-3.09	-2.41	-0.93	
focal length: f (mm)	-14.94	48.09	128.68	100.06	58.74	
focal distance: s_1 (mm)	14.94	45.46	128.68	98.79	53.5	
focal distance: s_2 (mm)	13.63	48.09	125.59	97.65	59.67	13.41

Table 4.1. All lenses used for the spatial and temporal fluctuation microscope with the position of their principle planes ($H_{1,2}$) related to the surfaces of the lenses, the corresponding focal length, f , and the focal distances relative to the surfaces of the lenses, $s_{1,2}$.

The positions of each lens and that of the slit were optimized using the ZEMAX program of the ZEMAX development corporation. This is commercial software for optical system design, based on the matrix approach for thick lenses described in section 2.4. The accuracy of the calculated positions was determined using this ZEMAX program and the matrix approach calculated using the program Matlab from MathWorks.

The standard accuracy range for the fine mechanical pieces of the instrument is $\pm 20 \mu\text{m}$, which can be reduced to $\pm 5 \mu\text{m}$ for single pieces that need high exactness. This impreciseness adds up for the number of pieces used, as for example the lens holders consist of four pieces, the imprecision of the lenses is larger estimated as two times larger. This restricts the accuracy of the position of the lenses and their focal planes, which has to be taken into account by the decision of fixing its position or making them fine adjustable for each of the three directions. Fixing the lens position leads to an estimated inaccuracy of $\pm 50 \mu\text{m}$. A fine-adjustable lens position is limited by the accuracy of the fine-adjustable screws that provide a mechanical imprecision of less than $5 \mu\text{m}$. According to these values, the lens positions are made fixed respectively fine adjustable.

4.3.2 The illumination beam path:

The illumination part of the microscope is composed of an entry slit, three cylindrical lenses, a dichroic mirror, the scanning mirror and the optical pathway through the Leica microscope. The upper view of the illumination beam path up to the entry port of the Leica microscope is shown in figure 4.4A and the side view in figure 4.4B. The dichroic mirror separates between the illumination and detection pathway, which are described separately here omitting the dichroic mirror. The laser beam enters the system with a $1/e^2$ beam diameter of 7.2 mm, shown in figure 4.4D, which is obstructed by a rectangular aperture leading to a rectangular beam shape (Fig. 4.4C) with side lengths $D_{X,1}$ and $D_{Y,1}$. The position of the second lens was varied slightly around its calculated position to find the optimal position, where the convergence angle of the out going laser beam decreases to zero, which implies that its shape (Fig. 4.4E) remains unchanged. The third cylindrical lens converges the laser beam at the scanning mirror, which position again was varied slightly to find the optimum. The illumination beam profile at the scanning mirror is shown in figure 4.4F, with the diameters in x- and y-direction $D_{X,\text{mirror}}$ and $D_{Y,\text{mirror}}$ as indicated. The y-dependence of the intensity profile is displayed in figure 4.4G.

Figure 4.4H displays the enlarged side view at the scanning mirror, which shows the $1/e^2$ radius of the illumination beam $R_{Y,\text{mirror}}$ as a function of the position at the optical axis. Accordingly, varying the distance between cylindrical lens III and the scanning mirror within the range of $\pm 50 \mu\text{m}$ will not alter the beam radius at the mirror more than 5%. With a fine mechanical accuracy range of $\pm 10 \mu\text{m}$ for each piece, this implies that small variations of this distance due to mechanical imprecision are uncritical for this distance. Compared to that, the distance between lens I and lens II is more sensitive to distance variations, although distance variations within the range of $\pm 20 \mu\text{m}$ will have a minor effect on the position of the focal plane at the scanning mirror that can be neglected. Additionally, the cylindrical lenses need precise mobility along their concave respectively convex axis, because small position variations along these axis results in large deviations of the beam angle relative to the optical axis. Beside that, the lenses will show a small deviation in the tilt of the lenses due to mechanical imprecision. Therefore, fine adjusters were used for position alignment along this y-axis, which made the fine alignment of the tilt of the lenses along this axis redundant.

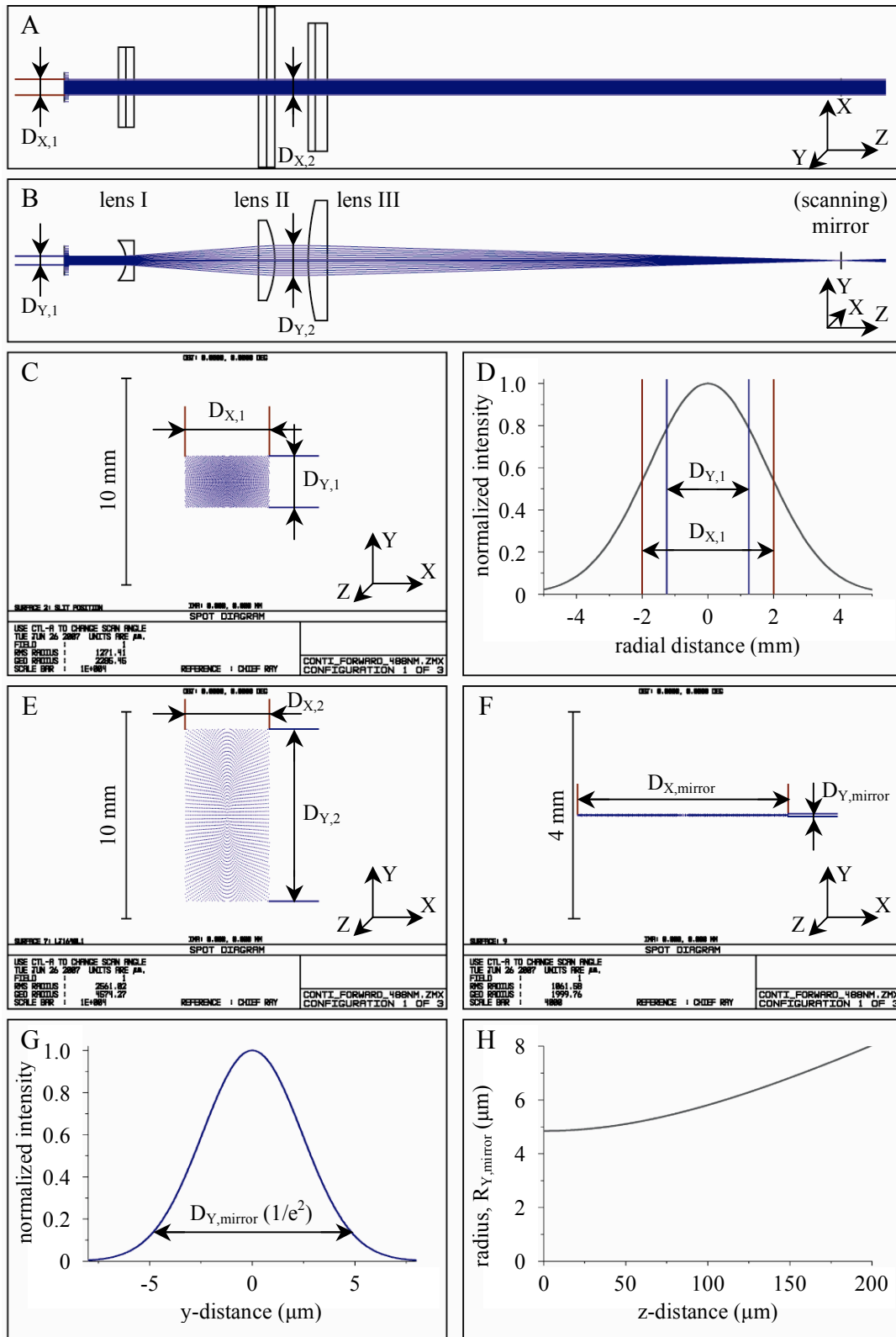


Figure 4.4. The illumination pathway with the first three cylindrical lenses and the scanning mirror indicated displayed in an upper view drawing (A) and in a side view drawing (B). This optical system was illuminated using a Gaussian laser beam (D), which was obstructed leading to a rectangular beam (C) with side lengths $D_{X,1}$ and $D_{Y,1}$. The beam size between lens II and lens III shows a rectangular beam (E) with side lengths $D_{X,2}$ and $D_{Y,2}$. The intensity profile at the scanning mirror is a line profile (F), with length, $D_{X,mirror}$ and a width, $D_{Y,mirror}$ (G). The z-dependence of the beam radius at the scanning mirror, $\frac{1}{2} \cdot D_{Y,mirror}(z)$, is displayed in (H).

The position of each lens and the position of the scanning mirror are assigned as described in table 4.2.

axis	cylindrical lens I		cylindrical lens II		cylindrical lens III		scanning mirror	
	x	fixed	--	fixed	--	fixed	--	adjustable
y	fine adjustable	$\pm 5 \mu\text{m}$	fine adjustable	$\pm 5 \mu\text{m}$	fine adjustable	$\pm 5 \mu\text{m}$	fixed	--
z	adjustable	$\pm 20 \mu\text{m}$	fixed	--	fixed	--	fixed	--

Table 4.2. The mobility degrees of freedom for the lenses in the illumination pathway of the spatial and temporal fluctuation microscope. The accuracy of the adjustment is written in the column on the right. This depends on the usage of fine adjuster screws.

The illumination pathway inside the Leica microscope consists of a scan lens, a mirror, the tubular lens and the objective successively. This is a commercial microscope optimized by the company. Nevertheless, this optical system was modeled too, leading to a description of the illumination beam profile at the back focal plane of the objective. Figure 4.5A shows this line illumination profile at the back focal plane of the objective, with length $D_{X,obj.}$ and a width $D_{Y,obj.}$ as indicated. Figure 4.4B shows the z-dependence of the $1/e^2$ radius of the illumination beam $R_{Y,obj.}(z)$. The x-dependence of the intensity profile at the back focal plane along the illumination line is displayed in figure 4.5C and the same for the y-dependence across the line in figure 4.5D.

4.3.3 The detection beam path

The detection part of the microscope is comprises the optical pathway through the Leica microscope, a scanning mirror, a dichroic mirror, two achromatic lenses, a $50 \mu\text{m}$ slit and an aspheric lens. The detection pathway inside the Leica microscope up to the dichroic mirror is the same as for the illumination described above. Accordingly, only the detection beam path from the scanning mirror is described omitting the dichroic mirror. The upper view of the detection beam path from the fourth lens until the detector is shown in figure 4.6A and the side view in figure 4.6B. Five fluorescence beams are displayed: the two outer beams, the beam in the centre and for the two beams between them as indicated by their numbers. The fluorescence light beam between the scanning mirror and the first achromatic lens consists of parallel beams with different angles with respect to the optical axis as shown in figure 4.1A and B. Due to this parallelism of the beams, the distance between the scanning mirror and the first achromatic lens is not critical. Compared to that, the position of the successive slit had to be adjusted with higher precision. An enlargement of the side view of the beam near this slit is shown in figure 4.6C.

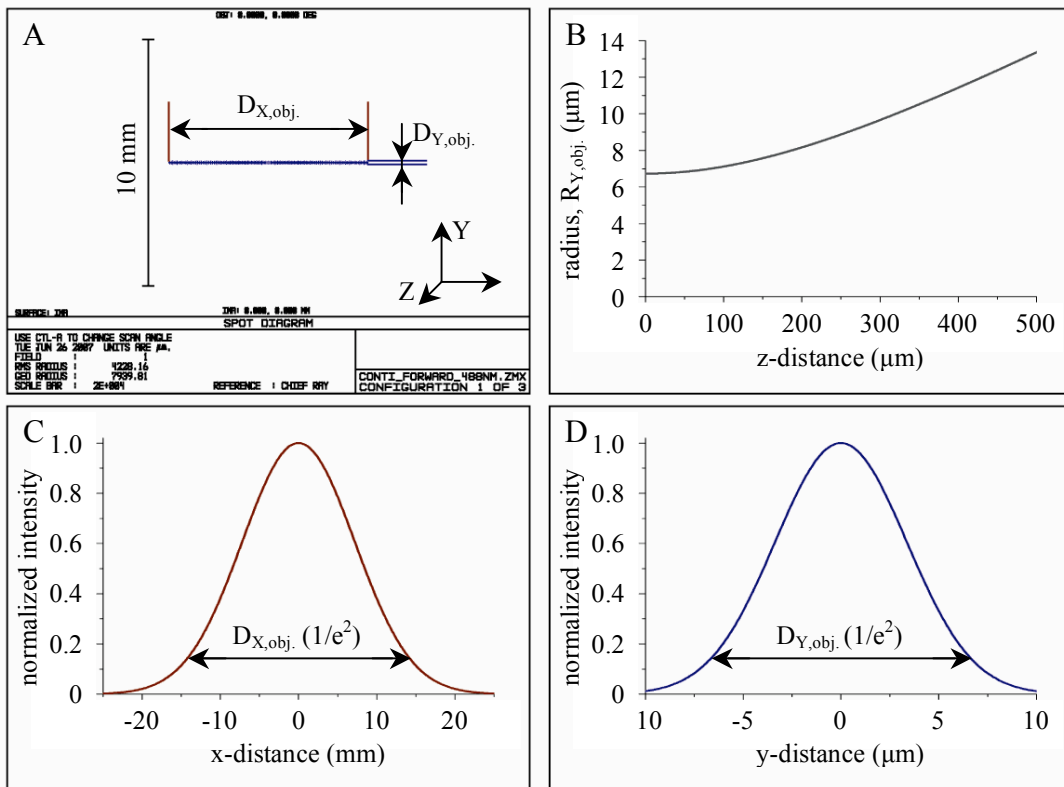


Figure 4.5. The illumination profile at the back focal plane of the objective (A). A line profile shape with length $D_{X,obj.}$ and width $D_{Y,obj.}$ is shown. The Z-dependence of the beam radius at the back focal plane of the objective $\frac{1}{2} \cdot D_{Y,obj.}(z)$, (B) the intensity profile along the x-direction (C) and the intensity profile along the y-direction (D) are displayed.

The light beam is focused in x-direction at the position of the slit. In y-direction, each parallel beam is focused itself at the plane of the slit position, but at different positions along the slit. This is shown for the five beams in figure 4.6C. Figure 4.6D displays the enlarged side view at the slit, which shows the z-dependence of the $1/e^2$ radius of the illumination beam $R_{Y,slit}(z)$. Accordingly, varying the distance between the first aspherical lens and the slit or between the slit and the second aspherical lens within the range of $\pm 300 \mu\text{m}$ will not alter the beam radius at the slit more than 5%. This implies that small variations of this distance due to mechanical imprecision are uncritical for these distances. Correspondingly, the position of the slit and that of lens IV are fixed in y- and z-direction. They are both fine adjustable in x-direction to position precisely the imaged detection volume in the probe, which makes the illumination and detection volume confocal. Figure 4.6E displays a spot diagram for the five fluorescence beams as indicated in figure 4.6C. The RMS radii and the geometrical radii of the beams at the indicated positions along the slit are presented in table 4.3. The RMS radius describes the mean radius of deviation of the mean intensity, whereas the geometric radius describes the radius of the outer boundary of the intensity. The geometric radius can be much larger as RMS radius, which is the case for both outer positions along the slit (position 4 and 5). At these outer positions, the intensity at the slit is smeared out over a large area because of the spherical aberrations of the lens system. The outer intensities are rather small compared to the intensity maximum, represented by a much smaller RMS radius.

Implementation and construction of the STFM

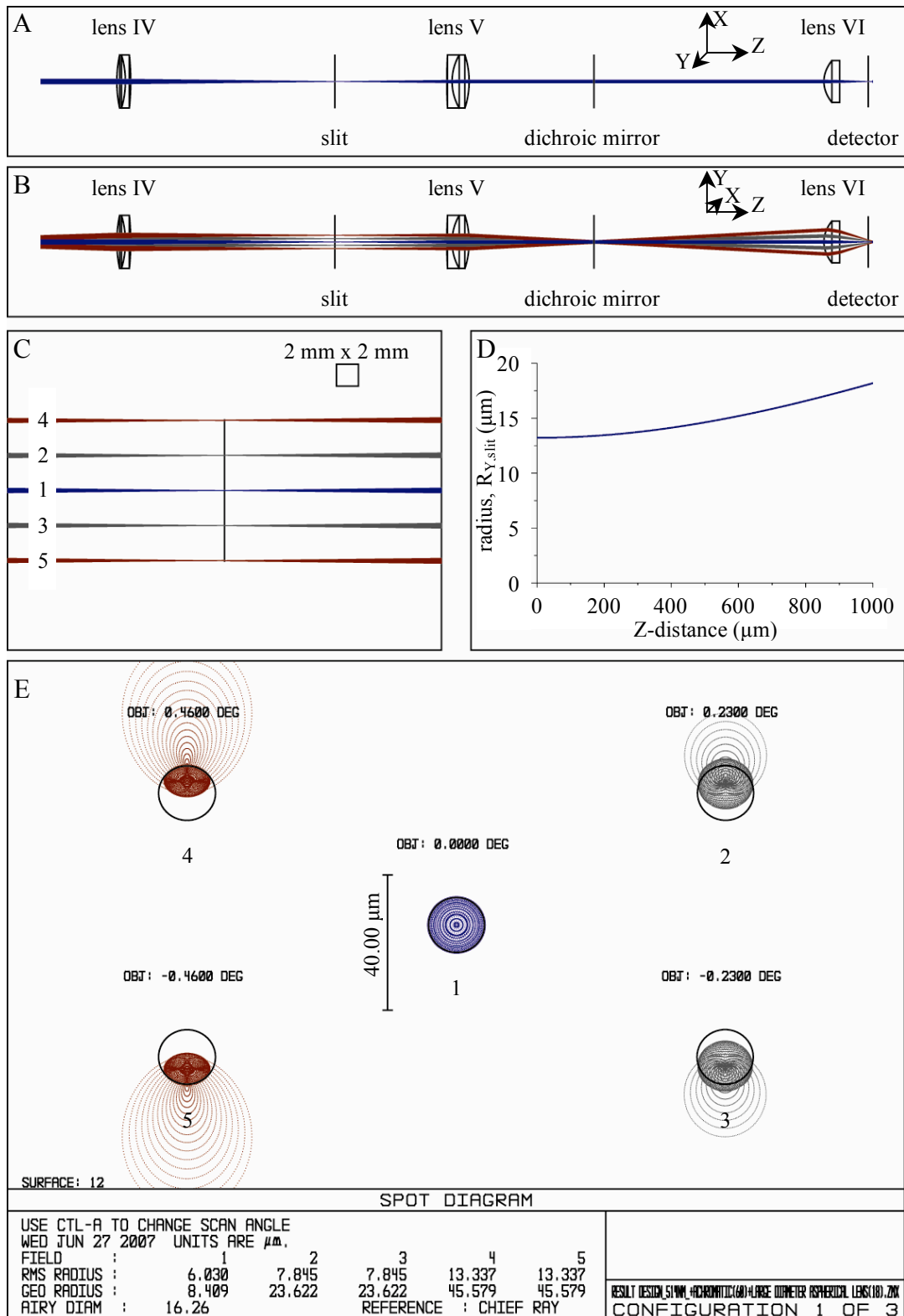


Figure 4.6. The detection pathway with the two achromatic lenses (lens IV and lens V), the spherical lens (lens VI), the slit, the dichroic mirror and the detector as indicated displayed in an upper view drawing (A) and in a side view drawing (B). Enlarged side view of the slit in the detection pathway, displayed for five fluorescence beams (C); the two outer beams, the beam in the centre and the two beams in the middle of them as indicated. The Z-dependence of the centered beam radius (D) and a spot diagram of each of the five beams (E) are shown.

position	slit			detector		
	1	2/3	4/5	1	2/3	4/5
y-position (mm)	0.00	±1.605	±3.209	0.00	±0.476	±0.954
RMS radius (μm)	6.030	7.845	13.337	3.952	3.759	4.006
geometrical radius (μm)	8.409	23.622	45.579	4.930	5.764	6.937

Table 4.3. The position and RMS and geometrical radii at different positions along the line as indicated in figure 4.6 for the slit and in figure 4.7 for the detector.

Another critical distance in the detection beam path is the distance between lens VI and the detector. Figure 4.7A shows the enlarged side view at the detector, which shows the $1/e^2$ radius of the illumination beam $R_{Y,detector}$ as a function of the position at the optical axis. Accordingly, the distance between lens VI and the detector is critical to variations, as a variation of more than $\pm 20 \mu\text{m}$ will alter the beam radius at the detector more than 5%, which was chosen as the critical range. Therefore, fine adjusters were used for position alignment of lens VI along the optical axis. This lens was also fine adjustable in x-direction to position the line focus precisely at the line detector.

The sixth lens is an aspherical lens to eliminate spherical aberrations at the focal plane. To make full use of the aspherical feature of this lens, more than 50% of the area of the lens must be illuminated. This can be achieved by increasing the distance between lens V and lens VI up to 170 mm (Fig. 4.1). The fluorescence beam is parallel in both directions between those lenses and this distance increase has no additional impact on the optical pathway. However, due to this increase in distance, small deviations in the parallelism of the fluorescence beams will affect the focus position at the detector to a large extent. Hence, the axial position of lens V is adjustable to ensure a parallel beam between lens V and VI. To provide a precise illumination of the pixels along the detector line, lens V is fine adjustable in y-direction and lens VI is fine adjustable in x-direction. To ensure a mechanical stability of these lenses, they are both fixed in respectively the x- and the y- direction. The position of each lens in the detection pathway and the position of the detector are described in table 4.4.

axis	achromatic lens IV		slit		achromatic lens V		aspheric lens VI	
	fine adjustable	±5 μm	fine adjustable	±5 μm	fixed	--	fine adjustable	±5 μm
X	fixed	--	fixed	--	fine adjustable	±5 μm	fixed	--
Z	fixed	--	fixed	--	adjustable	±20 μm	fine adjustable	±5 μm

Table 4.4. The freedom degrees of mobility of the lenses and of the slit in the detection pathway of the spatial and temporal fluctuation microscope. The accuracy of the adjustment is written in the column on the right.

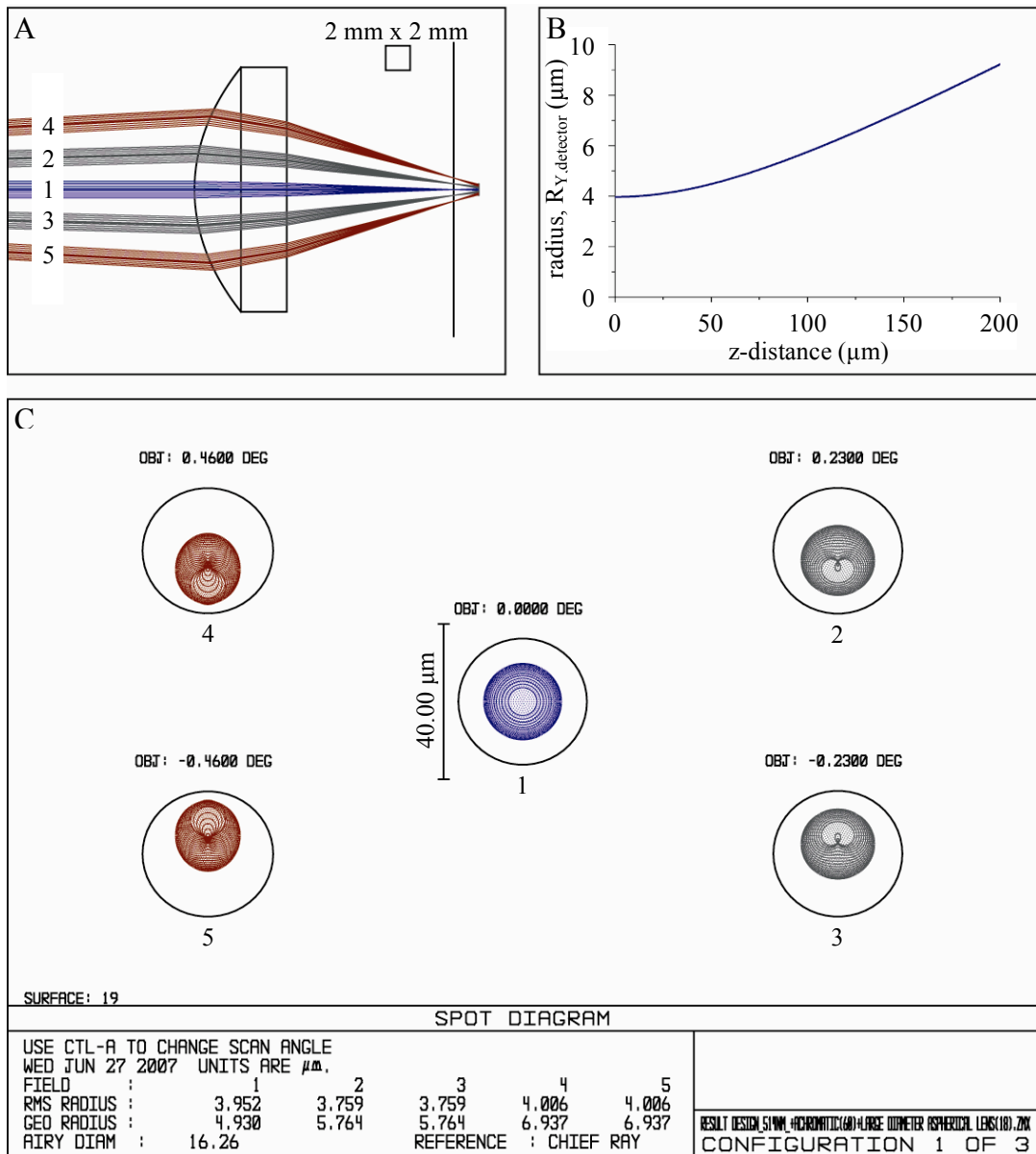


Figure 4.7. An enlarged side view at the detector in the detection pathway (A), displayed for five fluorescence beams; the two outer beams, the beam in the centre and the two beams in the middle of them as indicated. The z-dependence of the centered beam radius (B) and a spot diagram of each of the five beams (C).

4.4 Instrument components and their arrangement for the STFM

Table 4.5 displays a list of the used optical parts, the company name and their article number. These optical instruments and the control of these instruments are described in more detail in this section. A fine-mechanical construction held all these optical instruments and optical parts together, which allows additionally fine adjustment of them.

4.4.1 Microscope, objective lens, tubular lens and scan lens

A commercially available inverse optical fluorescence microscope from Leica was used as basic instrument. The company itself also uses this instrument for confocal laser-scanning microscopy and fluorescence correlation spectroscopy. The advantages of using this instrument are the optimization for a diffraction limited observation volume and the scattered light suppression. Additionally, this inverse fluorescence microscope enables a wide-field visualization of the specimen, which simplifies the positioning of the focal plane. The objective lens, the tubular lens and the scan lens are optimized to each other. The objective lens is a 63x water-immersion objective with a numerical aperture of 1.2. The size of the aperture at the back focal plane of the used objective is 10 mm. This objective lens and the tubular lens are a matching couple that provides an enlargement of 63x in the first image plane. The focal length of this tubular lens is 200 mm.

For an optimized small size of the focal volume, the back focal plane has to be illuminated with a more or less constant intensity distribution over the whole aperture. This implies an illumination of the back focal plane with a wide illumination beam. A disadvantage of such overexposure of the entry aperture is that the amount of the illumination laser light in the probe decreases.

As scan lens, the f-theta lens HC FSA TCS MR11 UVI from Leica was used. This scan lens is the regularly used lens for confocal laser-scanning in these type of microscopes. This lens exists of a total of seven lenses optimized to reduce spherical aberrations. An f-theta lens supplies an image in accordance with the so-called F-theta condition described in section 2.5.3. Proportionality between the scanning angle and the image height ensures proportionality between the angular velocity of the deflecting system and the scanning speed in the image plane.

Implementation and construction of the STFM

instrument description	company	article number
inverse microscope	Leica Microsystems GmbH	Leica DM IRBE
water immersion objective, 63x, 1.2NA	Leica Microsystems GmbH	HCX PL APO 63x/1.2 W CORR CS
f-theta lens 50 mm	Leica Microsystems GmbH	HC FSA TCS MR11 UVI
Charged Multiplier CCD camera SamBa SE-34	Sensovation AG	SVSB06-MB-1001
NI frame grabber PCI-1422 LVDS and cable	Sensovation AG	KT00EP-02-0012 SVSB01-EA-0008
closed-loop galvanometer scanner, +/- 25°, with y-spiegel 5 mm, nodge filter and cable	GSI Group Inc.	VM500
high-speed multifunction DAQ, M series and shielded cable	National Instruments	NI PCI-6251 SHC68-68-EPM
connector block	National Instruments	CB-68LP
AC/DC power supply +15V with 10A	MEAN WELL Enterprises Co.	S-150-15
AC/DC power supply +5V(5A), +15V(2A), -15V(0.5A)	MEAN WELL Enterprises Co.	T-60C
laser, 488 nm, 200 mW	Coherent Inc.	Sapphire 488 High Power
laser clean-up filter, z 488/10	AHF analysentechnik AG	F34-488
laser beamsplitter, z 488	AHF analysentechnik AG	F73-507
emitter, HQ 525/50	AHF analysentechnik AG	F42-524
laser beam coupler	Schäfter+Kirchhoff GmbH	60SMS-1-4-M8-33
fiber collimator	Schäfter+Kirchhoff GmbH	60FC-T-4-M40-04
1.5m single-mode fiber: 400-600 nm	Schäfter+Kirchhoff GmbH	SMC-488-3.4-NA013-3-APC-0-150
plano-concave cylindrical lens, f -15 mm	Thorlabs Inc.	LK1753L2-A
plano-convex cylindrical lens, f 50 mm	Thorlabs Inc.	LJ1821L2-A
plano-convex cylindrical lens, f 130 mm	Thorlabs Inc.	LJ1640L1-A
achromatic doublet lens, f 100 mm	Thorlabs Inc.	AC254-100-A1-ML
achromatic doublet lens, f 60 mm	Thorlabs Inc.	AC254-100-A1-ML
aspheric lens, f 18 mm	Thorlabs Inc.	AL2018-A
50 µm slit	Thorlabs Inc.	S50R

Table 4.5. A list of the used instruments for the spatial and temporal fluctuation microscope with their company and their article number. The instruments with their accessories are divided into five subgroups: Leica microscope, camera, scanner mirror, laser and all lenses and slit.

4.4.2 EMCCD camera and frame grabber

The SamBa cameras from Sensovation are fast multi-channel detection systems for applications in spectroscopy and low light imaging. These cameras enable fluorescence single molecule detection. The detected photons signal is enhanced significantly based on the electron-multiplication described in section 2.5.2. This charge multiplier technology enables high sensitivity in combination with high image rates. Several features of the Samba SE-34 EMCCD camera used for the spatial and temporal fluctuation microscope are listed in table 4.6.

	SamBa SE-34
Number of pixels	656 x 496 mm (x2)
Pixel size	7.4 x 7.4 μm
Active area	4.9 x 3.7 mm
Readout noise	1 e ⁻ rms @ CMG 30x
Dark current	50 e ⁻ /pix·s @ 20 °C
Charge multiplication gain (CMG)	up to 30x
Peak quantum efficiency	40 %
Image rate (full frame)	30 fps
Line image rate (full line)	14 kHz
Digital resolution	12 bit

Table 4.6. Features of the EMCCD camera Samba SE-34 of the Sensovation company.

The readout mode of the EMCCD camera can be programmed by sending readout sequences through the RS232 bus interface. These readout sequences are based on SCPI commands that provide high flexible programmability. The data transfer between camera and PC is performed by the NI PCI-1422 LVDS frame grabber from National Instruments. This board is designed to acquire images at high image rates up to 16 bits of data at a clock speed of 40 MHz. A RTSI bus, which is an advanced triggering, on this board routes timing and triggering signals between different boards. This RTSI communication is described in more detail below. The data acquisition board can be controlled using the IMAQ-library from National Instruments. The functions in this library are described in the ‘NI-IMAQ Function Reference’.

The EMCCD camera from Sensovation is commercial available as area-scan camera. This area-scan camera transfers after each image frame three dummy lines to the PC before the next image frame can be transmitted. This is done to transmit the end of the image frame, which maximum size is 500 lines. For line the imaging STFM system, each detected line itself is an image frame. This dummy lines transfer leads to a four times line frequency decrease. Hence, the firmware of the EMCCD camera was modified to get rid of the dummy lines transfer resulting in the line-scan EMCCD camera used for the STFM developed within the scope of this thesis work.

4.4.3 Galvanometer scanner, driver and data acquisition board

In a confocal laser-scanning microscope, it is necessary to deflect laser beams fast and exactly. In general, galvanometer scanners are used for precise scanning of the laser beam through the specimen. A galvanometer scanner is an analog electromechanical transducer that produces a rotary deflection, over a limited angle, in response to an electric current flowing through its coil. The rotation of the mirror occurs electromagnetically. Controlled motion is achieved with an internal position detector. This internal position detector enables closed loop servo control of the motor by providing a position signal proportional to the rotation of the motor shaft.

For the construction of the spatial and temporal fluctuation microscope, the galvanometer scanner VM500 and the galvanometer servo controller MiniSAX from GSI Lumonics were used (Fig. 4.8). The galvanometer scanner and the MiniSAX were connected by the thermal control interface P1, the galvanometer drive P2 and the position sensor input P3 as indicated. Several features of the galvanometer scanner and controller are listed in table 4.7. This precision scanner fulfills the requirements of fast acceleration, high speed, exactness and stability. The position of the scanning mirror is controlled by the MiniSAX, which in return is controlled by the data acquisition board NI PCI-6251 from National Instruments. The MiniSAX and the data acquisition board are connected through the control signal connector interface as indicated (Fig 4.8B) and the connector block CB-68LP appropriate to the data acquisition board.

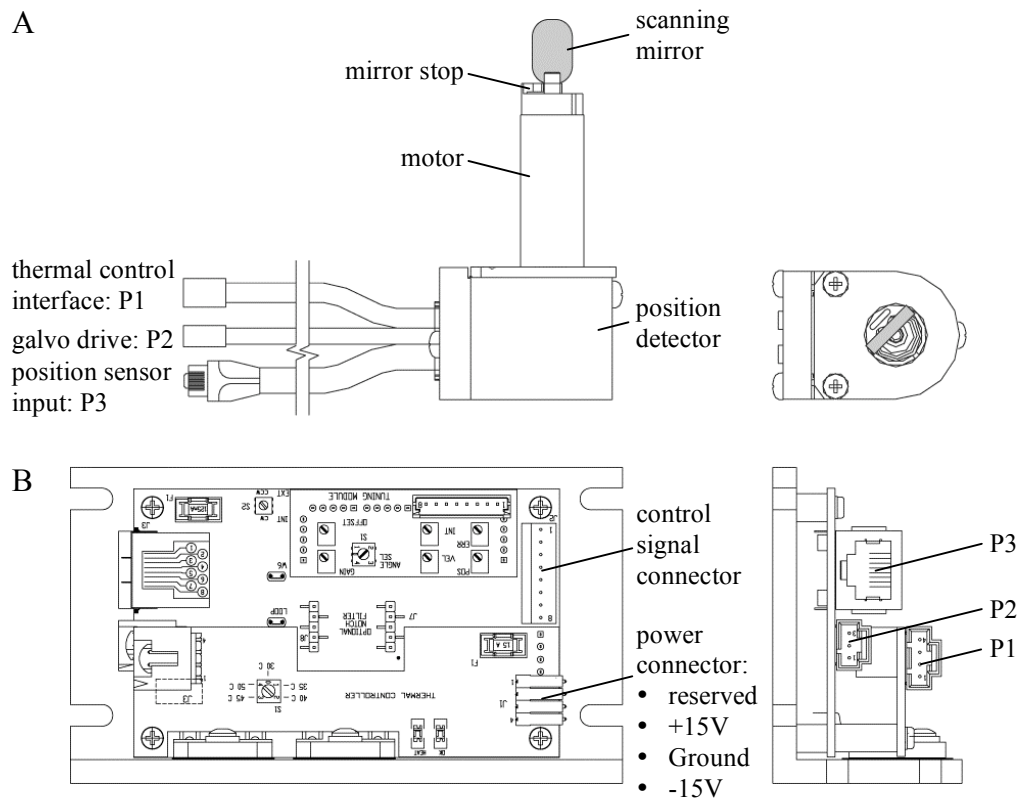


Figure 4.8. A schematic drawing of the VM500 galvanometer scanner (A) and of the MiniSAX galvanometer servo controller (B).

	VM500		MiniSAX
Mirror size	6 x 6 mm	Position output	±3 V for full scale
Max. scan angle	±50° optical	Voltage input	±15 V
Non-linearity	0.08 % over ±20° optical	Dynamic current	2.5 A RMS
Bandwidth	>3500 Hz	Peak current	10 A
Small step time	<175 µs		
Full step time	0.8 ms		

Table 4.7. Features of the VM500 galvanometer scanner and of the MiniSAX galvanometer servo controller.

The NI PCI-6251 is a data acquisition board that provides several analog and digital in- and output channels through the channels of the connector block. The channels used for the control of the galvanometer scanner are listed in table 4.8 with their corresponding pin connection at the MiniSAX according to the pin assignment of the control signal connector indicated in figure 4.8. The assigned position data is transmitted through the first three pins of the MiniSAX. The actual position of the scanner mirror is transmitted back to the PC by pin 7 and pin 8.

channel nr. of connector block	channel name of DAQ board	pin	function	I/O	range
22	AO 0	1	position command +	I	±3 V
55	AO GND	2	position command -	I	±3 V
55	AO GND	3	ground	I	-
52	P0.0	4	temperature status	O	0 - 25 V
17	P0.1	5	servo enable	I	active low
49	P0.2	6	servo ready	O	active low
68	AI 0	7	scanner position +	O	±3 V
34	AI8	8	scanner position -	O	±3 V

Table 4.8. Connection assignment of the connector block CB-68LP and the control signal connector interface of the MiniSAX. The table reveals successively the channels numbers on the connector block with their corresponding channel names at the data acquisition board NI PCI-6251, the pin number of the MiniSAX according to the control signal connector of figure 4.8, the function, if input or output channel and the range of the corresponding channel.

This data acquisition board again provides an RTSI bus, which is an advanced triggering that routes timing and triggering signals between different boards. This RTSI communication is described in more detail below. The data acquisition board NI PCI-6251 can be controlled using the NI-DAQ-library from National Instruments. The functions in this library are described in the ‘daqmxfunc.chm’-function reference.

4.4.4 Laser and corresponding filters

The laser used for the spatial and temporal fluctuation microscope is a high power, continuous wave blue laser from Coherent. It provides a wavelength of 488 nm at a power of 200 mW as listed in table 4.9.

	Sapphire 488 HP
Wavelength	488 ±2 nm
Output power	200 mW
Beam diameter (1/e ²)	0.70 ± 0.05 mm

Table 4.9. Features of the Sapphire 488 High Power laser.

The intensity transmission curves of the used filters are displayed in figure 4.9. The laser clean-up filter F34-488 (Fig. 4.9A) ensures a well-defined illumination wavelength of 488 ± 5 nm. The laser beamsplitter F37-507, (Fig. 4.9B) defines the pathway for illumination and detection, because the illumination wavelength around 488 nm is transmitted and the detection wavelength above 500 nm is reflected. The detection wavelength is cleaned-up further by the emitter filter F42-524 (Fig. 4.9C).

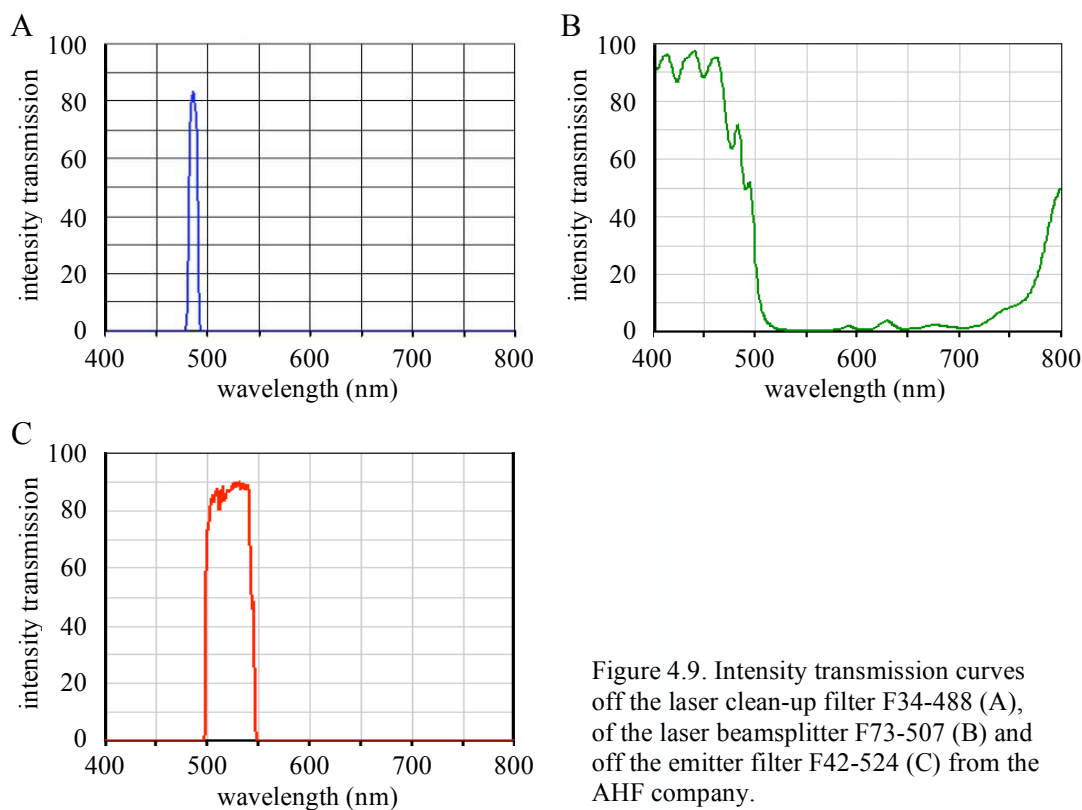


Figure 4.9. Intensity transmission curves off the laser clean-up filter F34-488 (A), of the laser beamsplitter F37-507 (B) and off the emitter filter F42-524 (C) from the AHF company.

4.4.5 Laser beam coupler, fiber and fiber collimator

The laser beam enters the spatial and temporal fluctuation microscope by the laser beam coupler 60SMS-1-4-M8-33, the single-mode fiber SMC-488-3.4-NA013-3-APC-0-150 and the fiber collimator 60FC-T-4-M40-04 from Schäfter&Kirchhoff. These components provide the following features for the alignment to optimize the coupling efficiency:

- 8° inclined fiber-coupling axis, which ensures optimal coupling efficiency.
- Tilt alignment to correct for deviations between the positions the optical axis of laser beam and the optical axis of the beam coupler respectively the fiber collimator.
- Adjustment of the focusing lens of the laser beam coupler and that of the collimation lens of the fiber collimator.

The laser beam coupler, single-mode fiber and fiber collimator were connected by the FC-connector with 8° inclined coupling axis. This 8° inclined polish prevented reflection of the radiation beam in the optical path, which ensured an optimized coupling efficiency. The optical features of the laser beam coupler, single-mode fiber and fiber collimator are listed in table 4.10.

	60SMS-1-4-M8-33	60FC-T-4-M40-04	SMC-488-3.4-NA013-3-APC-0-150
lens type	laser monochromat	monochromat	--
lens focal length	8.1 mm	40 mm	--
beam diameter (1/e ²)	1.72 mm (input)	7.22 mm (output)	3.4 mm (MFD)
numerical aperture	0.16	0.2	0.13
spectral range	390 - 670 nm	390 - 670 nm	480 - 630 nm

Table 4.10. Features of the laser beam coupler 60SMS-1-4-M8-33, the single mode fiber SMC-488-3.4-NA013-3-APC-0-150 and the fiber collimator 60FC-T-4-M40-04 from Schäfter&Kirchhoff.

4.4.6 Circuit diagram of the control instruments of the STFM

The opto-electronic components described above were controlled and synchronized for the implementation of the STFM. These opto-electronic components include the laser, the microscope, the scanner mirror and the camera. A separate laser controller, which in return is controlled through the serial port interface of the computer (COM 3), controls the laser. Laser features that can be controlled include the laser output power, temperature and error check. The microscope was controlled directly through the serial port interface of the computer (COM 4). Microscope features that can be controlled are the precise height control of the specimen and objective lens selection.

The control of the scanning mirror and that of the camera require much faster communication with the computer. Therefore, those instruments were controlled by a data acquisition board and a frame grabber respectively, which provide a much faster communication through the PCI bus interface of the computer. A circuit diagram of all opto-electronic components used for the implementation of the spatial and temporal fluctuation microscope developed is displayed in figure 4.10.

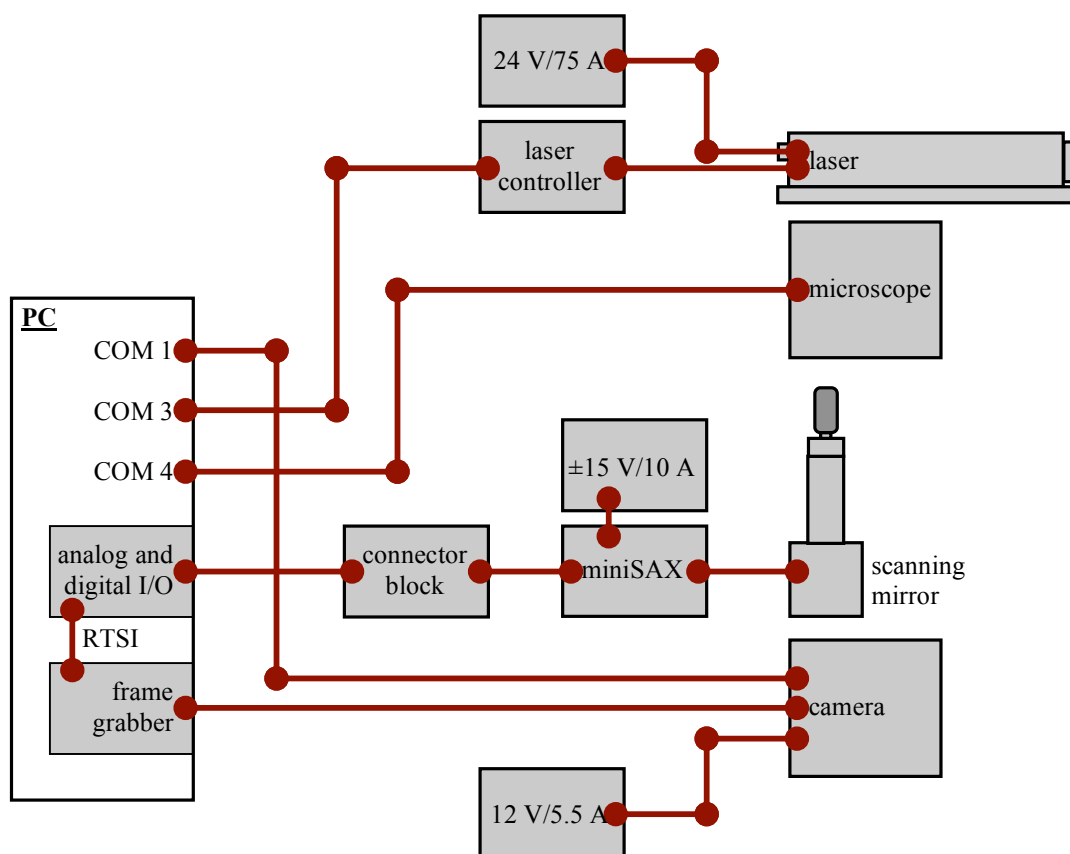


Figure 4.10. Circuit diagram of the control instruments of the spatial and temporal fluctuation microscope. The two data acquisition boards were used to control the scanner mirror and camera data. They were connected together by their RTSI port. In addition, three serial ports of the PC are used.

The angle position of the scanning mirror is controlled by the MiniSAX, which in return was controlled by the analog and digital in- and output data acquisition board. This board provides a total of 16 analog inputs, 2 analog outputs and 24 digital in- or outputs. Hence, a connector block is used, which simplify the connection arrangement. Scanning mirror features that can be controlled include the reading and the writing of the angle position and temperature control. The readout of the camera was controlled directly through the serial port interface of the computer (COM 1). Camera features that can be controlled include the integration time, charge multiplication gain, image size and the readout mode of the camera. The image data was transferred through the interface of the framegrabber. This board provided 16 differential channels for image transmission and 3 differential channels that organize

the image transfer: the clock signal and the line and frame enable signal. All additional control of the image transfer is done by the serial port interface.

For the development of the spatial STFM, the RTSI bus was used to share a trigger start signal between the data acquisition board of the scanning mirror and the frame grabber of the camera (Fig. 4.10). This trigger start signal synchronizes the angle position of the scanning mirror and the detected line in the probe.

4.4.7 RTSI triggering connecting the two data acquisition boards

The real-time system integration (RTSI) bus is a high-speed digital internal bus that chain different data acquisition boards that provide a RTSI bus together inside the PC. The RTSI bus is designed to enable high-speed, real-time communication between data acquisition boards due to the direct connection. Real-time digital signals as for example the clock data or trigger signals, for precise synchronization are shared between the boards.

For the development of the STFM, the RTSI bus between both data acquisition boards was used to share a trigger start signal between the scanning mirror and the camera. This start signal triggered by the RTSI bus, synchronizes the angle position of the scanning mirror and the detected line in the probe. For the setup described in this thesis work, RTSI pin 1 is used transmission of the trigger signal from board PCI-6251 to board PCI-1422. The clock signal was shared automatically. The RTSI triggering is schematically represented in figure 4.11 for uni- and bi-directional imaging. Two different clock signals are generated by the data acquisition board, PCI-6251. One clock signal for the start of the transmission of each single angle position to the galvanometer scanner (Fig. 4.11A₁). This scanner position data (Fig. 4.11A₃) transfer was controlled by a second clock signal, which starts and stops the overall position data transfer (Fig. 4.11A₂). On the falling edge of this second clock signal, φ_0 , the scanner starts the data transmission of the single position data. After one full data position transfer, φ_4 , the scanning mirror stays at the last transmitted position. The single position data transfer waits for the falling edge of the second clock signal, $\varphi_5 = \varphi_0$, of the data acquisition board. This second clock signal was shared between the data acquisition board PCI-6251 and the frame grabber PCI-1422 by the RTSI bus. On the falling edge of this RTSI signal, φ_0 , the camera starts grabbing the lines at the same time as the scanning mirror starts its angle position curve. The image frame grabbing starts a little bit ahead of time, as it actually should record only at the linear part of the angle position curve, between φ_1 and φ_2 , and not at the start up of the mirror, between φ_0 and φ_1 (Fig. 4.11A₃). Removing these redundant recorded lines afterwards was easier than changing the RTSI signal to falling edge and rising edge start for the angle position transfer and the camera image acquisition. Figure 4.11B_{1,2,3} shows the same two clock signals and the scanner position angle curve respectively, but the way the bi-directional imaging is implemented in the STFM. For this type of imaging both linear parts, the rising part, between φ_1 and φ_2 , and the falling part, between φ_4 and φ_5 , were used for image recording, which resulted in faster imaging. All redundant recorded lines, between φ_0 and φ_1 , between φ_2 and φ_4 and between φ_5 and φ_6 , will be removed afterwards. The two in one turn recorded images, between φ_1

and φ_2 and between φ_4 and φ_5 , were flipped vertically to each other. The second image was flipped back afterwards.

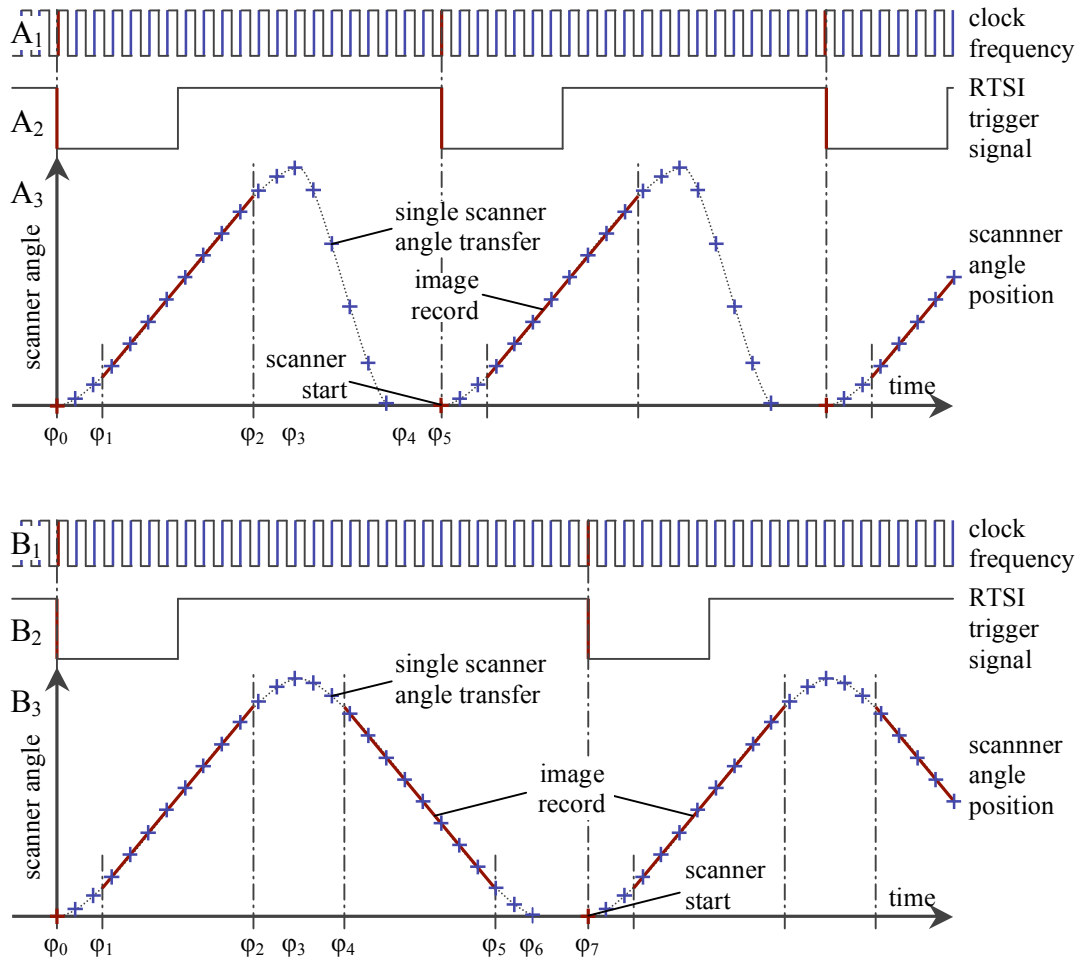


Figure 4.11. Clock signal (A_1), real-time system integration (RTSI) signal (A_2) and the corresponding scanning mirror angle position (A_3) used for the implementation of the spatial and temporal fluctuation microscope for uni-directional imaging ($A_{1,2,3}$) and for bi-directional imaging ($B_{1,2,3}$). At each raising edge of the clock signal, the data acquisition board transmits a new position to the galvanometer scanner. At the falling edge of a second clock signal, φ_0 , the RTSI signal, the transmission of the scanner position data and the camera acquisition starts.

4.4.8 The mechanical construction of the STFM

The requirements for the STFM described above (section 4.1), especially the mechanical long-term stability requirement, implies a rigid construction connecting the components with each other. Compared with the more open construction on an optical table, this design requires a highly precise calculation of the positions of each element, because it provides substantial fewer degrees of freedom for the alignment of the elements. On the other hand, this rigid design provides a considerable stability of

the instrument. In addition, this way of construction facilitates the darkening of the optical pathway, which is necessary for the low-light FCS measurements.

The three-dimensional image of the mechanical construction for the spatial and temporal fluctuation microscope is displayed in figure 4.12. The laser beam enters the mechanical construction by the fiber collimator through the indicated transmits. The laser beam leaves the construction through the side port of the Leica microscope and the fluorescence photons enter it the same way. These photons are detected by the camera positioned right after the camera port as indicated. A detailed cross section of the upper view of the STFM shows the position of all optical and opto-electronic elements and the position of the mechanical elements (Fig. 4.13). The drawings of each element of the mechanical construction are given in appendix 1.

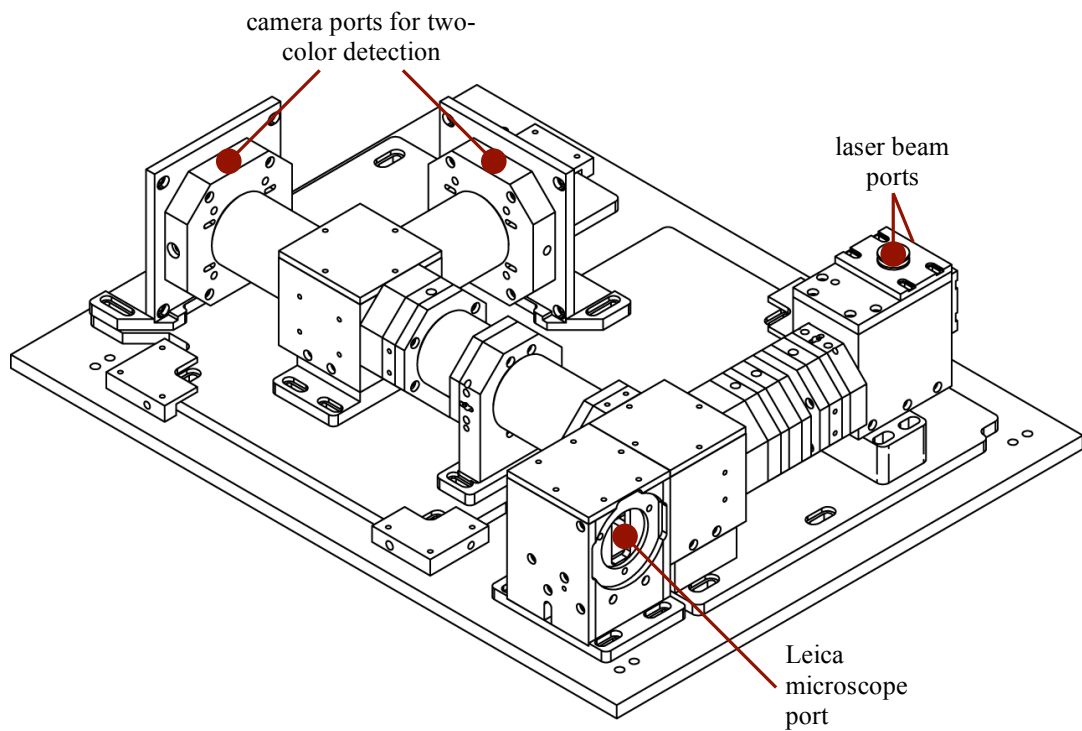


Figure 4.12. A 3-dimensional image of the mechanical construction for the implementation of the spatial and temporal fluctuation microscope

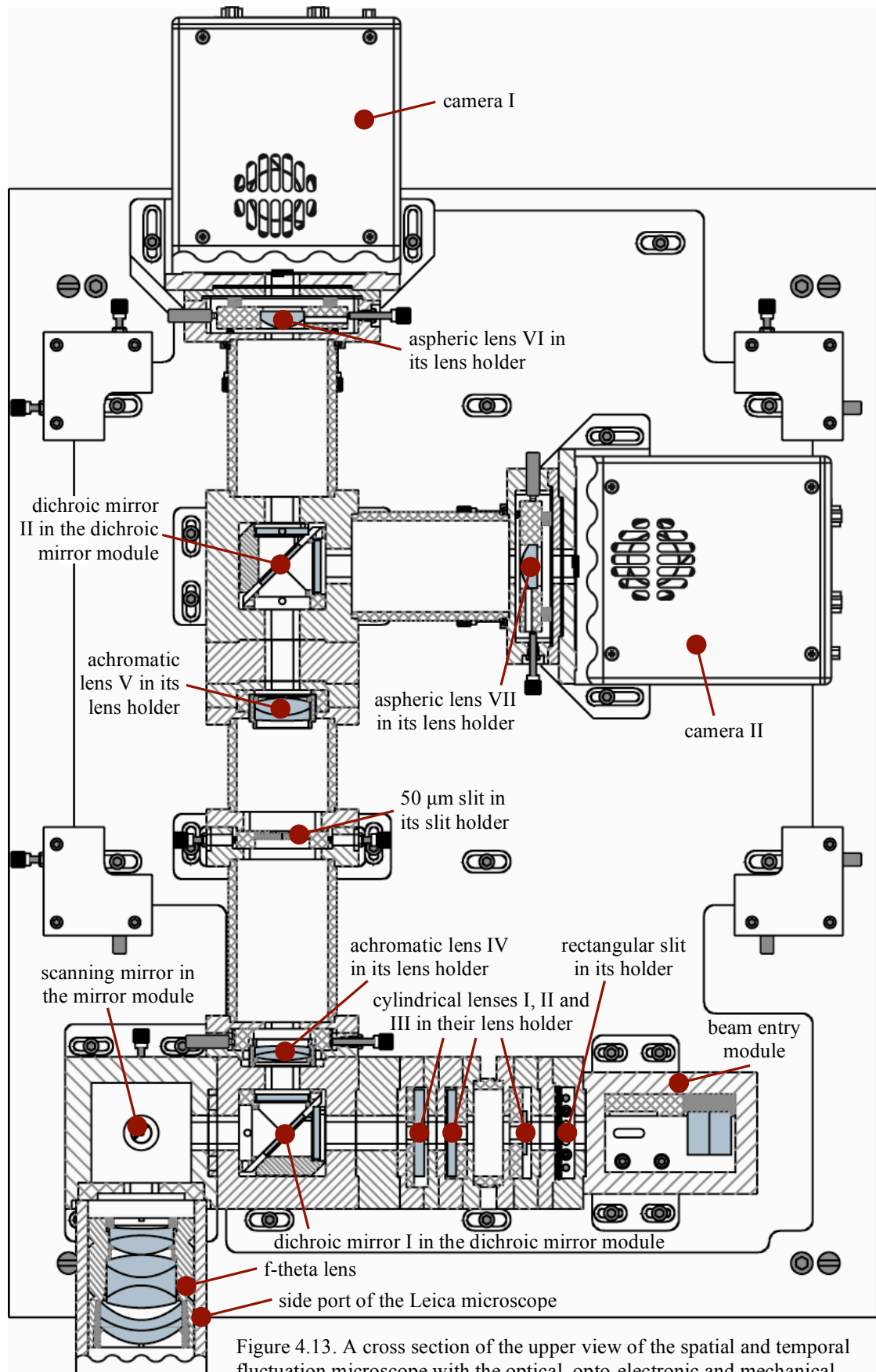


Figure 4.13. A cross section of the upper view of the spatial and temporal fluctuation microscope with the optical, opto-electronic and mechanical elements as indicated.

4.5 Software for the control of the STFM instrument

In this section, the software used for the instrument control of the spatial and temporal fluctuation microscope is described. This instrument control includes the camera-scan mirror synchronization, the positioning of the scan mirror, the readout of the camera and the positioning of the height of the microscope. The software supply of the company for each of these instruments is used. Within the scope of this thesis work, these software-packages are integrated into the STFM software to control the spatial and temporal microscope.

4.5.1 Description of the user-interface of the STFM software

The user-interface for the spatial and temporal fluctuation microscope software is shown in figure 4.14. At startup, the name of the user is inquired for proper assignment of the imaged to save. Each image is saved in the folder named by the imaging date as indicated (Fig. 4.14A). In addition, the hardware connections and the status of each instrument are verified. On proper establishment of all connections, the user-interface for imaging and FCS measurements appears (Fig. 4.14B). This user-interface can be divided into five sub groups as indicated and described below.

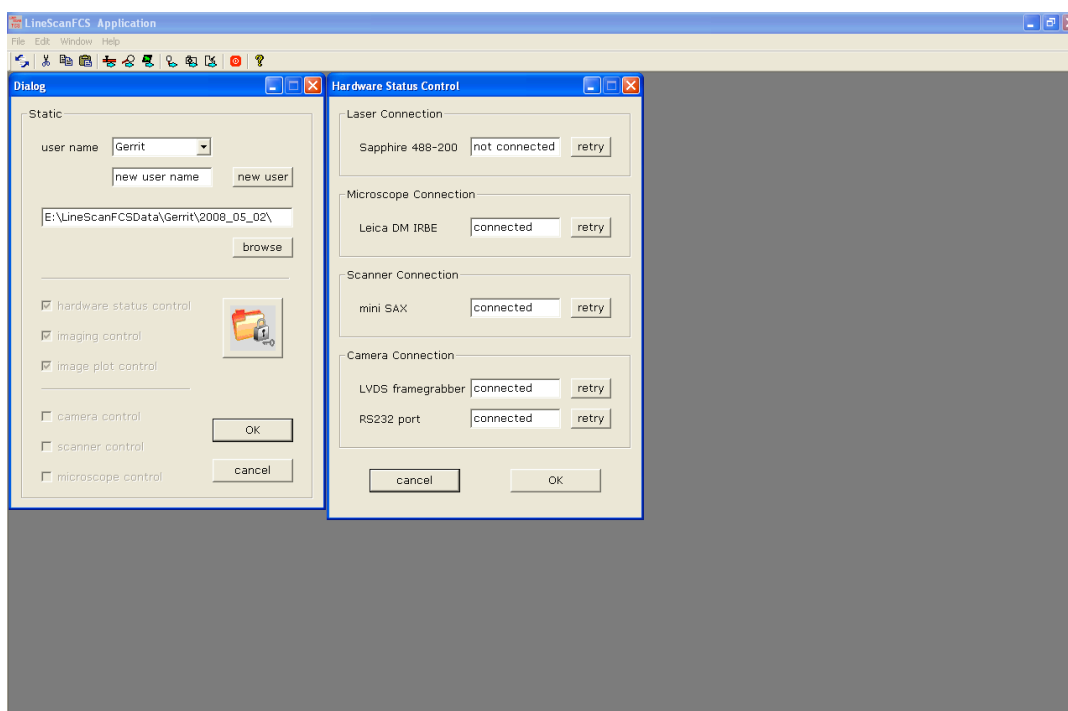
geometry controls: in this sub group, the geometry parameter input for the imaging can be assigned as image size, image number and delta distance of the z-stacks. The scanning mirror moves the laser beam bidirectional through the probe, which provides an image for both directions assigned by the uni- and bidirectional check box. The height of the microscope can be controlled using the buttons at the right. The default-button can be used to reset all editors to their initial values.

time and gain controls: The integration time is the time photons are collected at the camera for each line. This is not the same as the actual line image frequency, because for small integration time the readout velocity is the limiting factor. The actual line frequency is displayed underneath the integration time. The camera is an EMCCD camera. Therefore, the overall gain is divided into an electron-multiplication gain, which is an on-chip gain, and a digital gain that acts after the analog to digital conversion.

line scan imaging: The STFM imaging can be started using the buttons in this subgroup. Using the first button will capture one image of the probe. Using the second button, several images will be captured. The number of images and the time between two images can be assigned as indicated by their editors. The imaging can be stopped in between using the third button. The duration of the imaging is printed. The captured images are plotted in the image display.

Implementation and construction of the STFM

A



B

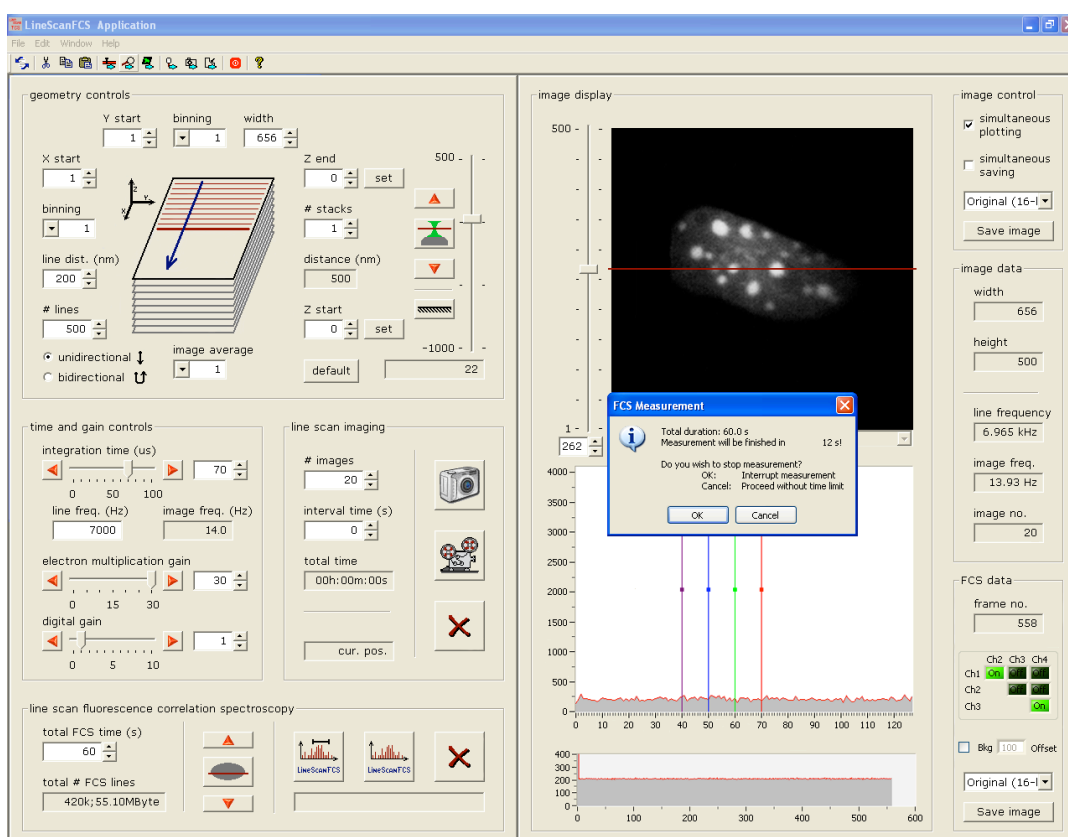


Figure 4.14. The user interface of the software for instrumental control of the STFM. At startup of the software, the start dialog and the hardware status dialog (A) appear that after initializing lead to the user interface for imaging and FCS parameter input the plot output (B).

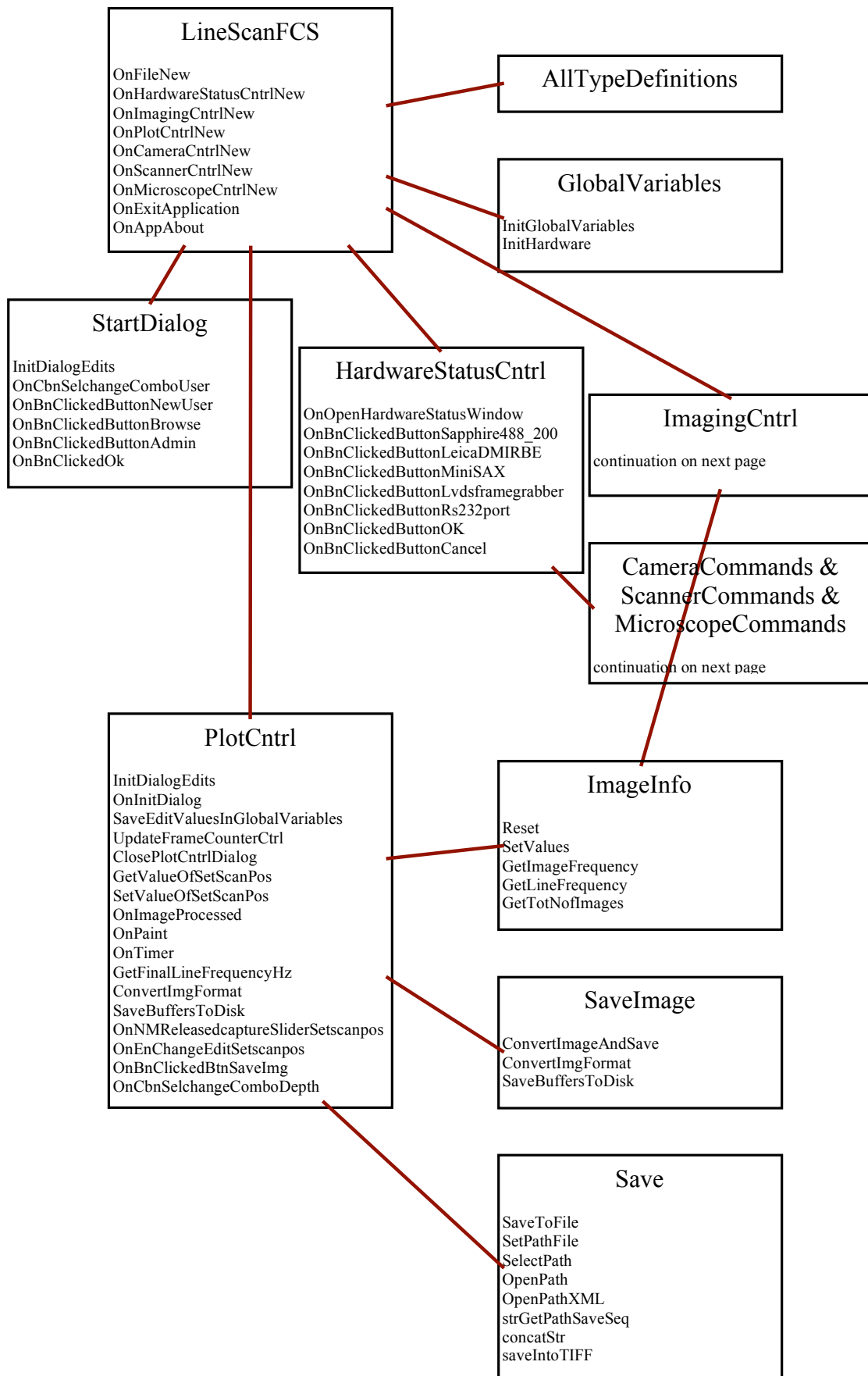
line scan fluorescence correlation spectroscopy: After imaging the probe, the position of the line for FCS measurements can be assigned using the buttons in this sub group. The total number of lines and the RAM-space needed for one measurement is calculated according to the FCS time limit. The FCS measurement can be realized using the time limit or without time limit for continuous measurement, that can be stopped using the stop button. For time limited FCS measurement, a dialog box appears as indicated (Fig.4.14B) with the remaining measurement time.

image display: The image display contains three types of images. The first image displays the spatial distribution of the fluorescently labeled particles, the second plot shows the measured FCS intensity profile along the captured line and the third the averaged intensity over the whole line versus time.

image control: The upper buttons and editors of the image control are associated with the imaging feature of the STFM. Here, the image can be saved using different saving types. Low intensity images can be saved as 8-bit images instead of 16-bit images throwing away the upper 8-bit of the image. The width, height, line and image frequency and the number of images of the realized recording are displayed and saved in an additional xml-file. The lower buttons and editors of the image control are associated with the FCS feature of the STFM. For FCS, frames including 1000 lines are imaged. The number of recorded frames is displayed during the FCS measurement. The recorded FCS lines will be saved as image frames again with the transfer to 8-bit possibility. The colored lines in the second plot of the image display are assigned to Ch1 (purple), Ch2 (blue), Ch3 (green) and Ch4 (red). The assigned positions of these lines correspond with a certain pixel or with a range of pixels. The FCS measurements along these pixels will be saved additionally according to the selected channels.

4.5.2 Program structure of the STFM software

The main file of the STFM program is the 'LineScanFCS' file. All other files are controlled by this file. The data flow diagram of the STFM software is displayed in figure 4.15. Both dialogs that appear at start up (Fig. 4.14A) are defined by the 'StartDialog' file respectively the 'HardwareStatusCntrl' file. The control editors on the left side of the user-interface for imaging and FCS measurements (Fig. 4.14B) are implemented in the 'ImagingCntrl' file and the images and their controls on the right side are implemented in the 'PlotCntrl' file. This implies that the 'ImagingCntrl' file is the main control file for the control of all opto-electronic instruments including the camera, scanning mirror and microscope. The control of each of these instrument is implemented in respectively the 'CameraCommands' file, the 'ScannerCommands' file and the 'MicroscopeCommands' file.



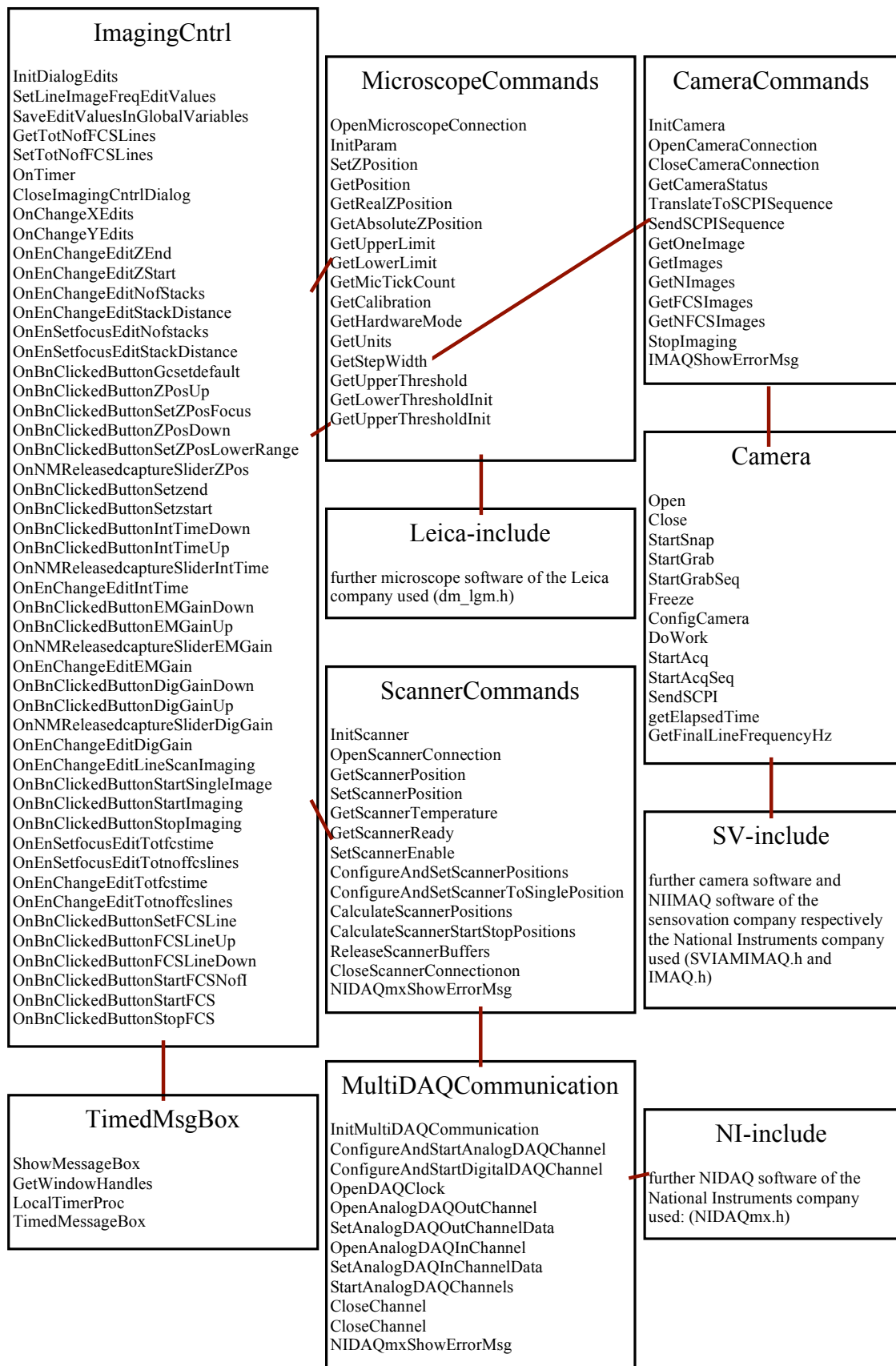


Figure 4.15. The data-flow diagram of the STFM software that controls and synchronizes the used instruments of the spatial and temporal fluctuation microscope.

The 'CameraCommands' file controls the camera communication and readout of the image data by the supplied software from Sensovation. The main file of this camera program is the 'SVIAMIMAQ' file. The control of the framegrabber is implemented using the NIIMAQ software from National Instruments. The 'ScannerCommands' file controls the 'MultiDAQCommunication' file, which in return controls the data acquisition board for the communication with the scanning mirror. The communication with the data acquisition board occurs by the supplied NIDAQ software from National Instruments. The main file of this program is the 'NIDAQmx' file. The 'MicroscopeCommands' file controls the communication with the microscope by the supplied software from Leica. The main file of this microscope program is the 'dm_lgm.h' file.

Chapter 5

Optical alignment of the STFM

5.1 Overview of the adjustable modules

The spatial and temporal fluctuation microscope instrument is schematically represented in three different views (Fig. 5.1); the upper, side and front view. For simplicity, only the optical part is drawn without the actual microscope and the laser. The laser beam reaches the Spatial and temporal fluctuation microscope instrument through one of the two fiber collimators C. In the beam coupler module D, two different laser beams are coupled and aligned to the coordinates of the instrument. In the illumination path of the instrument, the laser beam passes a rectangular slit E₁ and three cylindrical lenses F₁₋₃ that transform the shape of the laser beam in one direction. In the beam splitter module G, a wavelength-dependent beam splitter defines the pathway of the emitted and that of the fluorescent light. In the mirror holder module H, a scan mirror turns round the illumination beam into the microscope where a tubular lens and an objective lens focus the illumination beam in the probe. Changing the angle of the scan mirror moves the position of the focus in the probe.

The first part of the detection pathway is the same as the way back through the objective lens, the tubular lens and the mirror holder module H. For the wavelength of the fluorescent light, the beam splitter G₁ acts like a mirror and the light is reflected through a spherical lens F₄, through a few micron slit inside the slit holder E₂ and another spherical lens F₅. The few micron slit acts like the pinhole in the usual confocal microscopes, nevertheless only in one direction. In the second beam splitter module G₂, different wavelengths can be split up for two-color detection. The lens F₆ and F₇ right before the detector J₁ respectively J₂, focuses the fluorescent light on the detector.

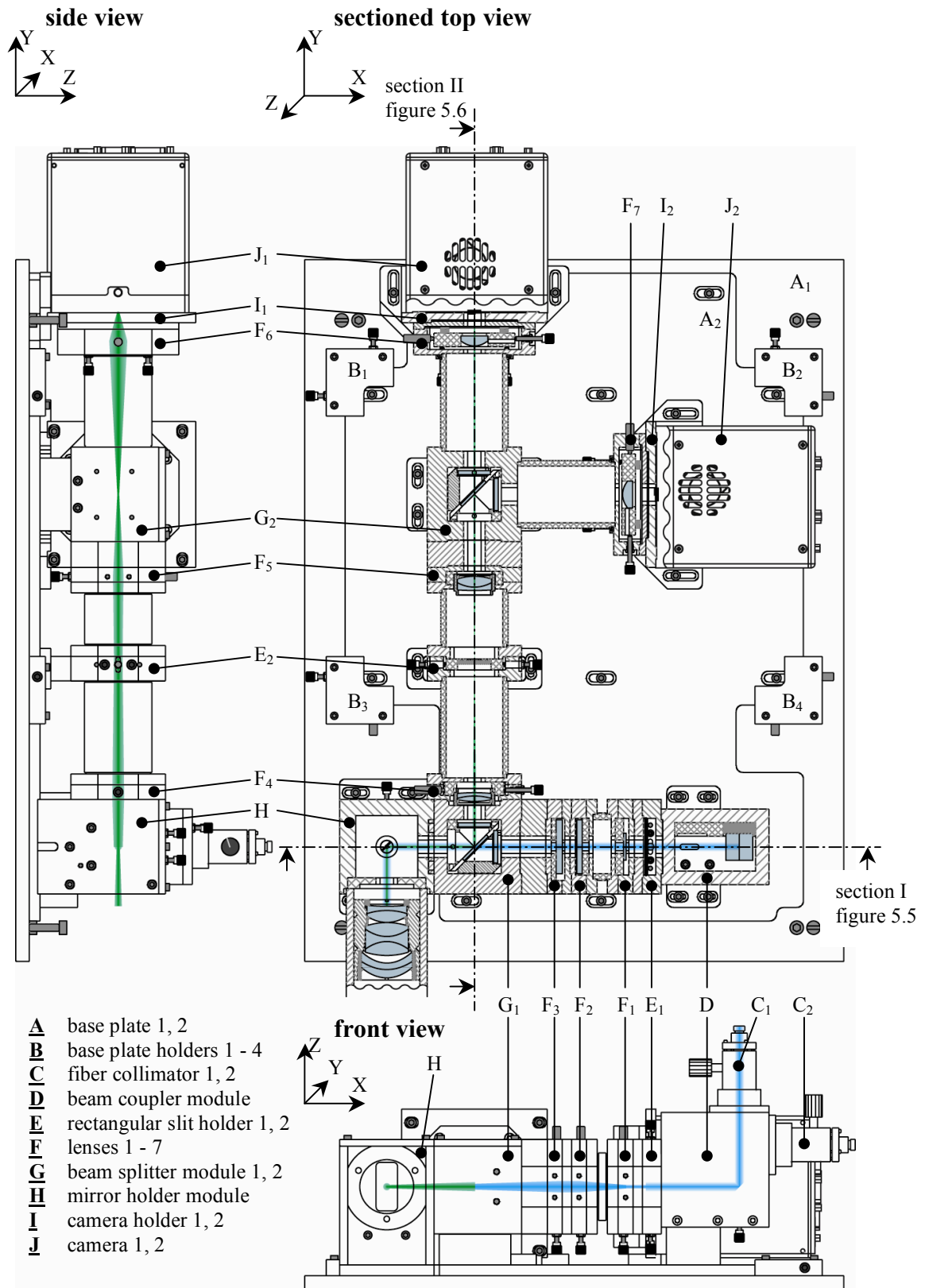


Figure 5.1. A schematic drawing of the setup of the spatial and temporal fluctuation microscope. The first image is a view from the left, the second an upper view and the third image a front view of the spatial and temporal fluctuation microscope.

5.2 Alignment of the illumination and detection pathway

For proper use of the STFM instrument, all components drawn in figure 5.1 have to be adjusted carefully. Below, an instruction guide shows the appropriate procedure how to collimate the illumination and the detection pathway.

1. Unscrew the mirror holder module H from base plate A_1 . Do not demount this module from the microscope port. Demount the screws that fix base plate A_2 and base plate A_1 and shift base plate A_2 with all its components about 8 mm away from the mirror holder module H, that there is no connection between them anymore.
2. The height of base plate A_1 can be changed by the four screws and the four counter screws at each edge of the plate. This base plate has to be at a height that the mirror holder module H is straight upon it and it has to be exactly horizontal.
3. Now the optical axes of the microscope and that of the base plate are equal. Tight the mirror module to base plate A_1 . Shift base plate A_2 back that the beam splitter module G_1 is close together to the mirror holder module H. Also tight base plate A_2 to base plate A_1 .
4. To adjustment the beam coupler module D, remove this whole module from base plate A_2 . Additionally, remove the three cylindrical lenses F_1 , F_2 and F_3 and the first rectangular slit E_1 in front of the beam coupler module in the illumination beam path.
5. Position the laser beam coming out of the beam coupler module as shown in figure 5.2. The beam should be 58 mm above the ground plate over a distance of about 1 meter and 45 mm apart from the housing base of the beam coupler module. The height position of the beam can be changed by the fine adjusted movable beam splitter D_a . The tilt of the out coming beam is adjustable by the three screws and the three counter screws C_{1a} on top of the fiber collimator C_1 . The collimation of the beam can be changed by screw C_{1b} , which displaces the collimation optic inside the fiber collimator. Here, only the alignment of one laser beam is described. Alignment of a second wavelength is in principle the same, only a few things have to be taken into account. These are described below.
6. Put the beam coupler module D back at its position on the base plate A_2 . Use the small bearing gabs of the screws to position the middle of the laser beam in xy-direction at the middle of the scanning mirror. Turn the objective lens of the microscope away that there is a free aperture for the laser beam. A reflection at the ceiling now shows up. Use a vertical board about one meter above the microscope for further use of the laser beam reflection. This reflection should remain symmetric on changing the collimation of the laser beam by screw C_{1b}

(Fig. 5.2), otherwise the optical axis of the microscope and that of the spatial and temporal fluctuation microscope instrument are not equal. For the case it is not symmetric, align the pathway of the laser beam as described in point 5 more carefully.

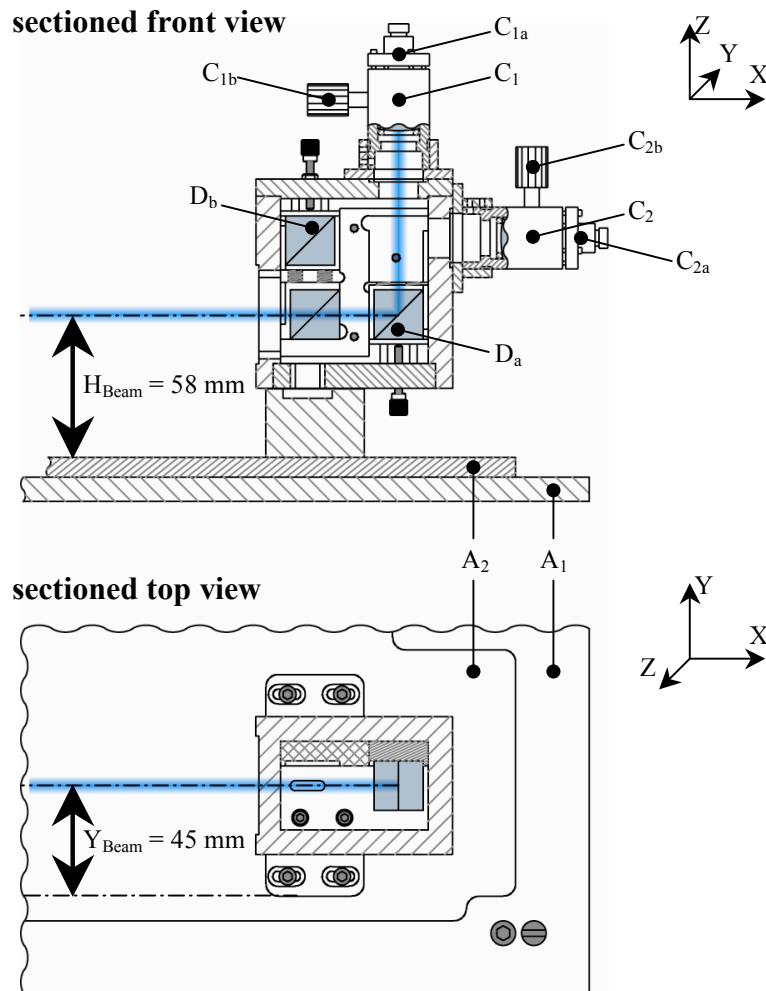


Figure 5.2. A schematic drawing of the beam coupler module of the line scan FCS (part D in the overview drawing of figure 5.1).

7. Mount rectangular slit holder E_1 back in front of the beam coupler module as shown in figure 5.3. Change the rectangular aperture of slit holder E_1 that the reflection at the vertical board is symmetrical with a width of 10 mm. The length of the reflection does not change on varying the position of the rectangular slit.
8. For further alignment, mark the position of the border of the laser spot at the vertical board. Mount cylindrical lens F_3 at its position at the beam splitter module G_1 as shown in figure 5.3. Turn back the objective of the microscope at its place that the laser beam goes through it. Held a sheet of paper about 20 cm

above the objective to have a look at the laser beam. Use the fine-adjustable screw and the counter screw to move cylindrical lens F_3 in the z-direction. The counter screws are spring plungers with a pressure pin to simplify the alignment. Now the laser beam coming out of the objective is parallel in the x-direction and divergent in y-direction. Adjust cylindrical lens F_3 until at the paper sheet a line appears. Remove the paper sheet and fine adjust this lens further that the position of the line coming out of the objective at the vertical board is as exact as possible at the middle of the marked range at the vertical board.

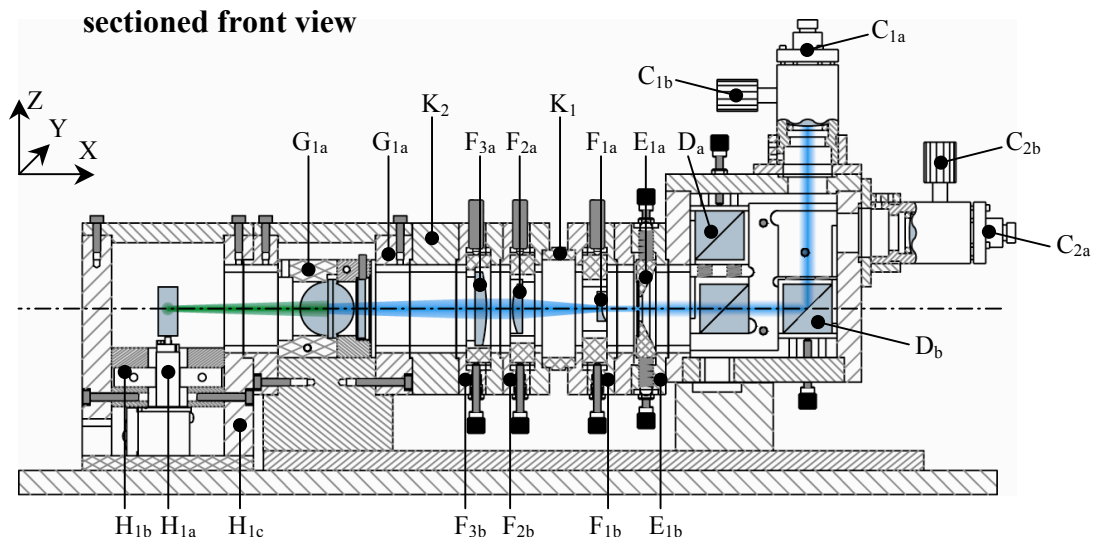


Figure 5.3. A schematic drawing of the illumination path of the line scan FCS. $C_{1a,2a}$ fiber collimator screw, $C_{1b,2b}$ fiber tilt adjustment, $D_{a,b}$ movable mirror for height adjustment, E_{1a} observation slit, E_{1b} slit holder, $F_{1a,2a,3a}$ cylindrical lenses, $F_{1b,2b,3b}$ lens holders, G_{1a} dichroic mirror holder, G_{1b} beam splitter housing, H_{1a} scan mirror, H_{1b} scan mirror holder, H_{1c} scan mirror housing, $K_{1,2}$ extension element.

9. To adjustment the first cylindrical lens F_1 , remove again the beam coupler holder module D from base plate A_2 and mount this lens at its position on top of the rectangular slit holder E_1 in front of the beam coupler holder module D as shown in figure 5.3. The middle of the laser beam again has to be 58 mm above the ground plate A_2 over a distance range of 20 cm (divergent beam in z-direction).
10. Mount the second cylindrical lens F_2 at its position on top of the third lens F_3 as shown in figure 5.3. Put the beam coupler module D back at its position on the base plate A_2 . Do not forget the small tube between the first and the second lens. Again use the small bearing gabs of the screws to position the beam coupler module in xy-direction to the middle of the laser beam at the scanning mirror. Additionally, adjust the second cylindrical lens F_2 that a line appears at a sheet of paper. Remove the paper sheet and fine adjust this lens further that the position of the line coming out of the objective at the vertical board is as exact as possible at the middle of the marked range at the vertical board.

11. For the spatial and temporal fluctuation microscope instrument, the laser beam in the back focal plane of the objective has to be parallel in the x- and focused in the y-direction to get a focus line in the probe that is focused in the x- and parallel in the y-direction. To examine the parallelism of the laser beam in the x-direction at the back focal plane objective, turn away the objective lens of the microscope that an open aperture appears. Use the beam collimation tester about one meter above the microscope aperture because the collimation tester needs a certain beam area for proper use and the divergence of the laser beam in the other direction. Use the fiber collimator screw C_{1a} (Fig. 5.3) to change the collimation of the laser beam; the lines on the screen of the collimation tester have to be vertical for a parallel laser beam at the back focal plane of the objective.
12. After parallelization of the laser beam in x-direction at the back focal plane of the objective, the other direction has to be aligned. For alignment of the laser beam in y-direction turn back the objective at its place that the laser beam goes through it. In the focal plane of the objective, the laser beam in y-direction has to be parallel. Held a sheet of paper about 10 cm above the objective to have a look at the laser beam. Changing the distance between the cylindrical lenses F_{1a} and F_{2a} will change the parallelism in y-direction without altering the laser beam in the x-direction. To change this distance, unscrew the screws of the beam coupler module D a little bit, and carefully change this module along the x-axis. Mount the beam coupler module at that position on the base plate A_2 where the width of the line at the paper sheet is the smallest.
13. Up to now, the illumination path of the spatial and temporal fluctuation microscope is aligned. For alignment of the detection path, use a highly fluorescent medium for the wavelength used, to get a visible intensity of the fluorescent light. For alignment of the detection path, demount the camera holder I_1 , the beam splitter holder G_2 and the rectangular slit holder E_2 from the base plate A_2 and remove them (Fig. 5.1). Additionally, demount the spherical lens holder F_4 from beam splitter holder G_1 , examine that this lens it is exactly in the middle of the holder and put it back at its position. Because of the bad construction of the holder, the lens can change position over time.
14. Put the rectangular slit holder E_2 and extension element K_3 (Fig. 5.4) back at its position. Slide the slit holder as close as possible towards the beam splitter module G_1 and fix it at the base plate A_2 .
15. Turn the camera J_1 90° ccw around the optical axis that the active area of the sensor is above the inactive area and mount it back at its holder I_1 as shown in figure 5.4. Remove the spherical lens holder F_6 from the camera holder I_1 . Demount the camera holder that it is movable over the base plate A_2 . Use the imaging program of the camera described in section 4.5. Put the camera right behind the rectangular slit E_2 . Maximize the intensity at the camera by moving the slit by the lower two fine adjustment screws in the x-direction. The upper two fine adjustment screws will align the orientation of the slit a little. Use them to make the intensity signal symmetric.

16. The water objective of the microscope uses a ring to align for different heights of the deck glasses. Maximize the intensity on the camera by turning around this ring. Remove the camera inclusive holder after maximization of the intensity and put the beam splitter module G_2 with the spherical lenses F_5 and extension element K_5 mounted and the round extension element K_4 back at its position on the base plate A_2 (Fig. 5.4).

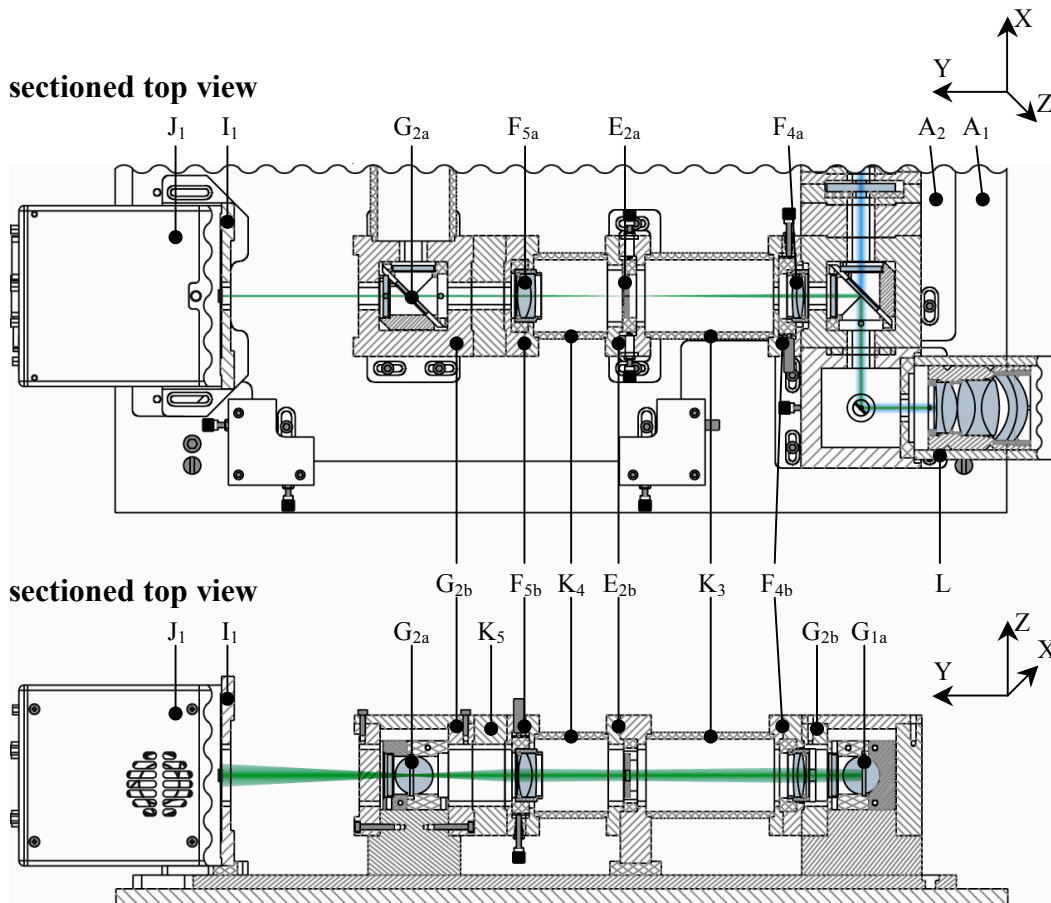


Figure 5.4. A schematic drawing of the detection path of the line scan FCS. $A_{1,2}$ base plates, E_{2a} rectangular slit, E_{2b} rectangular slit holder, $F_{4a,5a}$ spherical lenses, $F_{4b,5b}$ lens holders, $G_{1a,2a}$ dichroic mirror holders, $G_{1b,2b}$ beam splitter housing, I_1 camera holder, J_1 camera, $K_{4,5}$ extension element, L scan lens inside microscope port.

17. The fluorescent light after passing lens F_5 has to be parallel in x-direction as shown in the sectioned top view of figure 5.4. Displacing this lens in y-direction changes the collimation of the fluorescent beam. Use the bearing gabs of the screws to move the beam splitter module over base plate A_2 . Take two images using the imaging program of the camera described in section 4.5. Leave the camera 90° ccw turned around for imaging these two images. For the first image, put the camera right behind the beam splitter housing G_{2b} . Take the second image a distance of about 20 cm away from the beam splitter housing as shown in figure

- 5.4. Use a round extension element for imaging the second image to decrease background light. Both images show an intensity band at different intensity levels for the two images. The intensity differs because of the divergence of the fluorescent light in z-direction so a part of the light is not detected when the camera is displaced over 20 cm. The widths of these gauss-like profiles have to be equal. The small Matlab program 'GetFluorescentLineProfile.m' measures the widths of these lines. The full width at half maximum of these lines must be equal. For the case the widths of the lines are not equal within 0.4 pixels over a distance of about 20 cm, move the beam splitter housing G_{2b} carefully along the optical axis and repeat point 17 again.
18. Before mounting spherical lens holder F_6 , vertically align the start position of the lens in the y-direction in its housing using the four fine adjustment screws. Mount lens holder F_6 back at its position at the camera holder I_1 as shown in figure 5.1. Leave the camera 90° ccw turned around. Put the camera holder I_1 , camera J_1 and the round extension element K_6 back at its position on base plate A_2 as shown in figure 5.1. Again, use the STFM imaging program of the camera for imaging this focused fluorescent light. Reduce the laser intensity until the measured fluorescent intensity is just below the saturation level of the camera. For the 90° turned camera, the electric charges are transport downward during reading out each point along the fluorescent line, which is also vertically orientated. Therefore, using the camera 90° turned around, the fluorescent line will be focused on a few pixels of the sensor of the CCD camera. Decreasing the width of these few pixels on the sensor will increase the resolution of the spatial and temporal fluctuation microscope instrument. Decrease the width on the sensor by alignment of lens F_{6a} in the y-direction using the four fine adjustment screws. Align until the line is focused on only one pixel and the intensity levels of the two neighboring pixel are below 40% of the maximum intensity of the pixel itself.
 19. Turn the camera J_1 90° cw back at position as shown in figure 5.1 and mount it to the camera holder I_1 . The line-scan instrument is aligned and ready for use. If two different wavelengths are coupled in only one fiber, only one fiber coupler has to be aligned. Alignment of one wavelength includes the alignment for the other wavelength. Although for possible chromatic differences between these two wavelengths cannot be corrected. The next issue describes the alignment of a second laser beam using two different fibers and fiber couplers.
 20. For alignment of the second laser beam, it must be aligned without altering the pathway of the other laser beam. Turn on the second laser beam. The height of this laser beam can be adjusted by the fine adjusted movable beam splitter D_b . The tilt of the out coming beam is adjustable by the three screws and the three counter screws C_{2a} on top of the fiber collimator C_2 . Use these alignment screws to superimpose the two laser beams. This overlay can be examined at the mirror H_{1a} , and at the vertical board about 1m above the microscope; the objective has to be turned away.

21. Both wavelengths have to be confocal to each other, focused the same focus volume in the probe. Use the beam collimation tester about one meter above the microscope aperture. Use the fiber collimator screws C_{2a} (Fig. 5.3) to change the collimation of the laser beam in y-direction; the lines on the screen of the collimation tester have to be vertical for a parallel laser beam at the back focal plane of the objective.
22. For further alignment of the second laser beam, use a highly fluorescent medium for the wavelength used, to get a visible intensity of the fluorescent light. Remove the camera J_2 , the camera holder I_2 and the round extension element K_7 . Put a beam splitter in beam splitter module G_2 and use camera J_2 90° ccw turned right behind the beam splitter module. Additionally, use the STFM imaging program for imaging this focused fluorescent light. Use the fiber collimator screws C_{2a} to fine adjust the tilt of laser beam coming out of the fiber collimator C_2 by maximizing the intensity on the camera. Do not change the collimation of the laser beam.
23. Further alignment of the second laser beam is the same as described in issue 17 up to 19 for the first laser beam. Now lens holder F_7 , camera holder I_2 , camera J_2 and the round extension element K_7 has to be read instead of lens holder F_6 , camera holder I_1 , camera J_1 and the round extension element K_6 .

5.3 Alignment of the laser coupler

The laser beam reaches the STFM instrument through one of the two fiber collimators. A proper alignment of the laser collimator is important to get optimal laser intensity. For the laser coupler module described below two different lasers are coupled by a dichroic mirror into one fiber. In figure 5.5, the laser coupler module is schematically represented. The appropriate procedure how to collimate the illumination and the detection pathway involves the following steps

1. Uncouple the fiber at the laser collimator I as shown in figure 5.5. Also, remove the beam expander E_1 , holder D_1 and the laser collimator I.
2. Turn on laser A_1 and mark the position of the middle of the laser beam at the wall for further alignment.
3. Put the beam expander holder D_1 and the beam expander E_1 back at its position at the base plate B_1 as shown in figure 5.5. Put the laser beam of laser A_1 at the marked position on the wall by positioning the position and tilt of the beam expander D_1 . For the adjustment of the beam expander, use the z-adjusters for the base plate C_1 and the bearing gabs of the beam expander holder D_1 . The axial orientation of the beam expander E_1 can slightly be changed by loosening the screw at the beam expander holder D_1 .

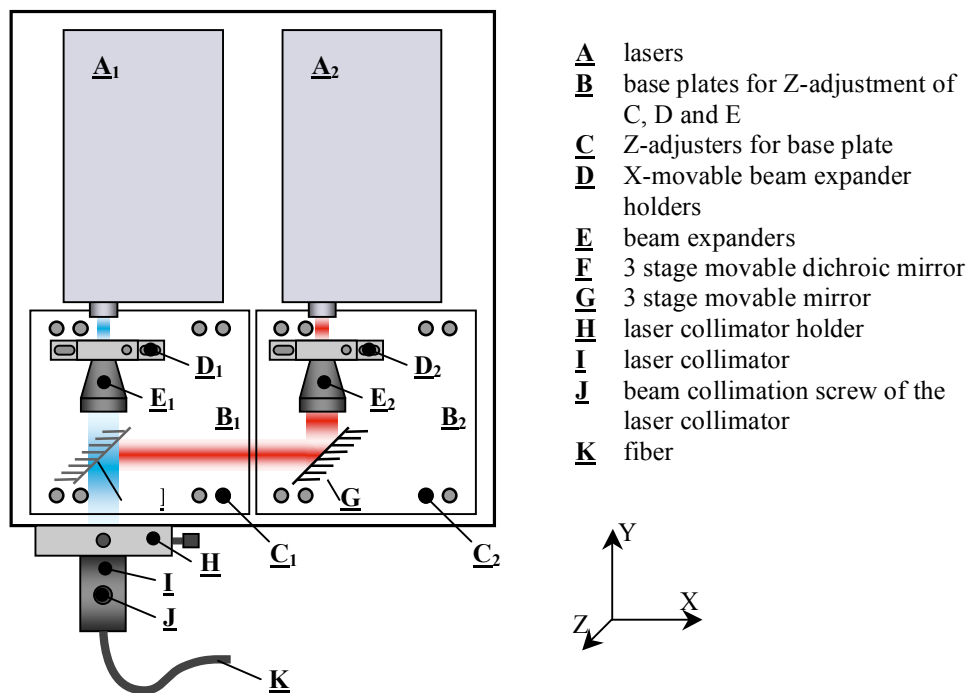


Figure 5.5. A schematic drawing of the laser coupler module.

4. Put the laser collimator I back at its position as shown in figure 5.5 without mounting the fiber K. Change the xz-position of the laser collimator I using the fine adjustment screws of its holder, that the laser beam illuminates the marked position at the wall.
5. For the positioning of the beam of the second laser A_2 , turn on the second laser A_2 and overlay the laser beam of this one with the laser beam of laser A_1 , using beam expander holder D_2 , movable dichroic mirror F and movable mirror G. Examine the overlay of the beam at the dichroic mirror and at the wall.
6. Put the fiber K back into the laser collimator I. Use a highly fluorescent solution for the wavelength used, to get a visible intensity of the fluorescent light. Measure the fluorescent intensity by the camera using the STFM imaging program.
7. Maximize the fluorescent intensity at the camera by adjusting the fine xy-adjusters of the laser collimator holder H.
8. The collimation of the laser beam at the entrance of the laser collimator and the output intensity of the fiber are correlated with each other. Use the beam collimation screw J to change the output intensity.

Chapter 6

Performance, evaluation and basic applications of the STFM

6.1 Characterization of instrument components used for the STFM

6.1.1 EMCCD camera characterization for line-scan detection

In order to measure fast particles in the focal volume, the line imaging frequency has to be adequately fast. Therefore, this camera feature is described in more detail. For the implementation of the spatial and temporal fluctuation microscope, an area-scan EMCCD camera was modified to a line-scan EMCCD camera. Therefore, a camera noise test was performed to characterize the modified line-scan EMCCD camera. The results were compared with the values provided by the manufacturer for the area scan implementation.

6.1.1.1 Line frequency of the line-scan EMCCD camera

For the STFM a line-scan EMCCD is used. Since line-scan EMCCD cameras are not commercially available, the area-scan EMCCD SamBa SE-34 from Sensovation was reprogrammed for use as a line-scan EMCCD.

The difference between the area-scan mode and the line-scan mode of the camera is the way the captured images are read out and transferred to the frame grabber. The area-scan mode reads out the whole frame as one image. After acquisition of the frame, the camera sends three dummy lines to indicate to the frame grabber the end of the image. Using the area-scan camera for detecting one single line, the whole frame consists of only one line. For this case, three dummy lines are sent after each single line imaged, which will reduce the imaging rate by a factor of four. To avoid the need for sending these dummy lines, the firmware of the camera was reprogrammed to line-scan mode, without sending information about the end of the captured frame to the frame grabber, thus increasing the image acquisition rate to a value of about 16000 lines per second containing 656 pixels. By only using a fraction of the line, the line imaging rate of the camera could be further increased. Fig. 6.1 shows the line frequency for different line lengths. For a length of 128 pixels, a rate of about 60 000 lines per second can be achieved.

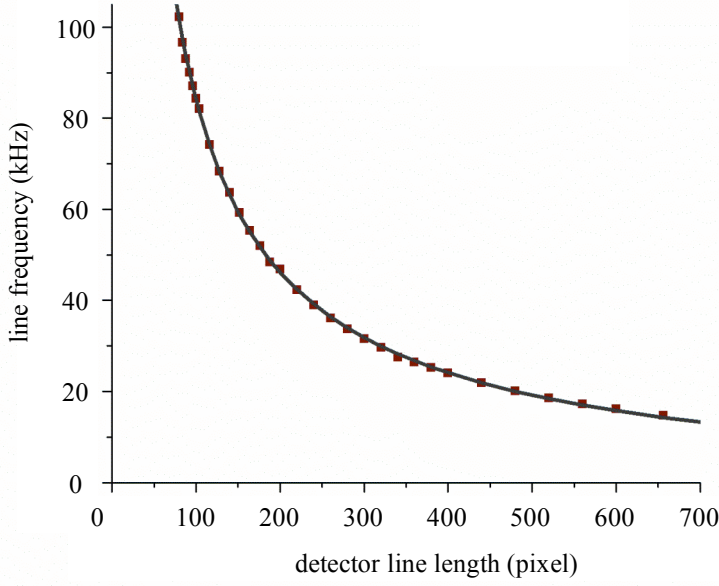


Figure 6.1. Line scan rate versus detector line length. Lines captured using the EMCCD camera SamBa SE-34 from Sensovation used for the development of the spatial and temporal fluctuation microscope. The measured values (red squares) and the smoothed line (grey). The values are measured using a 30x electron-multiplication gain.

6.1.1.2 Conversion factor of the camera using the photon transfer test

The photon transfer test describes how to measure the conversion factor of a CCD camera. The conversion factor described in electrons per analog-to-digital conversion unit (e^-/ADU) relates the pixel value to the number of captured electrons. This conversion factor will be extracted from the photon transfer curve derived from different CCD images as described below (Janesick, 2007). The photon transfer curve is a graphic representation that shows the variance of the signal σ_{pv}^2 as a function of the average signal \bar{I}_{pv} for a set of flat-field images. The average signal \bar{I}_{pv} and the variance σ_{pv}^2 correspond to the average and the variance, respectively of an array of pixel values. The pixel values are expressed in analog-to-digital conversion unit (ADU) and correspond to the number of electrons present in the pixels contained on a CCD array. In such a representation, σ_{pv} and \bar{I}_{pv} are expressed in ADU. The variance of the captured signal σ_{pv}^2 is related to the average of this signal \bar{I}_{pv} by the linear equation (Christen et al., 2006)

$$\sigma_{pv}^2 = \frac{1}{g} \bar{I}_{pv} + \frac{1}{g^2} \sigma_{ron}^2 \quad (6.1)$$

With g the conversion factor (in e^-/ADU), \bar{I}_{pv} the average pixel value (in ADU), σ_{pv} the total rms noise (in ADU) and σ_{ron} the readout rms noise (in e^-). In such a so-called photon transfer curve, the variance of the signal σ_{pv}^2 is plotted versus the mean signal \bar{I}_{pv} . The inverse of the slope of a linear fit of this plot provides the conversion factor g . From the cross section of the linear fit with the y-axis, a value for the total readout noise σ_{ron} can be extracted.

For the acquisition of the images for this test, the illumination of the CCD has to be homogeneous all across the surface; the fluctuations must be less than 1%. Otherwise, the method described is still usable, but the CCD images have to be flattened for proper use of the test or, if the inhomogeneity is partial, only the homogeneous part of the captured frame should be taken into account. For the captured images described below, the intensity drops down at both sides of the captured frame, because the sensor is not fully homogeneously illuminated. To get rid of this inhomogeneity, the respective areas of the captured frames are rejected.

In order to plot the photon transfer curve, the variance σ_{pv}^2 is computed for frames imaged at different integration times. Varying the integration time also changes the mean intensity level of the captured images. The acquired intensity has to be at a low light level, so that the camera is not saturated even for large integration times. Figure 6.2 shows the frame transfer curve for the EMCCD camera used for the STFM. The four blue squares at the right of the plot are not taken into account for the linear fit, because these data points contain saturated pixels. From a linear fit, a conversion factor of $g = 0.091 \text{ e}^-/\text{ADU}$ is obtained.

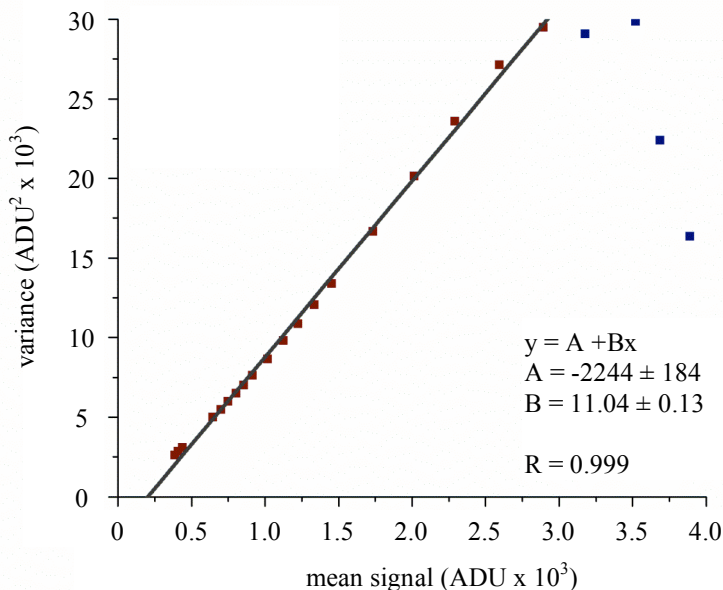


Figure 6.2. The photon transfer curve for the EMCCD camera SamBa SE-34 from Sensovation used for the spatial and temporal fluctuation microscope. The squares are the measured points. The blue squares are rejected for the linear fit (grey line). The inverse of the slope of the linear fit gives the conversion factor $g = 0.091 \text{ e}^-/\text{ADU}$. The values are measured using a 30x electron-multiplication gain.

6.1.1.3 Dark current and readout noise of the line-scan EMCCD camera

Dark current is the relatively small signal record by the camera even when the device is not illuminated. To measure the dark current, the photo-sensitive area of the EMCCD camera was occluded and dark image frames were captured at different

integration times (Zhang et al., 2000). The mean signal was plotted versus the integration time. The slope of this plot provides the number of dark current electrons per pixel per second in ADU/pixel/s. Since the CCD images are captured using time delay integration, each line is integrated over the integration time of the line multiplied with the number of line shifts over the photosensitive area of the CCD camera. Figure 6.3A shows the mean signal plotted versus the integration time for the EMCCD camera used for the spatial and temporal fluctuation microscope instrument. According to this curve, the dark current is $\bar{I}_{DC} = 107 \text{ ADU/pixel/s} = 9.7 \text{ e}^-/\text{pixel/s}$. Using the pixel size of the camera and the charge of an electron, this value can be rewritten as $\bar{I}_{DC} = 2.84 \text{ pA/cm}^2$. Figure 6.3B shows the same curve as in figure 6.3A but for much smaller integration times. According to this curve, the dark current is $\bar{I}_{DC} = 670 \text{ ADU/pixel/s} = 61 \text{ e}^-/\text{pixel/s}$, or rewritten $\bar{I}_{DC} = 17.8 \text{ pA/cm}^2$. The difference between the values measured for different integration times originates from the construction of the CCD sensor as described in section 2.5.2. Small integration times imply fast shift frequencies in the photosensitive sensor of the camera. These fast charge movements along the sensor cause an additional noise source, which increases the dark current.

Readout noise is an electronic noise that originates from different electronic effects during conversion and transfer of the charges in each pixel well into pixel values on the frame grabber including the charge-to-voltage conversion. In order to measure the readout noise of a CCD, two similar dark image frames are captured using the smallest possible integration time to reduce dark current as described above. Subtraction of these two images from each other reduces the impact of pattern noise. The standard deviation of the mean pixel value of the subtracted image gives a value for the readout noise. This value is then divided by $\sqrt{2}$ because the standard deviation contains the readout noise of both images. The readout noise for the EMCCD camera SamBa SE-34 used for the STFM is $\bar{I}_{RON} = 10.3 \pm 0.3 \text{ ADU} = 0.94 \pm 0.03 \text{ e}^-$.

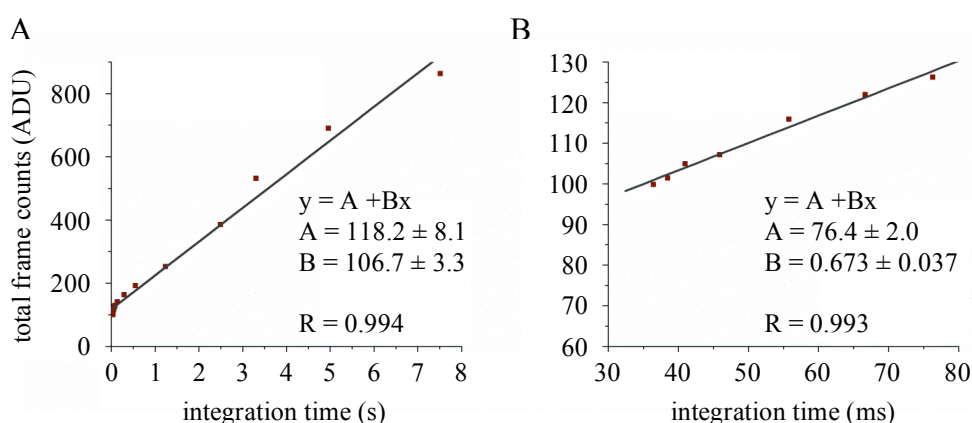


Figure 6.3. Two dark current curves for the EMCCD camera SamBa SE-34 from Sensovation used for the STFM. Plot (A) shows the dark current for large integration times, plot (B) shows the dark current noise for smaller integration times. The slope of the linear fit gives the dark current. For large integration times, the dark current is $\bar{I}_{DC} = 107 \text{ ADU/pixel/s} = 9.7 \text{ e}^-/\text{pixel/s}$. For smaller integration time, the dark current is $\bar{I}_{DC} = 0.67 \text{ ADU/pixel/ms} = 61 \text{ e}^-/\text{pixel/s}$. The values are measured using a 30x electron-multiplication gain.

6.1.1.4 Comparison of the line-scan versus area-scan EMCCD camera

The measured conversion factor, dark current and readout noise of the line-scan EMCCD camera are listed in table 6.1. The product specification values of the area-scan EMCCD camera SamBa SE-34 as provided by the manufacturer Sensovation are listed beside for comparison. The values for the conversion factor of the two implementations differ only faintly within the measurement error range and the values for the readout noise are also in agreement. The value for the dark current of the area-scan EMCCD lies between the two values measured for the line-scan EMCCD implementation, which on the other hand differ substantially by varying the integration time of the camera detection. The value of the integration time corresponding to the value of the dark current in the product specifications is unknown. Therefore, this value is not discussed further.

	line-scan EMCCD	area-scan EMCCD
conversion factor (e^-/ADU)	0.091 ± 0.01	0.086
dark current ($\mu A/cm^2$)	2.84 ± 0.01 (int. times > 0.4 s) 17.8 ± 0.5 (int. times < 80 ms)	9.6
Readout noise (e^-)	0.94 ± 0.03	< 1

Table 6.1. Comparison of the measured features of the line scan EMCCD with product specification values for the area-scan EMCCD Samba SE-34 from Sensovation. The values are measured using a 30x electron-multiplication gain.

6.1.2 Galvanometer scanner characterization

6.1.2.1 Galvanometer scanner noise

The position jitter of the galvanometer scanning mirror forms a considerable noise contribution to the signal acquired with the EMCCD camera (Fig. 6.4A). This jitter is induced mainly by the electric field of the EMCCD camera. In contrast, the noise contribution due to the mechanical vibrations of the ventilation system of the camera can be neglected. According to figure 6.4A, the jitter movements of the scanning mirror measured in volts due to the electric field of the camera amount to up to ± 15 mV, which corresponds to a translation in the probe of ± 700 nm. These additional movements are intolerable because they expand the width of the focal volume by roughly the same value. Shielding of the galvanometer scanner and decoupling it from the mechanical construction using rubber inserts reduced this noise to a feasible level of ± 1 mV (Fig. 6.4B), which corresponds to a translation of ± 50 nm in the probe. The undisturbed vibrations of the galvanometer scanner gave rise to a movement of ± 0.2 mV (Fig. 6.4C), which corresponds to ± 10 nm in the probe.

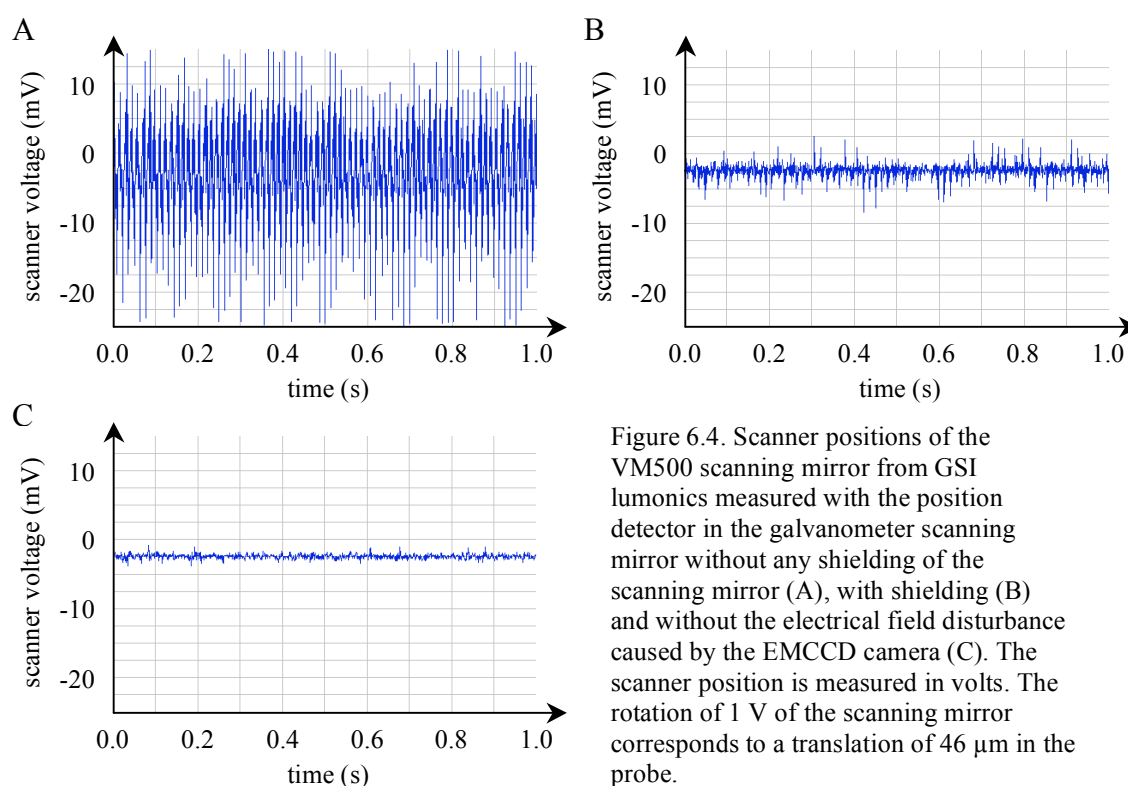


Figure 6.4. Scanner positions of the VM500 scanning mirror from GSI lumonics measured with the position detector in the galvanometer scanning mirror without any shielding of the scanning mirror (A), with shielding (B) and without the electrical field disturbance caused by the EMCCD camera (C). The scanner position is measured in volts. The rotation of 1 V of the scanning mirror corresponds to a translation of $46 \mu\text{m}$ in the probe.

6.1.2.2 Galvanometer scanner signal response

The response of the position of the galvanometer scanning mirror (red line) according to the position command transmitted by the data acquisition board (grey line) is displayed in figure 6.5A. At start up of the communication (I), the position of the scanning mirror, remains unaltered. After that, the scanning mirror needs an acceleration period (II) to reach the required velocity (III). This velocity is calculated to match the image rate of the camera. The time needed for starting is defined by the assigned maximal acceleration and velocity of the mirror. During the return (IV), the mirror slows down and accelerates to the velocity of the flyback (V). After one full cycle, the scanning mirror slows down and waits (VI) until the next cycle is started. The enlargement of the position signal of the scanning mirror (Fig. 6.5B) displays a small shift between the position command transmitted by the data acquisition board (grey line) and the response of the position of the Galvanometer scanning mirror (red line). The origin of this small difference is the delay due to the inertia of the rotating scanning mirror. This time shift is about 0.6 ms. For the measurement displayed, this corresponds at the linear part of the curve to a voltage difference of 8.6 mV, which corresponds to an image displacement of 390 nm in the probe. This displacement of the images depends on the scanning mirror velocity related to the image rate. It has to be taken into account for bi-directional imaging and for the positioning of the line for FCS measurement.

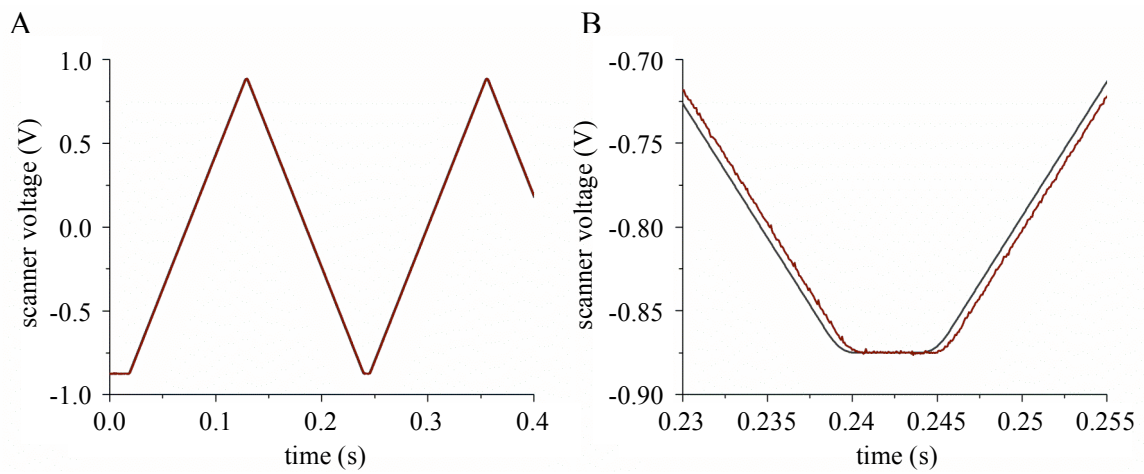


Figure 6.5. Scanner positions (A) transmitted by the data acquisition board NI PCI-6251 (grey) and the actual scanner position of the VM500 scanning mirror measured by the position detector in the galvanometer scanning mirror (red). The enlargement of the position signal of the galvanometer scanner (B) displays a small shift between the written and the read signal.

6.2 Imaging and mobility measurements of particles by STFM

In this section, the measurements with the spatial and temporal fluctuation microscope are described. First, the fast imaging features of the STFM were applied. Then, the size of the focal volume was determined by measuring fluorescent beads. PML nuclear bodies were traced over time in the nucleus of living cells. The performance of the microscope in terms of spatially resolved fluorescence correlation spectroscopy measurements was evaluated by line imaging of floating beads. The FCS measurements on quantum dots were conducted in comparison with the conventional FCS instrument. Finally, spatially resolved fluorescence correlation spectroscopy measurements of GFP in a cell were obtained.

6.2.1 STFM focal size measurement by imaging 100 nm beads

The size of the focal volume was determined with fluorescently labeled beads with a diameter of 100 nm (Duke Scientific, 5010A). These beads were fixed on a microscope slide and imaged at different z positions. The distance between the images in this z-stack was 112.5 nm and the pixel size in the xy-plane was 200 x 200 nm. Figure 6.6A displays such a xy-image with six imaged beads as indicated. For the determination of the focal size, those beads that were too close to each other were left out (see for example bead III in Fig. 6.6A). As expected the 100 nm beads were elongated in the y-direction and in the z-direction (Fig. 6.6B,C).

The imaged 100 nm beads were fitted using a three-dimensional Gaussian with variable width and variable position for each of the three dimensions. The bead diameter of 100 nm was subtracted to get the actual size of the focal volume. The histograms of the full widths at half maximum for each of the three focal dimensions are plotted in figure 3.7A-C. These histograms were again fitted with a Gaussian function. The results are summarized in table 6.2. Additionally, the values of the focus size for the conventional CLSM using an objective lens with the same numerical aperture, are listed (Pawley, 2006).

	STFM focus size	theoretical STFM focus size	STFM structure factor	CLSM focus size
x-axis (across line)	198 ± 4.7 nm	180 nm	$\kappa_x = 1$	200 nm
y-axis (along line)	382 ± 28 nm	270 nm	$\kappa_y = 1.93$	200 nm
z-axis (optical axis)	704 ± 23 nm	520 nm	$\kappa_z = 3.56$	500 nm

Table 6.2. Comparison of the determined focus size of the spatial and temporal fluctuation microscope with the theoretical values (Fig. 3.5) and the focus size of the confocal laser scanning microscope (Pawley, 2006). The structure factors of the STFM instrument describe the normalized three-dimensional shape of the focal volume, using the width in x-direction for normalization.

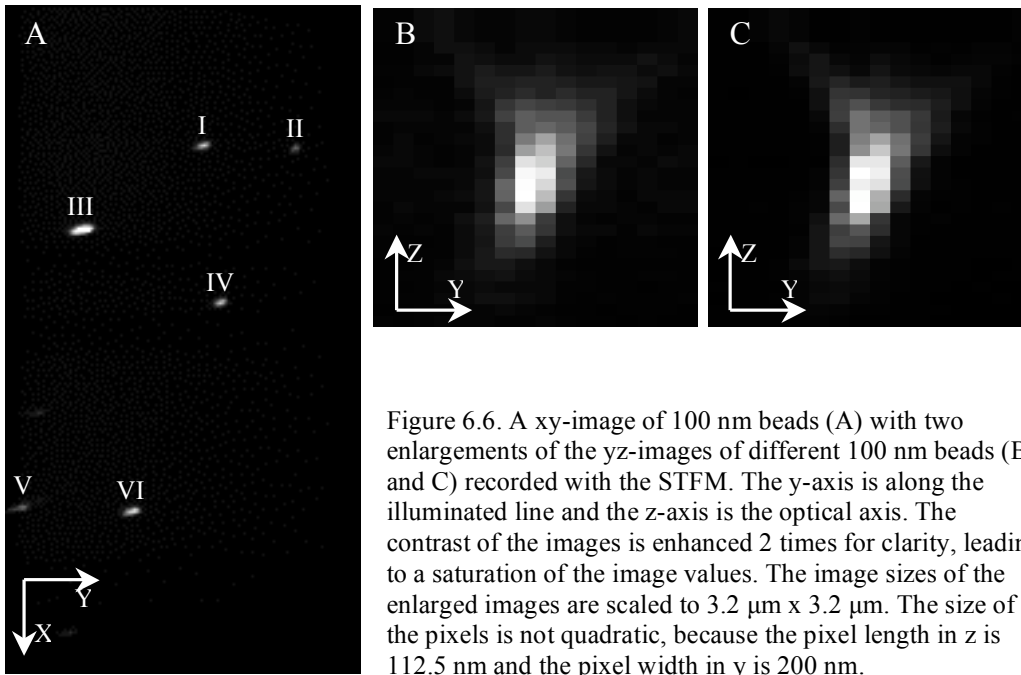


Figure 6.6. A xy-image of 100 nm beads (A) with two enlargements of the yz-images of different 100 nm beads (B and C) recorded with the STFM. The y-axis is along the illuminated line and the z-axis is the optical axis. The contrast of the images is enhanced 2 times for clarity, leading to a saturation of the image values. The image sizes of the enlarged images are scaled to $3.2 \mu\text{m} \times 3.2 \mu\text{m}$. The size of the pixels is not quadratic, because the pixel length in z is 112.5 nm and the pixel width in y is 200 nm.

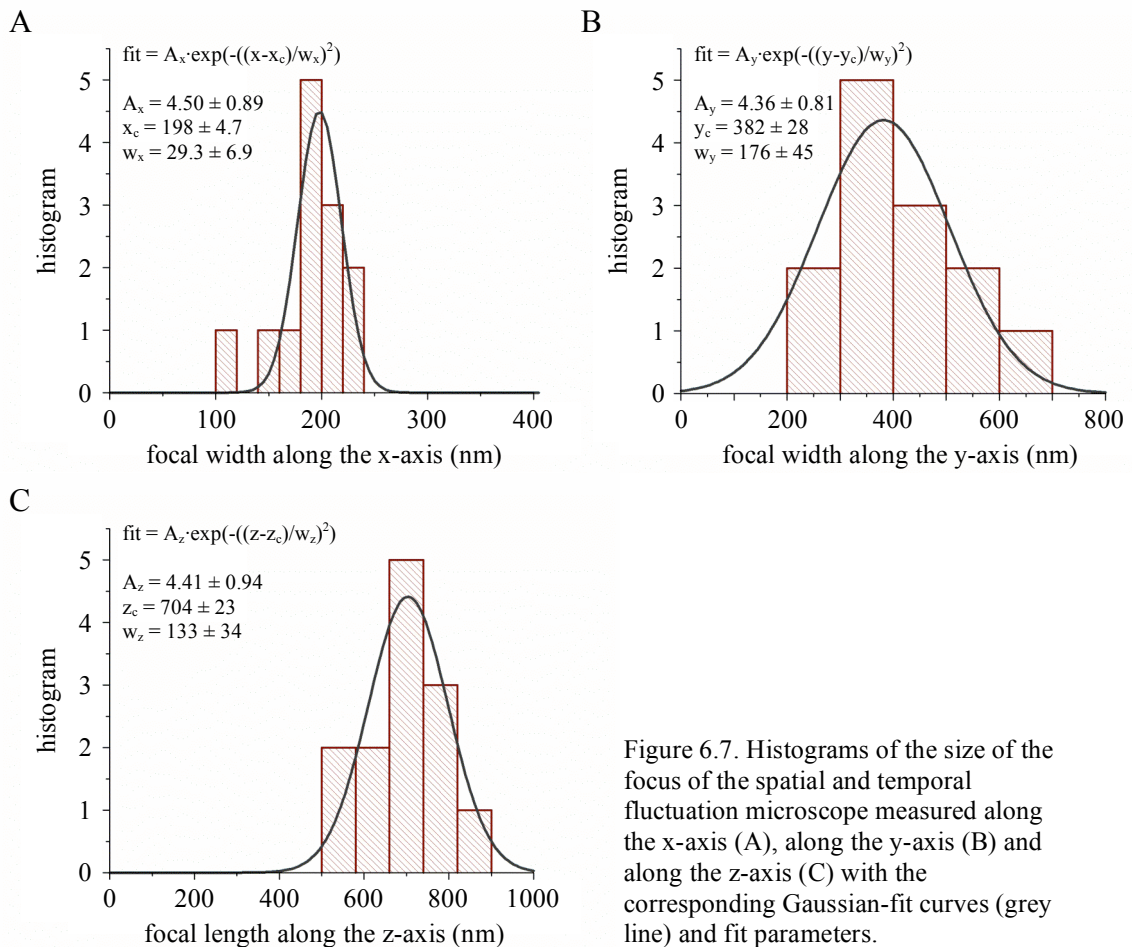
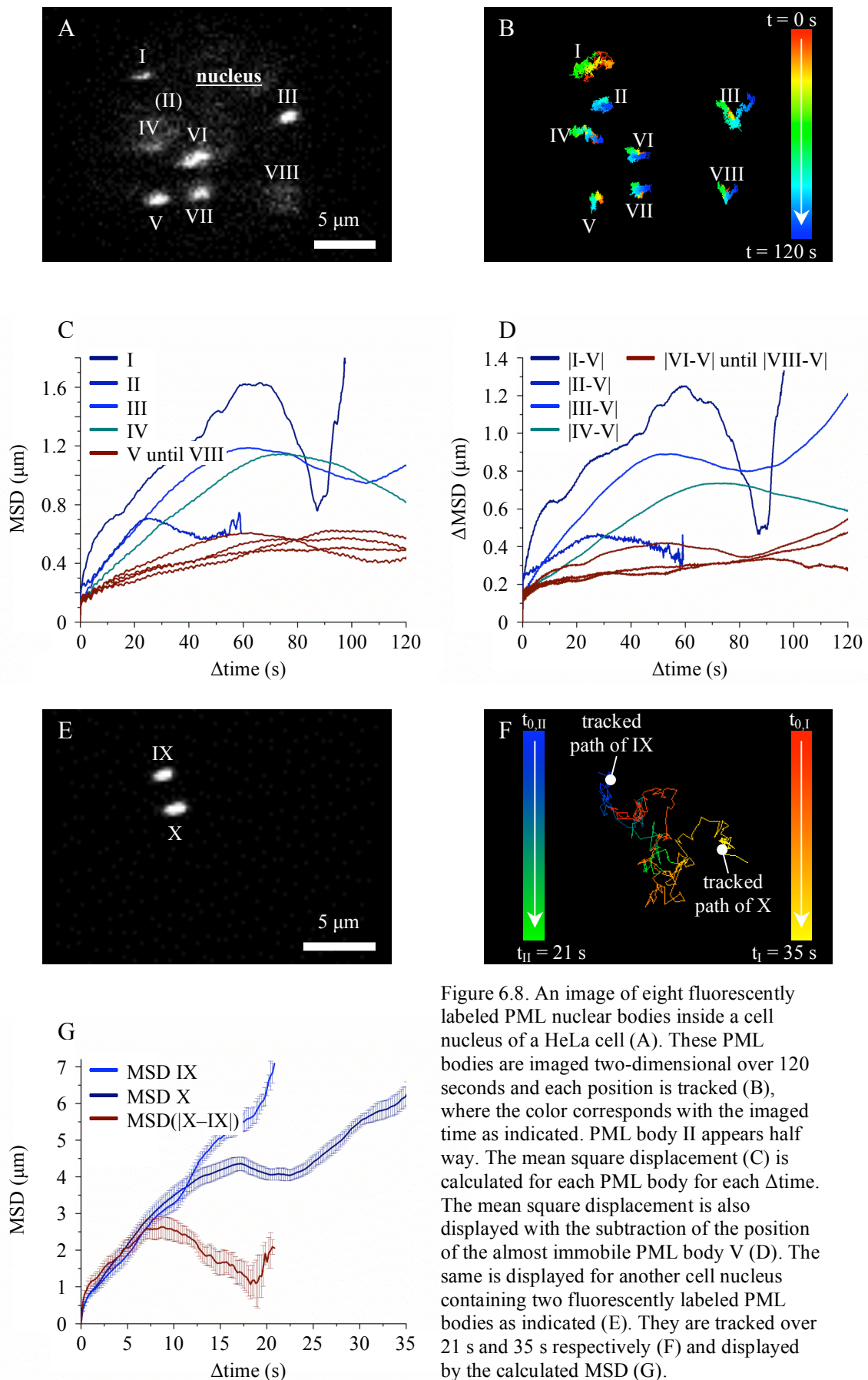


Figure 6.7. Histograms of the size of the focus of the spatial and temporal fluctuation microscope measured along the x-axis (A), along the y-axis (B) and along the z-axis (C) with the corresponding Gaussian-fit curves (grey line) and fit parameters.

In the x-direction, across the illumination line, the width of the focal volume was found to be about 200 nm. In the y-direction, along the illumination line, the width of the focal volume was elongated by a factor of 1.9 and in the z-direction by a factor of 3.6 compared to the x-direction. These focal size elongation values describe the structure factor for each direction. In the x-direction, the width of the focal volume was comparable to the width of the focal size of the conventional point-CLSM and slightly larger than the theoretical value (Fig. 3.5A). In the y- and z-direction, the width and length of the focal volume was elongated compared to the size of the focal volume of the point-CLSM. These elongations are caused by illuminating a line rather than a point. These values differ considerably from the calculated values of 270 nm and 520 nm, respectively. These differences can be explained as follows. For the calculation of the theoretical values, the lateral and axial contributions to the illumination amplitude distribution are assumed independent of each other. For a point illumination system, this is an appropriate assumption. For a line illumination system, this lateral-axial independence assumption is apparently no longer valid. The second reason for the difference between the calculated and the experimental focal sizes are caused by small rotational mismatches of the cylindrical lenses, the slit and the detector. The beam path of the STFM is no longer rotational symmetric as is the case for the conventional CLSM. Due to this asymmetry of the beam path, small rotational shifts of the cylindrical lenses and slit effects the point spread function. The point spread function is slightly skewed as displayed in figure 6.6A for the xy-dependence and in figure 6.6B,C for the yz-dependence.

6.2.2 Fast STFM imaging of mobile PML nuclear bodies

Many activities of the nucleus are concentrated in mobile subnuclear structures called nuclear bodies, which include PML (promyelocytic leukaemia) nuclear bodies (Görisch et al., 2005; Görisch et al., 2004; Jegou et al., 2008; Lamond and Sleeman, 2003). PML bodies are shown to be involved in different processes such as apoptosis, senescence, cell proliferation, chromatin remodeling, DNA damage repair, transcription or telomere lengthening. PML nuclear bodies are mobile structures in the nucleus. Being a highly mobile structure inside the cell nucleus, this type of nuclear bodies was used for the characterization of the fast imaging feature of the STFM. The displayed cells were based on the HeLa cancer cell line. Figure 6.8 displays two measurements of fluorescently labeled nuclear bodies, one with eight (Fig. 6.8A) and the other one with two nuclear bodies (Fig. 6.8E). The displayed time series of two-dimensional images were acquired with a frame rate of 5.1 images per second. Each nuclear body was tracked over time as displayed in the color-coded trajectory plots (Fig. 6.8B and Fig. 6.8F). As body no. II appears in the focal plane and the nuclear bodies no. I and no. V leave the focal plane during the measurement, their trajectory plots stop and start during the measurement. According to these plots, the positions of nuclear bodies IX and X were highly mobile, nuclear bodies I, II, III and IV display moderate mobility and nuclear bodies V, VI, VII and VIII were almost immobilized. The mean squared displacement (MSD) was calculated for each PML body (Fig. 6.8C and Fig. 6.8G) over the imaged time. These MSD curves were calculated for each available displacement time and averaged according to



$$\text{MSD}(m) = \sum_{n=m}^N \sqrt{(x_n - x_{n-m})^2 + (y_n - y_{n-m})^2} \quad (6.2)$$

In this equation, N is the total number of images, (x_n, y_n) the tracked position of the nuclear body of image n and m is the amount of integration times between the two images, which stands for the displacement time (Δtime) between the two images. The curves of figure 6.8C show a clear distinction between the immobile (red) and mobile structures (blue). Unfortunately, the curve displays minute fluctuations of the MSD curve most visible for the immobile structure curves. The magnitude of these fluctuations is about 200 nm, which is the size imaged by one pixel. Alternatively, the mean squared distance displacement was calculated according to (Jegou et al., 2008)

$$\Delta\text{MSD}(m) = \sum_{n>m}^N \sqrt{(d_n - d_{n-m})^2} \quad (6.3)$$

with N the total number of images and d_n the distance between the tracked position of the nuclear body and the position of nuclear body V of the image n and m , which stands for the amount of integration times between the two images. Figure 6.8D displays the ΔMSD curves of the bodies and for the second measurement, this ΔMSD curve is displayed in the same figure as the MSD curves (Fig. 6.8G). Since the minute fluctuations have disappeared for these curves, these fluctuations must be assigned to an inaccuracy of the synchronization between the camera and the scanning mirror. The synchronization takes place by the RTSI bus interface, which assures an accurate synchronization of both instruments within a range far below the measured fluctuations. However, each cycle of scanning mirror angle positions is transmitted to the data acquisition board after a change of the trigger signal, which requires a task of the computer between the trigger signal and the start of the scanning mirror. The speed of computer processes is dependent of the number of task. This will add an uncertainty to the synchronization of the camera and the scanning mirror. This can be solved using the buffer of the MiniSAX transmitting the angle positions for the next cycle during the current cycle and not after the transmission process.

Comparing the MSD curves with the ΔMSD curve for PML nuclear bodies IX and X, one can say that each body moved fast through the nucleus resulting in a large MSD value. However, the distance between them is more or less constant and represented by a relative low value for ΔMSD . An additional advantage of these ΔMSD curves is the elimination of the movements of the whole cell nucleus, which for the MSD measurements normally must be taken into account for imaging times in the range of minutes (Jegou et al., 2008).

6.2.3 Tracking 100 nm beads with the STFM

In order to visualize the function of the FCS feature of the STFM, an illuminated line was positioned in a solution containing fluorescently labeled 100 nm beads. The illuminated line was detected with a line rate of 380 lines/s for a total of 13 seconds as displayed in five xt-images (Fig. 6.9). This is rather slow for the line-scan detector

used and an image width of 128 pixels (Fig. 6.1). Nevertheless, the experiment is an instructive demonstration for the fluorescence correlation spectroscopy measurements along a line. As the fluorescently labeled beads enter the focal line illumination volume, they give rise to a signal along the line on the line-scan detector. The measured intensity depends on the position in the focus. The particles spend a certain time in the illumination volume corresponding to the length of the trajectory curve along the time axis. While dwelling in the line illumination volume, the particle moved along the line corresponding to the width of the movement trajectory along the y-axis. These widths of the trajectories are for almost all imaged particles within 25 pixels, which correspond to 5 μm .

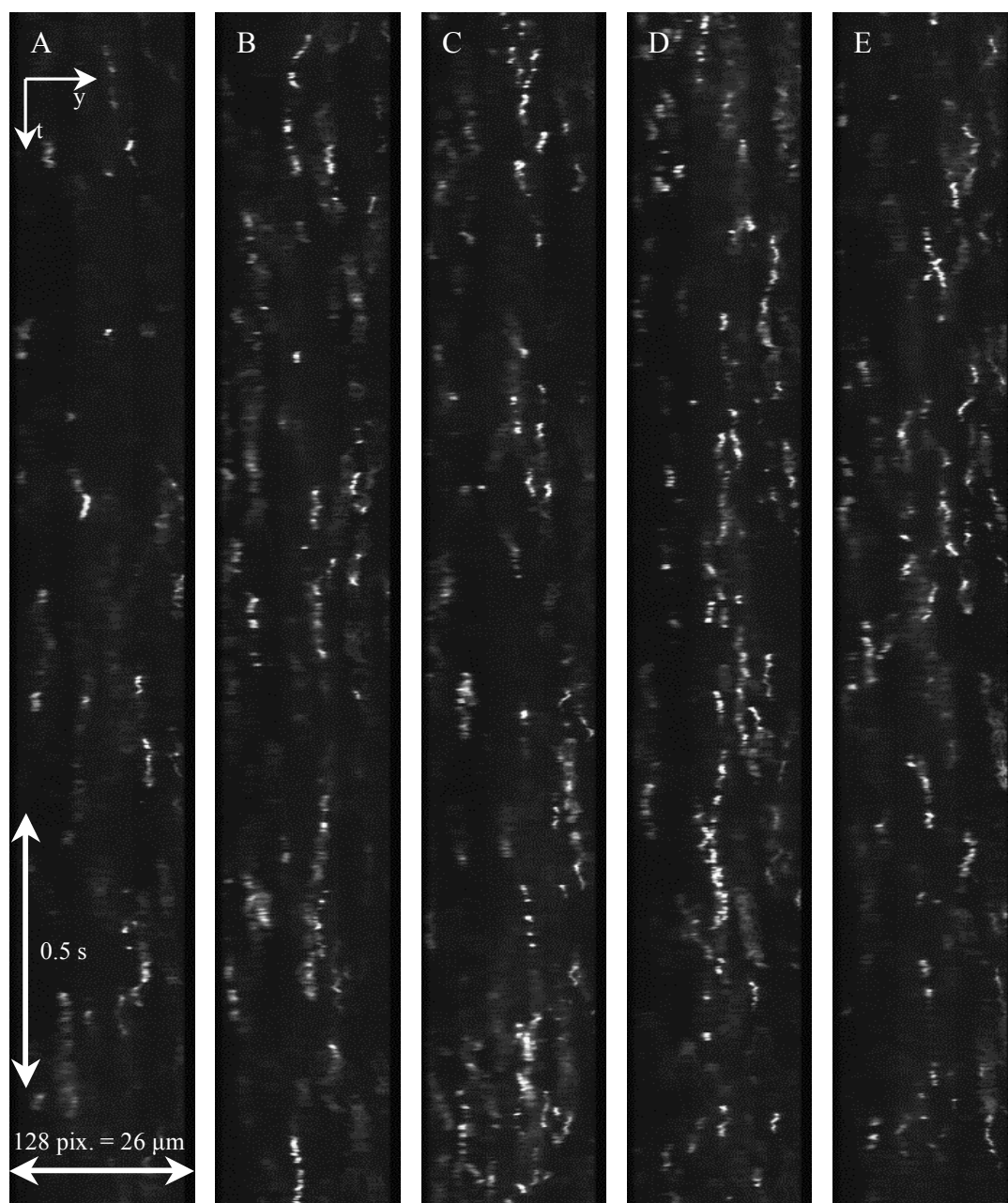


Figure 6.9. Position-time images of fluorescently labeled 100 nm beads floating freely through an illuminated and detected line in the probe. The time resolution is 380 lines/s.

This measurement illustrates the principle of the spatially and temporally resolved FCS capability of the STFM. The only differences between this measurement and the one described in the following section are the size of the imaged particles and the integration time. Large particles imply much more fluorescence signal per particle, as is the case for smaller particles. The integration time used for the measurement was 0.53 ms for imaging of 100 nm beads. In contrast, the integration time used for STFM measurements of much smaller macromolecules is defined by the maximum image rate of the camera and can be as small as 15 μ s.

STFM experiments measure the mean dwell time a particle spends in the focal volume. However, the fast line-imaging rate implies small integration times. Hence, the signal is rather low, often in the range of the noise of the detector. To determine the mean dwell time in this case, the intensity signal is autocorrelated as described in section 2.1.3. This autocorrelation can extract the mean dwell time a particle spends in the focal volume even in the presence of detector noise and other noise sources as these do not correlate over time (Fig. 6.9).

6.2.4 STFM and conventional FCS measurements of quantum dots

For the characterization of the fluorescence correlation spectroscopy feature of the STFM instrument, the developed instrument was compared with a conventional point-FCS instrument Leica SP2 FCS2 (Leica Microsystems, Mannheim, Germany). For these measurements the green-fluorescent quantum dots Qdot525 streptavidin conjugate (Invitrogen) were used. The core diameter of quantum dots ranging from 1.5 nm–6 nm. Due to their extreme brightness and photostability, they are very suitable for FCS measurements (Gomez et al., 2006; Heuff et al., 2007). However, blinking, which is observed for many types of single emitters, is a fundamental photophysical property of quantum dots. In order to get rid of this blinking, an additional blinking term was introduced for the autocorrelation fit function (Heuff et al., 2007). The intensity signal was measured over 60 seconds for both instruments. The FCS measurements with the conventional instrument were performed with a detection rate of 1 MHz. For the measurements using the STFM instrument, a detection rate of 38.9 kHz was used, which is the maximum detection rate of the line-scan camera when using 128 pixels of the line. The autocorrelation $G(\tau)$ of the measured intensity signals was calculated according to equation 2.1 for both the STFM instrument (Fig. 6.10A) and for the conventional FCS instrument (Fig. 6.10B). For the STFM instrument the autocorrelation was calculated using the ten pixels from pixel number 55 to pixel number 64 in the middle of the line-scan detector displayed by $G_{p55}(\tau)$ to $G_{p64}(\tau)$. The ten autocorrelation curves of the conventional FCS instrument were acquired successively. These curves were fitted using equation 3.17, with the structure parameters for both instruments as listed in table 6.3. Parameter w_x is the radius of the focus in the x-direction. The sizes of the focus in y- and z-direction are defined by this size and the corresponding structure parameter. For the point FCS setup, the lateral focus radius w_x was found to be 170 ± 9 nm by measuring the diffusion coefficient of a well-defined solution (K. Mueller), whereas for the STFM setup, the obtained value was 300.3 ± 2 nm using a different approach, see next section.

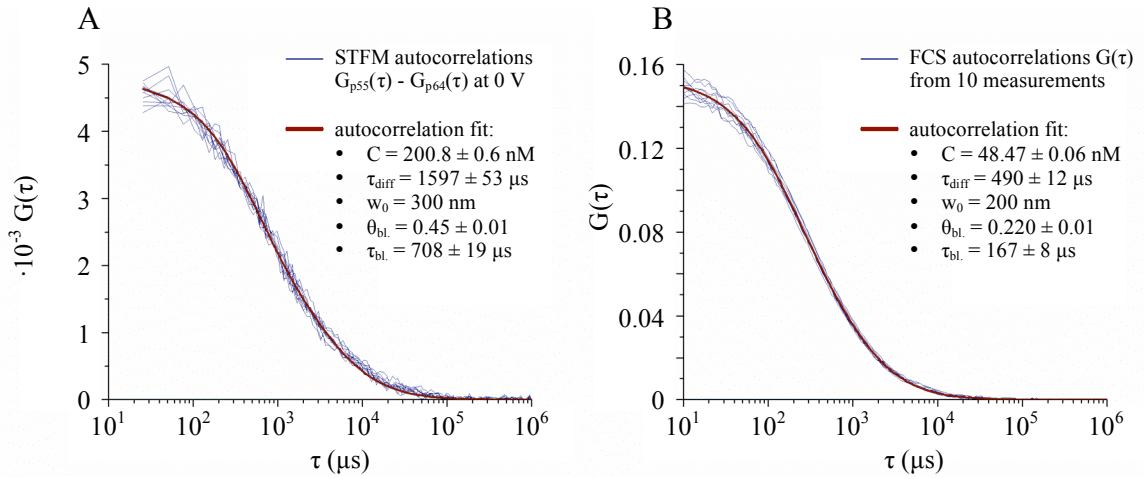


Figure 6.10. Comparison of the autocorrelation measurements acquired by the STFM instrument with that acquired by the conventional point-FCS instrument (Leica SP2 FCS2). The measurements were made with the quantum dots Qdot525 streptavidin conjugate. The STFM autocorrelation curve was obtained from the pixels 55 – 64 of the line-scan detector represented by $G_{p55}(\tau) - G_{p64}(\tau)$. The conventional FCS measurements were acquired successively in time.

	STFM	FCS	literature value
structure factors, $\kappa_x, \kappa_y, \kappa_z$	1; 1.93; 3.56	1; 1; 4.6	--
structure factors, A_{1sl} and γ_{1sl}	0.0175; 354	0; 0	--
concentration, c (nM)	200.8 ± 0.6	48.47 ± 0.06	1.38
diffusion time, $\tau_{diff} = w_x^2/4D_0$ (μ s)	1597 ± 53	490 ± 12	--
lateral focus radius, w_x (nm)	300.3 ± 0.2	170 ± 9	--
blinking factor, $\theta_{bl.}$	0.45 ± 0.01	0.220 ± 0.01	--
blinking time, $\tau_{bl.}$ (μ s)	708 ± 19	167 ± 8	--
diffusion coefficient, D_0 (μ m ² /s)	14.12 ± 0.02	14.74 ± 0.5	9.02

Table 6.3. Comparison of the STFM with the conventional FCS (Leica FCS2) and with a literature value (Swift et al., 2006) measured for the quantum dots Qdot525 streptavidin conjugate. The structure factors and lateral focus radius for the conventional FCS were measured by K. Müller.

The correction for fluorescence molecules that had been transferred to the triplet state as described by equation 3.18 was applied to the fit of both measurements. The measurements are fitted with the following degrees of freedom: the concentration c , the diffusion time τ_{diff} , the blinking time $\tau_{bl.}$ and the blinking factor $\theta_{bl.}$. The results and the resulting value for the diffusion coefficient D_0 are displayed in table 6.3. The diffusion coefficient is inversely proportional to the lateral focus radius w_x , which is assigned as a constant. Hence, the difference between its value to that reported in the

literature (Swift et al., 2006) provides an estimate for the correctness of the lateral focus radius, although the diffusion coefficient differ slightly with the concentration (Swift et al., 2006). Accordingly, the diffusion coefficient measured by both the point FCS and the STFM measurement differ slightly among each other and are quite close to the literature value, which is measured at a different concentration.

6.2.5 STFM focal size symmetry measurements

The size of the focal detection volume, as defined by the point spread function of the instrument depends slightly on the position in the probe as described in this section. Since the autocorrelation is considerably dependent on the size of the focus (see above), FCS was applied to this issue. The autocorrelation function $G(\tau)$ is calculated for the measured intensities at the four representative positions of the field of view (Fig. 6.11A-D) as indicated in the schematic probe image (Fig. 6.11E). For each of the four positions, the intensity of ten neighboring pixels was acquired and autocorrelated. The measurements were conducted again with the green-fluorescent quantum dots Qdot525 streptavidin conjugate. The intensity signal was measured over 60 seconds at a detection rate of 38.9 kHz.

The fit of the autocorrelation curves of the data acquired in the middle of the image (Fig. 6.11A) were used to determine the concentration of the probe c , its diffusion time τ_{diff} , the blinking time τ_{bl} and the blinking factor θ_{bl} as displayed. These parameters were assumed independent of the measured position in the probe. The lateral focus radius w_x for this fit curve was assigned to 300 nm, which was determined by the approach described in the next section. For the fit-curve of the autocorrelations of the measurements at the other extreme positions in the probe, this focus radius was used as the only degree of freedom assuming that the proportions of the focal volume, defined by the structure factors, were independent of the measured position in the probe. The resulting lateral focus radius w_x was normalized and plotted versus the pixel position at the line detector (Fig. 6.11F) for the line imaged in the middle of the probe ($x = 0 \mu\text{m}$) and for the line imaged at the extreme position of the image size ($x = 139 \mu\text{m}$). The size of the focal detection volume depended slightly on the position in the probe. At the edges of the imaged line, about 10 μm from the centre, the focus size was enlarged by a factor of 1.15 with regard to the size of the focus in the middle of the probe. For a vertical displacement of the line imaged over a distance of 139 μm from the middle, the focus size is enlarged by a factor of 1.1 and at the corner of the image by a factor of 1.5.

Accordingly, the lateral focus size w_x was dependent much more on displacements along the y-axis, i.e. the directly imaged direction along the focus line, as is the case for displacements along the x-axis, the scanned direction perpendicular to the line. Nevertheless, the size of the focus can be assumed to be constant (within 5%) over about 80 pixels around the center of the line. Only at the boundaries, the focus size was increased, most likely due to deviations from ideal imaging properties at the periphery of the optical elements in the detection path.

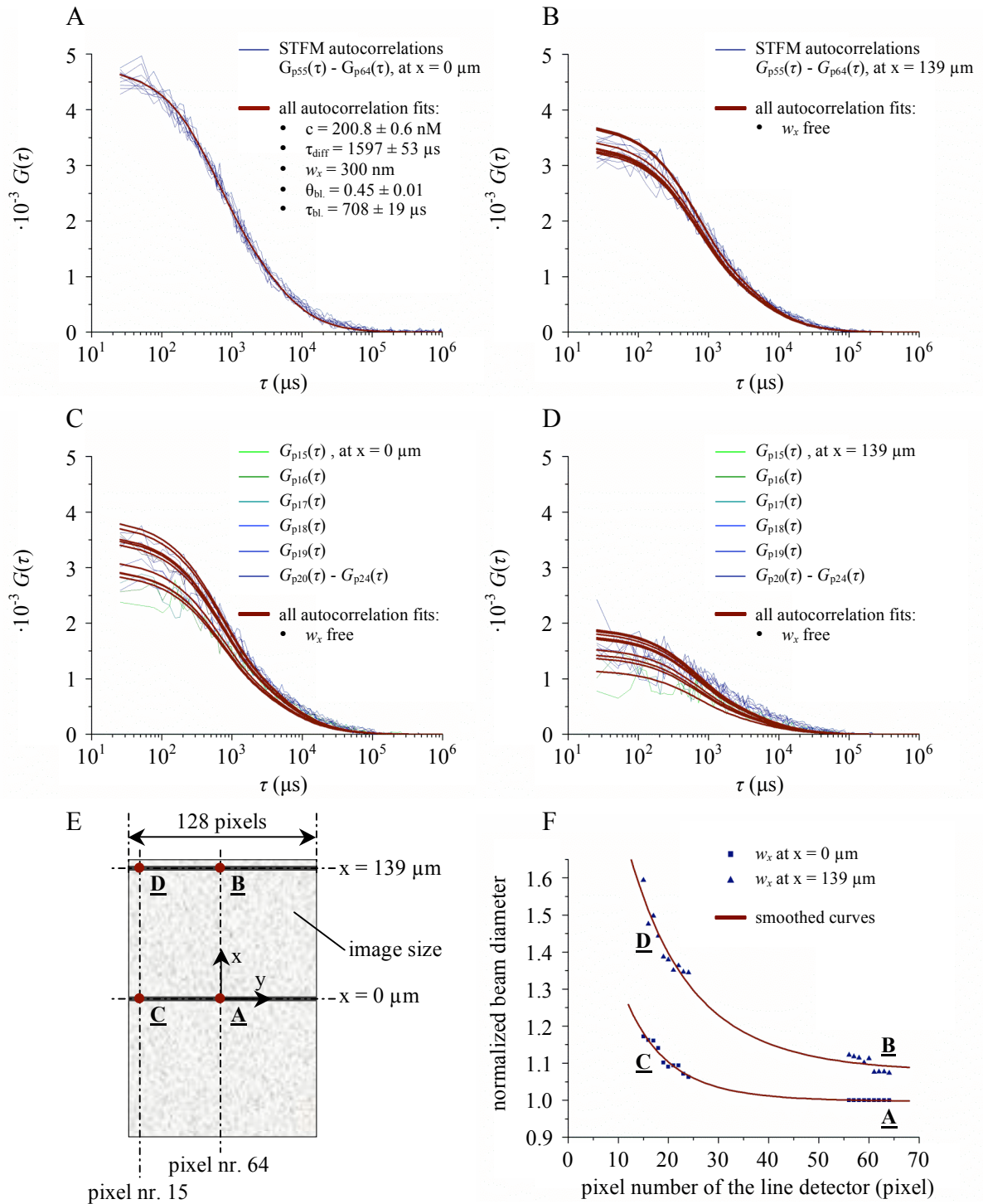


Figure 6.11. Autocorrelation functions and their corresponding fit functions of quantum dots Qdot525 streptavidin conjugate measured with the STFM at different positions in the probe: (A) Measurements for pixels in the middle of the imaged line at the optical axis, (B) At the middle of the detected line but with the line imaged at the extreme position of the image size at $x = 139 \mu\text{m}$. (C) Measurements for pixels at the edge of the imaged line with the line imaged in the middle of the probe at position at $x = 0 \mu\text{m}$. (D) Measurements for pixels at the edge of the imaged line with the line imaged at the extreme position of the image size at $x = 139 \mu\text{m}$ as indicated in the schematic image (E). The resulting lateral beam diameters are normalized to that in the middle of the probe and summarized in a plot (F). The red curves are smoothed curves.

6.2.6 Cross-correlation measurements of neighboring pixels of the STFM

For the autocorrelation form of the fit function according to equation 3.17, the distances are $d_x = d_y = d_z = 0$. Hence, the amplitude of the fit-function is determined by the concentration of the probe c and the effective focal volume V_{eff} , whose size is defined by the lateral focus radius w_x . Both parameters depend inversely on the amplitude of the fit-function, which implies that only one of them can be fitted whereas the other must be assigned as a constant value. For the autocorrelation experiments described above, the lateral focus radius was assumed constant at 300 nm. As indicated above, this lateral focus radius is determined in this section.

For the cross-correlation form of the fit function according to equation 3.17, the distance between the foci corresponding to two different pixels along the line is given by $d_y \neq 0$. Hence, the exponential part of equation 3.17 cannot be neglected. This exponential part is the third component that determines the amplitude of the cross-correlation fit function by the following parameters: the distance between the foci d_y , the lateral focus radius and the diffusion time τ_{diff} . Since the measurements were made with the green-fluorescent quantum dots Qdot525 streptavidin conjugate, movements of the quantum dots more than 200 nm apart can be assumed to be independent. Therefore, the cross-correlations of the intensity signals of the foci corresponding to two pixels along the line originate only from the spatial cross talk between these foci and not from correlated movements of particles in these foci. Cross-correlation functions between the intensity signals of several consecutive pixels along the imaged line depend largely on the size of the focus (Eq. 3.17), which makes it a very well suitable alternative method to determine the lateral focus radius.

The intensity signal of four consecutive pixels along the imaged line was acquired for 60 s. This was done for each of the four representative positions (Fig. 6.12E). The auto- and cross-correlation curves of the intensity measurements in the middle of the image size (Fig. 6.11A) were used to determine the concentration of the probe c , its diffusion time τ_{diff} , the blinking time τ_{bl} , and the blinking factor θ_{bl} , as displayed. These parameters were then fixed and used to determine the lateral focus radius from the pixel-distance dependence of the cross-correlation amplitudes as described in Eq. 3.17 at the extreme positions for the field of view (Fig. 6.12 E). According to figure 6.12, the cross-correlation fit leads to a lateral focus radius w_x of 300 nm in the center of the field view and shows some position dependence over the field of view. The movements of quantum dots more than one pixel size apart were assumed independent, which implies that the cross-correlations of the intensity signals of the foci corresponding to two pixels along the line originate only from the cross talk between them and not from correlated movements of the particles in these foci. For the STFM measurement of particle movements in complex structures, directed movements along the line will provide an additional contribution to cross-correlation, which contains information about this complex structure. To measure this additional contribution, the cross-correlation due to cross-talk measurements of distanced must be subtracted according to the distance between the measured foci. This cross-talk contribution is plotted in figure 6.12F for the quantum dots measurements.

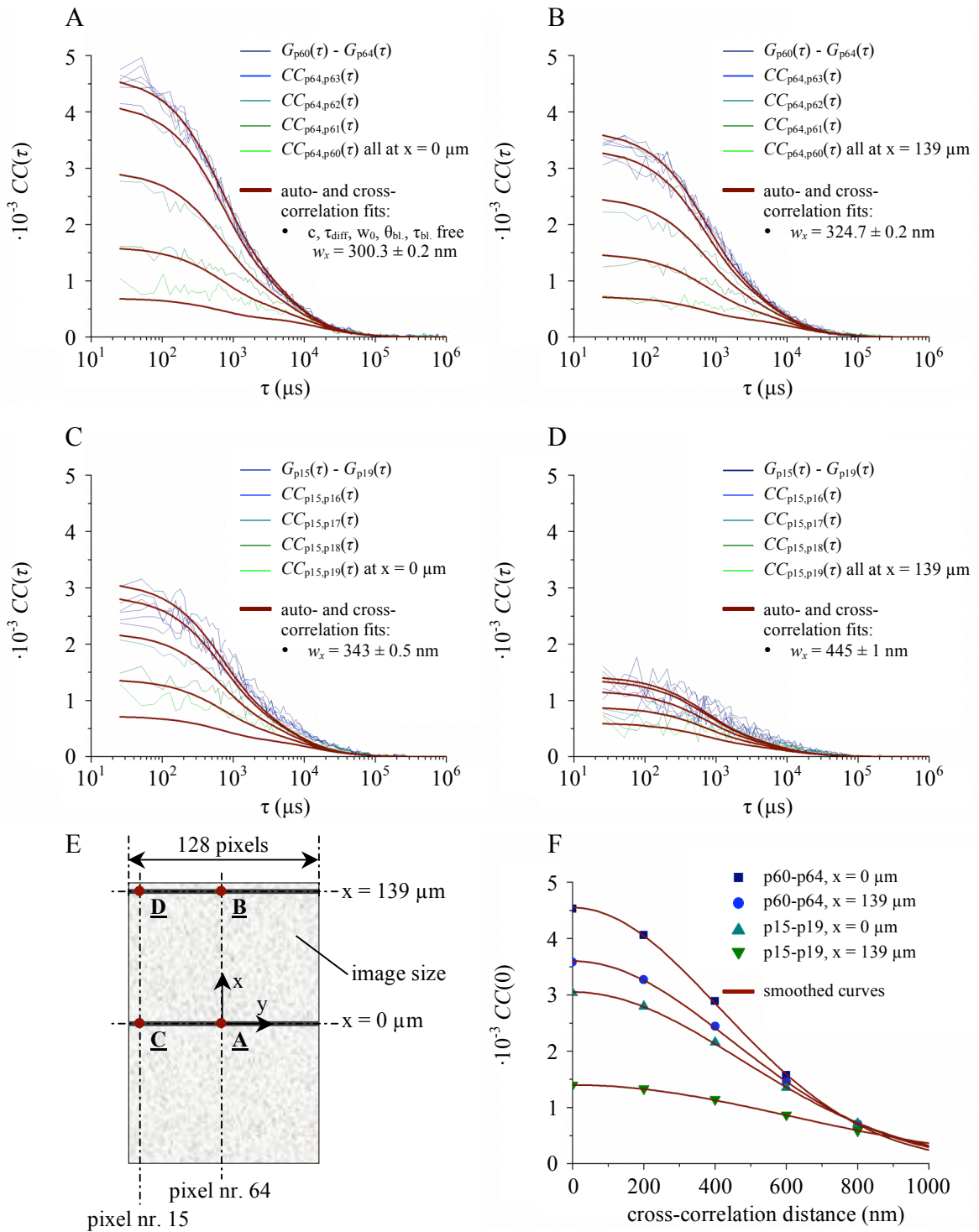


Figure 6.12. Auto- and cross-correlation functions and their corresponding fit functions of quantum dots Qdot525 streptavidin conjugate measured with the STFM at different positions in the probe: (A) Measurements for pixels in the middle of the imaged line at the optical axis and (B) at the middle of the line for a line imaged at the extreme position of the image size at $x = 139 \mu\text{m}$. (C) Measurements for pixels at the edge of the imaged line with the line imaged in the middle of the probe at position at $x = 0 \mu\text{m}$ and (D) for pixels at the edge of the imaged line with the line imaged at the extreme position of the image size at $x = 139 \mu\text{m}$ as indicated in the schematic image (E). The resulting amplitudes of the cross-correlation fit function $CC(0)$ are summarized in a plot as a function of the distance between the foci of the cross-correlated intensity signals (F). The red curves are smoothed curves.

6.3 In vivo measurements of GFP-expressing cells by FCS and STFM

For the analysis of fast dynamic processes of the green fluorescent protein (GFP) and its enhanced version, EGFP, FCS is a well-suited method. These proteins are genetically attached to the protein of interest. Therefore, they provide a convenient way to label proteins in living cells. However, they can display more or less distinct spontaneous reversibility of photobleaching or blinking (Wachsmuth and Weissart, 2007). GFP is a relatively small protein and is uniformly distributed throughout the nucleus without any apparent interactions with nuclear structures. FCS experiments on monomeric EGFP in living cells showed that diffusion of EGFP depends on their localization in the cell e.g. in the nucleus or in the cytoplasm (Beaudouin et al., 2006; Berland et al., 1995; Pack et al., 2006; Wachsmuth et al., 2000). Accordingly, an averaged diffusion coefficient of $81 \mu\text{m}^2/\text{s}$ in water at 25°C with a viscosity of 0.89 mPa s was determined. The difference to the value of $D_0 = 23 \mu\text{m}^2/\text{s}$ measured in the cell can be assigned to an apparent 3.5 fold higher viscosity of the cellular environment (Wachsmuth et al., 2008).

To demonstrate the capabilities of the STFM for characterizing in vivo the dynamics of cellular processes simultaneously at a series of positions along a line, the instrument was applied by acquiring concentration fluctuations of the GFP in living cells. The fluorescence correlation spectroscopy experiments conducted with the STFM were compared to single point-FCS measurements with a Leica confocal microscope (Leica SP2 FCS2). Hence, several conventional point-FCS measurements on GFP-expressing cells were carried out to study the variations of the apparent diffusion coefficient inside the cells displayed here for two different examples (Fig. 6.13). The displayed cells were based on the HeLa cancer cell line. These measurements show large variations of the apparent diffusion coefficients measured in different cells. Furthermore, the measured diffusion coefficients vary between those measured inside the cell nucleus and those measured in the cytoplasm (Fig. 6.13A,B) and even measurements inside the same nucleus show large variations (Fig. 6.13F).

Accordingly, it would be interesting to obtain spatially resolved image profiles of these diffusion coefficients measured along a line through the whole cell. This experiment is realized using the same GFP-expressing HeLa cells measured with the STFM displayed here for two different examples (Fig. 6.14 and Fig. 6.15). The intensity signals are measured along the indicated lines (Fig. 6.14A and Fig. 6.15A). The intensity profiles along both lines and their corresponding profiles of the apparent diffusion coefficients are displayed in figure 6.14B,C and figure 6.15B,C respectively. These profiles of the diffusion coefficients results from the diffusion times τ_{diff} determined from the autocorrelations of the measured intensity profile over a period of 90 seconds calculated for each pixel along the line. Eight of these autocorrelation functions corresponding to the eight indicated positions along both lines are displayed here (Fig. 6.14D,E and Fig. 6.15D,E). For the first ~ 40 pixels of the first measurement, the signal was too low and too noisy to yield a reasonable correlation function.

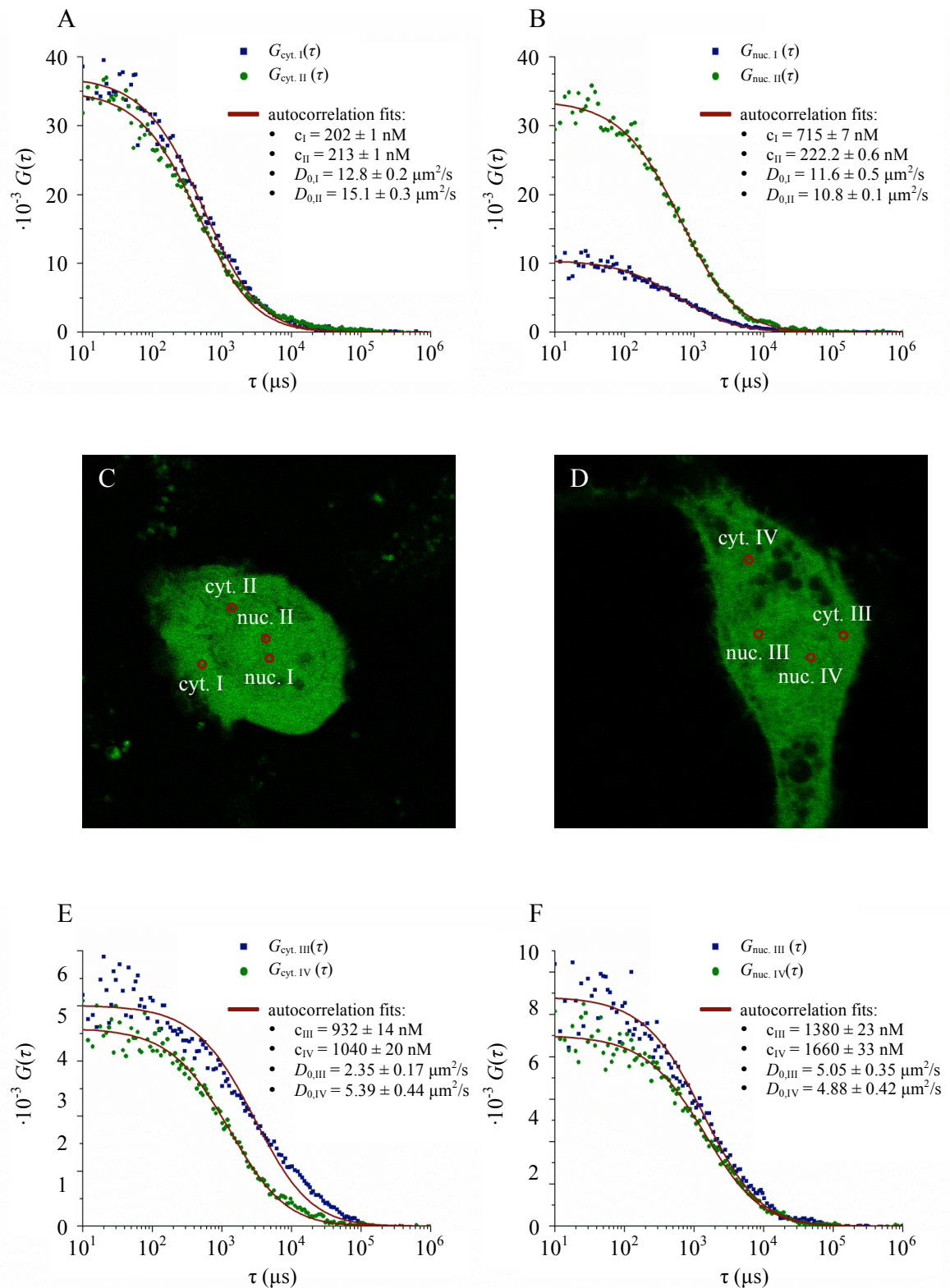


Figure 6.13. Autocorrelation functions and their corresponding fit functions of GFP in HeLa cells measured with the conventional FCS system at different positions in the cells as indicated. The autocorrelation function was calculated for intensity measurements inside the cytoplasm (A) and in the nucleus (B) both for cell I (C) and for cell II (D) in the cytoplasm (E) and in the nucleus (F). The position of the cell nuclei are localized by the bright-field imaging not displayed here.

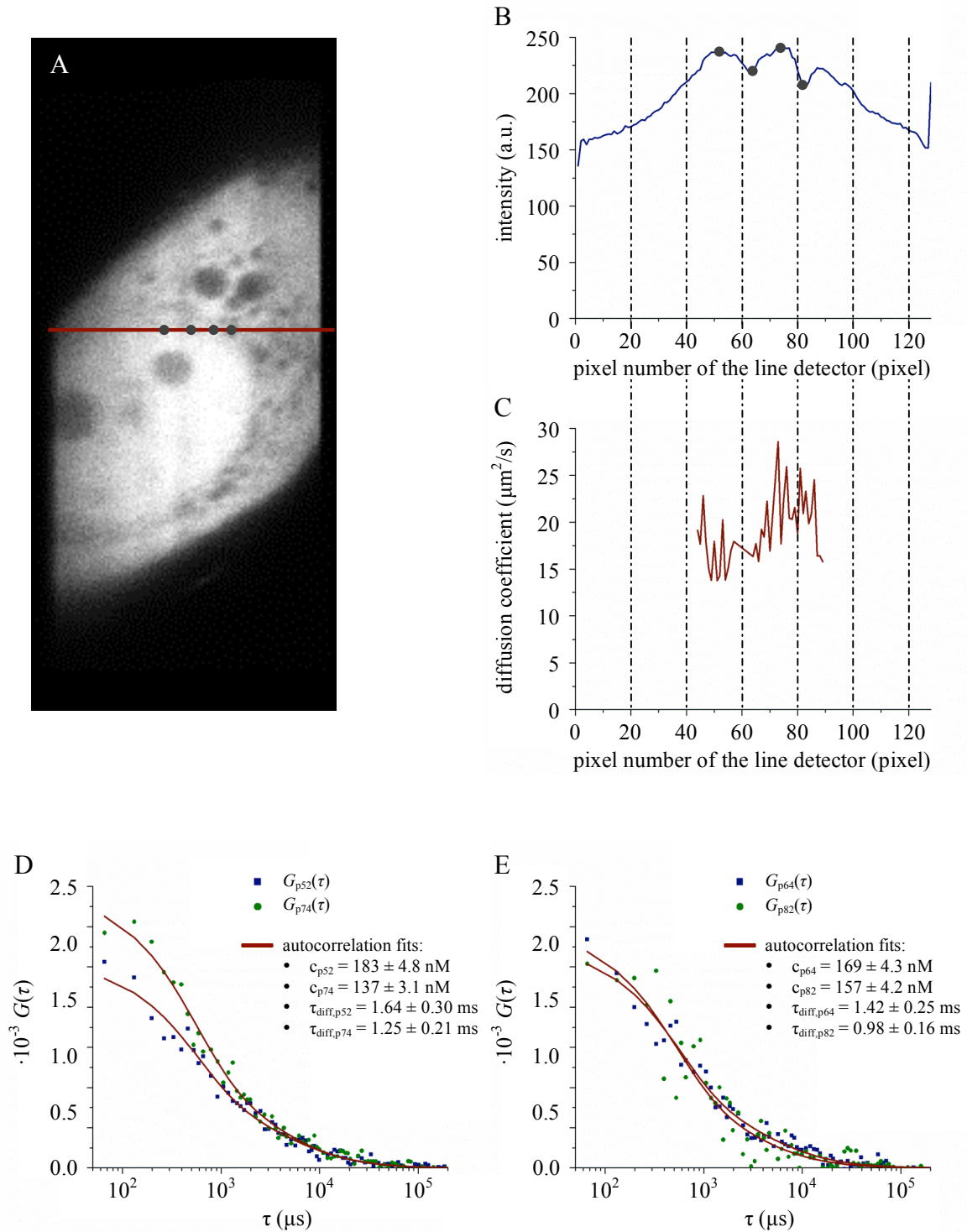


Figure 6.14. An image of a GFP labeled HeLa-cell (A) with the intensity distribution along the indicated line (B) and the corresponding diffusion coefficient (C) determined by autocorrelation of the measured intensity profile over time displayed for pixel number 52 and 74 (D) and for pixel number 64 and 82 (E) measured with the STFM.

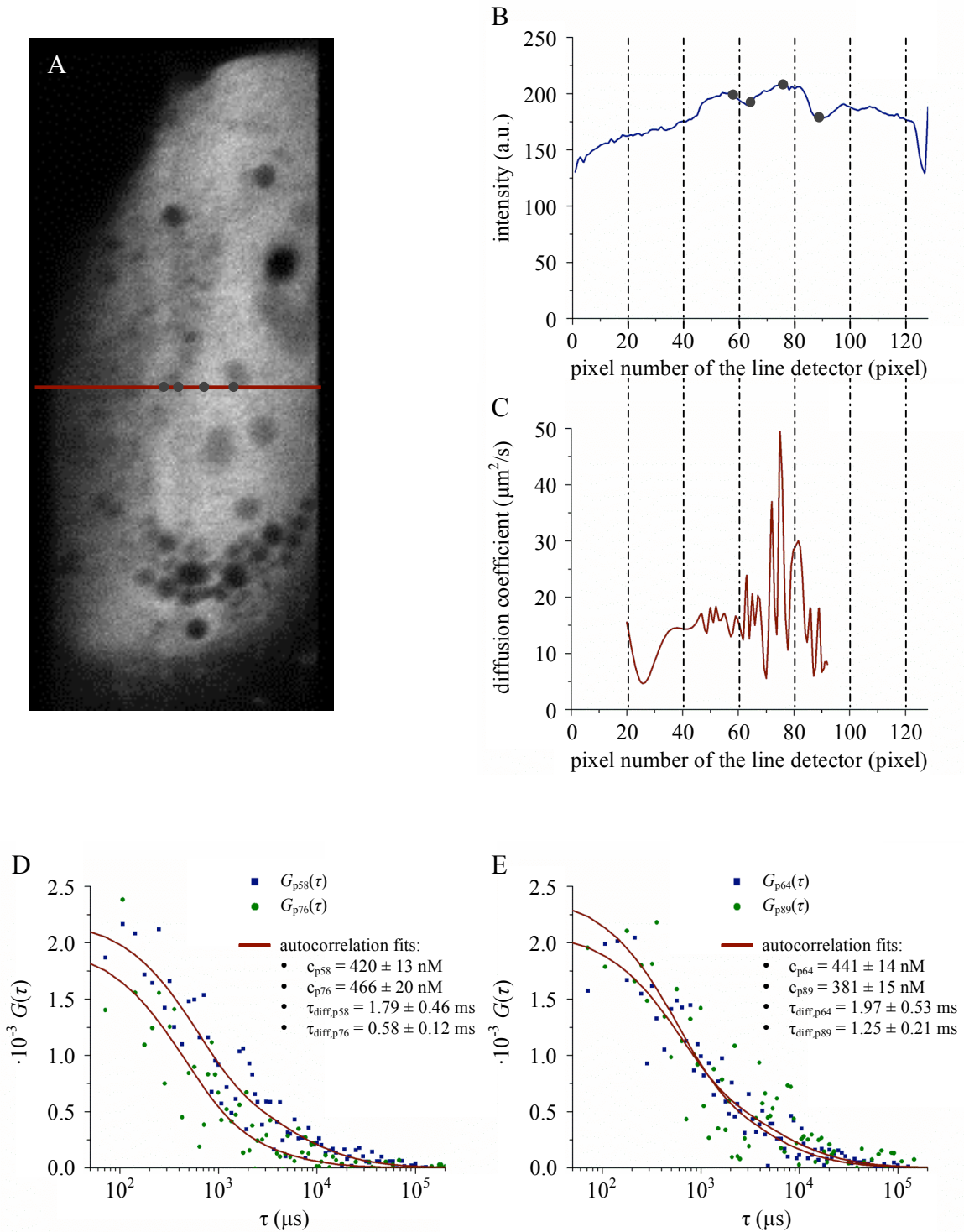


Figure 6.15. Another image of a GFP labeled HeLa-cell (A) with the intensity distribution along the indicated line (B) and the corresponding diffusion coefficient (C) determined by autocorrelation of the measured intensity profile over time displayed for pixel number 58 and 76 (D) and for pixel number 64 and 89 (E) measured with the STFM.

According to the displayed STFM measurements, the mean value of the diffusion coefficients determined in both nuclei are 20.2 ± 3.5 and $19 \pm 10 \mu\text{m}^2/\text{s}$ respectively and those determined in both cytoplasms are 16.9 ± 2.7 and $14.8 \pm 3.7 \mu\text{m}^2/\text{s}$ respectively. The diffusion coefficients vary quite a lot within the cellular substructures. There seems to be some differences between the diffusion coefficients measured in the cell nucleus compared to those measured in the cytoplasm, although those differences are rather small compared to the variations within them. According to these first experiments, the GFP molecules appear to be more mobile in the nucleus than in the cytoplasm. The boundaries of the nucleoli (dark spots inside the nucleus) of the second experiment seem to be a reason for these large fluctuations. Accordingly, it seems that around the nucleoli the GFP molecules is almost immobile. However, more experiments are needed for further discussions.

Comparison of the STFM diffusion coefficient values with those determined with the point-FCS method and the value according to the earlier work, which was measured at a averaged value of $D_0 = 23 \mu\text{m}^2/\text{s}$ as described above, the STFM provides a value for the diffusion coefficient, which is within the range of the variations between cells. According to the displayed experiment, it is obvious that the spatially resolved mobility measurement provides more insight that is not available in any other fluorescence-based signal so far.

Chapter 7

Conclusions and perspectives

For the analysis of fast dynamic processes in biological systems especially involving diffusion, transport and interaction processes fluorescence correlation spectroscopy (FCS) is well suited. One approach to obtain a spatially resolved image of the dynamics of particles using FCS is the serialization of point FCS measurements, as for example done with the scanning FCS approach (Berland et al., 1996; Palmer and Thompson, 1987; Petrasek and Schwille, 2008; Ruan et al., 2004; Skinner et al., 2005). Other approaches for the imaging of the dynamics using FCS are based on parallelized multifocal systems, which combine three-dimensional imaging with FCS in more than zero dimensions. Examples of this approach are double focus FCS (Bayer and Radler, 2006; Brinkmeier et al., 1997; Burkhardt and Schwille, 2006; Hwang and Wohland, 2007; Lumma et al., 2003; Pan et al., 2007), multifocal spinning disk FCS (Sisan et al., 2006) and total internal reflection fluorescence correlation microscopy (Kannan et al., 2007; Schwille, 2003). Another approach for the spatially differentiated FCS is the raster image correlation spectroscopy method (Brown et al., 2008; Digman et al., 2005a; Digman et al., 2005b; Kolin and Wiseman, 2007).

The scanning FCS (SFCS) collects multiple FCS measurements simultaneously by rapidly directing the excitation laser beam in a uniform, in general circular, scan in a repetitive fashion. The scan rate needs to be fast compared to the diffusion of the particles to provide accurate information on molecule mobility. This scanning FCS approach has the disadvantage that spatially differentiated measurements are extremely time consuming and are therefore often impossible in living cells. Parallelized FCS measurements reduce the data acquisition time significantly. Double focus FCS (dfFCS) describes a modified fluorescence correlation microscope using two excitation volumes in the probe in general separated a few micrometers that are recorded by two sensitive detectors. The limited number of simultaneous measurement positions and the rather complicated implementation are disadvantages of this technique. The spinning disk FCS approach parallelizes the FCS measurement using a spinning disk confocal microscope. This approach can spatially map diffusion coefficients or flow velocities at up to approximately 10 independent locations simultaneously (Sisan et al., 2006). The total internal reflection fluorescence correlation microscopy (TIR-FCM) is a combination of TIRF and FCS. The best time resolution possible with this system is 4 ms for a region of interest close to the sample

surface comprising 20 lines in the CCD (Kannan et al., 2007). Thus, current setups suffer disadvantages from the bad time resolution of the camera systems, typically in the range of milliseconds, as well as the restriction of the observation level to a few 10 nm above the cover slip in the case of TIR-FCS or limited optical resolution and low quantum yield of the overall system in the case of spinning disk FCS systems. The raster image correlation spectroscopy (RICS) method uses conventional confocal laser-scanning microscope images to determine the dynamics of particles. As the CLSM is a raster-scan instrument, the imaged focal points contain a time difference. This method provides spatially resolved dynamics information in the microsecond to second time range (Digman et al., 2005b). However, mobilities in the range of and faster than the capture rate for complete images, regularly in the range of tens of milliseconds, are determined by correlation of neighboring pixels, which implies averaging of them and hence loss of spatial resolution. Slower mobilities are determined from successive images, and hence each focal positions is measured only a fraction of the measurement time. Additionally, the quantum yield of this method is rather low and the resulting effective spatial optical resolution is rather poor.

The described developments demonstrate the importance of the imaging possibility of particle mobilities. To obtain spatially resolved imaging of the dynamics of particles without these restrictions, the existing CLSM-based spatially resolved FCS approach with the point illumination and confocal point detection setup was extended here to a new scanning microscope with a line illumination and confocal line detection system. This enables spatially resolved simultaneous detection of the intensity signal fluctuations of the particles at a series of foci along a line in the probe, and has the potential to image rapidly dynamics at high spatial resolution. The construction of the STFM included its design, the implementation into an optical-mechanical system and the development of the instrument control and data acquisition software.

The applications of the spatial and temporal fluctuation microscope are:

- Imaging of the spatial distribution of fluorescently labeled particles with high spatial resolution.
- Acquisition of the dynamics of fluorescently labeled particles by taking fast time series of two-dimensional images and three-dimensional image stacks with a high imaging frame rate.
- Imaging of faster particle mobilities simultaneously at a series of positions along a line by an extended FCS system.

The optical resolution of the STFM was analytically approximated by the theoretical description of the point spread function (PSF) that was derived from conventional point confocal laser-scanning microscopy (CLSM) and adapted to the STFM. Diffraction-limited spatial resolution for all three directions was obtained that allowed good three-dimensional reconstruction of the spatial distribution of fluorescently labeled particles, as is the case for the CLSM. A comparison with the experimentally determined PSF showed rather good agreement. The optical resolution of the STFM was experimentally determined by imaging 100 nm beads and additionally by in vitro FCS measurements of quantum dots in solution to be 200 x

380 x 700 nm in x-, y- and z- direction. Thus, the system provides a good optical resolution in three dimensions, which is only slightly worse than a point confocal system. The STFM provides some advantages for imaging. Due to a longer dwell time for a whole line in comparison to the scanning of a single focus over the same line length, the laser intensity per pixel can be decreased for STFM imaging resulting in a much higher photon yield and less photobleaching.

One way to quantify the dynamics of molecules and structures is the acquisition of time series of two-dimensional images and three-dimensional image stacks with a high imaging frame rate (Edelmann et al., 2001). The STFM was developed for fast confocal imaging to determine the mobility of fluorescently labeled particles. Hence, it is a suitable technique for single particle tracking microscopy. This capability of the STFM in terms of fast imaging and mobility measurements was applied to *in vivo* imaging of floating 100 nm beads and *in vitro* studies of the movement of PML nuclear bodies in living cells. The STFM system provided fast confocal imaging up to 30 images per second with an image size of about 25 μm x 25 μm .

Faster processes cannot be followed by imaging. Therefore, the existing implementation of a point FCS method was extended. The line-scan imaging FCS mode allows the acquisition of the diffusion properties of fluorescently labeled particles simultaneously at hundreds of points in parallel along a line profile with the potential to reconstruct two-dimensional mobility images. Using the theoretically determined and experimentally confirmed PSF, detailed theoretical descriptions of the autocorrelation and cross-correlation fit functions were derived from the conventional point FCS system and further developed for the STFM. These theoretical descriptions of the fit functions were required for the analysis of the experiments with the line scanning FCS system. The capability of the STFM in terms of FCS measurements was applied *in vitro* by measuring floating 100 nm beads and quantum dots and *in vivo* by acquiring fluctuations of the green fluorescent protein (GFP) in living cells. The STFM system provided high temporal resolution down to 15 μs to measure fast particles that spend down to 50 μs in the focal volume. Both the *in vitro* and the *in vivo* fluorescence correlation spectroscopy experiments conducted with the STFM were compared to single point FCS measurements with a Leica confocal microscope. The results demonstrate the unique capabilities of the STFM to characterize the position-dependent diffusive translocations of macromolecules in the cell.

The camera used for the detection of the fluorescence intensities was an electron multiplying charged coupled device (EMCCD). Other concepts and experimental setups described in the literature already used this detector technology, as for example TIR-FCM (Kannan et al., 2007), dfFCS (Burkhardt and Schwille, 2006) and the spinning disk FCS approach (Sisan et al., 2006). The data acquisition of the camera was modified here to a line-scan detector. Accordingly, a line acquisition rate up to 80 kHz could be achieved, which is one to two orders of magnitude faster than setups used previously. It was shown that the EMCCD camera yields a quantum efficiency of approximately 30% and a signal-to-noise ratio of about one photon, which enables high sensitivity measurements, up to single photon detection combined with high image rates. This combination fulfilled the requirements for FCS for a detailed and

exact analysis of interaction and mobility properties at a series of positions along the imaged line. On the other hand, the EMCCD camera currently determines the optimum performance of the instrument, as this is the major component of the STFM.

- The quantum efficiency is quite high although somewhat lower compared to the avalanche photodiode regularly used for point-FCS. This implies that the resulting correlation curves of the intensity signals of the STFM are noisier and concentrations below 50 nM cannot be measured.
- Higher imaging rates of the EMCCD would lead to faster acquisition of the STFM, which implies that even faster particles (faster than free GFP) could be measured. It appears likely that EMCCD cameras will reach higher speeds in the near future.
- The imaging readout of the used EMCCD camera is not optimized for line imaging as the data acquisition of the area-scan camera was modified to a line-scan detector. It seems likely that specifically developed line-scan EMCCD cameras would further improve the performance.
- The pixel size of the EMCCD camera is $7.4 \times 7.4 \mu\text{m}$, which is quite small and not the optimal size for the optical resolution of the STFM as described in chapter 4. The described implementation maps 200 nm in the probe onto one pixel, which could be optimized using a three times over sampling as is the case for the conventional point systems.

In addition to the autocorrelation measurements shown, the STFM enables the measurement of the cross-correlation of the intensity fluctuations of two spatially separated positions along the line. This is important for analyzing interactions between macromolecules in biological processes of complex structures. Two associated proteins exhibit a certain spatio-temporal correlation while two proteins that do not interact will show no cross-correlation. The developed instrument is constructed for the use of two color illumination and detection. Up to now, only one color illumination of 488 nm and detection above the 510 nm is implemented. However, this can be upgraded for fluorescence cross-correlation spectroscopy measurements as the instrument allows the easy exchange of lasers and the corresponding filters and detectors.

In summary, the system developed in this thesis offers a number of new applications for studying the dynamics of cellular processes. It is expected that this type of imaging the spatial distribution of macromolecular mobility and interaction in the cell will serve to develop a better understanding of how transitions between different functional cell states like proliferation, differentiation and senescence, are established.

Literature

- Aragón, S.R., and Pecora, R. (1976). Fluorescence correlation spectroscopy as a probe of molecular dynamics. *J of Chem Phys* *64*, 1791-1803.
- Bacher, C.P., Reichenzeller, M., Athale, C., Herrmann, H., and Eils, R. (2004). 4-D single particle tracking of synthetic and proteinaceous microspheres reveals preferential movement of nuclear particles along chromatin - poor tracks. *BMC Cell Biol* *5*, 45.
- Bacia, K., Kim, S.A., and Schwille, P. (2006). Fluorescence cross-correlation spectroscopy in living cells. *Nat Methods* *3*, 83-89.
- Baddeley, D., Carl, C., and Cremer, C. (2006). 4Pi microscopy deconvolution with a variable point-spread function. *Appl Opt* *45*, 7056-7064.
- Bayer, J., and Radler, J.O. (2006). DNA microelectrophoresis using double focus fluorescence correlation spectroscopy. *Electrophoresis* *27*, 3952-3963.
- Beaudouin, J., Mora-Bermúdez, F., Klee, T., Daigle, N., and Ellenberg, J. (2006). Dissecting the contribution of diffusion and interactions to the mobility of nuclear proteins. *Biophys J* *90*, 1878-1894.
- Berg, O.G., and von Hippel, P.H. (1985). Diffusion-controlled macromolecular interactions. *Annu Rev Biophys Biophys Chem* *14*, 131-160.
- Berland, K.M., So, P.T., and Gratton, E. (1995). Two-photon fluorescence correlation spectroscopy: method and application to the intracellular environment. *Biophys J* *68*, 694-701.
- Berland, K.M., So, P.T.C., Chen, Y., Mantulin, W.W., and Gratton, E. (1996). Scanning 2-Photon Fluctuation Correlation Spectroscopy - Particle Counting Measurements for Detection of Molecular Aggregation. *Biophys J* *71*, 410-420.
- Born, M., Wolf, E. (1999). *Principles of Optics: Electromagnetic Theory of Propagation, Interference and Diffraction of Light* 7th (expanded) edn (New York, Cambridge University Press).
- Bornfleth, H., Edelmann, P., Zink, D., Cremer, T., and Cremer, C. (1999). Quantitative motion analysis of subchromosomal foci in living cells using four-dimensional microscopy. *Biophys J* *77*, 2871-2886.
- Boyde, A. (1985). Stereoscopic images in confocal (tandem scanning) microscopy. *Science* *230*, 1270-1272.
- Brinkmeier, M., Dorre, K., Riebeseel, K., and Rigler, R. (1997). Confocal spectroscopy in microstructures. *Biophys Chem* *66*, 229-239.
- Brown, C.M., Dalal, R.B., Hebert, B., Digman, M.A., Horwitz, A.R., and Gratton, E. (2008). Raster image correlation spectroscopy (RICS) for measuring fast protein dynamics and concentrations with a commercial laser scanning confocal microscope. *J Microsc* *229*, 78-91.
- Bulsecu, D.A., and Wolf, D.E. (2007). Fluorescence Correlation Spectroscopy: Molecular Complexing in Solution and in Living Cells. In *Methods in cell biology* (Elsevier Inc.), pp. 525-559.
- Burkhardt, M., and Schwille, P. (2006). Electron multiplying CCD based detection for spatially resolved fluorescence correlation spectroscopy. *OPTICS EXPRESS* *14*, 5013-5020.

- Cabal, G.G., Genovesio, A., Rodriguez-Navarro, S., Zimmer, C., Gadal, O., Lesne, A., Buc, H., Feuerbach-Fournier, F., Olivo-Marin, J.C., Hurt, E.C., *et al.* (2006). SAGA interacting factors confine sub-diffusion of transcribed genes to the nuclear envelope. *Nature* 441, 770-773.
- Chen, Y., Muller, J.D., So, P.T., and Gratton, E. (1999). The photon counting histogram in fluorescence fluctuation spectroscopy. *Biophys J* 77, 553-567.
- Christen, F., Kuijken, K., Baade, D., Cavadore, C., Deiries, S., and Iwert, O. (2006). Fast Conversion Factor (Gain) Measurement of a CCD Using Images With Vertical Gradient. In *Scientific detectors for astronomy 2005* (Groningen, Springer Netherlands).
- Chu, B. (1979). Dynamics of macromolecular solutions. *Phys Scri* 19, 458-470.
- Cremer, C., and Cremer, T. (1978). Considerations on a laser-scanning-microscope with high resolution and depth of field. *Microsc Acta* 81, 31-44.
- Cremer, T., and Cremer, C. (2001). Chromosome territories, nuclear architecture and gene regulation in mammalian cells. *Nat Rev Genet* 2, 292-301.
- Davidovits, P., and Egger, M.D. (1969). Scanning laser microscope. *Nature* 223, 831.
- Digman, M.A., Brown, C.M., Sengupta, P., Wiseman, P.W., Horwitz, A.R., and Gratton, E. (2005a). Measuring fast dynamics in solutions and cells with a laser scanning microscope. *Biophys J* 89, 1317-1327.
- Digman, M.A., Sengupta, P., Wiseman, P.W., Brown, C.M., Horwitz, A.R., and Gratton, E. (2005b). Fluctuation correlation spectroscopy with a laser-scanning microscope: exploiting the hidden time structure. *Biophys J* 88, L33-36.
- Dusch, E., Dorval, T., Vincent, N., Wachsmuth, M., and Genovesio, A. (2007). Three-dimensional point spread function model for line-scanning confocal microscope with high-aperture objective. *J Microsc* 228, 132-138.
- Edelmann, P., Bornfleth, H., Zink, D., Cremer, T., and Cremer, C. (2001). Morphology and dynamics of chromosome territories in living cells. *Biochim Biophys Acta* 1551, M29-39.
- Egger, M.D., and Petran, M. (1967). New reflected-light microscope for viewing unstained brain and ganglion cells. *Science* 157, 305-307.
- Eigen, M., and Rigler, R. (1994). Sorting single molecules: Application to diagnostics and evolutionary biotechnology. *Proc Natl Acad Sci USA* 91, 5740-5747.
- Elson, E.L., and Magde, D. (1974). Fluorescence correlation spectroscopy. I. Conceptual basis and theory. *Biopolymers* 13, 1-27.
- Elson, E.L., Schlessinger, J., Koppel, D.E., Axelrod, D., and Webb, W.W. (1976). Measurement of lateral transport on cell surfaces. *Prog Clin Biol Res* 9, 137-147.
- Elson, E.L., and Webb, W.W. (1975). Concentration correlation spectroscopy: A new biophysical probe based on occupation number fluctuations. *Annu Rev Biophys Bioeng* 4, 311-334.
- Gomez, D.E., Califano, M., and Mulvaney, P. (2006). Optical properties of single semiconductor nanocrystals. *Phys Chem Chem Phys* 8, 4989-5011.
- Görisch, S.M., Lichter, P., and Rippe, K. (2005). Mobility of multi-subunit complexes in the nucleus: chromatin dynamics and accessibility of nuclear subcompartments. *Histochem Cell Biol* 123, 217-228.
- Görisch, S.M., Wachsmuth, M., Itrich, C., Bacher, C.P., Rippe, K., and Lichter, P. (2004). Nuclear body movement is determined by chromatin accessibility and dynamics. *Proc Natl Acad Sci USA* 101, 13221-13226.

-
- Grunwald, D., Cardoso, M.C., Leonhardt, H., and Buschmann, V. (2005). Diffusion and binding properties investigated by Fluorescence Correlation Spectroscopy (FCS). *Curr Pharm Biotechnol* 6, 381-386.
- Guenther, R. (1990). *Modern optics* (New York, John Wiley & Sons).
- Hanley, Q.S., Verveer, P.J., Arndt-Jovin, D.J., and Jovin, T.M. (2000). Three-dimensional spectral imaging by hadamard transform spectroscopy in a programmable array microscope. *J Microsc* 197, 5-14.
- Haustein, E., and Schwille, P. (2004). Single-molecule spectroscopic methods. *Curr Opin Struct Biol* 14, 531-540.
- Haustein, E., and Schwille, P. (2007). Fluorescence correlation spectroscopy: novel variations of an established technique. *Annu Rev Biophys Biomol Struct* 36, 151-169.
- Hecht, E. (1989). *Optics* (New York, Addison Wesley Longmann Inc.).
- Hess, S.T., Huang, S., Heikal, A.A., and Webb, W.W. (2002). Biological and Chemical Applications of Fluorescence Correlation Spectroscopy: A Review. *Biochemistry* 41, 697-705.
- Hess, S.T., and Webb, W.W. (2002). Focal volume optics and experimental artifacts in confocal fluorescence correlation spectroscopy. *Biophys J* 83, 2300-2317.
- Heuff, R.F., Swift, J.L., and Cramb, D.T. (2007). Fluorescence correlation spectroscopy using quantum dots: advances, challenges and opportunities. *Phys Chem Chem Phys* 9, 1870-1880.
- Hwang, L.C., and Wohland, T. (2007). Recent advances in fluorescence cross-correlation spectroscopy. *Cell Biochem Biophys* 49, 1-13.
- Jameson, D.M., and Sawyer, W.H. (1995). Fluorescence Anisotropy Applied to Biomolecular Interactions. *Meth Enzymology* 246, 283-300.
- Janesick, J.R. (2007). *Photon Transfer: DN \rightarrow λ Vol PM170* (SPIE Press Book).
- Jegou, T., Heuvelman, G.L., Wachsmuth, M., Görisch, S.M., Greulich-Bode, K., Boukamp, P., Lichter, P., and Rippe, K. (2008). Dynamics of telomeres and PML nuclear bodies in a telomerase negative human cell line. *submitted*.
- Kang, K.I., Devin, J., Cadepond, F., Jibard, N., Guiochon-Mantel, A., Baulieu, E.E., and Catelli, M.G. (1994). In vivo functional protein-protein interaction: nuclear targeted hsp90 shifts cytoplasmic steroid receptor mutants into the nucleus. *Proc Natl Acad Sci U S A* 91, 340-344.
- Kannan, B., Guo, L., Sudhakaran, T., Ahmed, S., Maruyama, I., and Wohland, T. (2007). Spatially resolved total internal reflection fluorescence correlation microscopy using an electron multiplying charge-coupled device camera. *Anal Chem* 79, 4463-4470.
- Kastrup, L., Blom, H., Eggeling, C., and Hell, S.W. (2005). Fluorescence fluctuation spectroscopy in subdiffraction focal volumes. *Phys Rev Lett* 94, 178104.
- Kett, P., Geiger, B., Ehemann, V., and Komitowski, D. (1992). Three-dimensional analysis of cell nucleus structures visualized by confocal scanning laser microscopy. *J Microsc* 167, 169-179.
- Kim, S.A., Heinze, K.G., and Schwille, P. (2007). Fluorescence correlation spectroscopy in living cells. *Nature Methods* 4, 963-972.
- Kino, G.S. (1995). Intermediate optics in Nipkow disk microscopes. In *Handbook of biological confocal microscopy*, J.B. Pawley, ed. (New York, Plenum Press), pp. 155-166.

- Kolin, D.L., and Wiseman, P.W. (2007). Advances in image correlation spectroscopy: measuring number densities, aggregation states, and dynamics of fluorescently labeled macromolecules in cells. *Cell Biochem Biophys* 49, 141-164.
- Kubitscheck, U., Kuckmann, O., Kues, T., and Peters, R. (2000). Imaging and tracking of single GFP molecules in solution [In Process Citation]. *Biophys J* 78, 2170-2179.
- Kusumi, A., Sako, Y., and Yamamoto, M. (1993). Confined lateral diffusion of membrane receptors as studied by single particle tracking (nanovid microscopy). Effects of calcium-induced differentiation in cultured epithelial cells. *Biophys J* 65, 2021-2040.
- Lamond, A.I., and Sleeman, J.E. (2003). Nuclear substructure and dynamics. *Curr Biol* 13, R825-828.
- Langowski, J. (2008). Protein-Protein Interactions Determined by Fluorescence Correlation Spectroscopy. In *METHODS IN CELL BIOLOGY* (Elsevier Inc.), pp. 471-484.
- Langowski, J., Wachsmuth, M., Rippe, K., and Tewes, M. (2000). Biomolecular shape and interactions determined by fluorescence correlation spectroscopy. In *Energies et forces de l'interaction entre macromolécules biologiques: l'aspect quantitatif*, J.-P. Frénoy, ed. (Paris, Publications CNRS), pp. 65-77.
- Lumma, D., Best, A., Gansen, A., Feuillebois, F., Radler, J.O., and Vinogradova, O.I. (2003). Flow profile near a wall measured by double-focus fluorescence cross-correlation. *Phys Rev E Stat Nonlin Soft Matter Phys* 67, 056313.
- Magde, D., Elson, E.L., and Webb, W.W. (1972). Thermodynamic fluctuations in a reacting system - measurement by fluorescence correlations spectroscopy. *Phys Rev Let* 29, 705-708.
- Magde, D., Elson, E.L., and Webb, W.W. (1974). Fluorescence correlation spectroscopy. II. An experimental realization. *Biopolymers* 13, 29-61.
- Meyer-Arendt, J.R. (1995). *Introduction to Classical and Modern Optics*, 4th Ed edn (Prentice-Hall).
- Minsky, M. (1957). *Microscopy apparatus* (Bowdoin St., Cambridge).
- Nakayasu, H., and Berezney, R. (1989). Mapping replicational sites in the eucaryotic cell nucleus. *J Cell Biol* 108, 1-11.
- Pack, C., Saito, K., Tamura, M., and Kinjo, M. (2006). Microenvironment and effect of energy depletion in the nucleus analyzed by mobility of multiple oligomeric EGFPs. *Biophys J* 91, 3921-3936.
- Palmer, A.G., and Thompson, N.L. (1987). Theory of sample translation in fluorescence correlation spectroscopy. *Biophys J* 51, 339-343.
- Pan, X., Foo, W., Lim, W., Fok, M.H., Liu, P., Yu, H., Maruyama, I., and Wohland, T. (2007). Multifunctional fluorescence correlation microscope for intracellular and microfluidic measurements. *Rev Sci Instrum* 78, 053711.
- Pawley, J.B., ed. (2006). *Handbook of biological confocal microscopy*, 3rd edn (New York, Springer).
- Petrasek, Z., and Schwille, P. (2008). Precise measurement of diffusion coefficients using scanning fluorescence correlation spectroscopy. *Biophys J* 94, 1437-1448.
- Qian, H., and Elson, E.L. (1991). Analysis of Confocal Laser-Microscope Optics for 3-D Fluorescence Correlation Spectroscopy. *Appl Opt* 30, 1185-1195.

-
- Qian, H., and Elson, E.L. (1999). Quantitative study of polymer conformation and dynamics by single- particle tracking. *Biophys J* 76, 1598-1605.
- Qian, H., and Elson, E.L. (2004). Fluorescence correlation spectroscopy with high-order and dual-color correlation to probe nonequilibrium steady states. *Proc Natl Acad Sci U S A* 101, 2828-2833.
- Rieger, B., Molenaar, C., Dirks, R.W., and Van Vliet, L.J. (2004). Alignment of the cell nucleus from labeled proteins only for 4D in vivo imaging. *Microsc Res Tech* 64, 142-150.
- Rigler, R. (1995). Fluorescence correlations, single molecule detection and large number screening Applications in biotechnology. *J of Biotechnology* 41, 177-186.
- Rigler, R., Foldes-Papp, Z., Meyer-Almes, F.J., Sammet, C., Volcker, M., and Schnetz, A. (1998). Fluorescence cross-correlation: a new concept for polymerase chain reaction. *J Biotechnol* 63, 97-109.
- Rigler, R., Grasselli, P., and Ehernberg, M. (1979). Fluorescence correlation spectroscopy and applications to the study of Brownian motion of biopolymers. *Phys Scr* 19, 486-490.
- Rigler, R., Mets, Ü., Widengren, J., and Kask, P. (1993). Fluorescence correlation spectroscopy with high count rate and low background: analysis of translational diffusion. *Eur Biophys J* 22, 169-175.
- Rippe, K. (2000). Simultaneous binding of two DNA duplexes to the NtrC-enhancer complex studied by two-color fluorescence cross-correlation spectroscopy. *Biochemistry* 39, 2131-2139.
- Rippe, K. (2007). Dynamic organization of the cell nucleus. *Current opinion in genetics & development* 17, 373-380.
- Ruan, Q., Cheng, M.A., Levi, M., Gratton, E., and Mantulin, W.W. (2004). Spatial-temporal studies of membrane dynamics: scanning fluorescence correlation spectroscopy (SFCS). *Biophys J* 87, 1260-1267.
- Sage, D., Neumann, F.R., Hediger, F., Gasser, S.M., and Unser, M. (2005). Automatic tracking of individual fluorescence particles: application to the study of chromosome dynamics. *IEEE transactions on image processing* 14, 1372-1383.
- Santos, A., and Young, I.T. (2000). Model-based resolution: applying the theory in quantitative microscopy. *Appl Opt* 39, 2948-2958.
- Saxton, M.J., and Jacobson, K. (1997). Single-particle tracking: applications to membrane dynamics. *Annu Rev Biophys Biomol Struct* 26, 373-399.
- Schwille, P. (2001). Fluorescence Correlation Spectroscopy and Its Potential for Intracellular Applications. *Cell Biochemistry and Biophysics* 34, 383-408.
- Schwille, P. (2003). TIR-FCS: staying on the surface can sometimes be better. *Biophys J* 85, 2783-2784.
- Schwille, P., and Haustein, E. (2002). Fluorescence Correlation Spectroscopy: An Introduction to its Concepts and Applications (Göttingen).
- Seisenberger, G., Ried, M.U., Endress, T., Buning, H., Hallek, M., and Brauchle, C. (2001). Real-time single-molecule imaging of the infection pathway of an adeno-associated virus. *Science* 294, 1929-1932.
- Sheppard, C.J.R., and Matthews, H.J. (1987). Imaging in high-aperture optical systems. *J Opt Soc Am A* 4, 1354-1360.

- Sisan, D.R., Arevalo, R., Graves, C., McAllister, R., and Urbach, J.S. (2006). Spatially resolved fluorescence correlation spectroscopy using a spinning disk confocal microscope. *Biophys J* 91, 4241-4252.
- Skinner, J.P., Chen, Y., and Muller, J.D. (2005). Position-sensitive scanning fluorescence correlation spectroscopy. *Biophys J* 89, 1288-1301.
- Sorscher, S.M., Bartholomew, J.C., and Klein, M.P. (1980). The use of fluorescence correlation spectroscopy to probe chromatin in the cell nucleus. *Biochim Biophys Acta* 610, 28-46.
- Swift, J.L., Heuff, R., and Cramb, D.T. (2006). A two-photon excitation fluorescence cross-correlation assay for a model ligand-receptor binding system using quantum dots. *Biophys J* 90, 1396-1410.
- Tewes, M. (1998). Aufbau eines Experiments zur Fluoreszenzkreuzkorrelationsspektroskopie, Erweiterung der theoretischen Grundlagen und biologische Anwendungen. In Fakultät für Physik und Astronomie (Heidelberg, Ruprecht-Karls-Universität Heidelberg).
- Thomann, D., Rines, D.R., Sorger, P.K., and Danuser, G. (2002). Automatic fluorescent tag detection in 3D with super-resolution: application to the analysis of chromosome movement. *J Microsc* 208, 49-64.
- Thompson, N.L. (1991). Fluorescence Correlation Spectroscopy. In Topics in Fluorescence Spectroscopy, J.R. Lakowicz, ed. (New York, Plenum Press), pp. 337-378.
- van Kampen, N.G., ed. (1992). Stochastic processes in physics and chemistry, 2nd edn (Amsterdam, Elsevier).
- Verveer, P.J., Hanley, Q.S., Verbeek, P.W., van Vliet, L.J., and Jovin, T.M. (1998). Theory of confocal fluorescence imaging in the Programmable Array Microscope (PAM). *J Microscopy* 189, 192-198.
- Von Tiedemann, M., Fridberger, A., Ulfendahl, M., Tomo, I., and Boutet de Monvel, J. (2006). Image adaptive point-spread function estimation and deconvolution for in vivo confocal microscopy. *Microsc Res Tech* 69, 10-20.
- Vukojevic, V., Pramanikb, A., Yakovlevaa, T., Rigler, R., Tereniusa, L., and Bakalkina, G. (2005). Study of molecular events in cells by fluorescence correlation spectroscopy. *Cellular and Molecular Life Sciences* 62, 535-550.
- Wachsmuth, M. (2001). Fluoreszenzfluktuationmikroskopie: Entwicklung eines Prototyps, Theorie und Messung der Beweglichkeit von Biomolekülen im Zellkern. In Fakultät für Physik und Astronomie (Heidelberg, Ruprecht-Karls-Universität Heidelberg).
- Wachsmuth, M., Caudron-Herger, M., and Rippe, K. (2008). Genome Organization: Combining Dynamics and Specificity. *Biochem Biophys Acta* *submitted*.
- Wachsmuth, M., Jegou, T., Nehrbass, U., and Rippe, K. (2007). Differences in dynamics of hetero- and euchromatin as revealed by fluorescence correlations spectroscopy of linker histone H1. *in preparation*.
- Wachsmuth, M., Jegou, T., Nehrbass, U., and Rippe, K. (in preparation). Chromatin dynamics and organization studied by fluorescence fluctuation microscopy of linker histone H1.
- Wachsmuth, M., Waldeck, W., and Langowski, J. (2000). Anomalous diffusion of fluorescent probes inside living cell nuclei investigated by spatially-resolved fluorescence correlation spectroscopy. *J Mol Biol* 298, 677-689.

-
- Wachsmuth, M., Weidemann, T., Muller, G., Hoffmann-Rohrer, U.W., Knoch, T.A., Waldeck, W., and Langowski, J. (2003). Analyzing intracellular binding and diffusion with continuous fluorescence photobleaching. *Biophys J* 84, 3353-3363.
- Wachsmuth, M., and Weisshart, K. (2007). Fluorescence Photobleaching and Fluorescence Correlation Spectroscopy: Two Complementary Technologies To Study Molecular Dynamics in Living Cells. In *Imaging Cellular and Molecular Biological Functions*, S.L.S.a.F. Frischknecht, ed. (Springer), pp. 179-229.
- Webb, W.W. (2001). Fluorescence correlation spectroscopy: inception, biophysical experimentations, and prospectus. *Applied Optics* 40, 3969-3983.
- Weidemann, T., Wachsmuth, M., Tewes, M., Rippe, K., and Langowski, J. (2002). Analysis of ligand binding by two-colour fluorescence cross-correlation spectroscopy. *Single Mol* 3, 49-61.
- Widengren, J., Mets, Ü., and Rigler, R. (1995). Fluorescence Correlation Spectroscopy of Triplet States in Solution: A Theoretical and Experimental Study. *J Phys Chem* 99, 13368-13379.
- Widengren, J., and Rigler, R. (1998). Fluorescence correlation spectroscopy as a tool to investigate chemical reactions in solutions and on cell surfaces. *Cell Mol Biol (Noisy-le-grand)* 44, 857-879.
- Young, J.Z., Roberts, F., and 167, r. (1951). A flying-spot microscope. *Nature* 167, 231.
- Zeiss (2004). *Confocal Laser Scanning Microscopy*.
- Zhang, Z., Liu, H., and He, J. (2000). [Progress in charge-coupled device and its applications]. *Guang Pu Xue Yu Guang Pu Fen Xi* 20, 160-166.

List of publications and patents

Wachsmuth, M., Rippe, K. and Heuvelman, G.L., published German patent application DE 10 2005 000 915.8 from January 6, 2005. “*Vorrichtung zur multifokalen konfokalen mikroskopischen Bestimmung der räumlichen Verteilung und zur multifokalen Fluktuationsanalyse von fluoreszenten Molekülen und Strukturen mit spektral flexibler Detektion*”

Wachsmuth, M., Rippe, K. and Heuvelman, G.L., published US patent application US 2006-0146325 A1 from January 4, 2006. “*Setup for multifocal confocal microscopic determination of spatial distributions and for multifocal fluctuation analysis of fluorescent molecules and structures with spectrally variable detection*”

Kepert, J. F., Mazurkiewicz, J., Heuvelman, G.L., Fejes Tóth, K. and Rippe, K. (2005). *NAP1 modulates binding of linker histone H1 to chromatin and induces an extended chromatin fiber conformation*. J. Biol. Chem. **280**, 34063-34072, advance online publication, 17 August 2005.

Jegou, T., Chung, I., Heuvelman, G.L., Wachsmuth, M., Görisch, S. M., Greulich-Bode, K., Boukamp, P., Lichter, P. and Rippe, K., *Dynamics of telomeres and PML nuclear bodies in a telomerase negative human cell line*, Mol. Biol. Cell submitted 2008.

Acknowledgements

PD Dr. Karsten Rippe danke ich sehr für die Möglichkeit diese Arbeit in seiner interdisziplinären Arbeitsgruppe machen zu dürfen, für die große Freiheit bei der Ausrichtung der Arbeit und seine immer wieder kritischen Nachfragen und Ratschläge während der Arbeit. Herzlichen Dank insbesondere für den Spaß, während und außerhalb der Arbeitszeit, der diese Jahre zu einer schönen Zeit gemacht hat, wie z.B. die gemeinsame Teilnahme am Heidelbergman inclusive Gewinnessen.

Dr. Malte Wachsmuth danke ich sehr für seine hilfreiche Unterstützung dieser Doktorarbeit sogar über eine Entfernung von mehr als 7000 km. Ohne seine Grundidee für die Konzeption der STFM, seine viele guten weiteren Ideen, Anregungen und Diskussionen und seine Freude am Gelingen der Arbeit wäre diese Arbeit nicht das, was sie jetzt ist.

Prof. Dr. Dr. C. Cremer danke ich herzlich für das Interesse an diesem Thema und die Bereitschaft diese Arbeit vor dem Promotionsausschuss der Naturwissenschaftlich-Mathematischen Gesamtfakultät der Universität Heidelberg zu vertreten.

Dr. Thibaud Jegou danke ich für seine Hilfsbereitschaft beim Bereitstellen aller in dieser Arbeit beschriebenen und auch nicht-beschriebenen biologischen Systeme und für seine Erklärungen der biologischen Welt für einen 'dummen' Physiker.

Katharina Müller danke ich für die für das Bereitstellen von einige ihrer Punkt-FCS Bestimmungen.

Dr. Jacek Mazurkiewicz danke ich für den CNC-Fräse Konstruktions Spaß, mit dem wir um einiges schneller erfolgreich waren als es der Fall war für das im Rahmen dieser Arbeit gebaute Mikroskop.

Dummkopf, Polska Huje, Le Killer Team and Pantoffel danke ich für die Wormszeit im Labor und der Chef für der CD

Ich bedanke mich herzlich bei meinen Chromcon-Kollegen alt und neu für den Spaß im Labor während dieser letzten viereinhalb Jahre.

Maik Kutzner und Michael Vachek danke ich für die Hilfe beim Englisch Korrigieren.

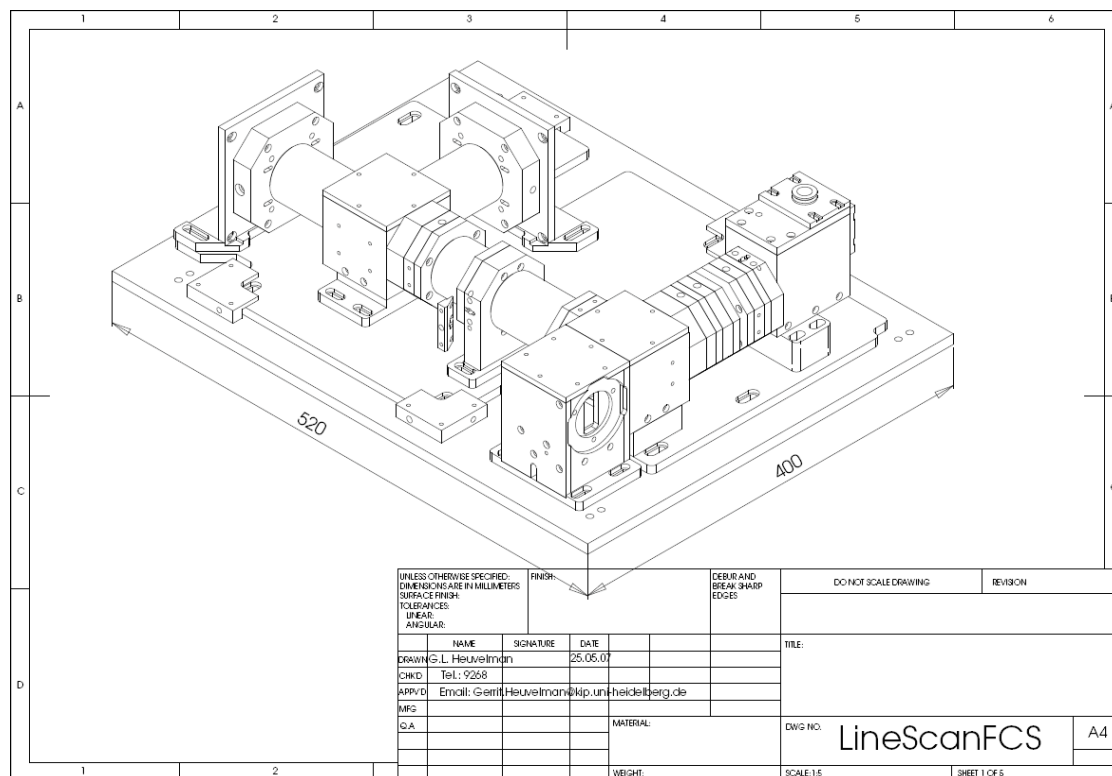
Mein größter Dank gilt Doreen. Ohne ihre Liebe und Unterstützung wäre diese Arbeit nicht zustande gekommen.

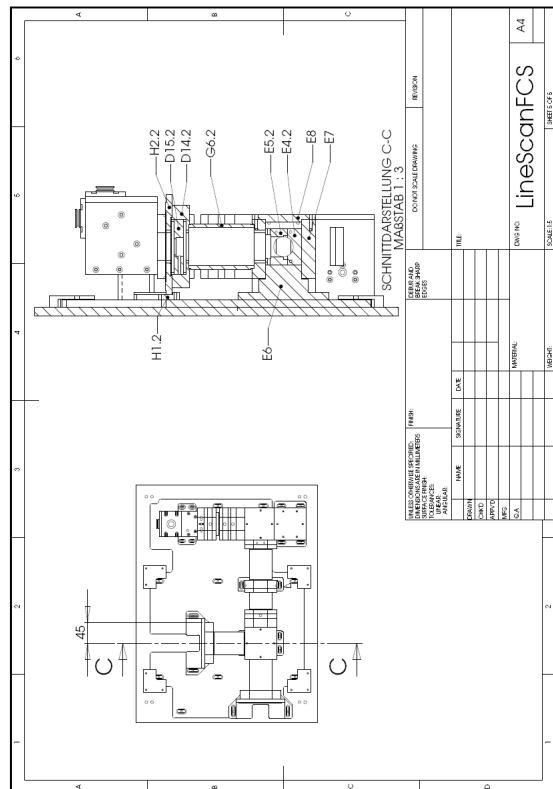
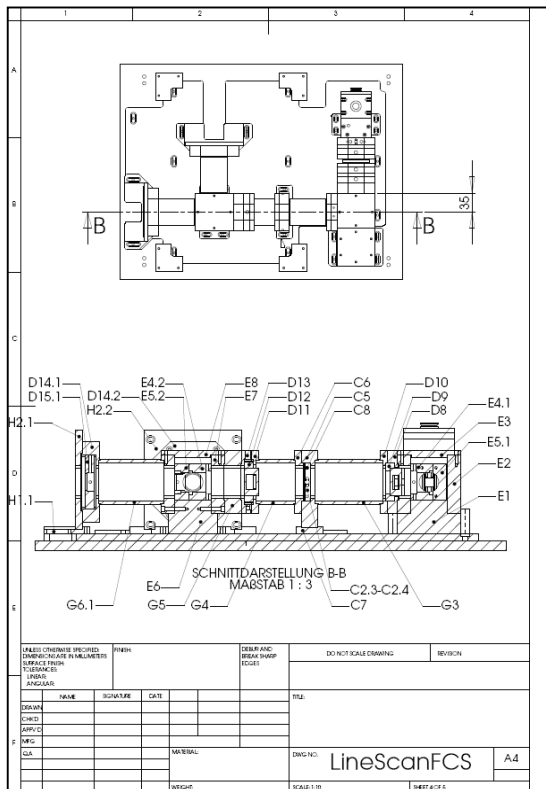
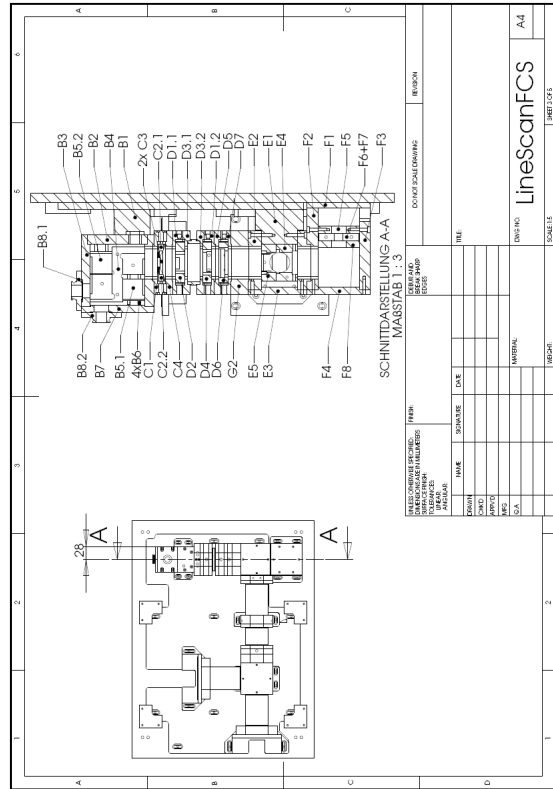
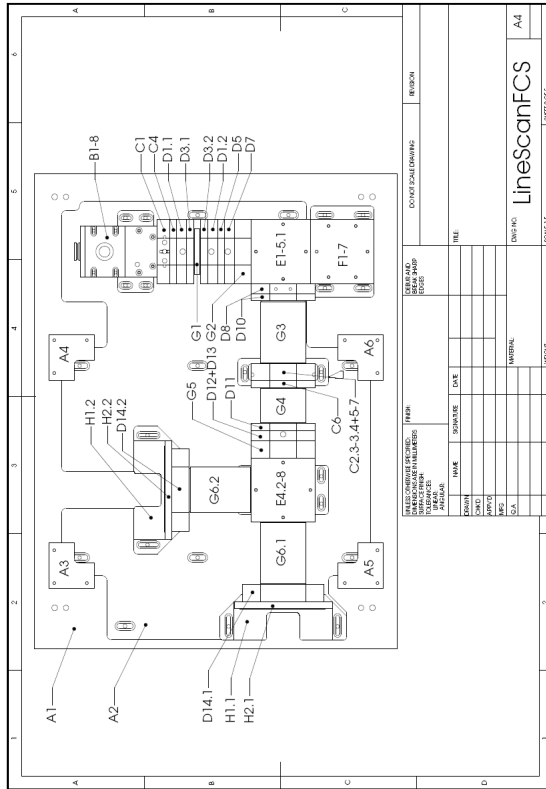
Appendix

The mechanical construction of the spatial and temporal fluctuation microscope is divided into different modules:

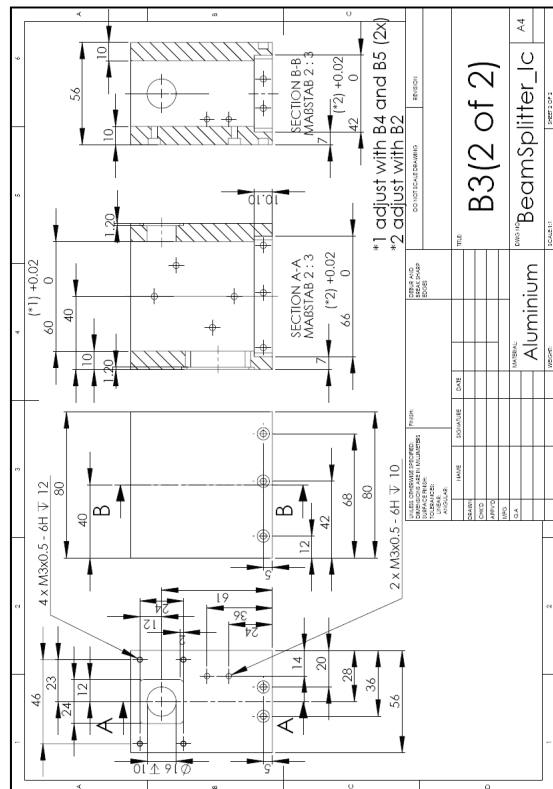
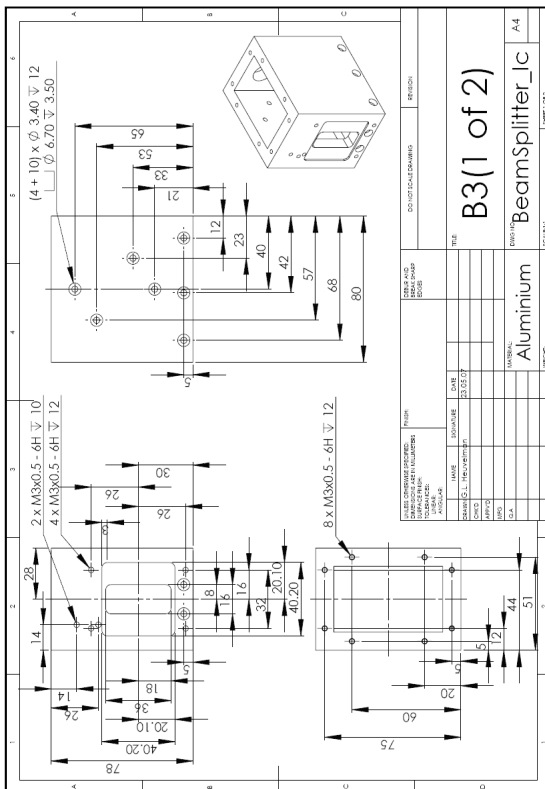
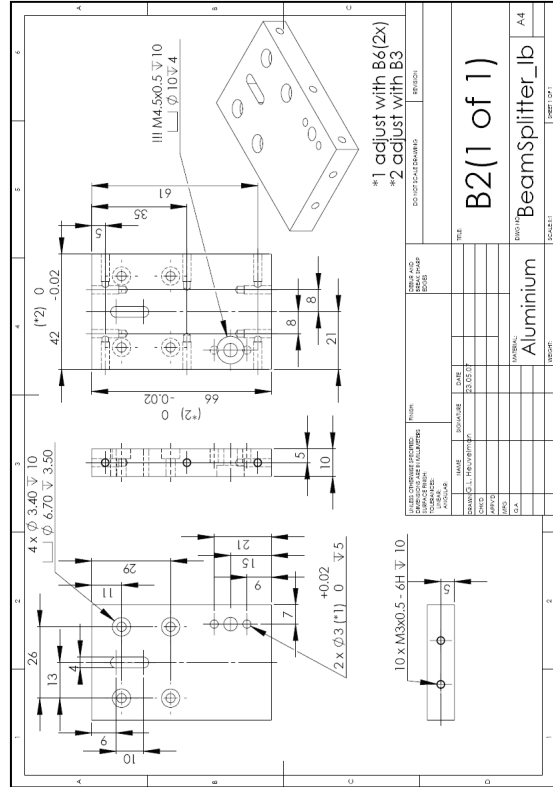
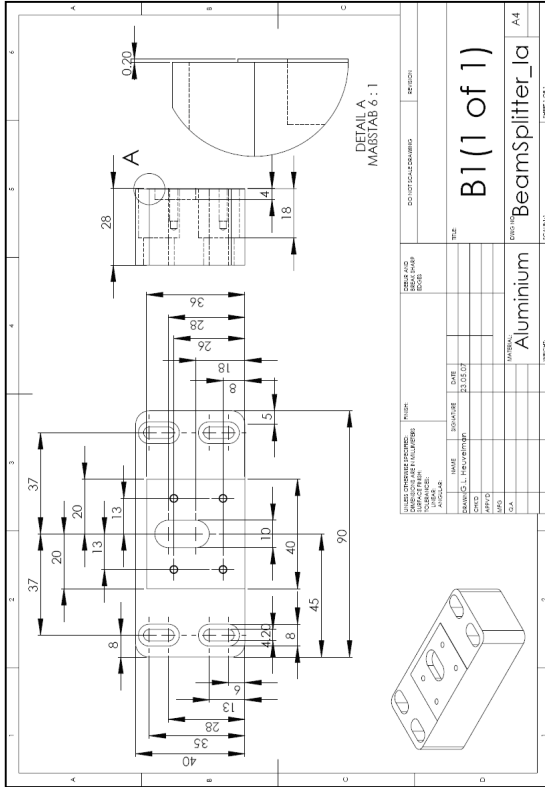
- A Ground plates and adjusters
- B Beam entry module
- C Both rectangular slit modules
- D Lens holder modules
- E Beam splitter holder modules
- F Mirror holder module
- G All Connectors between different modules
- H Camera holder module
- I Laser coupler module

Complete construction

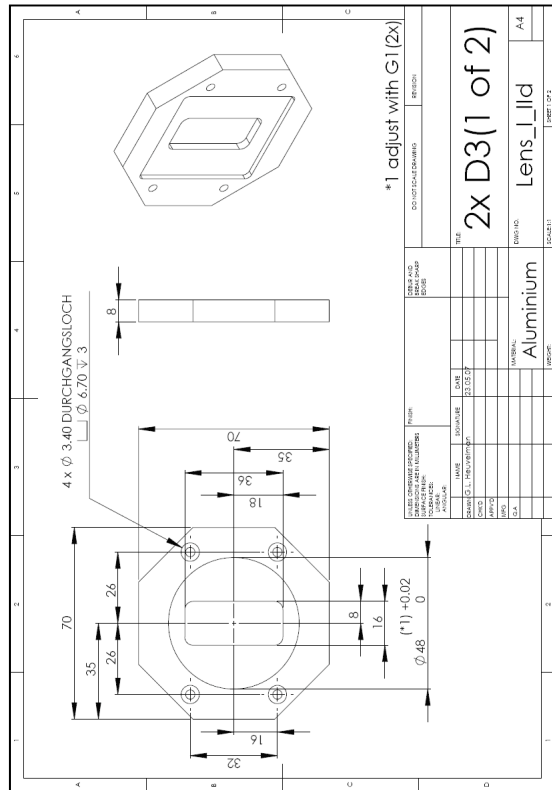
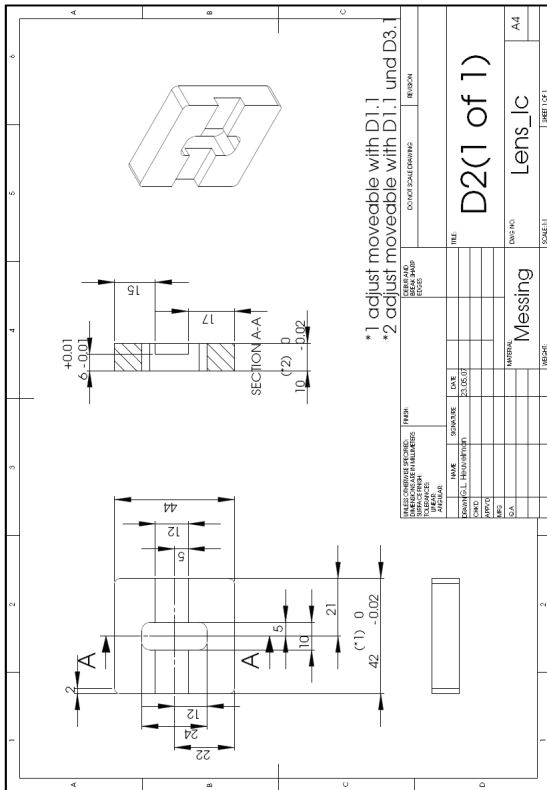
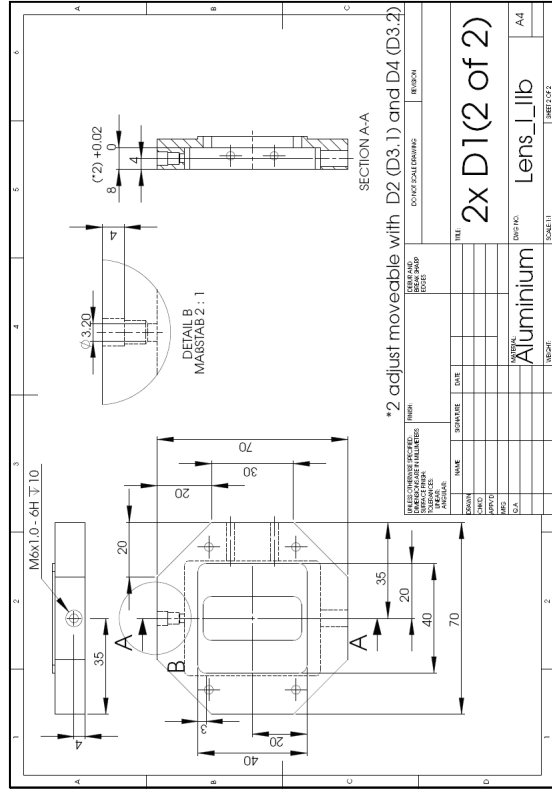
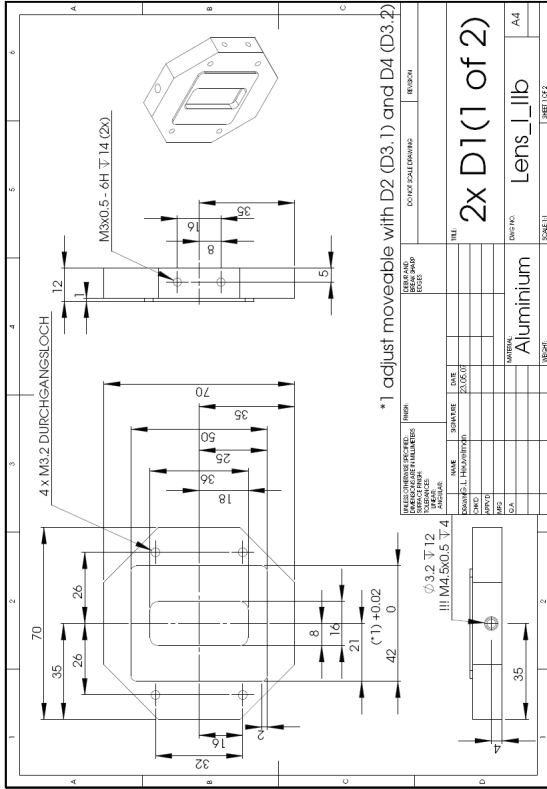


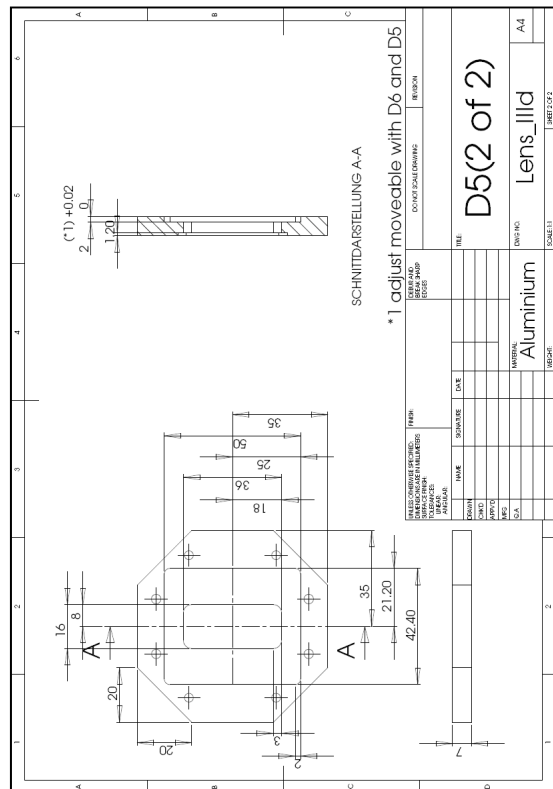
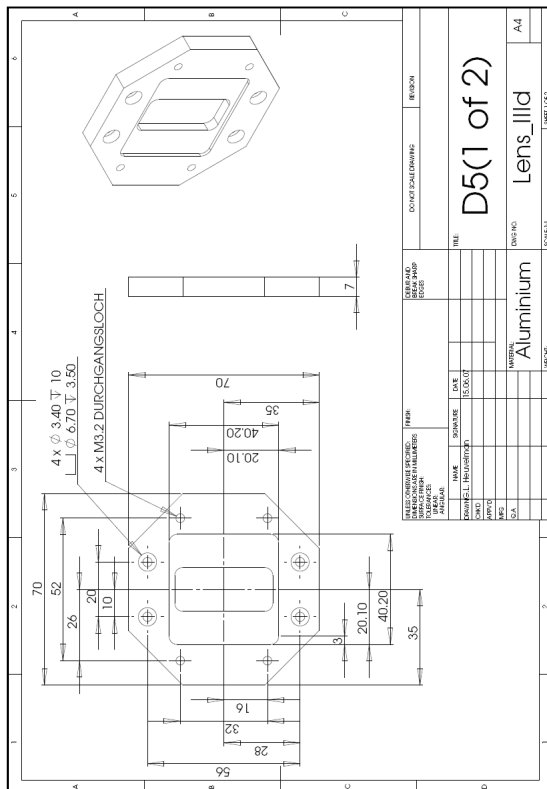
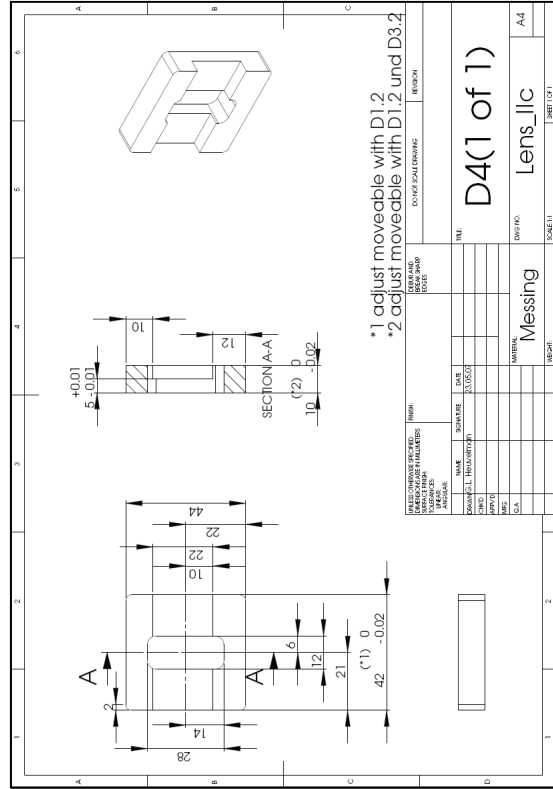
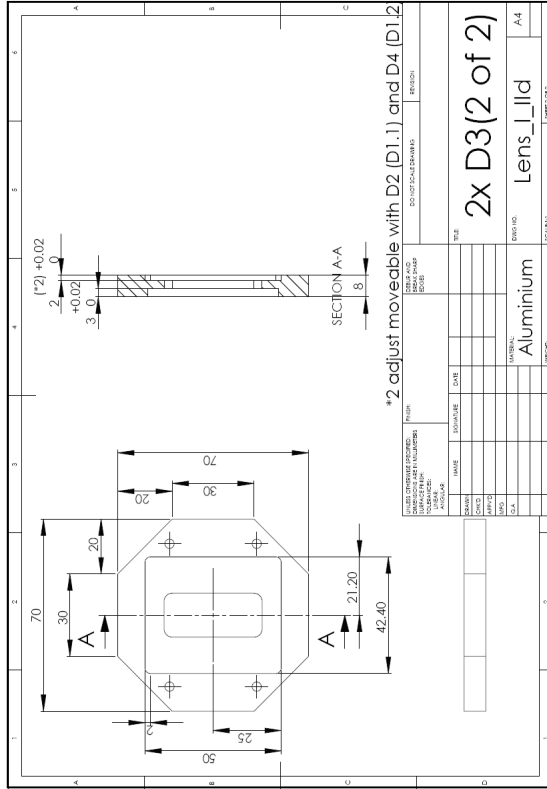


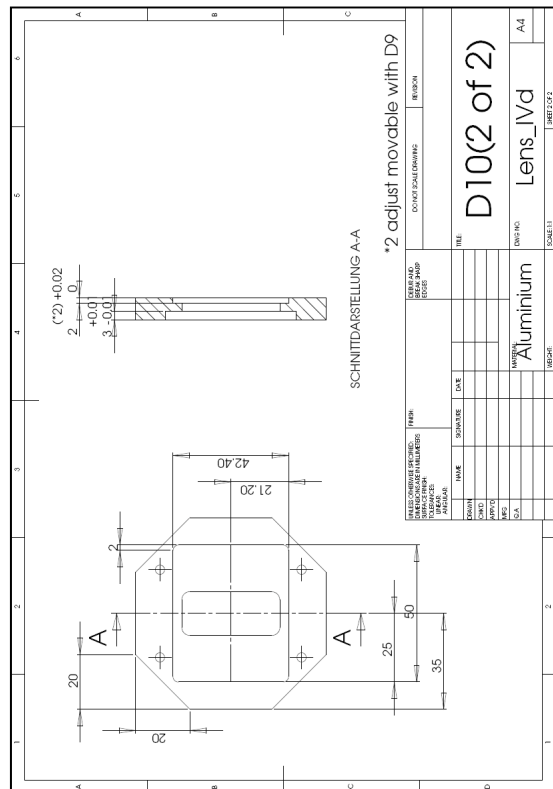
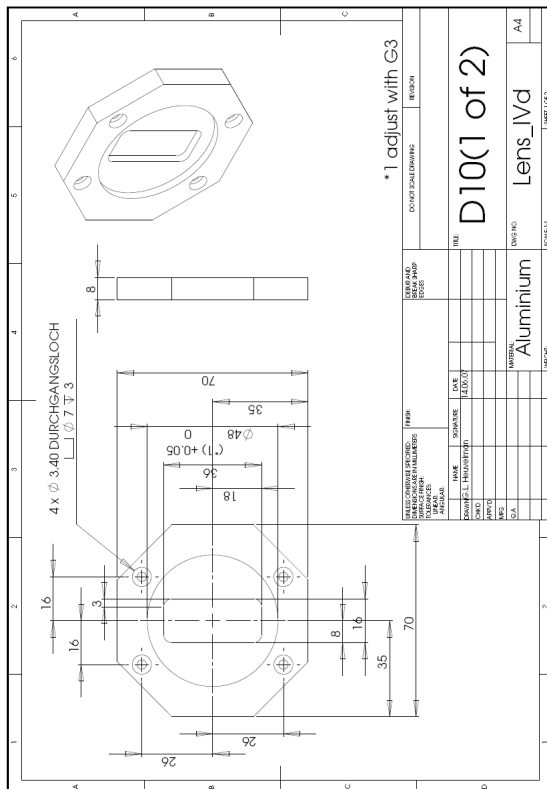
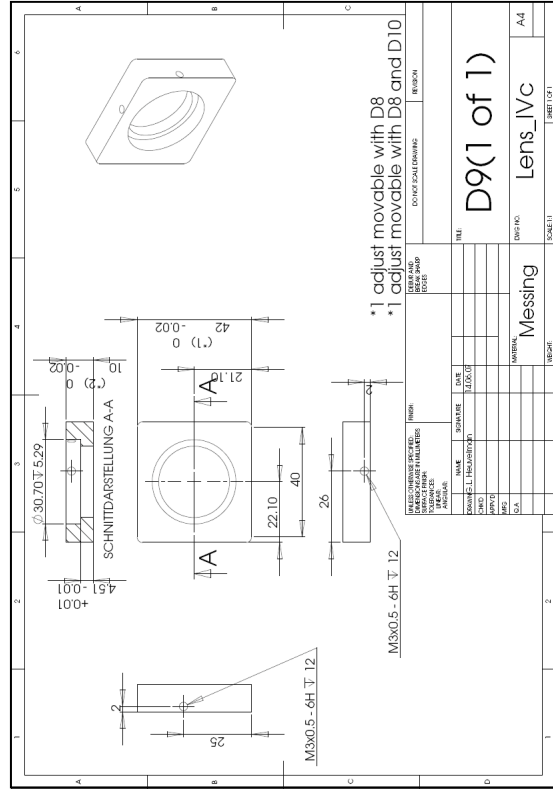
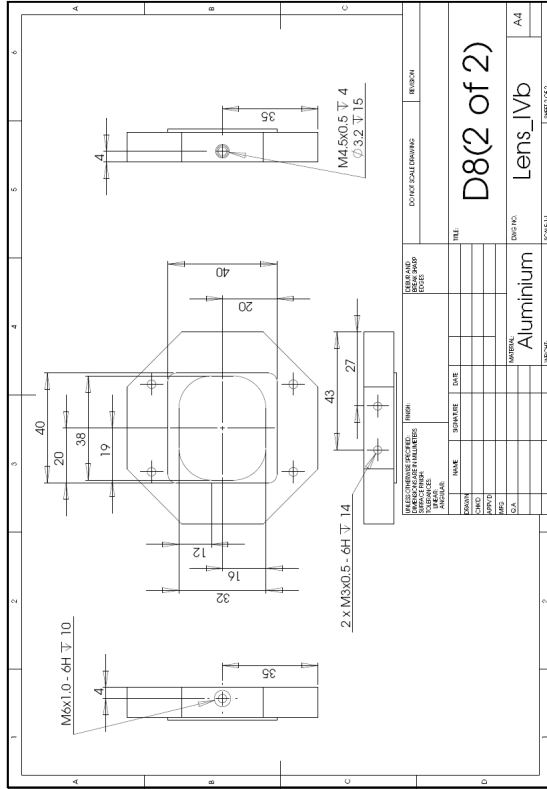
Beam entry module

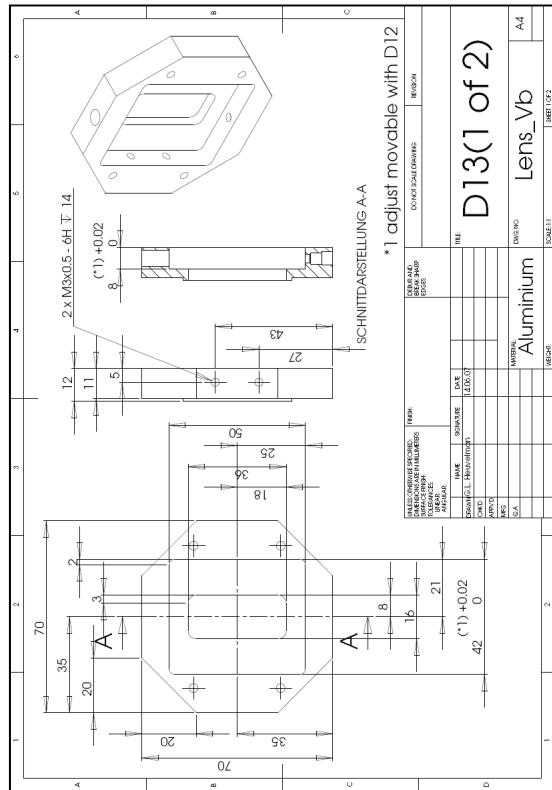
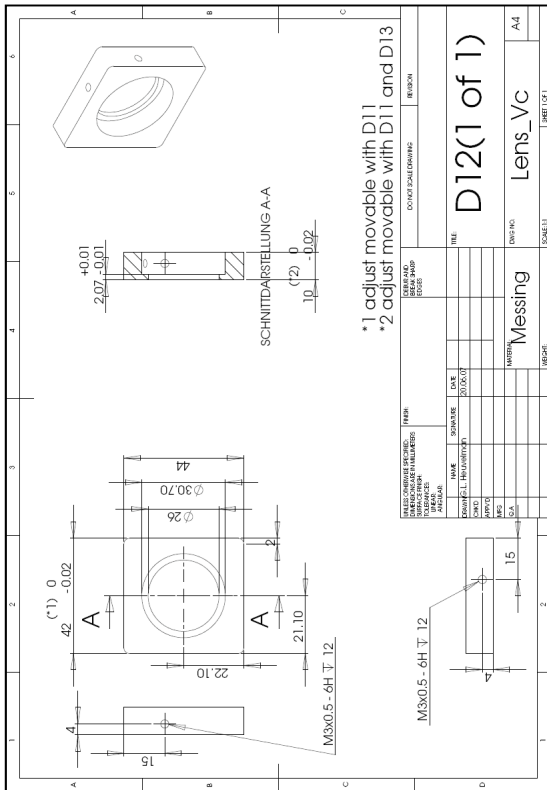
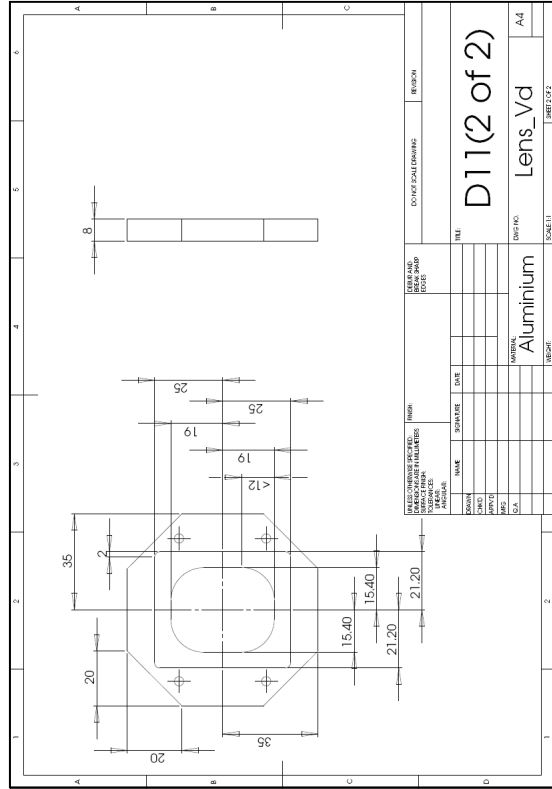
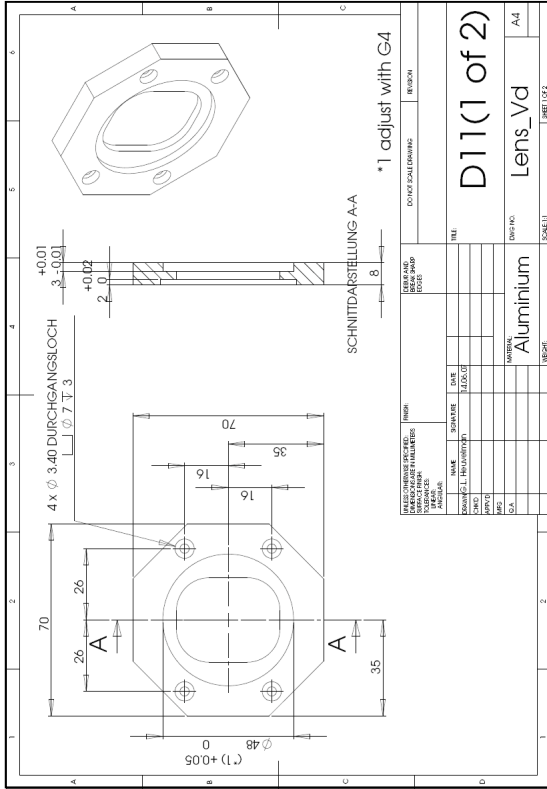


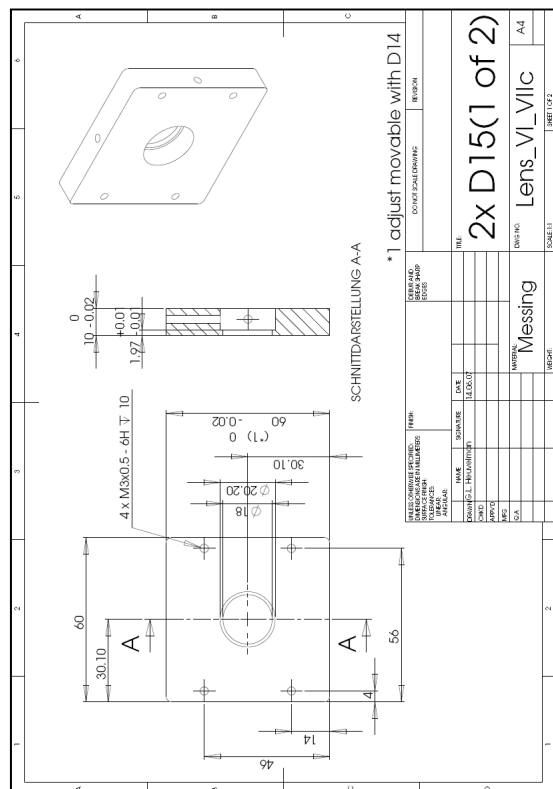
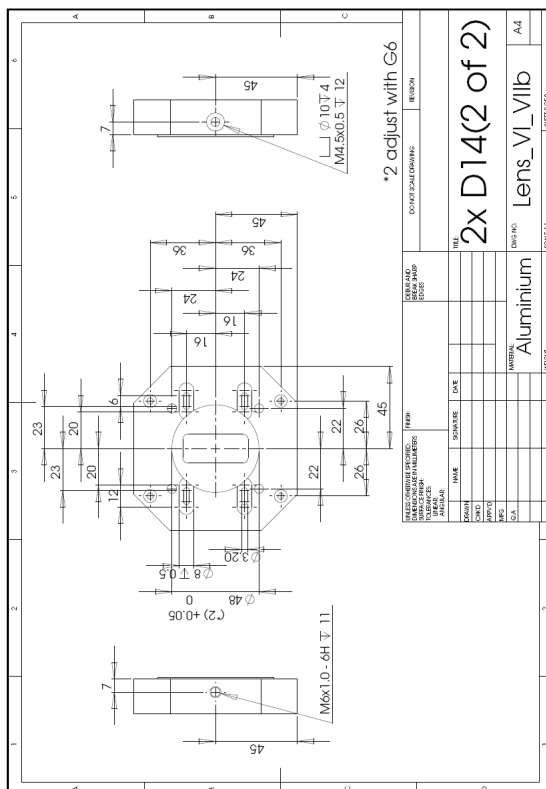
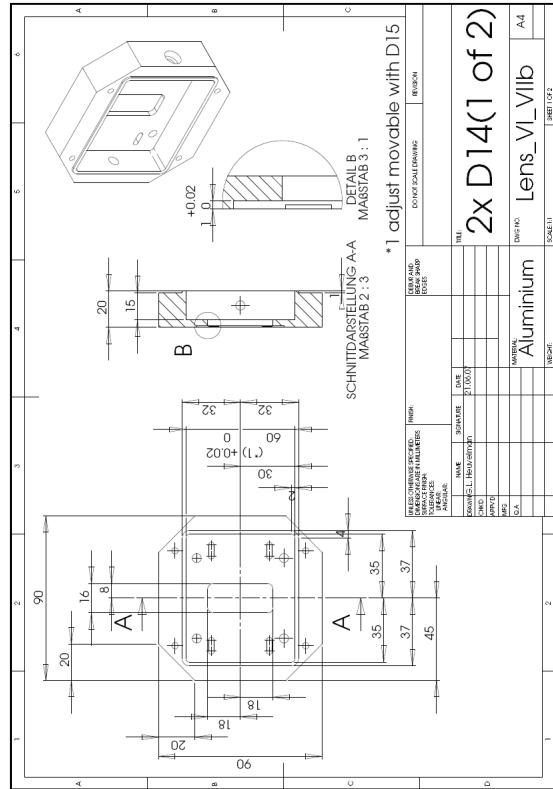
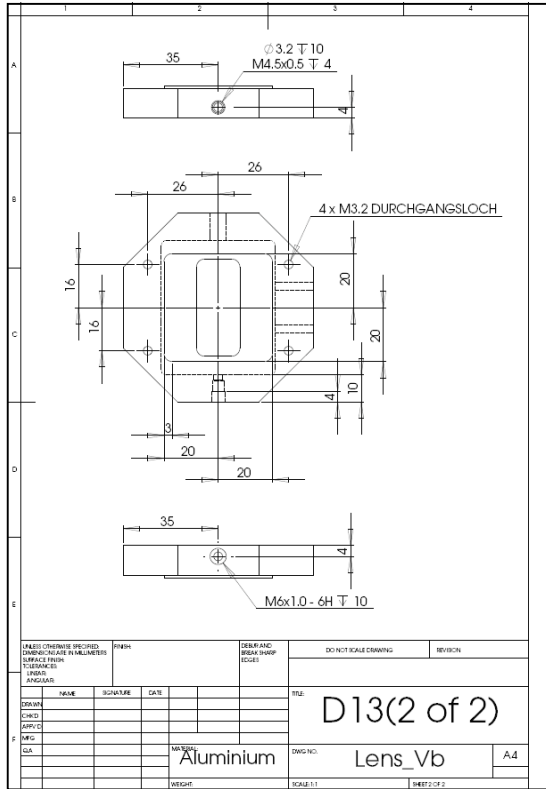
Lens holder modules

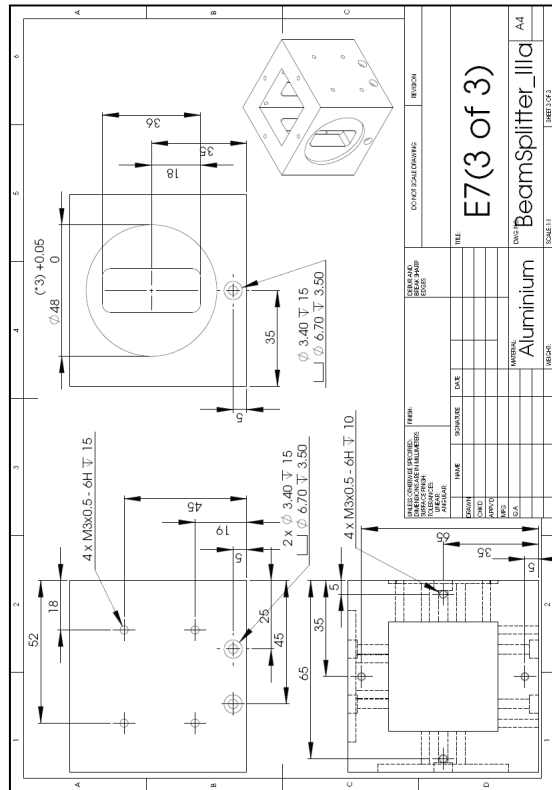
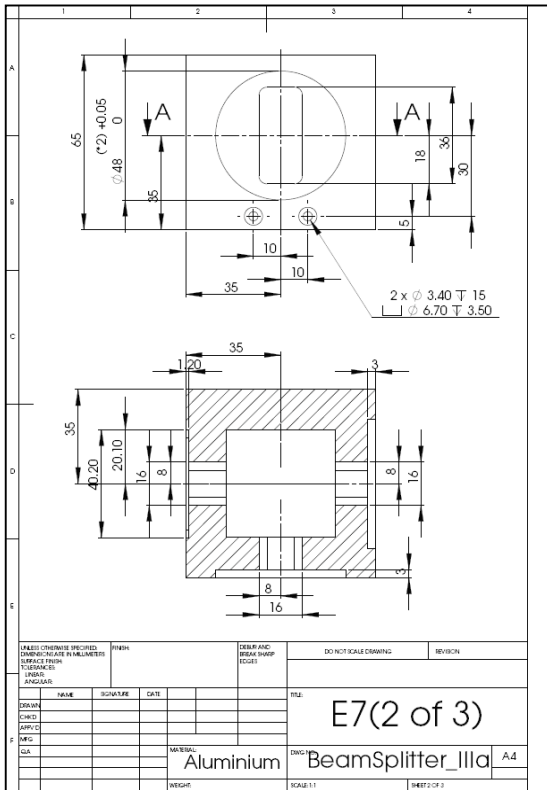
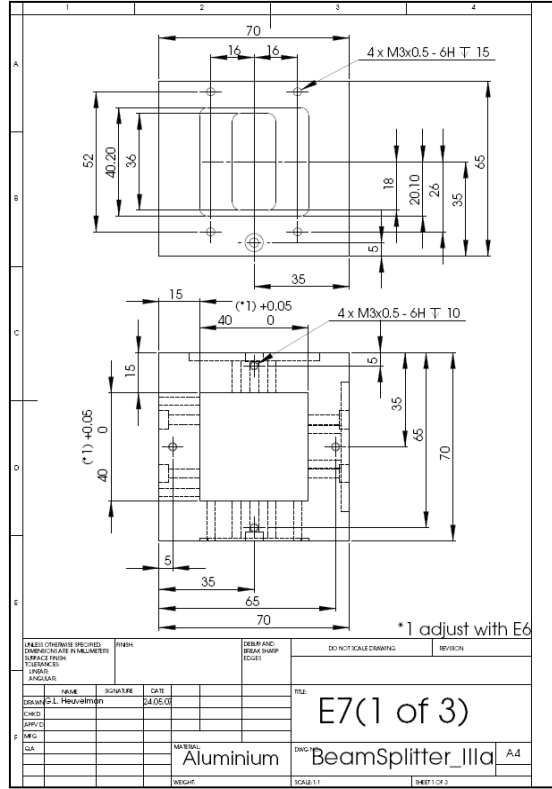
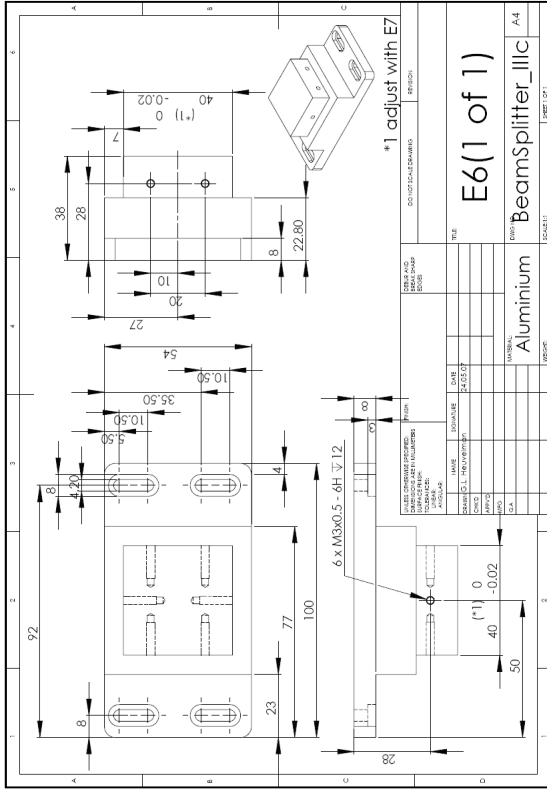


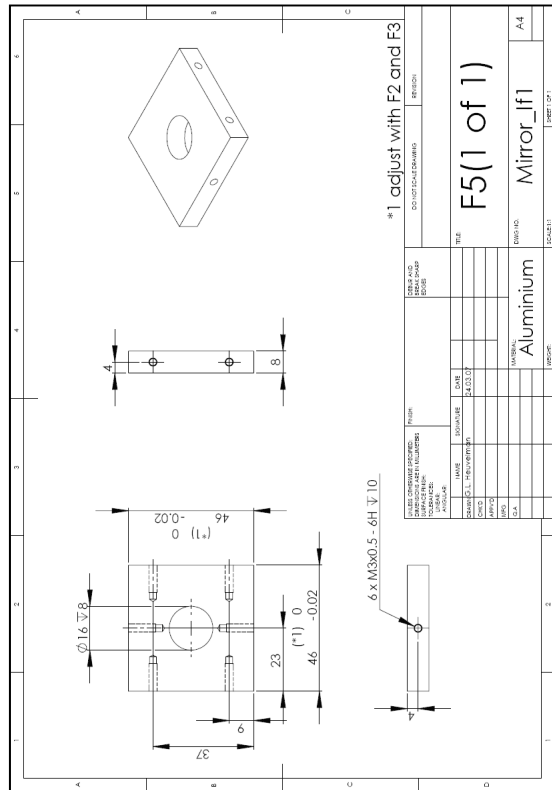
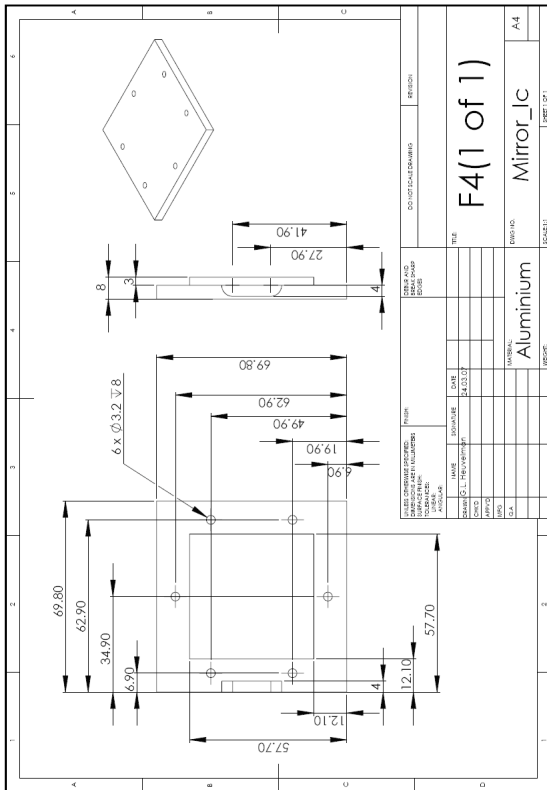
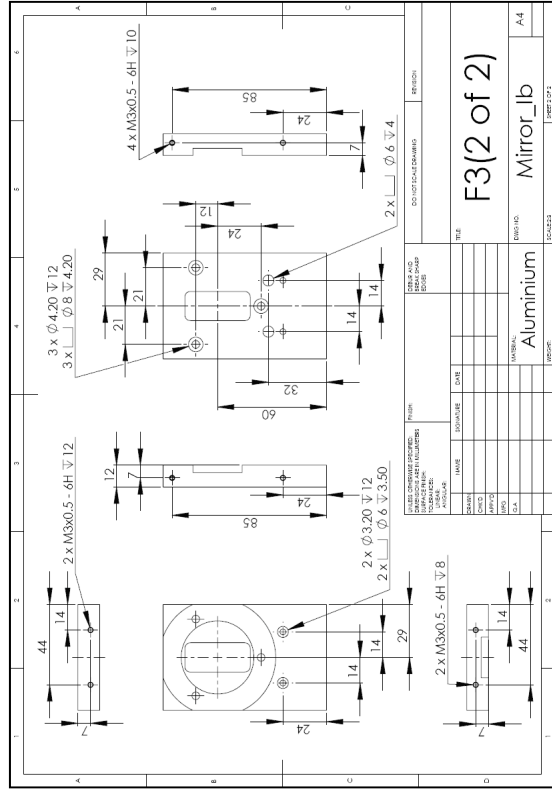
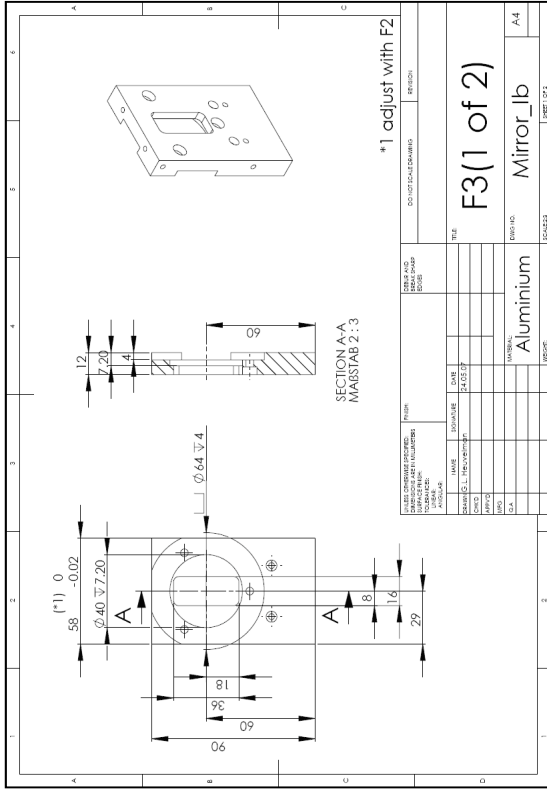




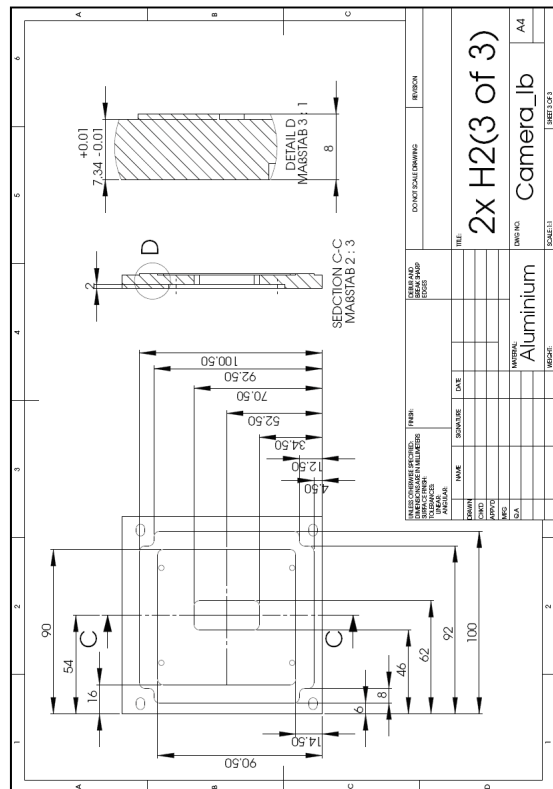
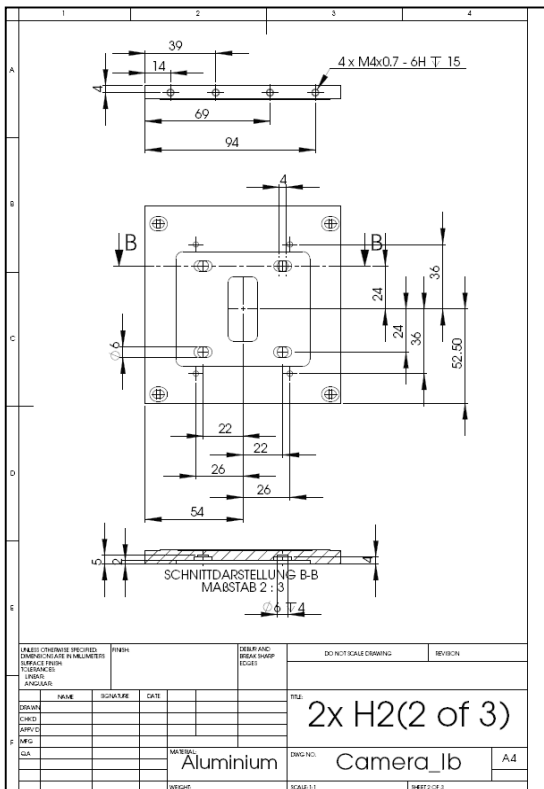
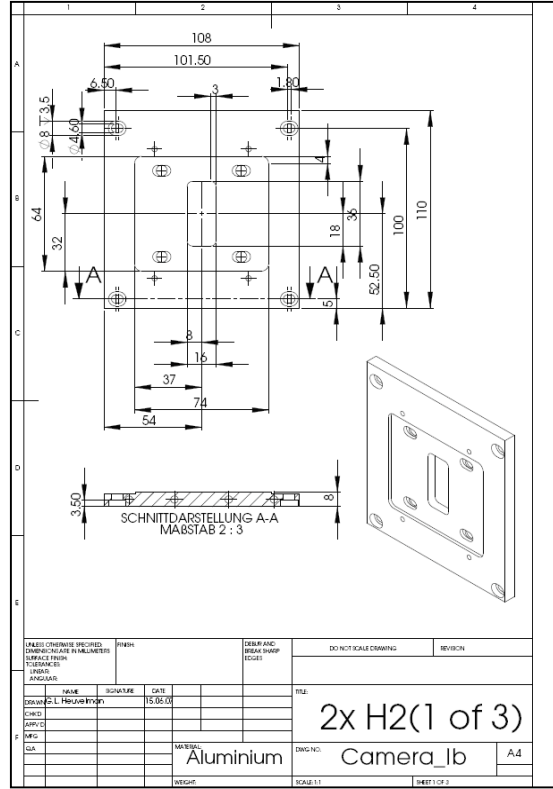
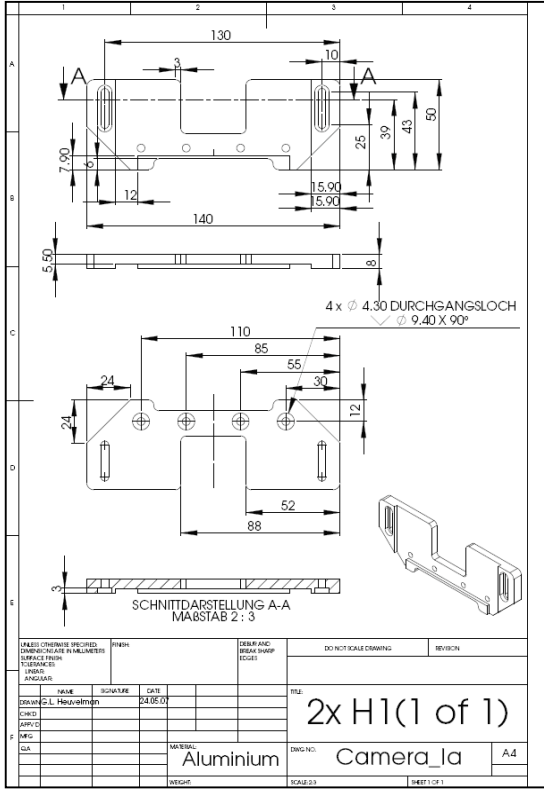








Camera holder module



Laser coupler module

